

Electron and Impurity Transport Studies in the TCV Tokamak

THÈSE N° 5720 (2013)

PRÉSENTÉE LE 2 MAI 2013
À LA FACULTÉ DES SCIENCES DE BASE
CRPP - THÉORIE
PROGRAMME DOCTORAL EN PHYSIQUE

ÉCOLE POLYTECHNIQUE FÉDÉRALE DE LAUSANNE

POUR L'OBTENTION DU GRADE DE DOCTEUR ÈS SCIENCES

PAR

Dávid WÁGNER

acceptée sur proposition du jury:

Prof. H. Rønnow, président du jury
Dr O. Sauter, Dr B. Duval, directeurs de thèse
Dr E. Fable, rapporteur
Dr I. Furno, rapporteur
Dr S. Zoletnik, rapporteur



ÉCOLE POLYTECHNIQUE
FÉDÉRALE DE LAUSANNE

Suisse
2013

To my parents.

Abstract

In this thesis electron and impurity transport are studied in the Tokamak à Configuration Variable (TCV) located at CRPP-EPFL in Lausanne. Understanding particle transport is primordial for future nuclear fusion power plants. Modeling of experiments in many specific plasma scenarios can help to understand the common elements of the physics at play and to interpret apparently contradictory experiments on the same machine and across different machines.

The first part of this thesis deals with electron transport in TCV high confinement mode plasmas. It was observed that the electron density profile in these plasmas flatten when intense electron heating is applied, in contrast to observations on other machines where the increase of the profile peakedness was reported. It is shown with quasi-linear gyrokinetic simulations that this effect, usually interpreted as collisionality dependence, stems from the combined effect of many plasma parameters. The influence of the collisionality, electron to ion temperature ratio, the ratio of temperature gradients, and the Ware-pinch are studied with detailed parameter scans. It is shown that the complex interdependence of the various plasma parameters is greatly simplified when the simulation results are interpreted as a function of the average frequency of the main modes contributing to radial transport. In this way the model is able to explain the experimental results. It was also shown that the same basic understanding is at play in L-modes, H-modes and electron internal transport barriers.

The second part of the thesis is devoted to impurity transport. A multi-purpose gas injection system is developed, commissioned and calibrated. It is shown that the system is capable of massive gas injections to provoke disruptions and delivering small puffs of gaseous impurities for perturbative transport experiments. This flexible tool is exploited in a series of impurity transport measurements with argon and neon injections. The impurities are observed by detecting their radiation in the soft x-ray range. The effect of

varying background plasma parameters on the soft x-ray emissivity temporal and spatial evolution is tested. Argon emissivity displays a rising emissivity signal following the injection with a time constant of about 15 ms, and a clear decay phase about ten times slower than the rise time. Neon stays considerably longer in the plasma, much longer than the expected difference in transport properties. It is shown that centrally deposited electron heating enhances impurity transport, whereas increasing plasma current leads to better argon confinement. Varying the plasma position relative to the injector and the background electron density did not result in significant effect on impurity transport. The shape scans varying the plasma elongation, triangularity and comparing limited and diverted configurations, were inconclusive and possible future experiments are proposed. It is shown that their effect are not sufficiently significant to study them separately, therefore a combined experimental campaign accounting for the various coupling is required. The experimental results are interpreted using a diffusive-advective picture. A tool chain is developed and tested providing transport coefficients for the plasma current and electron cyclotron heating experiments. The inverse diffusive-advective transport equation is solved and the obtained transport coefficients reproduce well the experimental soft x-ray emission profile evolution. It is shown, however, that the soft x-ray evolution is somewhat insensitive to variations in the advection velocity profile, that is a strongly positive (outward) or strongly negative (inward) advection result in very similar soft x-ray evolution. This is shown to be due to both the high sensitivity of SXR radiation on T_e and hence of the limited range of relevance ($\rho_\psi \leq 0.4$) and on the sawtooth activity which acts as a large effective diffusion.

Keywords: diffusive-advective, gyrokinetics, impurity transport, inverse methods, particle transport, quasi-linear, radiation, TCV, tokamak transport modelling, turbulence, x-ray

Version abrégée

Cette thèse porte sur les études du transport d'électrons et celui des impuretés dans les plasmas du Tokamak à Configuration Variable (TCV) situé au CRPP-EFPL à Lausanne. La compréhension du transport des particules est primordial pour la future construction des centrales nucléaires à fusion. La modélisation des nombreuses situations expérimentales contribue à l'identification des éléments communs de la physique sur la même machine et à travers des machines différentes.

La première partie de la thèse traite du transport des électrons dans les plasmas à haut confinement (H-mode) dans TCV. Il a été observé que le profil de densité électronique dans ces plasmas s'aplatit lorsque le chauffage d'électrons intense est appliqué, contrairement aux observations sur d'autres machines où l'augmentation du picage du profil a été signalé. Il est démontré par le truchement des simulations gyrocinétiques quasi-linéaires que cet effet, habituellement interprété comme une dépendance de collisionnalité, découle de l'effet combiné de plusieurs paramètres du plasma. L'influence de la collisionnalité, le rapport des températures électronique et ionique, le rapport des gradients de température, et le Ware-pinch sont étudiés en modifiant ces paramètres du plasma dans les simulations. L'interdépendance complexe des divers paramètres du plasma est largement simplifiée lorsque les résultats des simulations sont interprétés en fonction de la fréquence moyenne réel des modes contribuant le plus au transport.

La deuxième partie de la thèse est consacrée au transport des impuretés. Un système d'injection de gaz polyvalent est commissionné et calibré. Il est montré que le système est capable d'injections massives de gaz pour provoquer des disruptions, aussi bien que de livrer des petites bouffées d'impuretés gazeuses pour des expériences de transport perturbatives. Cet outil flexible est exploité dans une série de mesures de transport d'impureté avec l'injection d'argon et de néon. Les impuretés sont observées en détectant leur rayonnement dans la région spectral des rayons x mous. L'effet des paramètres de plasma sur

l'évolution de l'émissivité de rayons x mous est testée. Suite à l'injection, l'émissivité dû à la présence d'argon augmente, avec un taux de croissance de 15 ms et affiche une phase de décroissance nette d'environ dix fois plus lente que le temps de montée. Neon reste beaucoup plus longtemps dans le plasma que prévu. Il est démontré que le chauffage électronique déposé au centre du plasma amène un transport plus rapide de l'impureté, tandis qu'une augmentation de courant de plasma résulte en un meilleur confinement. Faire varier la position du plasma par rapport à l'injecteur et la densité électronique n'ont pas abouti à des effets significatifs sur le transport d'impuretés. L'expérience avec les variations de l'allongement et de la triangularité du plasma et la comparaison des configurations limitées et divergées, ne sont pas concluantes et des futures expériences sont proposées. Les résultats expérimentaux sont interprétés à l'aide d'une image par diffusion-advection. Une chaîne d'outils est développée et testée, donnant des coefficients de transport pour les expériences avec la variation du courant du plasma et celles sans et avec chauffage électronique cyclotron. L'équation diffusion-advection inverse est résolue et les coefficients de transport obtenus reproduisent bien l'évolution temporelle des profils de l'émissivité des rayons x mous. Cependant, on montre que l'évolution des rayons x mous est très insensible aux variations du profil de vitesse d'advection: une vitesse d'advection très positive (vers l'extérieur) ou très négative (vers l'intérieur) donne une évolution similaire de rayons x mous. Il a été montré que ceci est dû à la fois à la dépendance forte de l'émission x-mous à la température, et à la région sensible réduite à $\rho_\psi \leq 0.4$, et aux effets des dents-de-scie qui induisent une diffusion effective importante.

Mots clés: diffusive-advective, gyrocinétique, méthode inverse, modélisation du transport. quasi-linéaire radiation, rayons x, TCV, tokamak transport de particules, turbulence

Acknowledgements

I thank my supervisor Oliver Sauter without whom this thesis would not have been possible. His physical intuition, practical attitude and fast thinking prevented me being lost in the blind alleys of plasma physics. I warmly thank Basil P. Duval for sharing his blunt thoughts with me improving my critical thinking, even before he officially joined Olivier and me as supervisor. His remarks and advises are greatly helped to improve the manuscript.

The multi-purpose gas injection system described in chapter 4 was designed and installed by Hungarian colleagues of the Wigner Research Centre for Physics, Budapest: the help of Bencze Attila, Berta Miklós, Tál Balázs and Veres Gábor in the commissioning and calibration experiments is greatly appreciated. The fruitful discussions with E. Fable, N. Howard, F. Sattin, B. Teaca are greatly appreciated. I thank R. Dux for providing the STRAHL code and the filter coefficients for my simulations.

The everyday work around the TCV would have been impossible without the contribution of several technicians. The excellent work of Yanis Andr  be, Claude Raggi and Pascal Conti is proven to be invaluable. I could not have imagined a better person to share my office with than Lucia Federspiel. I had great pleasure in organizing the PhD seminars with Thibaut Vernay.

I thank Mario Konstantin Bucciarelli and Adrienne Butty Bucciarelli for introducing me in the world of tango in which a lot of pleasure and relaxation I found with my tango partner Sylvie Kohli.

I am truly indebted to M  rki J  nos and his family for helping me to start my new personal and professional life in Lausanne.

The weekend activities with absolutely no connection to the thesis were of great help to arrive to the Monday morning meeting with a clear head. I had a great pleasure in exploring the wonderful Swiss landscape hiking with Roger Motz, Falk Braunm  ller and Josef Kamleitner. The bike rides we did together with Cs  rdi G  bor, Halidi Nadia and

Kees de Meijere will never be forgotten. Running and competing with Tim Hohm and Kutalik Zoltán was always a pleasure. The parties and discussions with Kiss Gabriela, Coralie Rochat, Wouter Vijvers and Jeroen de Haart were memorable.

I am truly grateful for my friends Jahn Kornél and Szepesi Gábor for their availability and everyday support. Without them it would have been impossible to keep going. No words can describe how lucky I am to have Annamaria Mosetto by my side. Finally, I thank my family, especially my parents to whom I dedicate this thesis.

Lausanne, 14 February 2013

Contents

Abstract	v
Version abrégée	vii
Acknowledgements	ix
Symbols and definitions	xiii
1 Introduction	1
1.1 Nuclear fusion motivated plasma physics	1
1.2 The need for particle transport measurements and modeling	2
1.3 Outline of this dissertation	3
2 Elements of transport studies in TCV	5
2.1 The TCV experiment	5
2.2 Transport processes	14
2.3 Plasma emission	26
2.4 Numerical tools	38
3 Density profile behavior in H-modes	41
3.1 Experiments	42
3.2 Simulation results	48
3.3 Discussion	59
3.4 Summary	61
4 Multipurpose gas injection system	63
4.1 Gas injection experiments	63

4.2	Operating principles and setup	66
4.3	Calibration	69
4.4	Commissioning experiments	75
4.5	Summary	79
5	Impurity transport experiments	81
5.1	Ar and Ne injections into OH plasmas	82
5.2	Electron density scan	87
5.3	Plasma position relative to the injector	90
5.4	Current scan	94
5.5	ECH power	98
5.6	Shape scan	98
5.7	Multi-puff stationary experiments	110
5.8	Summary	114
6	Transport studies	117
6.1	Modeling impurity injection	118
6.2	Effect of ECH	134
6.3	Current scan	138
6.4	Analysis of the multi-puff experiments	140
6.5	On the central profile of $n_Z(r)$	147
6.6	Summary	148
7	Summary and conclusions	161
A	Diffusive-advective systems	165
A.1	Direct solution	165
A.2	Inverse solution	168
	Bibliography	172
	Publications and Conference Contributions	187

List of common symbols, definitions and abbreviations

CXRS Charge Exchange Recombination Spectroscopy

DA Diffusive Advective

DMPX Duplex Multiwire Proportional X-ray counter

DMV Disruption Mitigation Valve

ECH, ECRH Electron Cyclotron Resonance Heating

GK gyrokinetic

ITG Ion Temperature Gradient

LBO Laser Blow-Off

OH Ohmic Heating

SMBI Supersonic Molecular Beam Injection

SXR Soft X-Ray

TCV Tokamak à Configuration Variable

TE, TEM Trapped Electron, Trapped Electron Mode

VUV Visible Ultra-Violet (spectroscopy)

notation	description	unit
a, R	minor, major radius	m
α_k	rate coefficient of recombination <i>to</i> the $(k + 1)$ -th state	m^3s^{-1}
c_s	ion sound speed, $\sqrt{T_i/m_e}$	ms^{-1}
D, V	diffusion coefficient, advection velocity	m^2s^{-1} , ms^{-1}
$\Gamma_e, \Gamma_i, \Gamma_Z$	electron, ion, impurity particle flux	context
n_e, n_i, n_Z	electron, ion, impurity density	m^{-3}
n_Z^k	impurity density of the k -th charge state	m^{-3}
Q_e, Q_i, Q_Z	electron, ion, impurity heat flux	context
ρ_ψ	normalized poloidal flux defined by equation 2.1	-
S_k	rate coefficient of ionisation <i>from</i> the k -th state	m^3s^{-1}
T_e, T_i, T_Z	electron, ion, impurity temperature	eV
χ_e^{PB}	power balance electron heat diffusivity	m^2s^{-1}
ω_r, γ	real mode frequency and growth rate	c_s/R
κ, δ	elongation, triangularity	-
q	safety factor	-
y_k	fractional abundance of the k -th charge state, $y_k \equiv n_Z^k/n_Z$	-
Z	magnetic axis vertical position; $Z = 0$ being the midplane	m
	atomic number	-

Table 1: List of common symbols and definitions

The following conventions are used:

- all the units are in SI, except the temperature which is measured in eV,
- $\omega > 0$ (< 0) for modes propagating in the ion (electron) diamagnetic direction.
- positive flux means outward flow

Chapter 1

Introduction

1.1 Nuclear fusion motivated plasma physics

The grand goal to harness nuclear fusion to provide clean and practically abundant energy source on Earth brought a new part of classical physics alive [Freidberg, 2007]. At temperatures as high as 10 keV, where light nuclei can overcome their mutual repulsion to fuse and form a heavier nucleus, matter presents itself as *plasma*: a mixture of charged particles, ions and electrons. For six decades attempts have been made to develop and optimize ways whereby hot plasma can be confined as the heart of a fusion reactor. Among others, toroidal devices applying strong magnetic field to hold the charged particles together, in particular tokamaks [Wesson, 2011], are now operated in many research laboratories all around the world, as testbeds for magnetic confinement fusion plasma experiments. Experiments [Keilhacker et al., 1999] demonstrated that a plasma of deuterium-tritium mixture can deliver significant amount of fusion power. Today most tokamaks use deuterium as working gas, for at typical values of temperatures (several keV) in the core of a tokamak plasma, the production of high energy neutrons and the activation of the device's structure can be avoided, making the experimentation easier.

Tokamak plasmas are never pure, that is besides the major constituent, the plasma intrinsically contains other species, for example carbon and metals from structural elements. These are considered *impurities*, and their presence is usually disadvantageous, since they dilute the nuclear fuel in a reactor, decreasing its performance. On the other hand, radiation of impurities with high charge number at the plasma edge could help to mitigate the enormous power exhausted from the plasma and protect the plasma facing components. In

today's fusion experiments non-intrinsic impurities such as argon, neon for example, can be injected externally into the plasma to diagnose and study their behavior.

Measuring even such fundamental quantities as density and temperature of a hot plasma is cumbersome. Alongside the development of plasma physics, the field of plasma diagnostic has emerged [Hutchinson, 2005]. Passive detection of electromagnetic fields generated by the plasma or the emitted radiation; or active probing of the plasma with electromagnetic or particle beams are now routinely used to measure plasma parameters.

1.2 The need for particle transport measurements and modeling

A magnetically confined plasma exhibits a plethora of complex phenomena which affects the redistribution of particles and heat inside the device. The study of these transport processes are in the focal point of fusion oriented plasma physics research and understanding transport mechanisms in fusion plasmas is an important goal on the way towards energy producing fusion reactors.

In recent years numerous works have been devoted to particle transport studies (see the most recent review [Angioni et al., 2009] and references therein). The experimental observations and the theoretical predictions show good qualitative agreement. It is now widely accepted that the density profile in the core of tokamak plasmas is mainly tailored by turbulent mechanisms, similarly to the temperature profile. The research interest is turning towards quantitative comparison between modeling and experiments. To this end, the predictions of transport models are compared with experiments under different experimental conditions, scenarios on the same machine and across different machines. Fusion experiments, in particular tokamaks, are highly specialized and an exact reproduction of other machine's experiment is difficult, often impossible. This variability necessitates modeling various specific plasma scenarios and trying to identify the common elements of the physics, if any, in the sometimes, apparently, contradictory experiments.

Prior to this thesis, electron and impurity transport experiments in the Tokamak à Configuration Variable (TCV) had motivated further research in two main directions. Firstly, under certain experimental conditions, the electron density profile was seen to flatten when intense electron heating was applied. This contrasts with other experimental devices where

an increase of the profile peakedness is documented. A future fusion power plant is very likely to be a high temperature device [Ward, 2010], therefore a solid understanding of the density profile's response to heating is crucial. Secondly, in previous TCV impurity transport experiments [Scavino, 2002], an outward convection, resulting in hollow density profiles, of metallic impurities was identified. However, experiments on other machines support the theoretical prediction that the transport of impurities is governed by similar mechanisms to those of the bulk species predicting peaked impurity density profiles. In this thesis, a combination of experimental and numerical work, seeks to re-examine these atypical dependences.

1.3 Outline of this dissertation

This thesis aims to contribute to the understanding of transport of electrons and non-intrinsic impurities in tokamak plasmas: experimental and numerical techniques are discussed and applied to study electron and impurity, in particular argon and neon, transport in TCV.

Chapter 2 collects the ingredients necessary to perform particle transport experiments. Firstly, TCV and its diagnostic apparatus are presented. Then, transport processes in magnetized plasmas and a quasi-linear transport model are summarized. Parts of atomic physics are introduced to show how radiation from impurities is generated. Finally some numerical codes used in this thesis are presented.

Chapter 3 deals with electron transport: a recently developed quasi-linear gyrokinetic model is used to predict the peakedness of the electron density profile in high confinement (H-mode) TCV plasmas. It documents the unusual behavior of the electron density profile, namely that the profile peakedness is reduced when the collisionality decreases. It is shown that a quasi-linear model can explain the observed experimental behavior in this particular plasma scenario in the same way as it explains L-mode plasmas.

In Chapter 4 the commissioning and calibration of a new multi-purpose gas injection system is presented with which gaseous impurities can be injected into the plasma. This system is used in the argon and neon injection experiments in TCV, presented in Chapter 5, to map possible dependences of transport on various plasma parameters such as plasma current, shape and heating power. The injected impurities are diagnosed using TCV's soft x-ray detection system.

In Chapter 6 a tool chain is presented that is used to infer the impurity transport coefficients from the SXR in terms of a diffusive-advective model. Numerical simulations are compared to the observed experimental trends, in particular the relationship between the soft x-ray radiation peakedness and the shape of the impurity density profile is discussed.

Finally, in Chapter 7, summary and concluding remarks are given.

Chapter 2

Elements of transport studies in TCV

The present chapter provides the necessary background to understand the material in the rest of the thesis. Section 2.1 presents TCV itself and its main diagnostic tools. Section 2.2 briefly introduces transport processes in a toroidally confined plasma. Section 2.3 summarizes the atomic physics related to radiation emission of impurities in hot plasmas. Special attention is devoted to the emission in the SXR range. Finally, Section 2.4 enumerates the software packages exploited in the analysis and modelling.

2.1 The TCV experiment

2.1.1 Tokamak à Configuration Variable (TCV)

The Tokamak à Configuration Variable (TCV) is a device ($R = 0.88\text{ m}$, $a = 0.25\text{ m}$, $I_p \leq 1\text{ MA}$, $B_t \leq 1\text{ T}$, $\kappa \leq 2.8$) with the mission of supporting ITER and exploring alternative solutions for use in a fusion reactor. For the latest review of progress and scientific results see the reviews of Coda [2011], Coda and The TCV Team [2012] and the references therein. Confined plasmas can be placed virtually anywhere in the vacuum vessel thanks to the 16 independent shaping coils (blue coils in figure 2.1). In practice, however, to obtain a good diagnostic coverage, plasmas at, or slightly above the midplane are preferred. We shall return to this point later in Section 2.1.2.

TCV possesses a powerful 4.5 MW electron cyclotron resonance heating (ECRH) system [Goodman and the TCV team, 2008] (X3 ECH 118 GHz, $3 \times 0.5\text{ MW}$, 2 s, top launch and X2 ECH / ECCD 82.7 GHz, $6 \times 0.5\text{ MW}$, 2 s, side launch) with real-time steerable launchers

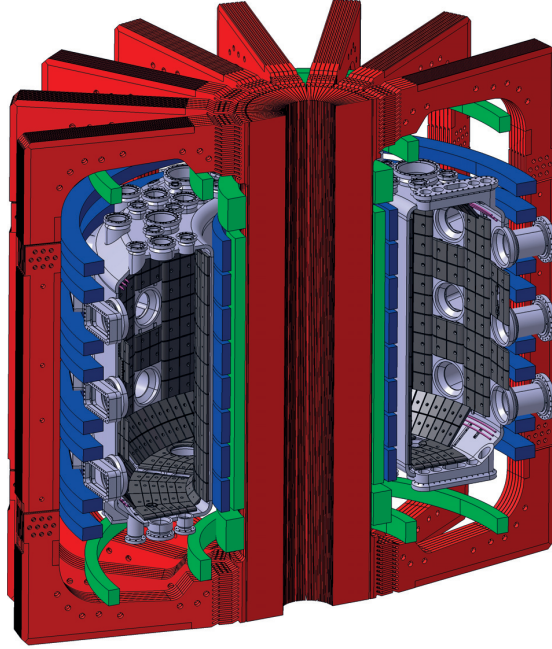


Figure 2.1: Overview of the TCV coil system. Courtesy of M. Toussaint.

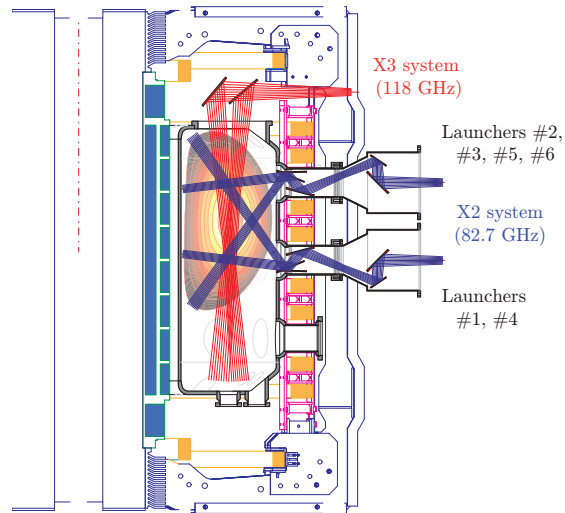


Figure 2.2: The TCV electron-cyclotron resonance heating (ECRH) system.

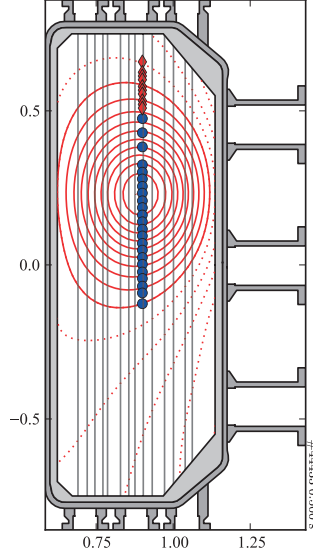


Figure 2.3: Measurement locations of the main (circles) and edge (diamonds) Thomson-scattering system and the far-infrared interferometer (FIR, vertical lines) on TCV.

(figure 2.2). The X3 system was used in experiments presented in Chapter 3. Plasmas in some of the experiments described in Chapter 5 were heated with the X2 system.

2.1.2 Density and temperature measurements

Profile measurements, that is the measurement of spatial variations, of local quantities such as density and temperature, are indispensable for any meaningful transport analysis. In particular, electron density and electron temperature profile measurements are of utmost importance which are provided by the Thomson-scattering (TS) system and the Far-Infrared Interferometer (FIR) on TCV. The Charge-Exchange Recombination Spectroscopy (CXRS) system provides temperature and density profiles of C^{6+} in addition to poloidal and toroidal rotation velocity profiles.

Thomson-scattering system

Thomson scattering describes the interaction of an electromagnetic wave with free electrons. The electrons are accelerated in the oscillating field of the incident electromagnetic wave and re-emit radiation. The frequency of the scattered radiation is shifted with respect to that of the incident wave due to the Doppler-effect. The power of the scattered light collected by the optical system is proportional to the electron density and from the Doppler-broadening the electron temperature can be deduced.

The Thomson scattering system is the main diagnostic tool for electron density and temperature profile measurements on TCV. Here only the most important characteristics of this system are outlined, further details can be found in Section 3 of Pitzschke [2011]. The profiles are measured with a Nd:YAG laser beam passing through the plasma in a vertical direction at $R = 0.9$ m (midradius of the TCV vessel). Wide-angle camera lenses, installed on 3 horizontal ports in sector 5, collect the scattered light from the observation volumes in the plasma and focus it onto sets of fiber bundles. The fiber bundles relay the collected light to the spectrometers.

The heat and particle transport time scales along the magnetic field lines exceed those perpendicular to them. Density and temperature are assumed to be *flux-surface quantities*, constants on a flux-surface. The flux surfaces can be labeled by arbitrary monotonic function of flux-surface quantities, providing a radial coordinate. The radial flux label throughout this thesis is

$$\rho_\psi = \sqrt{(\psi - \psi_0)/(\psi_b - \psi_0)}, \quad (2.1)$$

where ψ is the poloidal flux, ψ_0 and ψ_b are the poloidal flux at the magnetic axis and the plasma boundary, respectively.

The 35 observation positions together with the contours of constant poloidal flux are shown in figure 2.3. The Thomson-system covers the region from $Z = -17$ cm to $Z = +66$ cm, relative to the vessel's horizontal midplane, with a spatial integration length of 12 to 36 mm depending on the channel location. Spatial channels with higher resolution (lower integration length) are shown with diamonds for observation of plasmas exhibiting large gradients in electron temperature and density near the plasma edge.

Far infrared interferometer

A 14-channel Mach-Zehnder type interferometer is used to measure the line-integrated density along parallel chords in the vertical direction. The principle of interferometry and technical details of this system can be found in Section 2.5.2 of Schlatter [2009] and in the references therein. The system comprises a far infrared laser, pumped by a CO₂ laser, emitting a continuous wave at 214 μm , and a multi-element detector unit (InSb hot-electron bolometer). The laser beam is divided into a reference beam and 14 probe beams passing vertically through the plasma at different radial positions. The probe beams are shown as vertical lines in figure 2.3. When the probe beams pass through the plasma, the difference in refractive index will cause a phase delay with respect to the reference beam. Given the wavelength and polarization of the FIR beams, the refractive index of the plasma is directly related to the electron density. Therefore, the system provides continuous measurements of the line-integrated density along 14 chords. The measurement along the central chord is used during the discharge to regulate the line-integrated plasma density by means of a direct feedback onto the gas feed.

Ion density and temperature measurement

The Charge Exchange Recombination Spectroscopy (CXRS) provides local measurement of ion temperature, velocity and density from the observation of Doppler-shift and line broadening of impurity line emission. The upper state of this transition is populated by charge exchange reaction between an impurity ion and a neutral atom, hence the name. Since carbon is often the most abundant impurity in TCV whose inner wall is covered with carbon tiles, the CXRS spectrometers are optimized to observe the CVI($n = 8 \rightarrow 7$) line at 529.1 nm. The density and temperature are inferred from the intensity and the broadening of this spectral line, respectively. The neutral atoms provided by the Diagnostics Neutral Beam Injector (DNBI) is hydrogen. A more detailed description of the system can be found in Chapter 2 of [Bortolon, 2009].

Figure 2.4 shows the schematic of CXRS system on TCV. The neutral beam is injected through a midplane port in Sector 14 and ‘illuminates’ the plasma along its path: the neutral atoms from the beam donate an electron to fully stripped carbon, creating excited hydrogen-like C⁵⁺ ions with a relatively simple spectra. The observation locations are chosen such that a near perpendicular view in the horizontal and vertical plane is achieved:

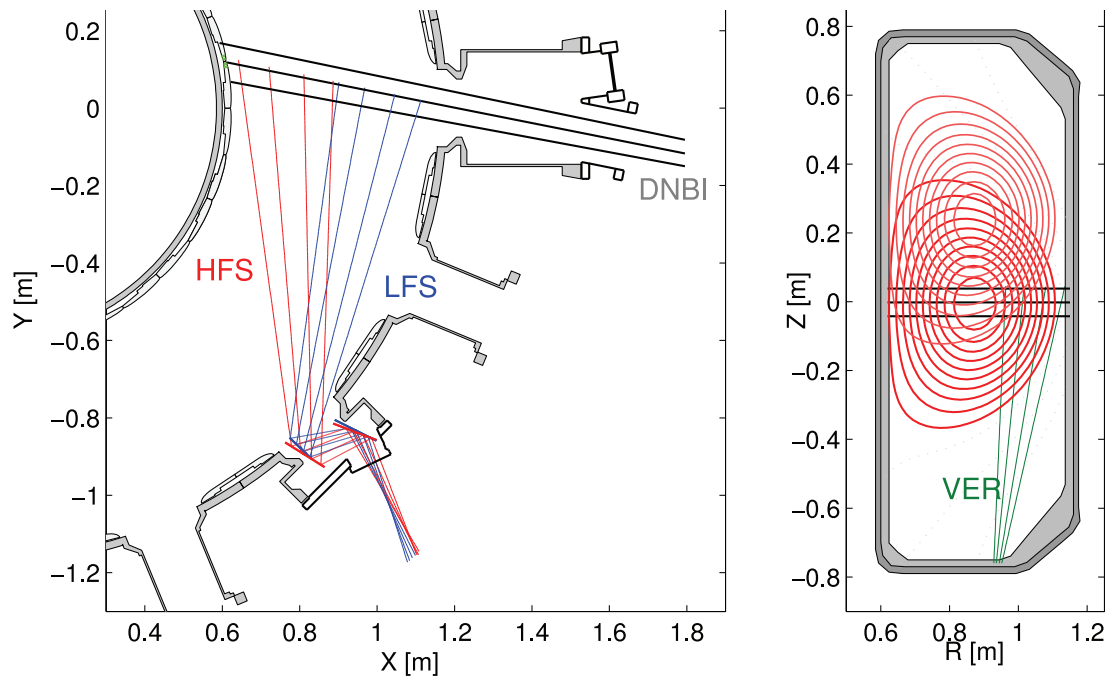


Figure 2.4: Overview of the TCV Charge Exchange Spectroscopy System (reproduction of Figure 2.7 in [Bortolon, 2009]). Note that not all the lines of sight are shown.

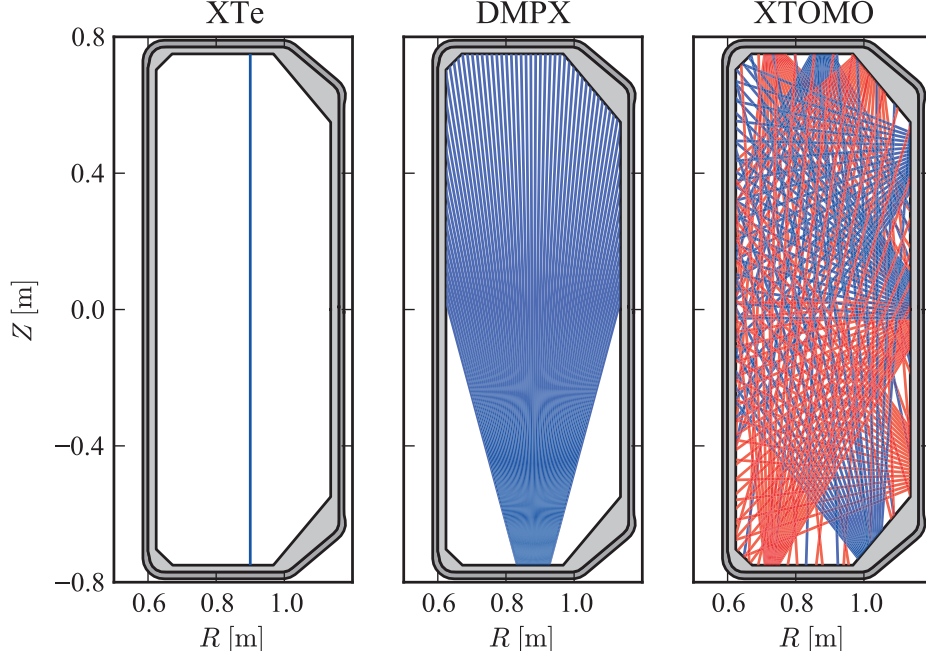


Figure 2.5: X-ray diagnostics on TCV. Complexity increases from left to right: XTe with a single chord, DMPX a multi-chord single-camera, and XTOMO a multi-chord multi-camera system.

the same sector for the vertical system and Sector 12 for the horizontal system. We see that the lines of sight give a good coverage for plasmas near $Z = 0$, however for plasmas above (or below) the midplane the inner flux surfaces are not sampled. For a slightly elongated ($\kappa = 1.2$) plasma at $Z = 23$ cm CXRS measurements are only available outside $\rho_\psi \approx 0.8$.

The working gas (typically deuterium in TCV) is fully ionized in the core, however, due to charge-exchange reactions with neutral atoms coming from the neutral gas surrounding the plasma, a certain number of hot core ions are neutralized and they may escape the plasma. The neutral particle analyzers (NPA) [Karpushov et al., 2006] measure the energy distribution of these neutral particles. From their energy distribution the central ion temperature can be estimated [Schlatter, 2009].

2.1.3 Soft x-ray diagnostics

In tokamak plasmas the soft x-ray radiation spectrum (x-ray radiation with energy < 10 keV, SXR) mainly comes from bremsstrahlung, line radiation of heavy impurities and electron recombination processes. SXR radiation is mainly emitted by the hot, central part of the plasma with electron temperatures $T_e > 600 - 700$ eV. The possibility to detect radiation from impurities, and eventually to infer impurity density from the radiation, makes the SXR range of particular importance for us. The atomic physics involved in these processes will be discussed later in Section 2.3. In the following, several of TCV's SXR diagnostics are presented (figure 2.5).

The XTe diagnostic is mainly used for central electron temperature estimation by method of filters. The diagnostic is situated at $R = 0.9$ cm (figure 2.5) and has four equivalent, vertically viewing diodes with 4 different filters ($50 \mu\text{m}$ Be, $150 \mu\text{m}$ Be, $650 \mu\text{m}$ Be, $61 \mu\text{m}$ Al). Data from each of the four channels are acquired at 10 kHz using two different gains simultaneously to avoid the need for checking possible saturation of signals.

The Duplex Multiwire Proportional X-ray counter (DMPX) [Camenen, 2006] is a helium filled camera located at the bottom of the TCV vessel. The plasma radiation passes through beryllium foils as thick as $100 \mu\text{m}$ that absorb photons with energies below 1 keV. With additional absorbers the low energy cut-off can be increased. The DMPX is sensitive to photons in the energy range between 1 and 30 keV. Figure 2.5 shows the 64 chords spanning across the plasma cross section with an effective spatial resolution about 1 cm. From the line integrated measurements the emissivity profile can be calculated with an inversion technique.

The XTOMO system [Anton et al., 1996] consists of ten linear detector arrays equipped with 20 silicon diodes. The arrays are distributed on 9 poloidal ports on the same toroidal sectors (Figure 2.5), resulting in 200 chords providing full poloidal coverage with a spatial resolution around 3-4 cm and acquisition rate of 80 kHz. The energy range that XTOMO is sensitive to is 1 to 15 keV.

2.1.4 Typical density and temperature profiles

To conclude this section about the experimental capabilities of TCV, in figure 2.6 we show typical density and temperature profiles from different plasma scenarios: low and high confinement modes (L- and H-mode, respectively) and plasmas with electron internal

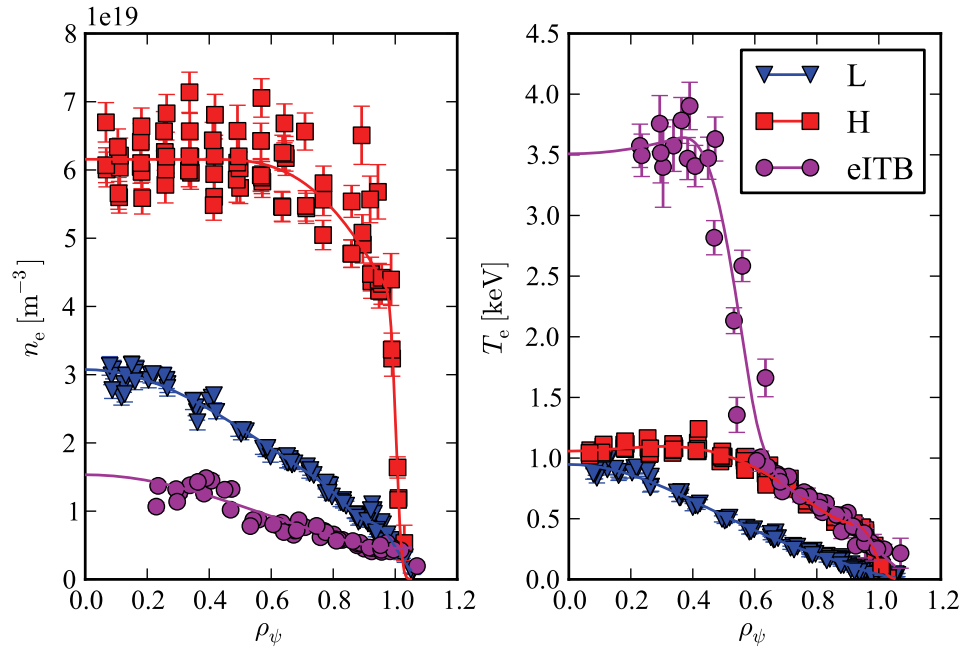


Figure 2.6: Electron density and temperature profiles of a typical TCV L-mode (triangles, #43768 0.5-0.7 s), H-mode (squares, #38012 1.52-1.58 s) and eITB (circles, #44662 1.3-1.41 s) plasma.

transport barrier (eITB). In H-mode [Martin et al., 2003] a steep gradient region, pedestal, forms at the plasma edge. The eITB scenario shows a barrier around $\rho_\psi \approx 0.4 - 0.6$ mainly on the electron temperature profile [Coda et al., 2007] and very high ($T_e \approx 4 \text{ keV}$) central electron temperature can be achieved. L- and H-mode plasmas can be sustained with ohmic (OH) only, on the other hand for the formation of the eITB powerful ECH/ECCD is indispensable.

2.2 Transport processes

In the description of the transport of a physical quantity such as mass, momentum, angular momentum, energy, we seek a balance equation that describe how this quantity evolves in space and time provided some boundary conditions, sources and sinks. In this section a short summary is given how a general balance equation is transformed into simple or more complex models that can be used to interpret transport phenomena observed in tokamak experiments.

First, in section 2.2.1 we show the relation between a general conservation law and a simplified diffusive-advective transport model. Then, in section 2.2.2 we briefly motivate how collisions between plasma particles in a toroidal magnetized plasma lead to transport. Section 2.2.3 introduces the notion of transport due to turbulence and presents the gyrokinetic model and finally in section 2.2.5 the quasi-linear approximation is explained by which we treat a truly non-linear and complex phenomenon such as the turbulence with a much simpler linear gyrokinetic model.

In addition to collisional and turbulent transport large-scale, magnetohydrodynamic (MHD) instabilities, such as sawteeth, tearing modes, fishbones etc., can have significant effect on transport. We do not treat these effects here, for a detailed review of MHD and the resulting tokamak operational limits see the review of [Hender et al., 2007] and the references therein.

2.2.1 The transport matrix

Consider a generalized quantity u that collects physical quantities of interest for a system under study such as n density, T temperature, momentum mv , etc.

$$u = \begin{pmatrix} n \\ T \\ mv \\ \vdots \end{pmatrix}. \quad (2.2)$$

The spatio-temporal evolution of u is usually governed by a conservation equation:

$$\frac{\partial u}{\partial t} + \nabla \cdot J(u) = S, \quad (2.3)$$

where J and S denote the flux and source of u , respectively. Using the u as of equation 2.2 the components of J would be the particle, heat and momentum flux, respectively. The relationship between J and u can be expressed from Fick's first law, as

$$J(u) = \mathcal{L} \nabla u, \quad (2.4)$$

where \mathcal{L} is the *transport matrix*. The goal of establishing a transport theory is to provide an explicit form of the transport matrix \mathcal{L} . Usually the transport matrix is not diagonal: for example in plasmas it is very common that temperature gradient drives not only a heat but a particle flux too. We note that \mathcal{L} , however, can not be arbitrary; the transport matrix of a physical system possesses some fundamental symmetries [Onsager and Machlup, 1953].

A complete transport theory provides a full description of the matrix \mathcal{L} , that unambiguously relates the components of J to u . Experimentally, the identification of *all* the forces is often very difficult and/or certain elements of the transport matrix remain unknown. Let us assume that experimentally one determines the flux J_u^i , then

$$J_u^i = \mathcal{L}_u^{i1} \nabla u^1 + \mathcal{L}_u^{i2} \nabla u^2 + \cdots + \mathcal{L}_u^{in} \nabla u^n. \quad (2.5)$$

Now if, for example the experiment yields only $\mathcal{L}^{ii} \nabla u^i$, then one could collect the remaining terms in a common term V representing all the off-diagonal contributions to the flux. In

this case a reduced

$$J_u^i = \mathcal{L}^{ii} \nabla u^i + V_i u^i \quad (2.6)$$

model provides a limited description of the system. This equation is of a well-known *diffusive–advective* type. The analytical and numerical techniques to solve equation 2.6 are well understood and documented (see Appendix A) and physics intuition often leads to reasoning in terms of diffusion and advection.

In the next sections we summarize the transport matrix of collisional and turbulent transport theories.

2.2.2 Collisional transport in strongly magnetized plasma

In strongly magnetized plasmas, the source of interest of magnetic confinement fusion research, the following ordering holds [Balescu, 1988]:

$$\lambda_D \ll \rho_L \ll \lambda_{\text{mfp}}, \quad (2.7)$$

here λ_D is the Debye length, the effective range of correlations between charged particles; ρ_L is the Larmor-radius; and λ_{mfp} the mean free path, the average distance travelled by a particle between successive collisions. The ordering between the hydrodynamic length λ_H – that is the spatial variation of the macroscopic quantities and of the magnetic and electric field – and the quantities in equation 2.7 define different *transport regimes*.

Magnetic plasma confinement in toroidal configurations such as the tokamak and the stellarator, made the following two regimes of particular importance [Balescu, 1988]:

- short mean free path regime: $\lambda_D \ll \rho_L \ll \lambda_{\text{mfp}} \ll \lambda_H$,
- long mean free path regime: $\lambda_D \ll \rho_L \ll \lambda_H < \lambda_{\text{mfp}}$.

The rich theory emerging from the study of these two regimes is generally referred to as *neoclassical* theory [Hinton and Hazeltine, 1976, Balescu, 1988]. The neoclassical theory of the transport processes describes the behavior of charged particles interacting through binary collisions in the presence of inhomogeneous and curved electromagnetic field.

The rigorous derivation of the full neoclassical transport matrix is a formidable task [Hinton and Hazeltine, 1976, Balescu, 1988], however often the full generality of the theory is not required. For illustration, we show the flux surface averaged thermodynamic forces

and their conjugated neoclassical fluxes for electron species, based on Angioni and Sauter [2000]

$$\begin{pmatrix} \Gamma_e \frac{d\psi}{d\rho} \\ \frac{Q_e}{T_e} \frac{d\psi}{d\rho} \\ \left\langle \frac{j_{\parallel} B}{T_e} \right\rangle - \left\langle \frac{j_{\parallel S} B}{T_e} \right\rangle \\ - \frac{I(\psi) \langle E_* B \rangle n_e}{\langle B^2 \rangle} \end{pmatrix} = \begin{bmatrix} \mathcal{L}_{11} & \mathcal{L}_{12} & \mathcal{L}_{13} & \mathcal{L}_{14} \\ \mathcal{L}_{21} & \mathcal{L}_{22} & \mathcal{L}_{23} & \mathcal{L}_{24} \\ \mathcal{L}_{31} & \mathcal{L}_{32} & \mathcal{L}_{33} & \mathcal{L}_{34} \\ \mathcal{L}_{41} & \mathcal{L}_{42} & \mathcal{L}_{43} & \mathcal{L}_{44} \end{bmatrix} \begin{pmatrix} \frac{1}{p} \frac{\partial p}{\partial \psi} \\ \frac{1}{T_e} \frac{\partial T_e}{\partial \psi} \\ \frac{\langle E_{\parallel} B \rangle}{\langle B^2 \rangle} \\ \frac{Q_e}{n_i T_e} \frac{K_i(\psi)}{I(\psi)} \langle B^2 \rangle \end{pmatrix} \quad (2.8)$$

This formula, which is in the form of equation 2.4 is completed with expressions for the \mathcal{L}_{ij} matrix elements which may be found in Angioni and Sauter [2000] but not repeated here. ρ is a generic radial coordinate and $\langle \cdot \rangle$ denotes the flux surface average.

We note, however, it is far from trivial to see in this form of \mathcal{L} , that the Onsager-symmetry [Onsager and Machlup, 1953], that with magnetic field generalizes as [Balescu, 1991]

$$\mathcal{L}_{ij}(\vec{B}) = \mathcal{L}_{ji}(-\vec{B}), \quad (2.9)$$

is robustly valid for the neoclassical transport equations [Sugama and Horton, 1996].

Let us focus on the first line of the transport matrix, the coefficients that multiplies the forces that drive particle flux. \mathcal{L}_{11} and \mathcal{L}_{12} terms contain the diffusion and thermodiffusion coefficients. Interestingly, \mathcal{L}_{13} is non-zero from a mechanism suggested by Ware [1970], hence the name *Ware-pinch*. In equation 2.8 only the toroidal electric field is included, however we note that non-inductive current drive causes cross-field neoclassical transport in a tokamak [Helander et al., 2005], in much the same way that the toroidal electric field used to drive the plasma current produces the Ware-pinch. We shall see in later chapters that the inclusion of the off-diagonal terms in the analysis of experimental data is essential to obtain agreement with experimental observations.

In Figure 2.7 (inspired by Figure 1. in Dux and Peeters [2000]) we show the neoclassical diffusion coefficient D^{neo} for fully ionized carbon that is the most abundant intrinsic impurity in TCV as a function of the collisionality $\nu^* = \nu q R / (v_{\text{th}}^i \epsilon^{3/2})$ where ν is the total collision frequency, accounting for collisions with all species. The calculation was performed with the Neoart code which will be introduced later in Section 2.4.4. The variation of ν^* results from a temperature scan with temperatures given on the upper x axis. The electron density and the impurity concentration are fixed. The parameters represent typical TCV plasma at mid-radius. We can see that the dependence of D^{neo} on ν^* in the banana and the Pfirsch-Schlüter regime ($\nu^* < \epsilon = 1$ and $\nu^* > \epsilon^{-3/2}$, respectively)

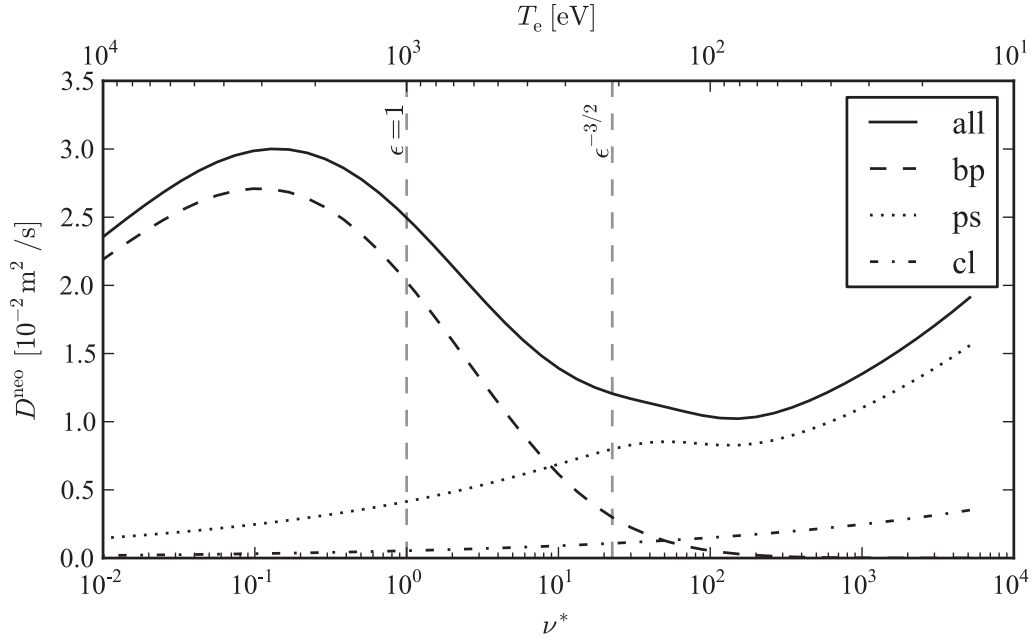


Figure 2.7: Total neoclassical diffusion coefficient, classical (cl), Pfirsch-Schlüter (ps) and banana-plateau term (bp) for C^{6+} as a function of the electron temperature at fixed electron density and impurity composition ($n_e = 5 \cdot 10^{19} \text{ m}^{-3}$, $c_C = 5\%$, $q = 2$, $r/a = 0.5$).

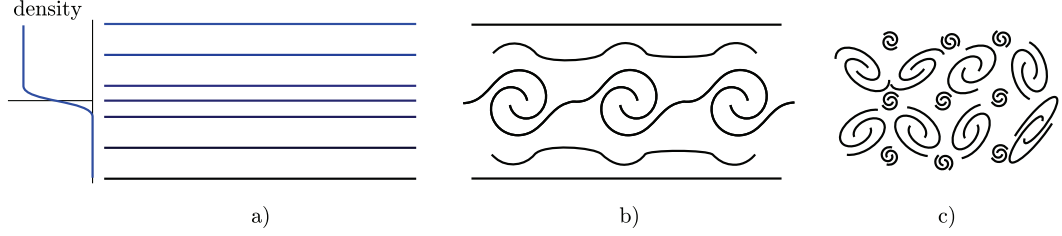


Figure 2.8: Growing instability and turbulence

displaying the well-known diffusion versus collisionality dependence, that is D^{neo} rises with increasing ν^* in these regions. The banana-plateau term dominates at low ν^* , whilst at large ν^* the major contribution is from the Pfirsch-Schlüter term. Conversely, the plateau region, where $\epsilon = 1 < \nu^* < \epsilon^{3/2}$ shows, D^{neo} decreases with increasing ν^* .

2.2.3 Instabilities driven transport and turbulence

Neoclassical theory is not in agreement with the experiments for all regimes of the present day's fusion devices such as tokamaks. For example, the observed heat and particle losses exceed the levels predicted by the neoclassical theory. Due to the collective nature of the plasma, it could be expected that particles organize themselves as larger, more or less coherent structures ("waves" or "modes") that are more efficient in transporting matter and energy than individual particle collisions. Indeed, in certain conditions, the linear response of these modes can be such that they become unstable, their amplitudes increase resulting in non-linear interaction between each other with saturation mechanisms coming into play and resulting in a more complex plasma behavior. In this turbulent state of plasma the contribution to heat and particle fluxes dominates classical and neoclassical mechanisms. This realm is usually referred to as anomalous or turbulent transport regime [Balescu, 2005].

Figure 2.8 elucidates the concepts of a growing instability and turbulence. Figure 2.8 (a) represents the initial unstable state: a higher density medium is layered atop a lower density medium. This is known as the Rayleigh-Taylor instability [Sharp, 1984]. When the system starts to evolve, the flux through a surface that cuts through the initial gradient is increasing. As the fluid velocity and velocity shear increase, the effect of viscosity damps

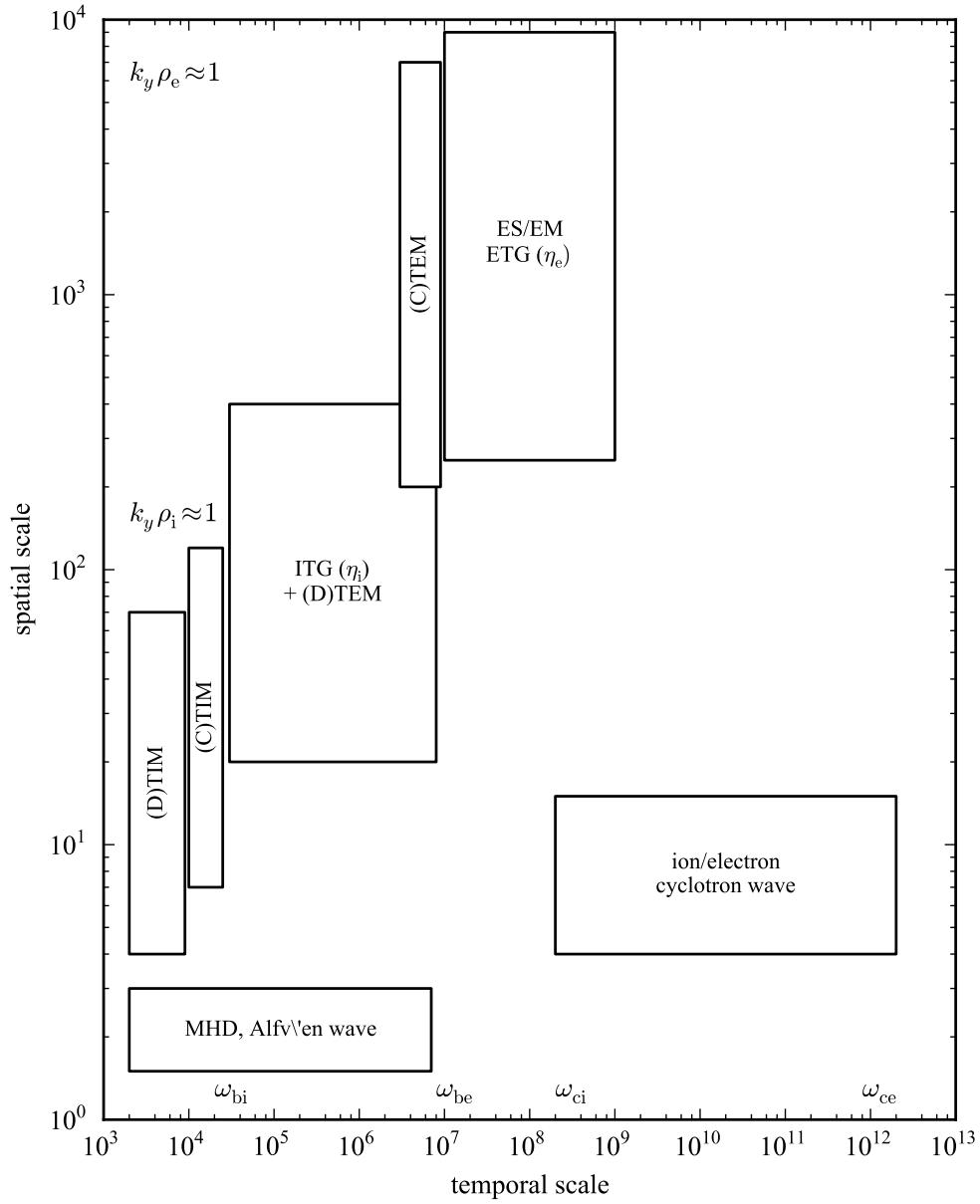


Figure 2.9: Inverse time and spatial scales of various plasma phenomena. Reproduction of figure 7 of Kishimoto [2000].

the initial growth and eddies of a certain size (Figure 2.8 (b)) mix the two media. If the initial gradient is not maintained and system is let to evolve freely, the mixing of the two media decreases the initial gradient, that is the drive of the instability, and the two media mix completely. On the other hand, if the gradient is sustained, the energy pumped into the system, due to non-linearity, is distributed across different spatial scales (Figure 2.8 (c)). An important aspect of the evolution to a turbulent state is the change in the system's symmetries: the initial state depicted on Figure 2.8 (a) is invariant under continuous translations perpendicular to the initial gradient, state (b) shows a *discrete* translation invariant phase, whilst at state (c) the initial symmetry is recovered only in a statistical sense.

It turns out that a large contribution to the energy and particle transport is originating from the turbulent activity generated by certain low frequency (lower than the ion cyclotron frequency) modes, so called drift waves, such as the Ion/Electron Temperature Gradient Mode (ITG, ETG) and the Trapped Electron Mode (TEM) [Horton, 1999]. Figure 2.9 illustrates the spatio-temporal scales of different modes. The temporal scale spans 10 and the spatial scales 4 orders of magnitude. This is to underline the inherent complexity of plasmas: these extended scale ranges impose difficulties in performing experiments, as well as numerical simulations and analytical calculations.

The starting point of modelling is to compile a set of plasma dynamical equations which is able to capture the phenomena under study. The most common frameworks to study transport, in the order of increasing complexity, are

1. primitive fluid models [Hasegawa and Mima, 1978, Hasegawa and Wakatani, 1983]
2. fluid models [Weiland et al., 1989, Angioni et al., 2004]
3. gyrofluid models [Beer, 1994]
4. gyrokinetic models [Brunner, 1997]
5. kinetic models

In practice, simpler models are obtained via simplifications introduced from more complex models, with a common point usually the kinetic Vlasov-equation. The primitive fluid models are usually used to study basic properties of turbulence in idealized, simple systems,

often using analytical methods. Unsurprisingly, these systems can already exhibit very complex behavior.

Fluid and gyrofluid models can be used to model and predict real experiments in realistic 3-dimensional geometry, since they can be run reasonably fast on today's computers. At present most of the transport oriented work is done or accompanied by gyrokinetic calculations and often *ad-hoc* fluid models are constructed to highlight the phenomenon under study.

In this thesis, linear gyrokinetic theory is used (in Chapter 3), therefore the gyrokinetic equation is now introduced.

2.2.4 The gyrokinetic equation

Gyrokinetic theory [Garbet et al., 2010] (GK) focuses on low-frequency electromagnetic fluctuations that are observed in inhomogeneous magnetized plasmas. It can describe low-amplitude turbulence with time scales long compared to the Larmor-frequency Ω_c and spatial scales comparable to ion Larmor radius ρ_i and system size L_0 in the directions across and along the mean magnetic field, respectively. This ordering provides the small parameter ε

$$\varepsilon \sim \frac{\tilde{X}}{X} \sim \frac{k_{\parallel}}{k_{\perp}} \sim \frac{\omega}{\Omega_c} \sim \frac{1}{k_{\perp} L_0} \sim \frac{\rho_i}{L_0} \ll 1, \quad (2.10)$$

which is extensively used in the derivation of the GK theory. \tilde{X} , k_{\parallel} , k_{\perp} , ω are the amplitude, the parallel and perpendicular to the magnetic field wavenumbers, and the frequency of the perturbation of the field X .

The particle motion in the strong magnetic field is decomposed into a slow streaming along the magnetic field line and a fast gyromotion. The idea is to eliminate the dynamical details of the fast gyromotion, providing enormous savings in computational time, while keeping certain physics elements, symmetries and conservation properties. The gyrokinetic equation describes the evolution of gyrocenter distribution function over a reduced, 5 dimensional phase space $(\mathbf{R}, v_{\parallel}, \mu)$, where \mathbf{R} denotes the gyrocenter position, v_{\parallel} is the gyrocenter velocity parallel to the magnetic field and μ is the gyrocenter magnetic moment (which can be written as a function of the perpendicular gyrocenter velocity v_{\perp}). The

gyrokinetic equation reads [Brizard and Hahm, 2007]

$$\frac{\partial f}{\partial t} + \frac{d\mathbf{R}}{dt} \cdot \nabla f + \frac{dv_{\parallel}}{dt} \frac{\partial f}{\partial v_{\parallel}} = C(f), \quad (2.11)$$

where the term C on the right-hand side accounts for collisions. Equation 2.11 is complemented by the gyrocenter equations of motion $(\frac{d\mathbf{R}}{dt}, \frac{\partial f}{\partial v_{\parallel}})$ which are *independent* of the gyrocenter gyroangle. Indeed, the essence of the gyrokinetic formulation is the construction of gyrocenter phase-space coordinates such that the gyrocenter equations of motions are independent of the fast gyromotion scale at arbitrary orders of the small parameter ϵ . Conventional derivation of the gyrokinetic equation is based on a regular perturbation expansion in terms of ϵ and a direct gyrophase average [Frieman and Chen, 1982], while the modern derivation [Brizard and Hahm, 2007] achieves the reduction of dynamical dimensionality via phase-space transformations.

We note that the nonlinear gyrokinetic equation can be cast in the form of equation 2.3 [Wang, 2012].

2.2.5 Linear response and quasi-linear approximation

The standard method for obtaining the plasma response is to solve the linearized plasma dynamical equations. After Fourier-transformation in time, the linearized equations yield a set of linear, homogeneous algebraic equations. The condition to obtain solutions generates the dispersion relation for the eigenmodes. We highlight this procedure in terms of the gyrokinetic theory, that is where the plasma dynamical equation is equation 2.11.

The distribution function is written as a sum of an equilibrium (f_0) and perturbed (\tilde{f}) part $f = f_0 + \tilde{f}$. Keeping only the linear terms in \tilde{f} in equation 2.11 yields:

$$\frac{\partial \tilde{f}}{\partial t} + \frac{d\tilde{\mathbf{R}}}{dt} \cdot \nabla f_0 + \frac{d\mathbf{R}_0}{dt} \cdot \nabla \tilde{f} + \frac{d\tilde{v}_{\parallel}}{dt} \frac{\partial f_0}{\partial v_{\parallel}} + \frac{dv_{\parallel 0}}{dt} \frac{\partial \tilde{f}}{\partial v_{\parallel}} = C(\tilde{f}). \quad (2.12)$$

Omitting the details of the derivation (see the references in [Fable, 2009]), the linear GK equation for electrostatic perturbations, neglecting collisions reads:

$$\left(\frac{\partial}{\partial t} + v_{\parallel} \nabla_{\parallel} + \omega_d \right) \tilde{f} = \frac{Ze}{T} f_0 (-v_{\parallel} \nabla_{\parallel} - \omega_d + \omega_*) \langle \tilde{\Phi} \rangle_g, \quad (2.13)$$

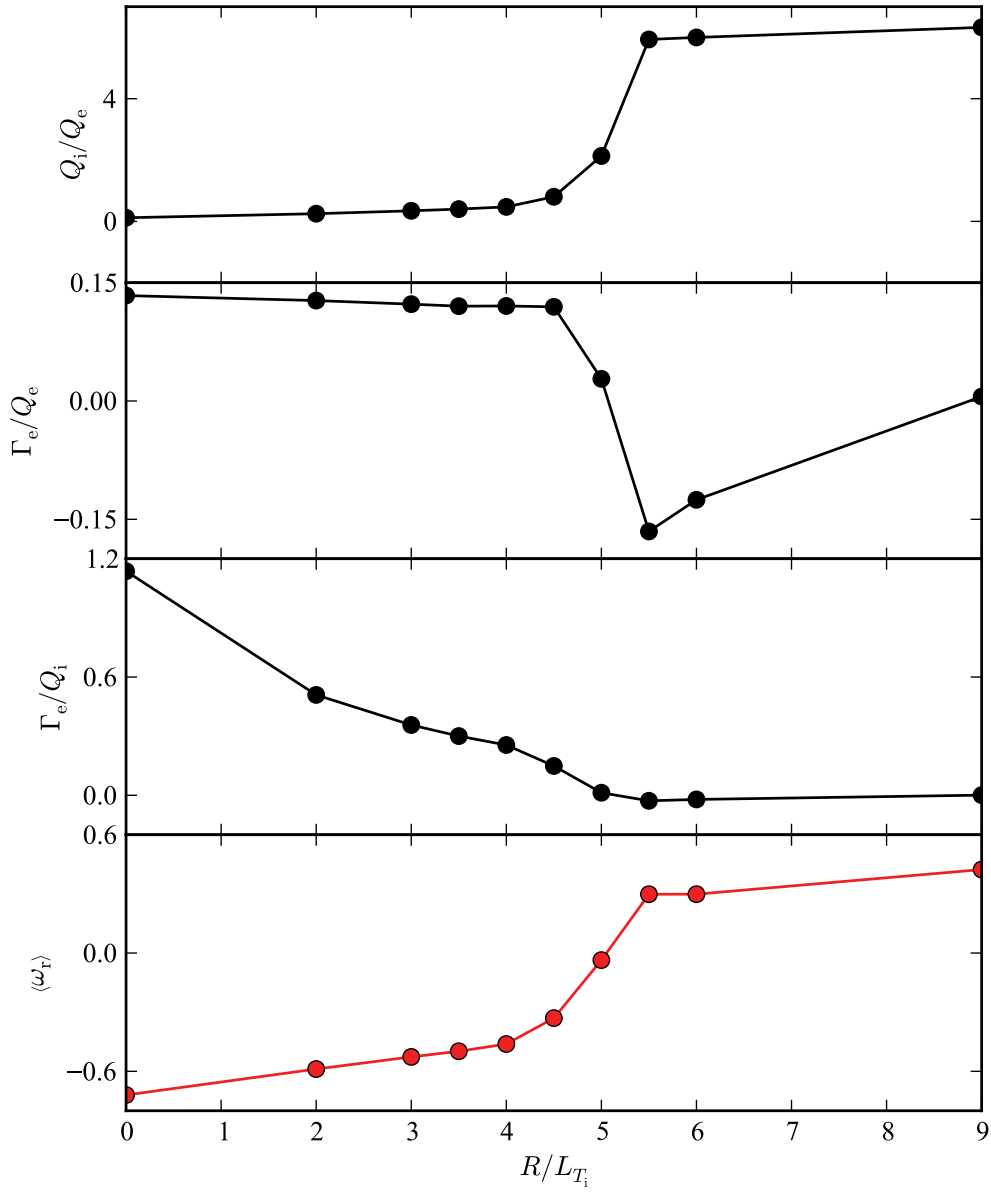


Figure 2.10: The ion temperature gradient scan in Merz and Jenko [2010] repeated with the quasi-linear model presented in Section 2.2.5. This figure is directly comparable to Figure 9. of Merz and Jenko [2010]

where ∇_{\parallel} is the parallel gradient operator, ω_d and ω_* are the magnetic curvature frequency and diamagnetic drift frequency operators. Explicit formulae for these quantities can be found in Fable [2009]. Z is the charge number, T denotes the temperature and e is the elementary charge, $\langle \tilde{\Phi} \rangle_g$ is the gyro-averaged electrostatic potential fluctuation. For given background profiles (density, temperature) and geometry (to evaluate gradients) equation 2.13, provides the linear response \tilde{f} to the perturbation $\tilde{\Phi}$. The solution \tilde{f} is usually given in terms of Fourier-eigenmodes and the corresponding complex eigenvalues written as

$$\omega \equiv \omega_r + i\gamma, \quad (2.14)$$

where ω_r is the real mode-frequency and γ is the growth rate. We will see later that the most-unstable mode or fastest growing mode, that is the eigenmode with the largest γ is of particular importance.

Quasi-linear theory uses the linear response to estimate the anomalous transport due to nonlinear turbulence [Diamond et al., 2010]. This can be considered as the *simplest* description of turbulence. In Ref. [Fable et al., 2010] a quasi-linear gyrokinetic framework has been proposed for particle transport with which TCV L-mode plasmas and electron internal transport barriers [Fable et al., 2008] were studied extensively. In Chapter 3 we will use this framework to model electron density peaking in TCV H-mode plasmas. What follows is a short summary of this quasi-linear model.

The linear GK equation 2.13 is solved for electrostatic perturbations with a wavenumber $\mathbf{k} = (k_x = 0, k_y)$ to obtain ω_r^k , γ^k , Γ^k , the real and imaginary part of the mode frequency and the particle flux, respectively, of the most unstable mode. $\omega_r^k > 0$ represents a mode turning in the ion diamagnetic (ITG) direction, while $\omega_r^k < 0$ corresponds to the electron diamagnetic direction (TEM).

ω_r^k , γ^k , Γ^k are evaluated on a range of k_y . We then obtain the quasi-linear fluxes and the average mode frequency of the turbulent state by a weighted average over the mode spectrum:

$$\langle R \rangle = \int_k w_k R^k dk / \int_k w_k dk, \quad (2.15)$$

where R^k can stand for Γ^k , Q^k , ω^k . The w_k weights are usually chosen according to a quasi-linear rule of the form:

$$w_k = A_0 \left(\frac{\gamma}{\langle k_{\perp}^2 \rangle} \right)^{\xi}. \quad (2.16)$$

We use the same parameters $\xi = 2$, $A_0 = 1$ as in [Fable et al., 2010]. We shall discuss the effects of this choice later, in section 3.2.6.

Although there is no general agreement in the community on the applicability of different quasi-linear models, significant efforts have been made to compare various models against non-linear simulations [Casati et al., 2009, Merz and Jenko, 2010, Bourdelle et al., 2007, Lapillonne, 2010, Lapillonne et al., 2011] and good agreement was found. It was also shown that the fully developed turbulence preserves many features of the linear evolution [Merz and Jenko, 2010], therefore with an ad-hoc weighting of the linear spectra, non-linear fluxes can be acceptably reproduced [Bourdelle et al., 2007]. Moreover, quasi-linear predictions fit very well to experimental observations [Fable et al., 2010, 2008, Angioni et al., 2011].

A comparison between non-linear and quasi-linear gyrokinetic calculation is presented by Merz and Jenko [2010]. We repeated the same scan with the quasi-linear model presented above. The results in Figure 2.10 shows that the fluxes given by the two quasi-linear models and the non-linear simulations are almost identical. The agreement between quasi-linear and nonlinear simulations, as well as quasi-linear simulations and experimental data, suggests that the simpler, quasi-linear models can be used to reproduce experimental parameter dependences in many, specific cases. We will return to the applicability of different quasi-linear models later, in section 3.2.6.

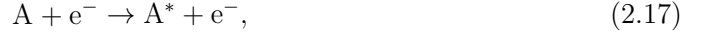
Before we continue with transport modelling in Chapter 3, we describe how plasma emission can be used to diagnose transport processes, in particular that of impurities.

2.3 Plasma emission

Detecting radiation emitted from a plasma can be used to determine information about many of its parameters [Hutchinson, 2005] such as plasma temperature, plasma composition, ion flow velocity, magnetic field, etc.. In this section we summarize the atomic processes that lead to photon emission. We mainly follow a route taken by the Introduction of Summers [2004], for a more complete overview see the monograph of Hutchinson [2005]. We shall devote special attention to the generation of photons in the *soft x-ray* range, that is photons in the 1-10 keV energy range, since the emission in this very range will be our most important diagnostic tool in the analysis of the impurity transport experiments in Chapter 6.

2.3.1 Radiation emission and transport in the coronal model

The mechanisms of radiation emission of hot plasma can be understood in the following picture: electrons collide with impurity ions and the kinetic energy of the former is transferred to the internal energy of impurity ions:



where the A^* denotes an excited state and A the ground state of the impurity ion. As the ion returns to its ground state a photon is emitted:



The photon energy corresponds to the energy difference of the excited and the ground state. Now let us assume that

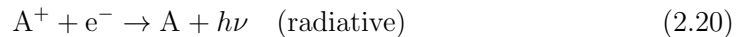
1. *all* excitation is according to equation 2.17, that is collisional, and,
2. de-excitation is solely as equation 2.18, in other words radiative.

These two approximations lead to the *coronal model* [Hutchinson, 2005], first coined to describe the radiation emitted by the Sun's external atmosphere, the corona. The first point implies that the radiation density is low, in other words the plasma is optically thin, so that the photons, once emitted, escape without being re-absorbed. The second point can be satisfied by such low electron density that photon emission is more likely than collisions with electrons. Before we justify the validity of these approximations we need to treat other consequences of the ion-electron collisions.

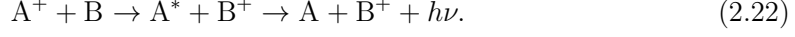
Collision with electrons can also result in increase or decrease of the ions' charge state as a result of ionisation



radiative and dielectronic recombination



and charge exchange



In cases where the total energy is shared among three participants, for example among ion, electron, photon in equation 2.21, the spectrum of the resulting radiation is continuous. In addition to these, charged particles accelerating in other's Coulomb-field emit continuous radiation known as *bremstrahlung*, with the main contribution mainly from electrons deflected by the ions' field [Furno, 2001].

Collisions with electrons excite the atoms and the processes of equations 2.19-2.22 change the charge states of the impurity. Particles at every charge state are transported by the processes seen in Section 2.2. Taking into account atomic physics and transport we write equation 2.3 for the impurity density n_Z^j

$$\frac{\partial n_Z^j}{\partial t} + \nabla \cdot J(n_Z^j) = Q_j, \quad (2.23)$$

where j indexes the ground and excited energy levels of the all charge states of impurity with atomic number Z . Note that the number of equations in this coupled set of partial differential equations can greatly exceed Z . In this general form this system is intractable.

In order to simplify equation 2.23, we must understand how the timescales involved in excitation, de-excitation and mixing charge states, and eventually generating radiation, relate to those of transport we wish to observe. We compare the typical timescales of the atomic and transport processes. Let $\tau_{\text{transport}}$ be a typical transport timescale, for example the time it takes for a particle to diffuse across density and temperature gradients. We also write characteristic times τ_{ioniz} for ionization, $\tau_{\text{metastable}}$ for metastable radiative decay, τ_o ordinary excited state radiative decay and τ_{e-e} free electron momentum relaxation time. Metastable states are excited levels from which transitions are forbidden by dipole selection rules, that is transitions are relatively unlikely to occur. This makes these states long-lived, hence the time-scale separation between ordinary and metastable state decay times. For fusion plasmas, the ordering

$$\tau_{\text{transport}} \sim \tau_{\text{ioniz}} \sim \tau_{\text{metastable}} \gg \tau_o \gg \tau_{e-e} \quad (2.24)$$

holds [Summers, 2004]. From these time-scales, it can be assumed that the free electron distribution function has been relaxed to some stationary distribution, and that the dom-

inant populations of impurities in the plasma are those of the ground and metastable states of the various ions. We note that the stationary electron distribution may not be Maxwellian in tokamaks: for example, with powerful ECCD [Coda et al., 2003] significant suprathermal electron population can be generated. In this thesis, however, we do not treat such effects and the electrons are assumed to have Maxwell distribution.

2.3.2 Time-dependent collisional-radiative model

The details of the modelling transport and radiation simultaneously will be presented later in Chapter 6. For now, neglecting transport we can write a set of ionisation rate equations describing the net effect of the ionisation and recombination processes [Carolan and Piotrowicz, 1983]

$$\frac{dy_0}{dt} = n_e (-y_0 S_0 + y_1 \alpha_0) \quad (2.25)$$

$$\frac{dy_k}{dt} = n_e (y_{k-1} S_{k-1} - y_k (S_k + \alpha_{k-1}) + y_{k+1} \alpha_k) \quad (2.26)$$

$$\frac{dy_z}{dt} = n_e (y_{z-1} S_{z-1} - y_z \alpha_{z-1}), \quad (2.27)$$

where $y_k \equiv n_Z^k / n_Z$ is the fractional abundance of the k -th charge state, n_Z^k is the impurity density at the k -th charge state and $n_Z = \sum_k n_Z^k$. S_k is the ionisation rate coefficient from state k to $k+1$, while α_k is the recombination rate coefficient from state $k+1$ to k and n_e is the electron density. The ionisation stage index runs from 0 (neutral atom) to $z = Z$ (fully ionized nucleus). Note that while for the ionisation coefficient S_k k designates the initial state, in α_k k is the final state. This notation is convenient for the numerical implementation of system (2.25)-(2.27) because the ionisation and recombination coefficients can be indexed from 0 to $Z-1$ in the same manner.

In figure 2.11 we show the effective ionisation and recombination coefficients for the charge states of carbon as a function of electron temperature. At densities of fusion interest ($10^{18} - 10^{21} \text{ m}^{-3}$) the cross-sections hardly depend on the density. The atomic data are taken from the ADAS [Summers, 2004] database. In order to highlight the balance between ionisation stages, in figure 2.12 the ionisation and recombination rate of C^{5+} and C^{6+} , respectively, can be directly compared: we see that below 100 eV the ionisation rate drops sharply and recombination dominates, while above this temperature the ionisation rate is

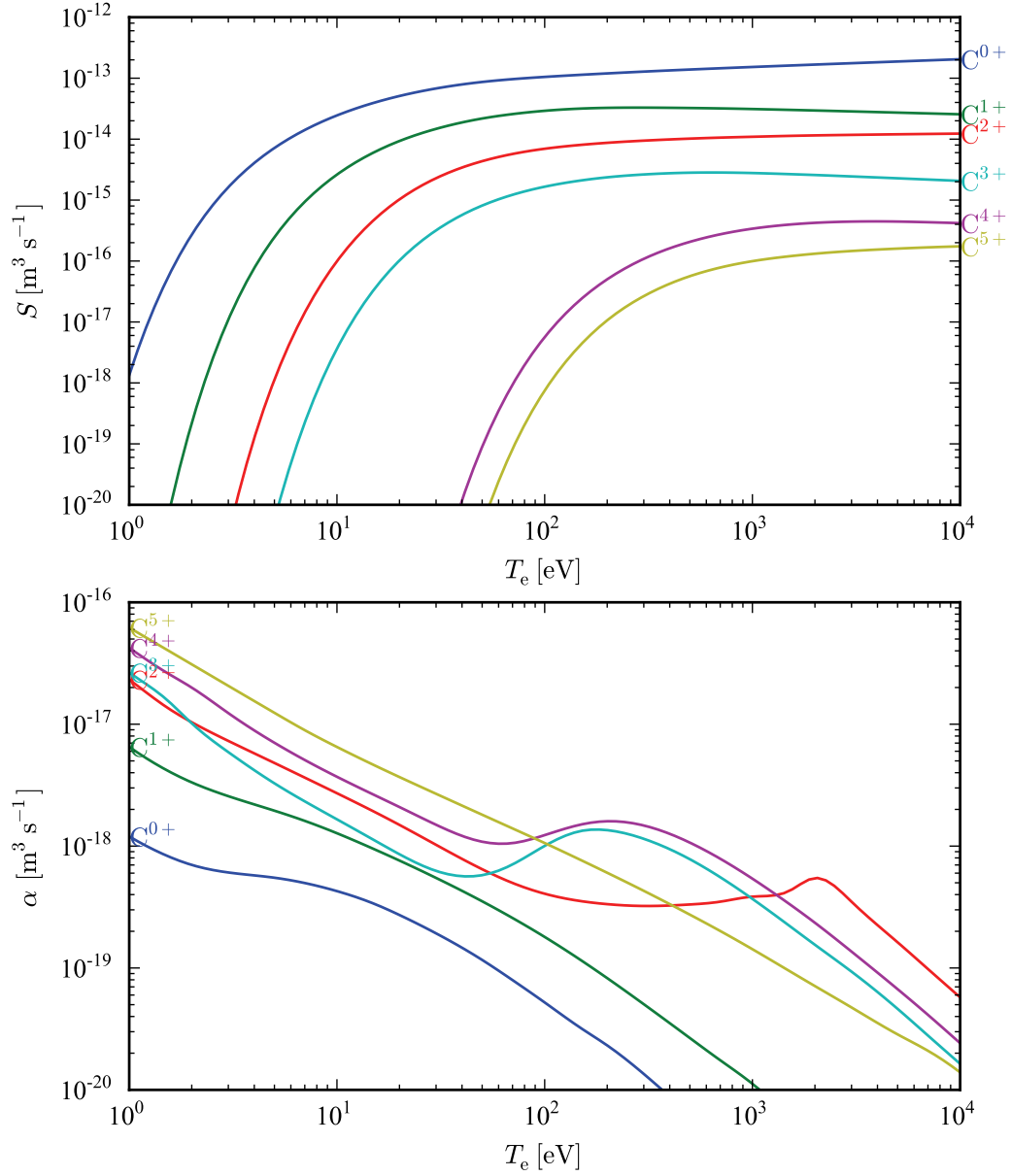


Figure 2.11: Effective ionisation (S) and recombination (α) coefficients as a function of the electron temperature for carbon. The ionisation curves are labeled by the initial state ($S_{\text{C}^{0+}} \equiv \text{C}^{0+} \rightarrow \text{C}^{1+}$), the recombination curves by the final state ($\alpha_{\text{C}^{0+}} \equiv \text{C}^{1+} \rightarrow \text{C}^{0+}$).

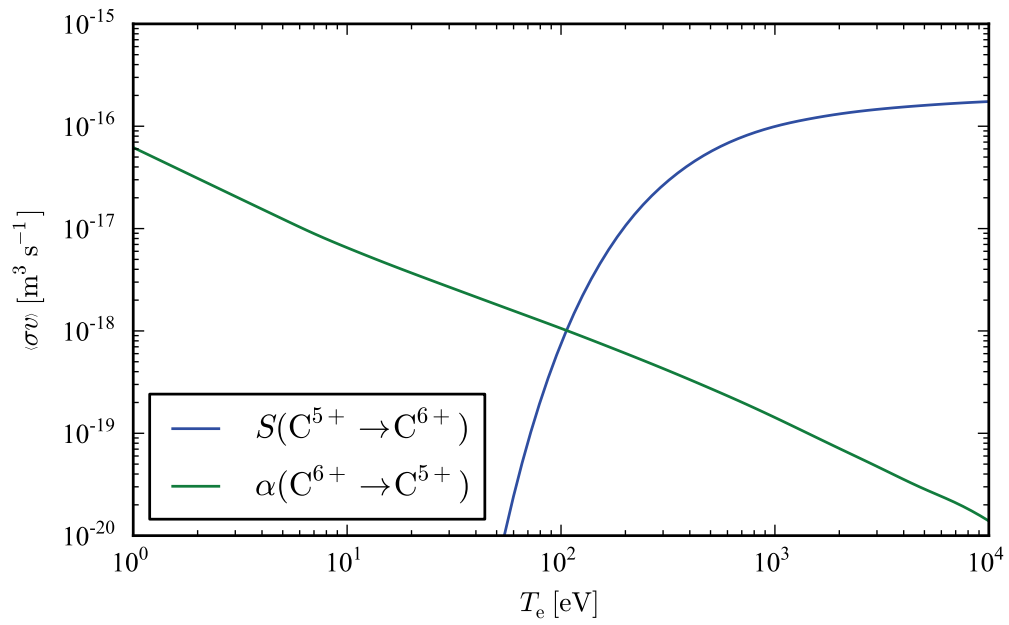


Figure 2.12: Same as figure 2.11, but only showing the ionisation coefficient from, and the recombination coefficient to C^{6+} (CV) as a function of the electron temperature.

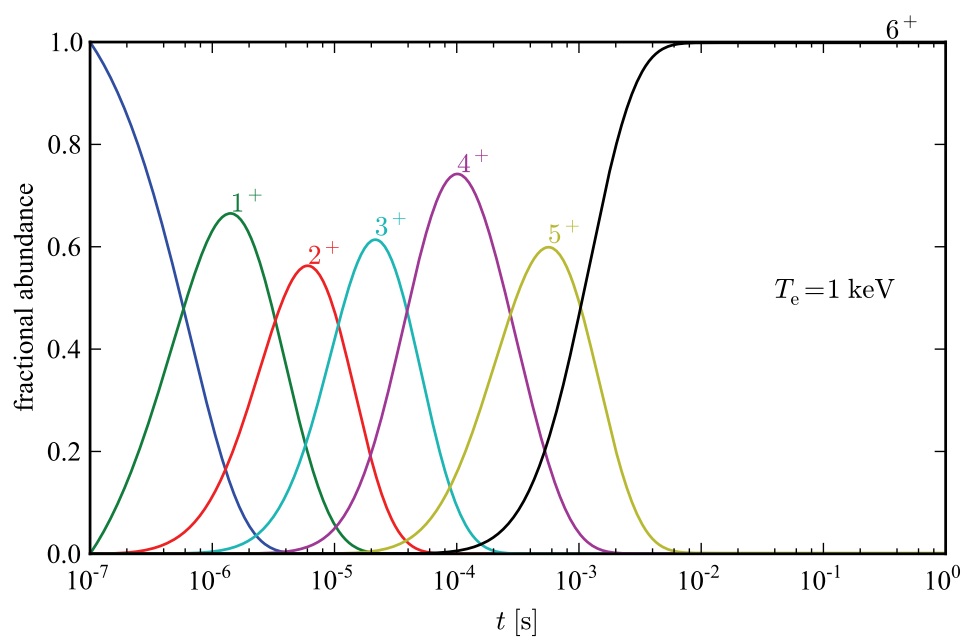


Figure 2.13: Time evolution of fractional abundances of carbon's ionisation stages.

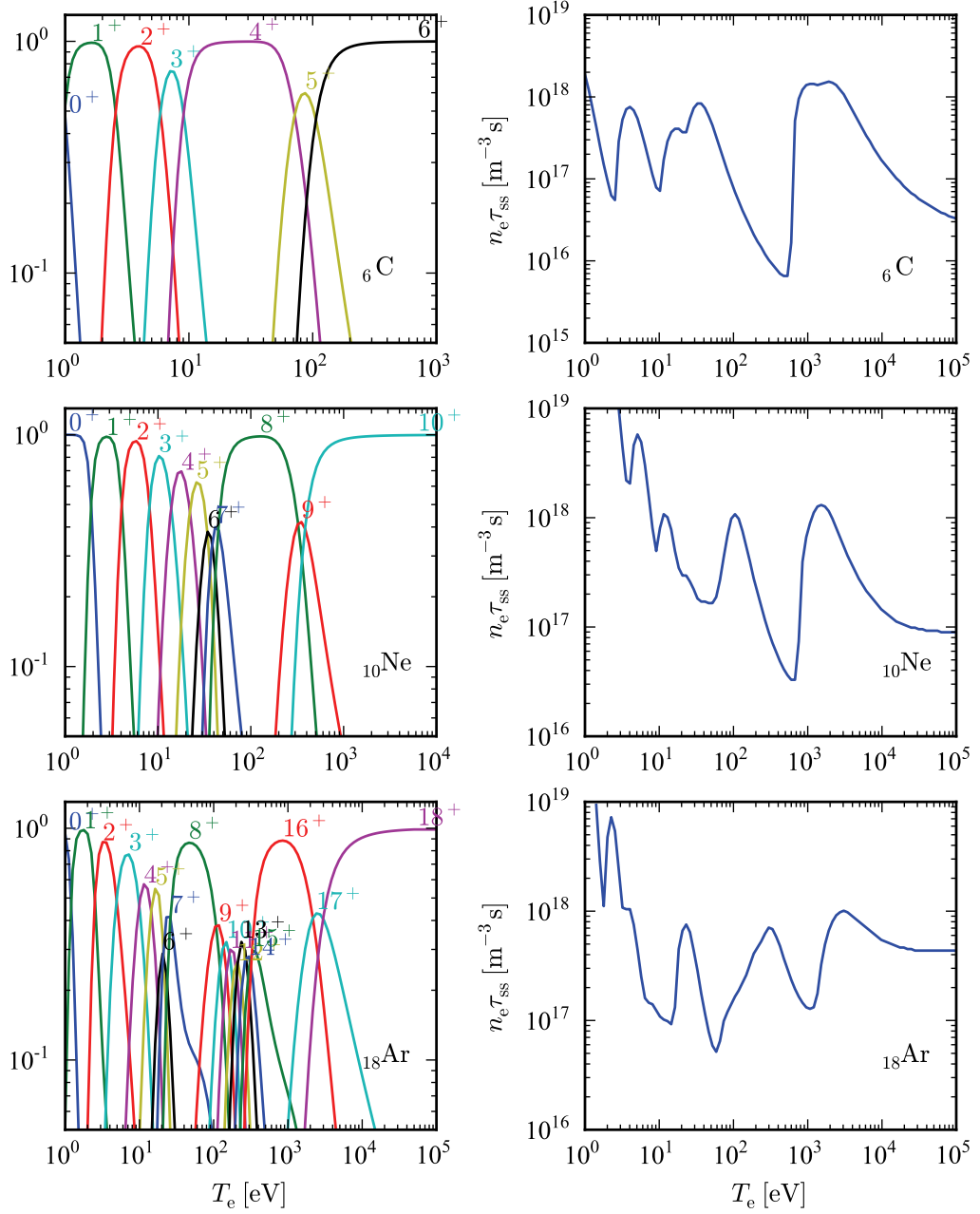


Figure 2.14: Left: fractional abundances of charge stages in coronal equilibrium; right: steady state time τ_{ss} (see equation 2.30 for carbon, neon and argon as a function of the electron temperature T_e).

larger than the recombination rate. This means that at low temperature the C^{6+} population will mostly recombine to C^{5+} (and eventually to lower stages too), whereas, when the temperature is higher (> 100 eV in this example) the C^{5+} population will decrease and by ionisation will feed the C^{6+} population. The ionisation stages act as sources and sinks of their respective neighbours depending on the electron temperature.

This chain of charge stages are elucidated in figure 2.13 where the abundance of carbon charge states are shown as a function of time. In this figure, at $t = 0$ neutral carbon atoms are inserted into a $T_e = 1$ keV plasma. From figure 2.11 we see that at this temperature ionisation dominates, the abundance of neutrals decreases filling up the singly ionized stage. Again, at this temperature $S(C^{1+} \rightarrow C^{2+}) > \alpha(C^{2+} \rightarrow C^{1+})$ means there is a source for C^{2+} population and so on. This fill-up and depletion of the consecutive ionisation stages can be clearly seen in figure 2.13. It continues until a balance between ionisation and recombination is reached. In this case at stationary state the carbon is essentially fully ionized after about 5 ms.

Indeed, the stationary solution of the system (2.25)-(2.27), that is where the left hand side of the equations is zero, is given by the simple relation

$$\frac{y_{k+1}}{y_k} = \frac{S_k}{\alpha_k}, \quad (2.28)$$

which has to be solved with the condition $\sum_k y_k = 1$ following from the definition of the fractional abundance y_k . This means that at equilibrium, the number of ionisation from the state k is equal to the number of recombined atom to this state. In other words if an excited ion decays radiatively before it suffers any other de-excitation, the level population of an excited state is the balance between the collisional excitation and radiative (spontaneous) decay. This so called *coronal equilibrium* is often a good approximation for high Z impurities with relatively high recombination rate.

The mean charge $\langle Z \rangle$ is used to calculate the number of additional free electrons produced when impurities are ionized:

$$\langle Z \rangle = \sum_k y_k k. \quad (2.29)$$

Steady-state conditions are never exactly obtained, but for practical purposes, we may define such state to exist when $\langle Z \rangle$ of the impurity in question is close to its true coronal

equilibrium values. Following Carolan and Piotrowicz [1983] we define the *steady-state time* as

$$\tau_{ss} = \min_t \left(1 - \frac{\langle Z \rangle_{eq}}{\langle Z \rangle(t)} \right) < 1\%, \quad (2.30)$$

where $\langle Z \rangle_{eq}$ is obtained by evaluating equation 2.29 with the fractional abundances from equation 2.28. The fractional abundance at coronal equilibrium, and the τ_{ss} steady-state time as a function of temperature for carbon, neon and argon are shown in figure 2.14. Strong correlation can be observed between the envelope of the ionisation distribution functions and the $n_e \tau_{ss}$ curves: a minimum is found in $n_e \tau_{ss}$ at those temperatures where closed shell configurations (He-like, Ne-like) predominate, that is where the envelope of the ionisation distribution has maxima [Carolan and Piotrowicz, 1983]. This is a result of the large difference between the ionisation rate of a single electron shell state and that of a closed shell state (see the difference in S of C^{3+} and C^{4+} in figure 2.11). The reduction of the ionisation rate of the closed shell configuration ensures its rapid population, hence the minima in $n_e \tau_{ss}$ curves.

2.3.3 Radiated power

When the population of the different ionisation stages, and the local plasma parameters are known the radiated power can be computed. The ADAS database [Summers, 2004] contains radiated power data: line emission and recombination radiation coefficients, bremsstrahlung and radiation coefficients from charge-exchange reactions are all accessible in tabulated form, grouped by element and wavelength.

Figure 2.15 shows the power of line emission, continuum emission (recombination and bremsstrahlung) and emitted power after charge-exchange assuming 1% neutral D concentration for carbon in coronal equilibrium. We see that the radiation function peaks at around 10 eV and this peak is almost entirely caused by a maximum in line radiation. Line radiation shows a minimum, around 40 eV, where the He-like C^{4+} is the most abundant (see figure 2.14). In general [Carolan and Piotrowicz, 1983] maximum of the line radiation is observed where closely packed ionisation stages are present, they are the strongest radiators, whilst minima are found when closed shell configurations are abundant. Closed shell configurations radiate the least due to their relatively high excitation energy, that is a sufficiently energetic electron is likely to ionize rather than excite the target ion.

If we now map this description in terms of spatial dependencies, this implies that line

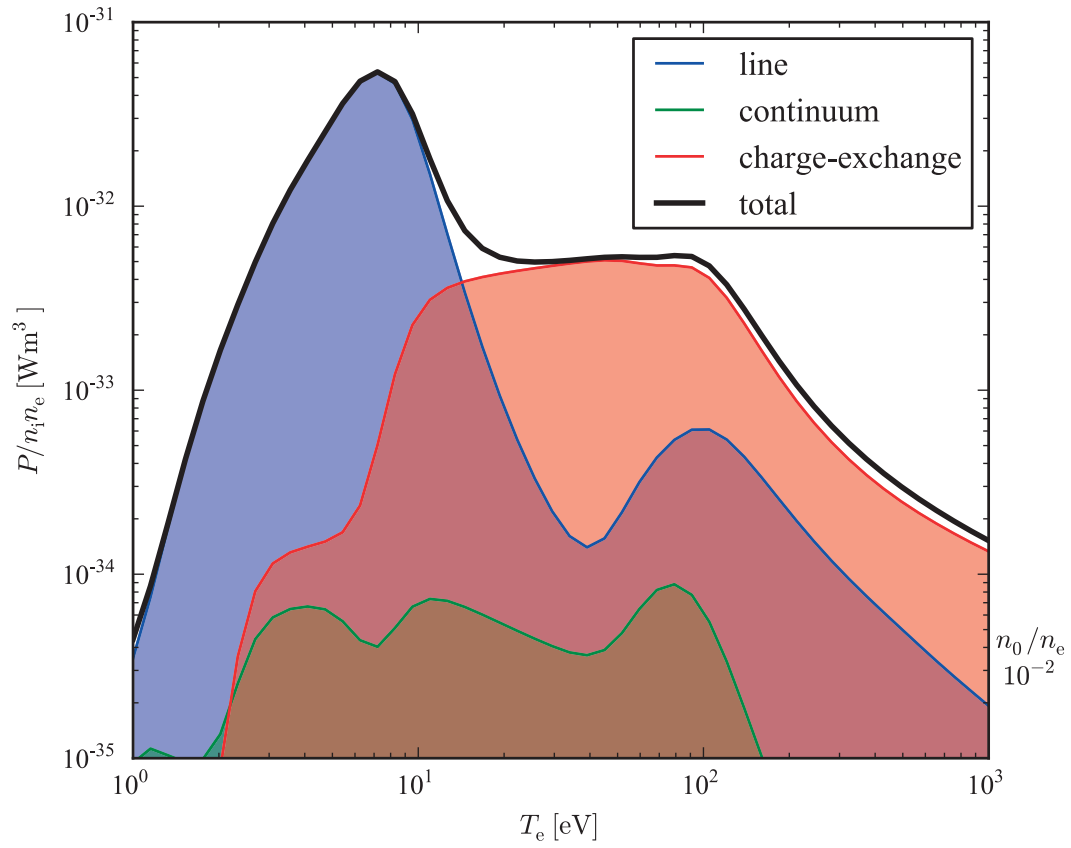


Figure 2.15: Contributions to the specific radiated power as a function of the electron temperature for carbon.

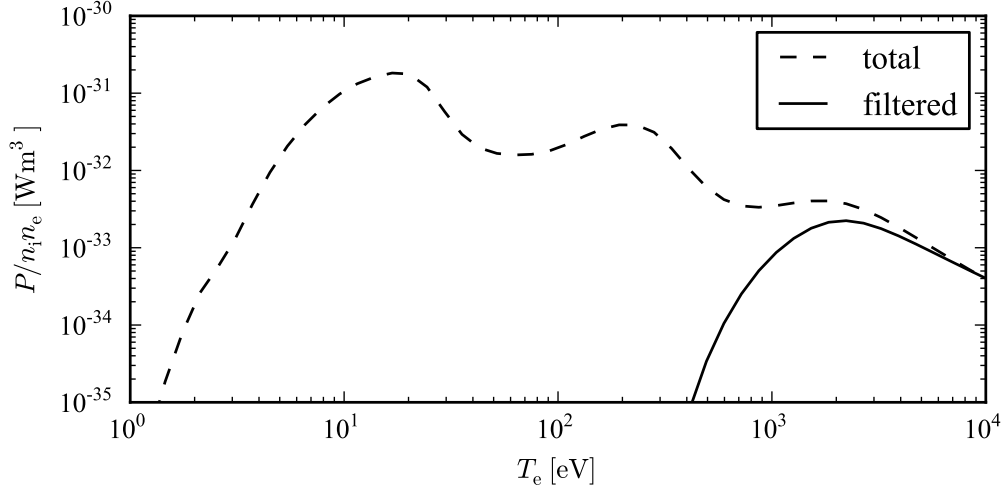


Figure 2.16: Total and filtered ($E_{\text{photon}} > 1 \text{ keV}$) specific radiated power as a function of the electron temperature for argon.

radiation dominates regions of the plasma that are relatively cold, that is the plasma edge. Radiated power from the plasma edge exceeds that from the central regions, where $T_e \approx 10^3 \text{ eV}$, by two orders of magnitude.

Plasma observations concentrating on the core emission should detect radiation that is weighted to higher energy photons. Figure 2.16 shows the same radiation function as figure 2.15 in addition to a filtered radiation function where only the part of the spectrum with $E_{\text{photon}} > 1 \text{ keV}$ is considered. This is a rough model of a typical camera in one of TCV's SXR diagnostic system seen in in section 2.1.3). It can be seen that radiation function decreases exponentially for $T_e < 1 \text{ keV}$, therefore it is expected that observation in the SXR spectral range only provides from the regions of the plasma which are relatively hot.

It must be stressed out that in the discussion of this section we neglected the effect of transport. As it is shown in figure 2.14, $\tau_{\text{ss}} = 10 - 100 \text{ ms}$ for plasma parameters of fusion interest. Transport time scales, or confinement times, observed in experiments lie in about the same range. Depending on the specific plasma parameters and the impurity species, the considered impurity may not spend sufficient amount of time in the hot plasma to reach coronal equilibrium. We will return to this point later in Chapter 6, where the

coupled modelling of transport and radiation emission will be presented.

2.4 Numerical tools

In this thesis many numerical codes have been used. In this section the most important pieces of software are enumerated.

2.4.1 General analysis software

In order to extract scientific information from the experiments, a chain of computer codes must be routinely run. At TCV the ensemble of this software is dubbed as the “CRPP toolbox”. We highlight this complex tool chain by an example, and review how density and temperature profiles we saw in 2.1.4 can be plotted. The Thomson-scattering system acquires its data during the experiment and run a set of routines that evaluates the recorded spectra and gives electron density and temperature values for the measurement position in (R, Z, t) coordinates. From the above arguments, it is assumed that the density and temperature are flux surface quantities and we wish to map these measurement points to flux coordinates given by the magnetic equilibrium. The magnetic equilibrium is computed with the LIUQE code [Hofmann and Tonetti, 1988] and the mapping is performed by Psi Toolbox [Moret, 2005]. If ECH power is used, the absorption profile of injected power is estimated by TORAY-GA [Matsuda, 1989, Kinsey and Choi, 2003]. If necessary, the bootstrap current is computed using the formulae described in Sauter et al. [1999].

2.4.2 CHEASE

CHEASE [Lutjens et al., 1996] is a fixed boundary equilibrium code. It solves the Grad-Shafranov equation, given the plasma boundary and the functions p' (pressure profile) and TT' (roughly speaking the current profile). The code is currently maintained in CRPP [Sauter, 2012].

2.4.3 GS2

GS2 is a gyrokinetic flux tube initial value solver for fusion plasmas. The original description of the equations and the implementation details can be found in [Kotschenreuther

et al., 1995]. The GS2 code is currently actively maintained and developed [The GS2 developer team, 2012]. In this work we only use a small subset of its features; to solve the linearized gyrokinetic equation along with the quasi-neutrality condition and Ampère’s law, using the high- n ballooning representation. The code solves the equation as an initial value problem using the Lorenz collision operator.

GS2 is extensively used in the simulations presented in Chapter 3.

2.4.4 Neoart

Neoart is a code that calculates the neoclassical transport coefficients for toroidal geometry. It solves the set of linear coupled equations for the parallel velocities in an arbitrary toroidally symmetric geometry for all collision regimes. The classical fluxes are given by equations (5.9) and (5.10) in Section 5 of Hirshman and Sigmar [1981]. The equations for the banana-plateau contribution are equivalent to those used by Houlberg et al. [1997]. The Pfirsch-Schlüter contribution is calculated from the coupled equations (6.1), (6.2) and (6.14), (6.15) of Hirshman and Sigmar [1981], as described in Peeters [2000]. Neoart includes the collisions of the considered impurity with the main plasma ions and all other impurities.

2.4.5 STRAHL

STRAHL is a code to compute the radial transport and the emission of impurities in the plasma bulk. The description of the numerical algorithm can be found in Behringer [1987]. The code has gone through several modifications, the technical details are summarized in the user’s manual [Dux, 2011b] available from the author on demand. The code solves a set of coupled equations in the form of equation 2.23 for ground and metastable states in cylindrical geometry, with the expression for the flux

$$J(n_Z^k) = -D\nabla n_Z^k + Vn_Z^k, \quad (2.31)$$

that is of the form of equation 2.6, with the diffusion coefficient D and advection velocity V profiles. The code is coupled to Neoart which means that neoclassical contributions to D and v can be taken into account. It also computes the emitted radiated power for given spectral lines or wavelength ranges. Table 2.1 show the datasets used in the simulations

data type	C	Ne	Ar
recombination	acd96	acd96	acd85
ionisation	scd96	scd96	scd85
radiated power (continuum)	prb96	prb96	prb00
radiated power (line)	plt96	plt96	plt97

Table 2.1: The ADAS [Summers, 2004] datasets used in the simulations.

presented in this thesis. STRAHL is an essential part of the analysis tool chain presented in Chapter 6.

Chapter 3

Electron density profile behavior in TCV H-modes

Results from a database analysis of H-mode electron density profiles on TCV under stationary conditions show that the logarithmic electron density gradient increases with collisionality[Wágner et al., 2012]. By contrast, usual observations of H-modes[Weisen et al., 2006, Angioni et al., 2007b] showed that the electron density profiles tend to flatten with increasing collisionality. Although in T-10 an inverse relation with collisionality was observed[Razumova et al., 2009], as well as on FTU[Romanelli et al., 2007]. In this chapter it is shown that the role of collisionality alone, depending on the parameter regime, can be rather weak and in these, dominantly electron heated TCV cases, the electron density gradient is tailored by the underlying turbulence regime, which is mostly determined by the ratio of the electron to ion temperature and that of their gradients. Additionally, mostly in ohmic plasmas, the Ware-pinch can significantly contribute to the density peaking.

The study in this chapter has been published [Wágner et al., 2012], what follows is a slightly modified version of that material. In the next section a brief overview of the TCV H-mode experiments is given with a particular attention to the typical parameter ranges within which these plasmas are sustained. In section 3.2 the results of the simulations, based on the theory introduced in 2.2.5, are discussed and compared to the experimental observations. In section 3.3, general discussion and concluding remarks are given. Finally, section 3.4 summarizes the main findings of the chapter.

3.7	<	$\langle n_e \rangle_{\text{vol}} [10^{19} \text{m}^{-3}]$	<	6.1
0.9	<	$T_e(0) [\text{keV}]$	<	2.5
280	<	$I_p [\text{kA}]$	<	420
1.35	<	$V [\text{m}^3]$	<	1.55
150	<	$P_{\text{OH}} [\text{kW}]$	<	600
250	<	$P_{\text{ECH}}^{\text{inj}} [\text{kW}]$	<	1000
$\delta_{\text{edge}} \approx 0.45, \kappa_{\text{edge}} \approx 1.7, q_{95} \approx 2.4$				

Table 3.1: Typical parameters of the TCV H-modes.

3.1 Experiments

In this chapter the TCV H-mode parameter regime is introduced. We show examples how the electron density and temperature profiles are modified when intense electron heating is applied. We then present the experimental dataset from a global viewpoint, that is the density peakedness as a function of the widely used collisionality parameter.

3.1.1 TCV H-mode plasmas

Plasma scenarios were briefly introduced in Section 2.1.4. In TCV, L-mode to H-mode transitions are obtained with and without additional heating [Hofmann et al., 1994, Martin et al., 2003]. The additional heating is provided by powerful third-harmonic electron cyclotron heating system (X3 ECH, 118 GHz, $3 \times 0.5 \text{ MW}$, 2 s, top launch) [Alberti et al., 2005] which was presented in Section 2.1.1. In this work we focus on standard ELMy H-modes with type I and type III ELMs with typical ELM frequencies around 35–100 Hz. Time traces of a typical pulse are shown in figure 3.1. Other scenarios such as the quiescent ELM-free [Porte et al., 2007] and snowflake [Piras et al., 2010] H-mode scenarios are beyond the scope of this present work and not considered in the analysis.

The experimental database is built on a representative set of sufficiently diagnosed H-mode deuterium pulses. Some typical parameters of these plasmas in the database are shown in Table 3.1. The dataset contains pulses with OH only and those with additional X3 ECH, the different power levels are relatively well covered. The dataset is somewhat less extended in terms of changes in plasma current and contains plasmas with very similar shape.

The majority ion species is deuterium and the most abundant impurity is carbon, originating from the wall tiles. The typical carbon concentration is a few per cent of

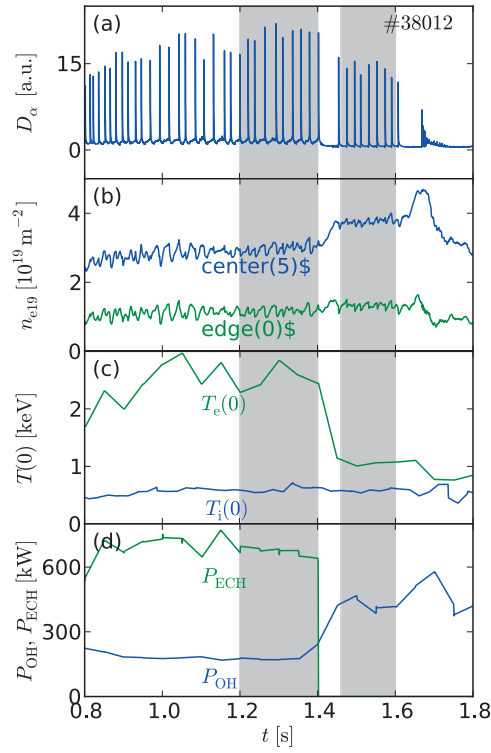


Figure 3.1: Time traces of (a) D_α emission; (b) central and peripheral FIR chords; (c) central electron and ion (C^{6+}) temperature; (d) OH and ECH power. The stationary profiles are taken from the shaded intervals 1.2–1.4 s and 1.46–1.6 s.

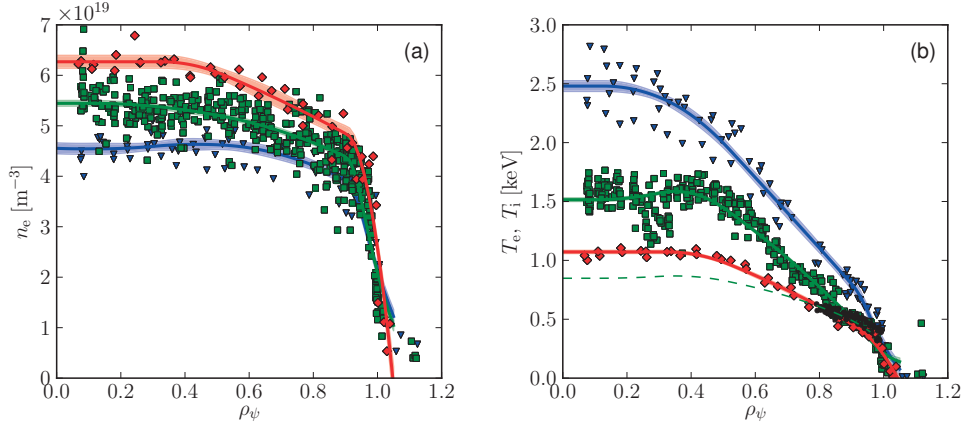


Figure 3.2: Profiles comparing conditions with ohmic heating only (diamonds, #38012 1.46 – 1.6 s) to those with additional 350 kW (squares, #40089, 0.7 – 1.61 s), 675 kW (triangles pointing down, #38012 1.2 – 1.4 s) ECH. (a) electron density, (b) electron temperature, ion temperature (points, #40089, 0.7 – 1.61 s). Solid lines show the piecewise polynomial fits which were used to compute the gradients. The shaded areas mark the confidence intervals corresponding to 95% confidence level. The dashed line represents $T_i(0.8) (T_e/T_e(0.8))^{0.5}$ (#40089, 0.7 – 1.61 s).

the electron density. The effective charge of these plasmas, estimated from soft x-ray measurements [Weisen et al., 1991], is found to be $Z_{\text{eff}} \approx 2$ for all the pulses considered in the analysis, independently on the heating scheme applied. The calculated total (OH plus bootstrap) current, assuming neoclassical conductivity [Sauter et al., 1999] with the measured Z_{eff} value, is consistent with the magnetic measurements.

3.1.2 Density and temperature measurements

The electron density and temperature profiles are measured via Thomson scattering (Section 2.1.2) and the density profile measurements are cross-calibrated with the FIR (Section 2.1.2). Typical temperature and density profiles are depicted in figure 3.2. The derivatives of the profiles with respect to ρ_ψ (see equation 2.1) are determined from cubic spline fits. The fit was performed on profiles collected during a stationary phase of pulses, i.e. where the main plasma parameters (plasma current, line averaged density, internal inductance) do not change significantly. The normalized inverse scale length (normalized

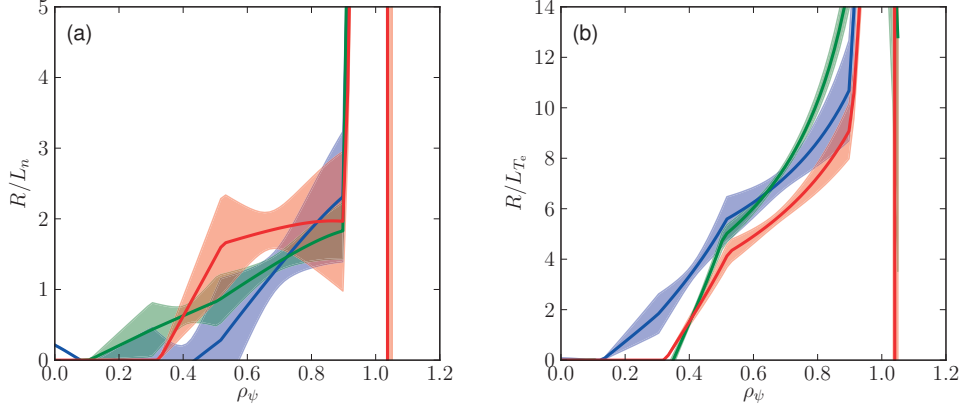


Figure 3.3: Profiles of the normalized logarithmic gradients calculated from the piecewise polynomial fits depicted in figure 3.2. The shaded areas mark the confidence intervals corresponding to 95% confidence level.

gradient) of a profile is defined as:

$$R/L_X = -R \langle |\nabla \rho_\psi| \rangle \frac{\partial \ln X}{\partial \rho_\psi}, \quad (3.1)$$

where R is the major radius and the $\langle |\nabla \rho_\psi| \rangle$ is the Jacobian of the $r \rightarrow \rho_\psi$ coordinate transformation with r being the distance from the magnetic axis on the outboard midplane. The profiles of the normalized gradients are shown in figure 3.3.

All the considered pulses exhibited sawteeth [Kadomtsev, 1975]. This results in flat average profiles within $\rho_\psi \approx 0.4 - 0.6$ surface, depending on I_p .

The C^{6+} ion temperature is measured by charge-exchange recombination spectroscopy (CXRS) and neutral particle analysers (NPA) [Karpushov et al., 2006] provide estimate of the central ion temperature (Section 2.1.2). In these H-mode plasmas, however, due to geometrical constraints, the ion temperature measurements are limited outside $\rho_\psi \approx 0.8$. This fact does not allow us to measure the ion temperature profile in the core.

Figure 3.2 (b) also shows a typical ion temperature profile between $\rho_\psi = 0.8 - 1$ overlaid on the electron temperature profiles. The ion temperature does not change significantly when the ECH is applied. From these typical profiles the local value of T_e/T_i at $\rho_\psi = 0.7$ ($\rho_{vol} \approx 0.6$) is around 1 for phases with ohmic heating only, and about 2 for phases with

ECH.

The present ion temperature data suggests that the ion temperature gradient is lower than that of the electrons. Assuming the functional form

$$T_i(\hat{\rho}) (T_e/T_e(\hat{\rho}))^\nu \quad (3.2)$$

for the ion temperature profile, the relation $R/L_{T_i} = \nu R/L_{T_e}$ follows. In figure 3.2 b) the dashed curve, derived from the electron temperature profile of #40089 using $\hat{\rho} = 0.8$ and $\nu = 0.5$, follows rather well the ion temperature measurements inside of $\rho_\psi \approx 0.8$. Following these considerations we estimate R/L_{T_i} to be around 3-5 at $\rho_\psi = 0.7$.

3.1.3 Collisionality dependence

Statistical analysis of JET [Weisen et al., 2006] and AUG [Angioni et al., 2007b] showed that collisionality is the most important scaling parameter for density peaking in H-modes. Both machines report the flattening of the density profile with increasing collisionality. Note that in these machines collisionality is controlled by the combination of neutral beam injection (NBI) heating and ECH. Despite its complexity, collisionality is a frequently used parameter to map parameter dependencies and for inter-machine comparisons. In this subsection the collisionality dependence of the density and temperature profile peaking is presented.

Later (in section 3.2), the results of the numerical modelling will be presented as a function of the following definition of collisionality:

$$\hat{\nu} = \nu_{ei}/(v_{th}/R), \quad (3.3)$$

where ν_{ei} is the electron-ion collision frequency, $v_{th} = \sqrt{T_i/m}$ the thermal velocity and R the major radius. In order to facilitate the comparison with previous results the experimental dependences are also plotted as a function of an effective collisionality adopted from [Angioni et al., 2005b]: $\nu_{eff} = 0.1 n_e Z_{eff} R / T_e^2 (\approx \nu_{ei} / \omega_{De})$, where n_e , T_e are the electron density in 10^{19} m^{-3} and the electron temperature in keV with $Z_{eff} = 2$.

Figure 3.4 shows the normalized logarithmic gradients of the electron temperature (R/L_{T_e}) and density (R/L_n) profiles at $\rho_\psi = 0.7$ as a function of collisionality $\hat{\nu}$ and ν_{eff} . Points around $\hat{\nu} \approx 0.02$, the most typical TCV OH H-mode pulses, have R/L_n around

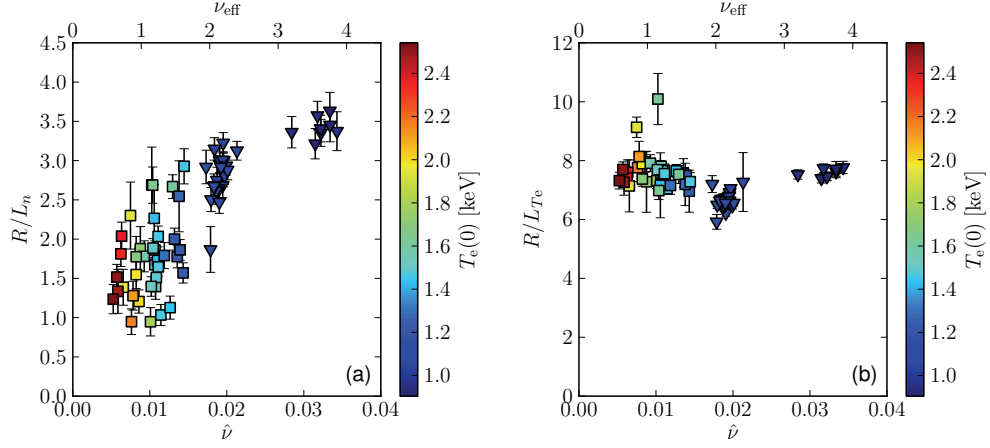


Figure 3.4: Scatter plots of the normalized logarithmic gradients at $\rho_\psi = 0.7$ as a function of collisionality over the considered database. (a) R/L_n (b) R/L_{T_e} . Different symbols indicate different heating phases, with ohmic heating only (triangles pointing down) and with central X3 ECH (squares). The colorscale (online) represents $T_e(0)$, the central value of the electron temperature.

3. Samples from reversed field campaigns with unfavourable ion ∇B drift direction with somewhat higher density, are located at around $\hat{\nu} = 0.03$ having $R/L_n \approx 3.5$. In the $0.008 < \hat{\nu} < 0.02$ range, which is reached by adding 0.5-1.5 MW ECH, R/L_n decreases to about 1.5.

Note that the global trend of R/L_n as a function of the collisionality is very similar to the one observed on FTU fully non-inductive, high density electron heated plasmas [Romanelli et al., 2007]. Also, T-10 reports the reduction of peakedness of the density profile with increasing ECH power and decreasing collisionality [Razumova et al., 2009]. By contrast, H-modes at JET [Weisen et al., 2006] and AUG [Angioni et al., 2011] showed that R/L_n is decreasing with increasing collisionality.

In this chapter we strive to test the model quasi-linear model presented in section 2.2.5 against TCV H-mode data to understand the density profile behavior. A relevant exception to this occurs near marginal stability, where a nonlinear upshift of the TEM critical density gradient has been found [Ernst et al., 2004], which increases with collisionality [Ernst et al., 2006]. This effect is clearly outside the framework of quasilinear theory. EC heated experiments are in general not near marginal stability to temperature gradient driven TEMs [Ernst et al., 2009] with $R/L_{T_e} \approx 8$ [Ryter et al., 2001] but may be near marginal

stability to longer wavelength density gradient driven TEMs [Ernst et al., 2004]. In our dataset, R/L_n ranges from about 1 to approximately 3.5, with the upper value lying above the density gradient driven TEM threshold (as shown later in figure 3.5).

3.2 Simulation results

In this section the normalized electron density gradient is predicted by numerical simulations to reproduce the experimental trend described previously. We explore how the different parameters influence the density peaking.

3.2.1 Setup for the simulations

Linear gyrokinetic calculations have been performed with the initial value flux-tube code GS2 (see section 2.4.3). We introduce two model cases representing TCV OH and ECH H-mode pulses. For both $R/L_{Te} = 9$, $R/L_{Ti} = 6$, $Z_{\text{eff}} = 2$. For the OH reference case $T_e/T_i = 1.0$, $\hat{\nu} = 0.024$, for the ECH case $T_e/T_i = 2.0$, $\hat{\nu} = 0.008$ which aim to represent the respective OH and ECH cases in figure 3.2.

The magnetic equilibrium of a representative discharge (see figure 3.1) was calculated by the equilibrium code CHEASE [Lutjens et al., 1996]. The $\rho_\psi = 0.7$ flux surface with $q = 1.2$, $s = 0.7$ was used for flux-tube simulations. For the collisions both pitch angle scattering and energy diffusion are taken into account. 13 k_y values are used in the range of $[0.08, 1.6]$ distributed in a logarithmic way. All growth rates and frequencies are normalized to v_{th}^i/R . The binormal wavenumber k_y is normalized to ρ_i , the normal wave number is always zero ($k_x = 0$). Note that on the outboard midplane the normal direction is radial. The timestep was fixed to $\Delta t = 0.05$ in units of R/v_{th}^i . 32 grid points for each 2π turn in θ , and 12 poloidal periods were used. The parameters are then scanned according to the various simulation results presented in the next subsections.

3.2.2 Finding the stationary density gradient

In the absence of core particle sources, as is the case in the TCV OH/ECH H-modes [Zabolotsky et al., 2006], the stationary value of the density gradient $R/L_n|_{\text{stat}}$ corresponds to the zero flux ($\Gamma = 0$) condition. Here we only consider the particle flux ascribed to turbulence, we shall deal with neoclassical contributions later, in section 3.2.5. Other

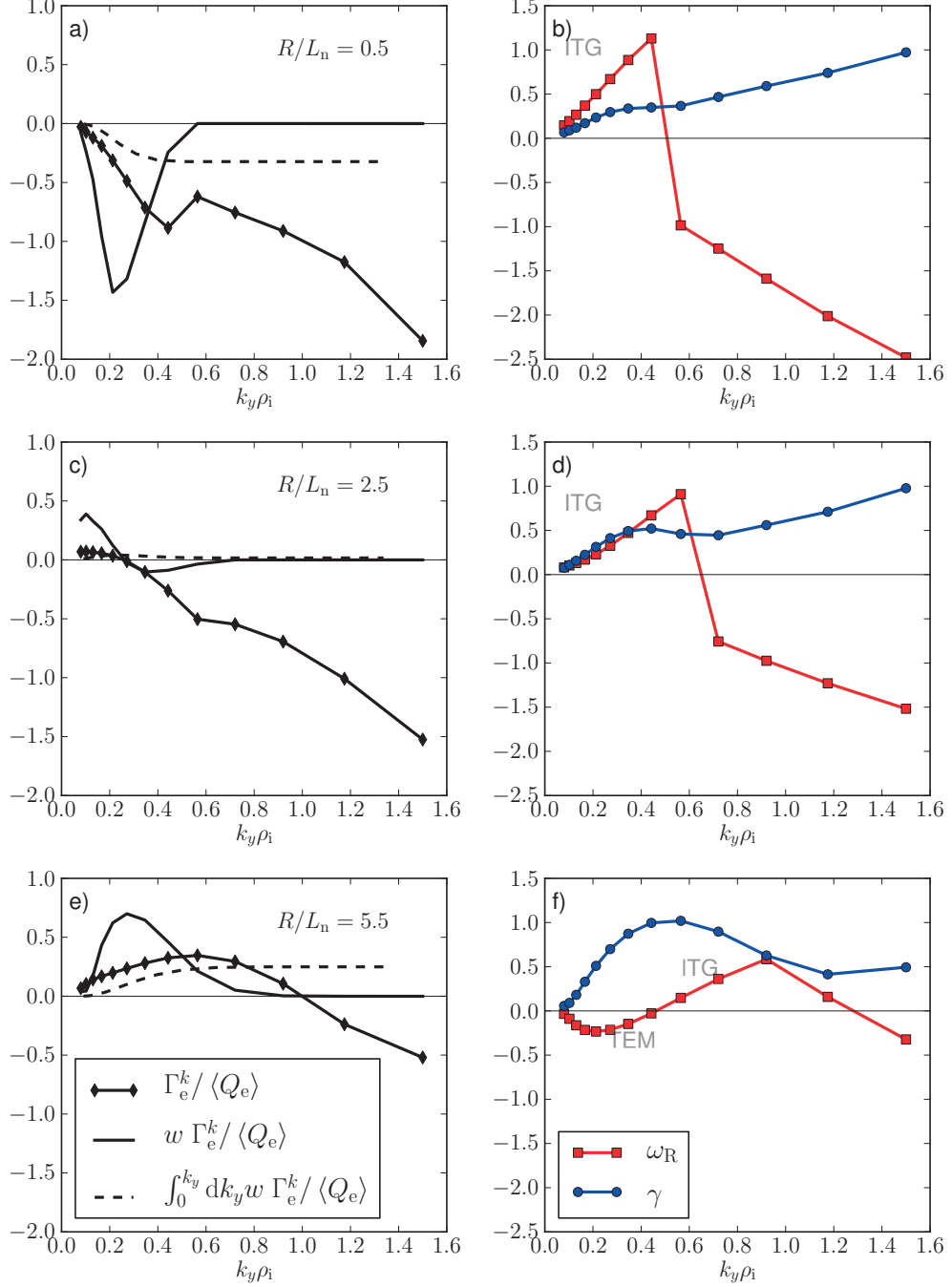


Figure 3.5: Left: particle flux Γ (diamonds); right: mode frequency ω and growth rate γ (squares and circles, resp.) as a function of k_y . (a), (b) low R/L_n where ITG is dominant and Γ negative (inwards); (c), (d) $R/L_n \approx R/L_n|_{\text{stat}}$ where $\Gamma \approx 0$; (e), (f) high R/L_n with TEM dominant and positive (outwards) particle flux. The simulation parameters correspond to the OH reference case (see section 3.2.1).

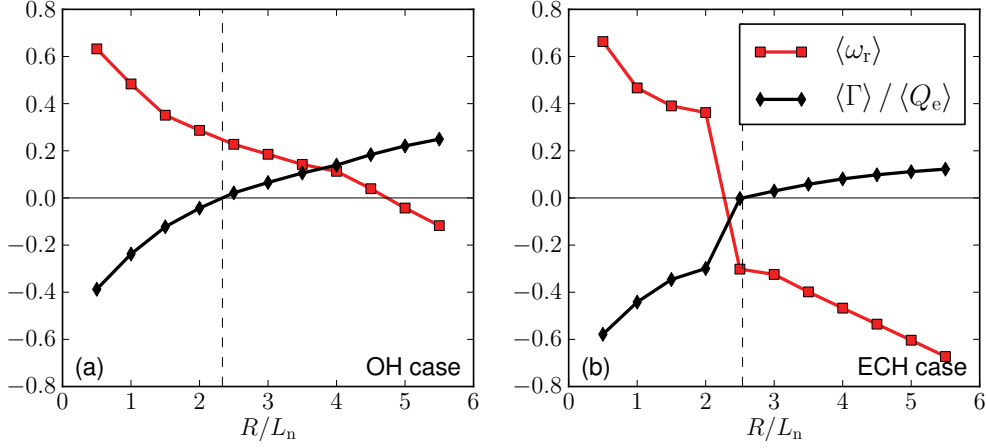


Figure 3.6: Quasi linear particle flux $\langle \Gamma \rangle$ (diamonds) and average mode frequency $\langle \omega_r \rangle$ as a function of R/L_n (a) OH reference case ($T_e/T_i = 1.0$, $\hat{\nu} = 0.024$), (b) ECH reference case ($T_e/T_i = 2.0$, $\hat{\nu} = 0.008$).

contributions to the total particle flux (e.g. MHD, ripple losses, etc) are neglected. It is also assumed that these approximations hold under both OH and ECH conditions. $R/L_n|_{\text{stat}}$ is obtained by making a set of simulations for different values for R/L_n , keeping all the other input parameters fixed. At each R/L_n , the quasi-linear particle flux $\langle \Gamma \rangle$ is evaluated using equation 2.15. Then the zero point is found by linear interpolation.

In order to understand the relationship between the linear and quasi-linear fluxes, in figure 3.5 we show the different contributions in equation 2.15 together with the mode frequency and growth rate of the most unstable mode as a function k_y for the OH reference case. First we note that the quasi-linear rule gives small weight at large wavenumbers (short scales), therefore $\langle \Gamma \rangle$ and $\langle \omega_r \rangle$ are mainly determined by the $k_y < 0.4$ – 0.5 wavenumber range (ITG and TEM range).

When the density gradient R/L_n is small (figure 3.5 a), b)), the most unstable modes are ITGs (positive ω_r), the $w_k \Gamma^k$ contributions to $\langle \Gamma \rangle$ throughout the covered wavenumber range is negative (inwards), making $\langle \Gamma \rangle$ pointing unambiguously inwards. Increasing R/L_n (figure 3.5 c) and d)), the growth rate of the most unstable modes decreases and at low k_y , $w_k \Gamma^k > 0$ contributions appear, making $\langle \Gamma \rangle = 0$ when $R/L_n = R/L_n|_{\text{stat}}$ is reached. Further increasing R/L_n ((figure 3.5 e) and f)) the mode frequency changes sign and TEM modes appear at small wavenumbers. When these modes dominate, the particle flux $\langle \Gamma \rangle$

is positive (outwards).

Figure 3.6 shows the quasi-linear particle flux $\langle \Gamma \rangle$ normalized to the total electron heat flux as a function of R/L_n for the two reference cases. Each point in the figure is a result of 13 simulations (averaged over the k_y spectrum as in figure 3.5). The average mode frequency $\langle \omega_r \rangle$ is also plotted showing that, indeed, the zero flux point is found between ITG and TEM type modes [Fable et al., 2010]. Note the role of ITG-TEM balance at a certain density gradient in the spectrum and also in adjusting the value of $R/L_n|_{\text{stat}}$. It must also be stressed out that at the co-existence of different modes, one must certainly account for non-linear effects [Ernst et al., 2004, 2006, Lapillonne et al., 2011, Görler et al., 2011]. It is not expected that the absolute value of $R/L_n|_{\text{stat}}$ from the quasi-linear estimate of the particle flux instantly matches the experimental values; however, its parametric dependence on the plasma parameters is remarkably well retained [Fable et al., 2010, 2008, Angioni et al., 2011].

3.2.3 $\hat{\nu}-T_e/T_i$ scan

We endeavour to reproduce the collisionality dependence reported in section 3.1.3 with numerical simulations. Since in TCV H-mode experiments collisionality is mainly controlled by intense electron heating, the T_e/T_i ratio certainly increases with additional ECH. It is expected that the temperature ratio has a significant effect on the nature of the dominant instabilities and hence on the particle flux. We also want to explore the effect of the electron-ion collisions at each considered temperature ratio. Therefore, we perform a double parameter scan in the range of $\hat{\nu} = [0.008, 0.012, 0.016, 0.020, 0.024]$ together with a scan in $T_e/T_i = [1, 1.5, 2]$.

The results are summarized in figure 3.7 a), which shows the predicted value of the density gradient $R/L_n|_{\text{stat}}$ as a function of the collisionality $\hat{\nu}$. Each point is obtained from a scan over R/L_n to determine $R/L_n|_{\text{stat}}$ where $\langle \Gamma \rangle = 0$. Therefore each point in figure 3.7 is the result of 11×13 linear simulations (11 R/L_n and 13 k_y points). When $T_e/T_i = 1.0$ the predicted density gradient is decreasing with collisionality. As the temperature ratio is increased, this trend is reversed and at $T_e/T_i = 2.0$ an increase of $R/L_n|_{\text{stat}}$ is predicted with increasing $\hat{\nu}$. These results show a clearer trend (figure 3.7 b)) if now one plots $R/L_n|_{\text{stat}}$ as a function of $\langle \omega_r \rangle$ which characterizes the nature of the background turbulence and orders very well the predicted values of $R/L_n|_{\text{stat}}$ [Fable et al., 2010, Angioni et al., 2011]

and also clearly shows that the change in the dominant instabilities alters the collisionality dependence. Therefore, an explanation of the different behavior of TCV H-modes with respect to JET/AUG plasmas can be due to the different T_e/T_i ratio and hence a different collisionality dependence.

Collisionality provides a purely convective term to the particle flux [Angioni et al., 2009] which is directed outwards for ITG and inwards for TEM modes and increases with increasing collisionality. Intuitively one expects that increasing $\hat{\nu}$ tends to push ω_r towards more positive values [Angioni et al., 2009] (towards ITG type turbulence) due the stabilizing effect of collisions on TEM turbulence [Ernst et al., 2004, Angioni et al., 2005a]. The net effect of collisionality on $R/L_n|_{\text{stat}}$ stems from these two effects: $\hat{\nu}$ influences the turbulence regime and, depending on the turbulence regime, the particle flux. Since an increase in collisionality implies an increase in the real mode frequency the effect of the collisionality on the TEM modes driven outward flux is expected to be weak [Angioni et al., 2009]. Indeed, in figure 3.7 we observe almost no collisionality dependence at $T_e/T_i = 1.5$, where $\langle\omega_r\rangle \approx 0$. Moving away from this point toward either more positive or more negative $\langle\omega_r\rangle$, the net particle flux is less inwards, and $R/L_n|_{\text{stat}}$ is found at a lower gradient. The increase of T_e/T_i at fixed T_i is destabilizing for ITG and enhances the TEM [Lang et al., 2007] activity as well. Their interplay is such that TEM takes over rapidly with increasing T_e/T_i , in particular with ECH i.e. by increasing T_e [Bottino et al., 2006]. Indeed, starting from the OH reference point in the ITG instability domain, with increasing T_e/T_i and decreasing $\hat{\nu}$, $\langle\omega_r\rangle$ decreases and the predicted value of $R/L_n|_{\text{stat}}$ is increasing. In the transition region between ITG and TEM, the largest $R/L_n|_{\text{stat}}$ is obtained, then moving towards the TEM domain the density peaking decreases, leaving the point corresponding to the ECH reference case with a very similar $R/L_n|_{\text{stat}}$ value.

We conclude that albeit ECH has a significant effect on the values of $\hat{\nu}$ and T_e/T_i , the change in these parameters only is not sufficient to explain the observed overall experimental behavior.

3.2.4 R/L_{T_e} and R/L_{T_i} dependence

It is expected that the temperature gradients have a large effect on the predicted value of the density gradient. As it was pointed out in section 3.1.2, the ion temperature gradient is generally lower than that of the electrons even at the high collisionality OH plasmas. The

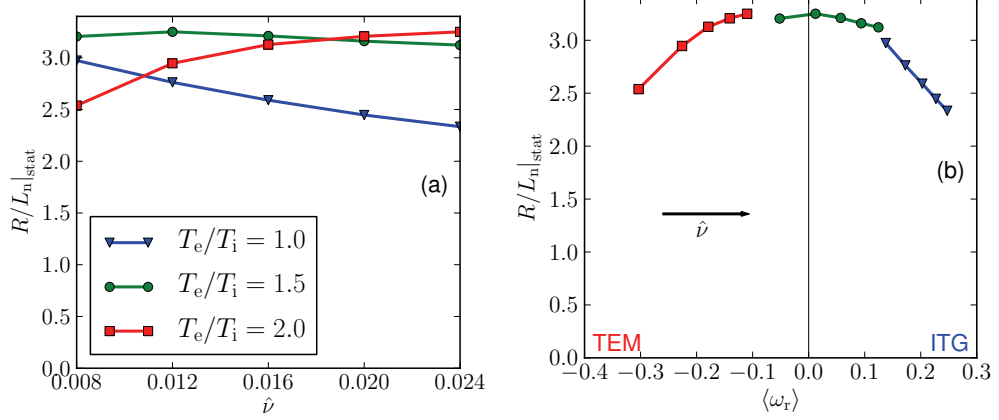


Figure 3.7: Predicted values of R/L_n for different values of the temperature ratio T_e/T_i , as a function of (a) the collisionality $\hat{\nu}$ and (b) the average mode frequency $\langle\omega_r\rangle$.

ions are even more decoupled from the electrons when intense electron heating is applied. Thus we expect that R/L_{T_i} does not change significantly in these plasmas (more precisely it does not increase). The experimental data are more clear on the R/L_{T_e} dependence; however it is useful to study the dependencies on the parameter, as well.

Two scans of R/L_{T_e} in the range of $[6, 7.5, 9, 10.5, 12]$ have been performed: the first with OH only parameter set ($T_e/T_i = 1.0$, $\hat{\nu} = 0.024$); the second with ECH parameter set ($T_e/T_i = 2.0$, $\hat{\nu} = 0.008$). The other parameters were kept fixed (see section 3.2.1). In the same way, we change the value of R/L_{T_i} in the range of $[4, 5, 6, 7.5, 9]$.

In figure 3.8 we present the results of these four scans in terms of $\eta_{ei} = (R/L_{T_e}) / (R/L_{T_i})$. Figure 3.8 a) shows that the change in R/L_{T_i} has a different effect on the OH and the ECH reference cases. Indeed, starting with the OH reference case (triangles), increasing R/L_{T_i} predicts smaller R/L_n . On the other hand, this parameter has the opposite effect on the predicted peaking for the ECH case. In figure 3.8 b), it is shown that increasing R/L_{T_e} increases R/L_n for the OH case, while the density peaking is rather insensitive to the change in the electron temperature gradient for the ECH case.

In order to separate the different mechanisms that are responsible for the density peaking, one can decompose the particle flux such as:

$$\Gamma = A \frac{R}{L_n} + B \frac{R}{L_{T_e}} + C, \quad (3.4)$$

which, assuming stationary plasma and using the zero flux condition when no particle sources are present (as is the case in the core of these ECH/OH plasmas), transforms into

$$\left. \frac{R}{L_n} \right|_{\text{stat}} = -C_T \frac{R}{L_{T_e}} - C_P. \quad (3.5)$$

The thermodiffusion coefficient $C_T = -B/A$ and the other pinch coefficient $C_P = -C/A$ are evaluated numerically [Fable et al., 2008, 2010]. In figure 3.9 we decompose the predicted R/L_n in terms of C_T and C_P as in equation (3.5) in order to identify the change in the thermodiffusive and the other contributions. We see that the larger contribution is always the thermodiffusive pinch $C_T R/L_{T_e}$ and usually the two pinches change in the opposite direction and a complicated interplay between the two yields the predicted R/L_n . This means that the parametric dependence of the density peaking is largely determined by the starting reference parameters as mentioned above.

In figure 3.10 a) we plot these results against $\langle \omega_r \rangle$ which, again, orders very well the simulation results R/L_n [Fable et al., 2010, Angioni et al., 2011]. As it was already shown in section 3.2.3, the OH reference (shaded triangle) case is in the ITG regime ($\langle \omega_r \rangle > 0$), while the ECH (shaded square) reference case is predicted to be more TEM ($\langle \omega_r \rangle < 0$). Increasing the electron temperature gradient results in moving to the left on the $\langle \omega_r \rangle$ axis (towards negative values), while the ion temperature gradient pushes towards larger $\langle \omega_r \rangle$ values. The density peaking is maximal around $\langle \omega_r \rangle \approx 0$ and the predicted value decreases towards both ITG and TEM regime as predicted for eITB and L-mode parameters [Fable et al., 2008, 2010]. We therefore show that this is a very general feature. In figure 3.10 b) c) we see the thermodiffusive contribution increases towards the ITG regime, while the C_P term decreases. This behavior of the two pinch terms reinforces their suggested universal role in particle transport [Fable et al., 2010].

As mentioned in section 3.1.2, the ion temperature measurements indicate that $(R/L_{T_i})/(R/L_{T_e}) \approx 0.5$, although we do not have measurements near $\rho_\psi = 0.7$, where we have based our analysis. If this ratio is further decreased in the simulations, moving left in figure 3.10 a), the value of $R/L_n|_{\text{stat}}$ decreases, following the trend seen previously. However the range of k_y where the ITG is the most unstable mode, typically $k_y = 0.1 - 0.6$, shrinks and slab-like electronic modes very elongated along the magnetic field lines appear as seen in Refs. [Hallatschek and Dorland, 2005, Angioni et al., 2007a]. Although their contribution to the particle flux is small, so is that of the remaining ITG and TEM. This domain re-

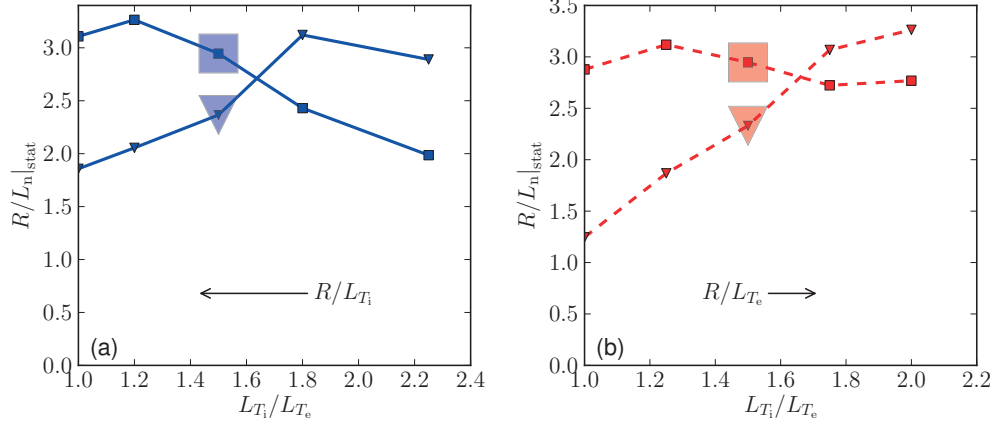


Figure 3.8: Predicted values of normalized density gradient R/L_n as a function of the temperature gradient ratio L_{T_i}/L_{T_e} changing R/L_{T_i} (solid) and R/L_{T_e} (dashed). Different symbols indicate different heating phases, with OH only (triangles) and ECH (squares). The larger shaded symbols show the reference cases.

quires non-linear simulations and the role of non-adiabatic passing electrons to be studied in detail, which is out of the scope of this thesis.

3.2.5 Effect of the Ware-pinch

In ohmic plasmas, the neoclassical Ware-pinch W_p [Ware, 1970] can have significant contribution to the density peaking [Stober et al., 2003, Ernst et al., 2004]. The strength of this effect depends also on the heating scheme applied [Ernst et al., 2004, Angioni et al., 2011]. In the presence of the Ware-pinch, one needs to find $R/L_n|_{\text{stat}}$ from: $\Gamma + n_e W_p = 0$ [Ernst et al., 2004]. In order to cancel normalization factors, it is more convenient to use the Γ/Q_e ratio; therefore, we divide with the electron heat flux Q_e :

$$\frac{\Gamma}{Q_e} + \frac{n_e W_p}{Q_e} = 0. \quad (3.6)$$

We evaluate the first term using the ratio of the normalized fluxes $\langle \Gamma \rangle / \langle Q_e \rangle$ from numerical simulations, while the second term is computed from experimental measurements using

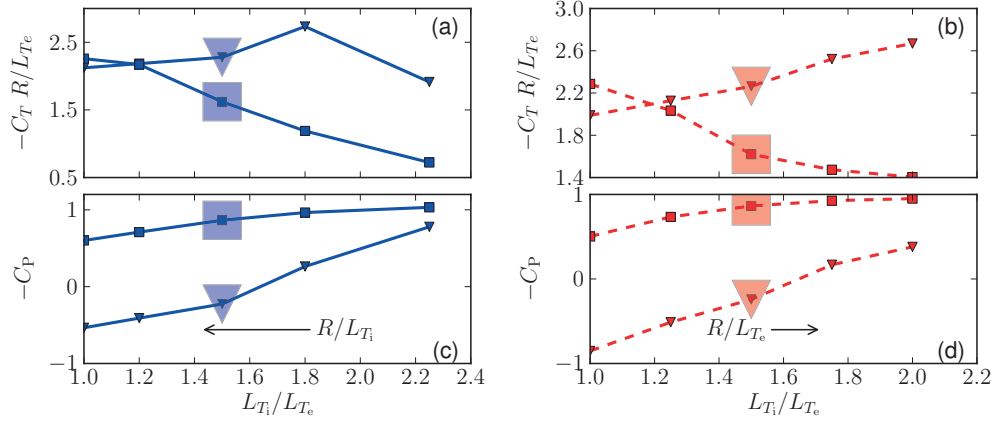


Figure 3.9: Thermodiffusive $-C_T R/L_{T_e}$ and the other pinch $-C_P$ contributions to the predicted value of R/L_n (see figure 3.8) as a function of the temperature gradient ratio L_{T_i}/L_{T_e} changing R/L_{T_i} (solid) and R/L_{T_e} (dashed). Different symbols indicate different heating phases, with OH only (triangles) and ECH (squares). The larger shaded symbols show the reference cases.

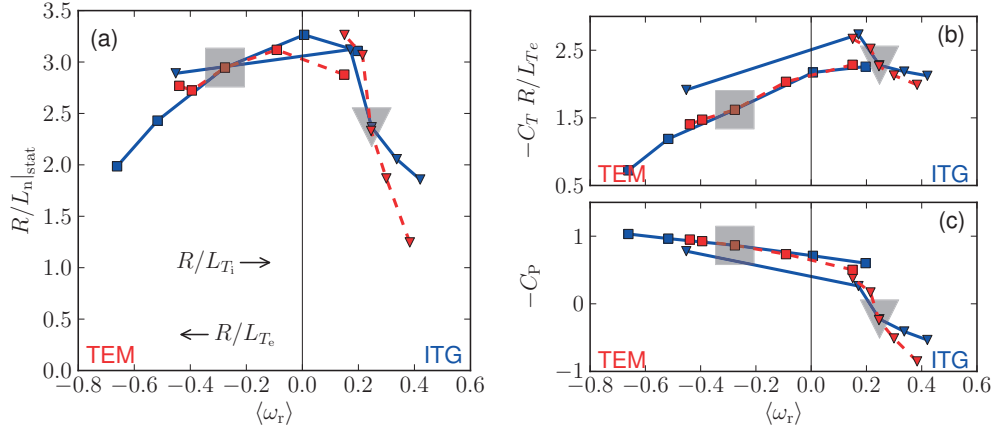


Figure 3.10: The predicted value of R/L_n , the thermodiffusive $-C_T R/L_{T_e}$ and the other pinch $-C_P$ contributions as a function of the average mode frequency $\langle \omega_r \rangle$ changing R/L_{T_i} (solid) and R/L_{T_e} (dashed). Different symbols indicate different heating phases, with OH only (triangles) and ECH (squares). The larger shaded symbols show the reference cases.

$Q_e = Q_e^{\text{exp}}$ and power balance (PB) arguments assuming a stationary plasma, where

$$Q_e^{\text{exp}} = -\chi_e^{\text{PB}} n_e \nabla T_e = \chi_e^{\text{PB}} \frac{R}{L_{T_e}} \frac{n_e T_e}{R}. \quad (3.7)$$

We find

$$\frac{\langle \Gamma \rangle}{\langle Q_e \rangle} + \frac{RW_p}{\chi_e^{\text{PB}} R / L_{T_e}} = 0, \quad (3.8)$$

from which one can find the stationary density gradient value with the Ware-pinch effect included. Note that $W_p < 0$. Note also that for any consistent normalization of $\langle \Gamma \rangle$ and $\langle Q_e \rangle$, T_e of equation 3.7 cancels in equation 3.8.

We compare the Ware-pinch contribution for the OH and ECH reference cases substituting typical values of W_p and χ_e^{PB} in equation 3.8, assuming that the intense ECH does not directly drive significant particle flux that must be countered by the turbulent flux to restore the total flux to zero. In figure 3.11 the ratio of the normalized fluxes $\langle \Gamma \rangle / \langle Q_e \rangle$ without (symbols), and with (no symbols) the Ware-pinch contribution are shown as a function of R/L_n ; (a) shows the OH reference case with $\chi_e^{\text{PB}} = 0.3 \text{ m}^2 \text{ s}^{-1}$, (b) is the ECH reference case with $\chi_e^{\text{PB}} = 1 \text{ m}^2 \text{ s}^{-1}$. For both cases $W_p = -0.3 \text{ ms}^{-1}$. It can be seen that the shape of the $\langle \Gamma \rangle$ curve around $R/L_n|_{\text{stat}}$ can influence the position of the new value of $R/L_n|_{\text{stat}}$. The addition of the Ware-pinch results in a vertical downshift of the curve. At the OH reference case $\langle \Gamma \rangle$ is almost linear with R/L_n . Due to its modest slope, the upshift in $R/L_n|_{\text{stat}}$ can be as large as 1. For the ECH case the slope of the Γ curve is somewhat reduced which would imply a larger change in $R/L_n|_{\text{stat}}$. However, for the ECH case the contribution of the Ware-pinch is negligible mainly because of two reasons. First, the loop voltage decreases as the electron temperature increases at constant current [Ernst et al., 2004]. This reduces the absolute value of W_p . Second, due to the profile stiffness the value of $\chi_e^{\text{PB}} R / L_{T_e}$ is larger in ECH plasmas, which makes the contribution of the second term in equation 3.8 much smaller.

3.2.6 Choice of the quasi-linear rule

Our analysis is consistent with the observed experimental data. However it is based on a specific quasi-linear rule (equation 2.16 with $\xi = 2$). Other similar studies reported successful interpretations with different quasi-linear theory [Angioni et al., 2011, Bourdelle et al., 2007, Casati et al., 2009, Maslov et al., 2009, Merz and Jenko, 2010, Fable et al.,

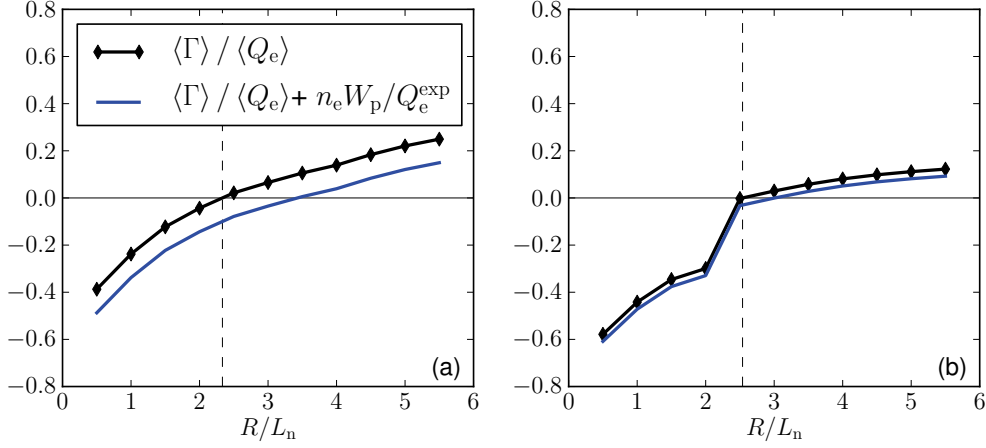


Figure 3.11: Normalized particle flux as a function of R/L_n , with (no symbols) and without (diamonds) the Ware-pinch contribution according to equation (3.8): (a) OH model scenario, $\chi_e^{\text{PB}} = 0.3 \text{ m}^2/\text{s}$ (b) ECH model scenario, $\chi_e^{\text{PB}} = 1 \text{ m}^2/\text{s}$. For both cases: $W_p = -0.3 \text{ m/s}$.

2008] using different summation rule, or even using only one k_y mode. A question arises whether the results reported here are strongly dependent on the choice of the w weights in equation 2.15.

We evaluated the quasi-linear fluxes and $R/L_n|_{\text{stat}}$ with several different choices of w for the parameter scans discussed previously. In figure 3.12 we show again the results of the temperature gradient scans (see figure 3.10) summing many modes with the power law used thorough this chapter and Ref. [Fable et al., 2010] (squares), summing with the classical mixing-length estimate (diamonds), summing with the exponential rule (triangles) motivated by fluctuation measurements [Bourdelle et al., 2007], using one mode where the mixing length transport is maximal (circles) [Merz and Jenko, 2010] and using one mode with $k_y = 0.3$ (stars) [Angioni et al., 2011]. Although, the differences in the predicted absolute value of $R/L_n|_{\text{stat}}$ can be as large as 1.5, the relative changes in $R/L_n|_{\text{stat}}$ and the parametric dependencies are nearly identical, independent on the choice of the quasi-linear rule. Figure 3.12 and 3.10 show that the main trends do not depend so much on the quasi-linear rule but rather on the main dependence of the underlying most unstable modes. However, it is safer to use the whole spectrum in order to be sure to capture both the effects of ITG and TEM modes. The importance of the most unstable modes explains why

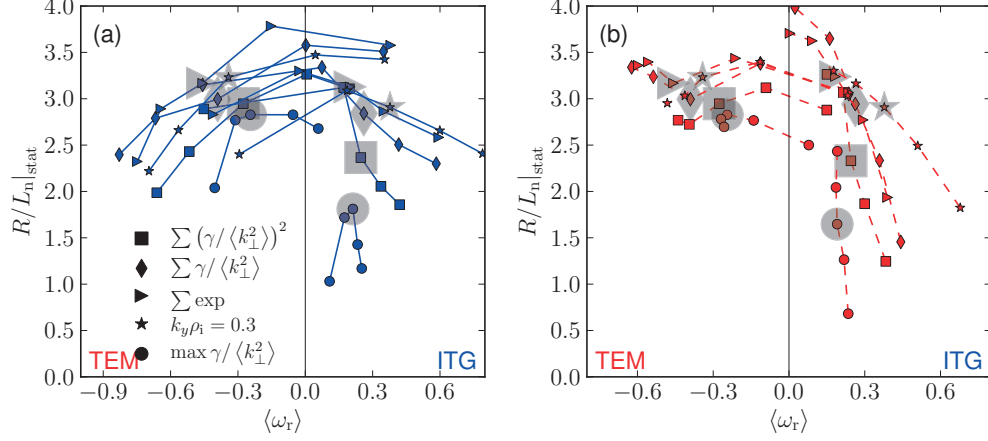


Figure 3.12: Same as figure 3.10 (a), using different quasi-linear rules: (a) R/L_{T_i} scan, (b) R/L_{T_e} scan. Different symbols show different prescriptions for the w weights in equation 2.15. The larger shaded symbols mark the reference cases as in figure 3.10: the OH case for $\langle \omega_r \rangle > 0$ and ECH case otherwise.

$\hat{\nu}$	0.5	\nearrow	
T_e/T_i	0.5	\searrow	
η	1 – 1.5	ECH \searrow	OH \nearrow
W_p	0.5 – 1	\nearrow	

Table 3.2: Change in R/L_n when the related parameter increases.

similar trends can be expected in non-linear simulations [Merz and Jenko, 2010, Lapillonne et al., 2011, Görler et al., 2011] and in the experiments.

3.3 Discussion

The collisionality dependence of the local logarithmic electron density gradient R/L_n has been investigated in ohmic and electron cyclotron resonance heated H-mode plasmas on TCV. The density profile flattens when ECH power is added, the normalized density gradient $R/L_n|_{\text{stat}}$ at $\rho_\psi \approx 0.7$ decreases from about 3 to approximately 1.5. The dependence of $R/L_n|_{\text{stat}}$ on collisionality is rather unusual: the density peaking increases with increasing collisionality. With local quasi-linear gyrokinetic simulations it was shown that the change in collisionality alone cannot reproduce the observed experimental behavior. The

simulation results show that the most important parameter is the ion temperature gradient R/L_{T_i} , which was not available in these experiments. Using $R/L_{T_i} = 6$ puts the OH and the ECH reference case in the ITG and the TEM regime, respectively, with predicted $R/L_n \approx 2.5$ and 3. For the OH case the contribution of the Ware-pinch can be as large as $\Delta R/L_n \approx 1$ resulting in a peaking around 3.5 which is in good agreement with the experiments. However, the flat ECH profiles are not recovered. If a lower ion temperature gradient $R/L_{T_i} = 4$ is assumed, the predicted OH density gradient increases to around 4 (with the Ware pinch included) and that of the ECH case decreases to 2. The experimental trends are, therefore, qualitatively explained. The edge ion temperature data suggest that R/L_{T_i} is about 3-5, however new experimental data are required to compare with our simulation results. We have also seen that at very low R/L_{T_i} , below 3-4, electron modes with large k_y are seen to play a role, therefore new simulations are also required in this domain with non-adiabatic passing electrons and non-linear model. The quasi-linear simulations predict that $R/L_n|_{\text{stat}}$ for the OH and the ECH reference case decreases as R/L_{T_i} is decreased, however dedicated experiments are needed to explore how the T_i profile changes between OH and ECH phases.

The simulation results, where the parameters can be changed individually, also show that the collisionality dependence can actually be due to a change in T_e/T_i and $(R/L_{T_e}/R/L_{T_i})$ rather than the collisionality itself. Table 3.2 summarizes the change in $R/L_n|_{\text{stat}}$ due to the considered parameters.

The $\langle \Gamma \rangle = 0$ stationary condition is set by the balance between ITG (yielding typically inward particle flux) and TE modes (yielding outward flux) as obtained in L-mode simulations [Fable et al., 2010]. Depending on the turbulence regime, the dependence of $R/L_n|_{\text{stat}}$ on the collisionality, temperature ratios and temperature gradients can be very different, but in all cases the average mode frequency $\langle \omega_r \rangle$ as a figure of merit of the background turbulence clarifies the simulation results. This property of real mode frequency of the most unstable modes was observed in the study of L- and H-mode AUG plasmas [Angioni et al., 2005b, 2011], L-mode and eITB TCV plasmas [Fable et al., 2008, 2010], and now has been confirmed for TCV H-mode parameters, as well. The neoclassical Ware-pinch can also contribute to the peaking in certain conditions typically when the stationary point lies in an ITG dominated regime and when the electron heat flux is not too large.

It is interesting to relate the present results to those of AUG reported recently in [Angioni et al., 2011]. The density peaking in those considered H-mode plasmas increases

with increasing additional ECH power, mainly due to the increase in the ratio of the logarithmic electron temperature gradient to the logarithmic ion temperature gradient and partly also from the increase in the electron to ion temperature ratio. Figure 7. (a) in [Angioni et al., 2011] can be directly compared to the curve with stars in figure 3.12. In purely NBI heated AUG H-mode plasmas ITG modes are the most unstable modes, positioned on the right part of the plot with positive frequencies. Adding ECH destabilizes the TEMs and $R/L_n|_{\text{stat}}$ increases as the mode frequency decreases. It is predicted that even larger amount of ECH would result in decreasing peaking [Angioni et al., 2011], however, this could not be validated by those experimental results. According to our interpretation, the TCV OH plasmas are positioned very close to the ITG-TEM boundary and the additional ECH moves $R/L_n|_{\text{stat}}$ down on the left branch of the curve in figure 3.12. Therefore our results combined with AUG observations [Angioni et al., 2011] recover the full non-monotonic $\langle\omega_r\rangle$ dependence.

3.4 Summary

In this chapter the 'unusual' collisionality dependence of the density peaking in TCV H-modes was analysed: the peakedness of the electron density profile decreases when the collisionality is decreased, in this case, by strong electron heating. A quasi-linear gyrokinetic theory [Fable et al., 2010] was compared against this H-mode dataset. The observed peaking dependence can be reproduced by this model. The strongly electron heated TCV H-mode experiments complement recent experiments on AUG-U [Angioni et al., 2011]. We showed that the experimental dependence is much more complex than simply a collisionality dependence; parameters such as the electron to ion temperature ratio, the ratio of electron to ion gradient length scales and the Ware-pinch play an important role and can significantly influence the density peaking. The global trend comes from the indirect effect of other background parameters. In fact, the collisionality dependence may be weak, or even reversed. It was demonstrated that the conclusions of the quasi-linear analysis do not depend on the chosen quasi-linear rule. When the simulation results are interpreted as a function of the average mode frequency: a simple picture of ITG and TEM modes can be drawn that explains very well particle transport. This is true for L-modes, electron internal transport barriers and H-modes and applies across tokamaks.

Chapter 4

Multipurpose gas injection system

In this chapter a new gas injection system is presented capable of massive injections and also delivering small pulses of gaseous impurities in the plasma. In section 4.1 experimental situations are described that require external gas injection to motivate the need for a multipurpose gas injection system. Section 4.2 presents the operating principles and setup of the system. Section 4.3 characterizes the performance of the injector by describing calibration experiments to measure the number and the velocity of injected particles outside TCV plasma operation. Finally, in section 4.4 commissioning experiments, with plasma, are presented.

4.1 Gas injection experiments

In the recent experimental campaigns on TCV, two groups of experiments required gas injection in plasmas. In the first group of disruption mitigation experiments, massive gas injection is used: the injected gas ionizes to low charge states that radiate the plasmas energy helping to reduce the damaging effects of the vivid collapse of the plasma on the plasma facing components. Secondly, for impurity transport studies, that is to measure how the injected impurity distributes in the plasma as a function of time and space, short puffs are desirable, small packages that do not perturb the plasma, but provide enough light intensity for the measurements.

4.1.1 Disruption mitigation

Disruptions, sudden terminations of the plasma discharge, occur due to a loss of stability and/or confinement of tokamak plasmas [Wesson et al., 1989, Hender et al., 2007]. The goal of disruption mitigation is to terminate the discharge in more controlled way than is possible during an unprogrammed disruption [Finken et al., 2001]. Disruptions are mainly caused by neoclassical tearing modes, control errors and operator mistakes [De Vries et al., 2011]. An unmitigated disruption typically exhibits two phases [Thornton et al., 2012]. In the first phase the plasma undergoes rapid cooling and the stored thermal energy is lost, resulting in high divertor loads. During this thermal quench the plasma resistivity increases and the stored magnetic energy is also converted to thermal energy via ohmic heating of the post thermal quench plasma. This second phase is usually referred to as current quench.

The enormous power flux density on the plasma facing components, halo currents and the creation of relativistic (runaway) electrons can cause significant damage, especially in large devices [Finken et al., 2001]. The mitigation of these effects requires rapid radiation of the plasma thermal and magnetic energies coupled with the timely delivery of large numbers of electrons to the plasma volume during the current decay [Hender et al., 2007]. Massive electron delivery can help to avoid runaway generation by increase the collision frequency. Both these requirements – for radiating impurity delivery and for electron delivery – can be satisfied by injection of impurity atoms. Inert noble gases are preferred since they are relatively easy to remove from the vessel.

The large number of atoms necessary to impede the evolution of runaway current can be supplied by injection of impurities in an amount that is comparable or greatly exceed the total particle content of the plasma itself [Bozhenkov et al., 2008]. TCV plasmas have a typical volume of 1 m^3 and average electron densities around 10^{20} m^{-3} , which means the plasma particle content is of the order of 10^{20} , therefore for disruption mitigation experiments we had aimed for the injection of at least several times 10^{20} species in a single pulse.

According to actual disruption mitigation experiments only that part of the injected gas which reaches the edge of the plasma before the thermal quench becomes ionized there and mixes into the plasma core. Hence, only this part can help radiate the plasma energy and increasing the collision frequency of the runaway electrons [Lehnen et al., 2009],

while the other part can even help generating runaways therefore should be minimized. Unfortunately, immediate disruption can be directly provoked by slowly increasing the impurity concentration, for example, with the slowly increasing part of the main gas pulse and with pre-pulses [Hollmann et al., 2008]. As far as the pulse shape is concerned, therefore, a gas pulse with a fast-rising edge, without pre-pulses is necessary.

Nowadays the disruption mitigation is mainly in the experimental phase: gas is injected into stationary tokamak plasmas and the properties of the provoked disruptions are investigated. Significant effort has been put in the development of control algorithms that are able to detect disruption precursors [Hender et al., 2007]. In ITER, disruption mitigation valves (DMVs) will be part of the machine safety system: the control system of the tokamak detects the precursors of the forthcoming disruption and inject gas to avoid the natural disruption process by controlled termination of the plasma. The reaction time of the system must be shorter than the time scale of the full disruption process. The reaction time is limited by various parameters: the time it takes the control system to identify that disruption will occur; the time the control system switches off the auxiliary systems, in particular, to prevent the overheating of the neutral beam injection duct and arcing in the ion cyclotron resonance heating antennae during gas injection; and the time between the valve opening and the arrival of the gas into the vacuum vessel [Kruezi et al., 2009]. The first two are tasks for control engineers to design a fast enough control system while the latter is determined by the physical properties of the DMV and special design is necessary for its minimization [Parks and Wu, 2011].

4.1.2 Transport studies

In experiments where the goal is to study the behavior of impurities in different plasma scenarios, the goal is to keep the impurity concentration low enough not to perturb the plasma (dilution, radiation cooling) but to still have a good diagnostic signal to noise ratio. This criterion poses a contradictory requirement for the injector. Indeed, in these experiments the number of injected particles must be kept orders of magnitude lower than in the disruption provocation/mitigation experiments. It is an important aspect of transport studies to compare the behavior of different impurities under similar experimental conditions. Therefore, an injection system where the gas can be changed easily is desirable.

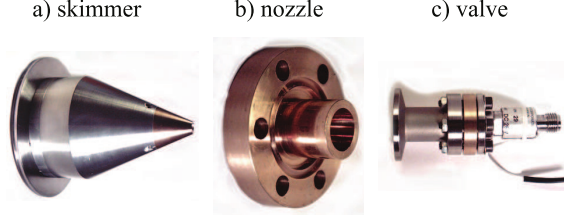


Figure 4.1: Components of the gas injection system: (a) skimmer, (b) nozzle and (c) valve.

valve type	orifice	maximum reservoir pressure
small	0.05 mm	70 bar
medium	0.8 mm	70 bar
large	1.6 mm	25 bar

Table 4.1: Solenoid valve properties.

4.2 Operating principles and setup

The injector was designed and manufactured in the Wigner Research Centre for Physics, Budapest. The components of the system are shown in figure 4.1: the skimmer (a), the nozzle (b) and the valve (c). The schematic drawing of this system is presented in figure 4.2 (a), the complete setup, as installed on the upper lateral port of TCV (0.455 m above the midplane) in Sector 4. Photographs of the installed system can be seen in figure 4.3, the left image is the injector on the torus, while the right image shows the gas switcher system and the gas bottles on the -1 level, under the tokamak.

Replaceable commercial fast switching solenoidal valves (Parker Hannifin Co. General Valve *Series 99 Pulse Valves*, Part ID: 9-181-900) were chosen to control the gas flow. The parameters of the three valves used with different orifice diameter are enumerated in table 4.2. When the valve is not powered it is closed. The force the valve can exert against the reservoir pressure to open is limited, therefore the valve with the largest orifice can only tolerate a lower pressure. If this pressure is exceeded the valve will remain closed.

The valve's state changes from open to closed or closed to open takes about $150 \mu\text{s}$. This determines the minimum rise time of the exiting gas packet. This time also imposes a lower limit for opening time: millisecond long pulses can be injected with a fully opened valve, which is sufficiently short for transport studies. The gas arrives to the valve from a plenum 150 cm^3 of volume acting as a buffer. It ensures that the pressure at the valve's

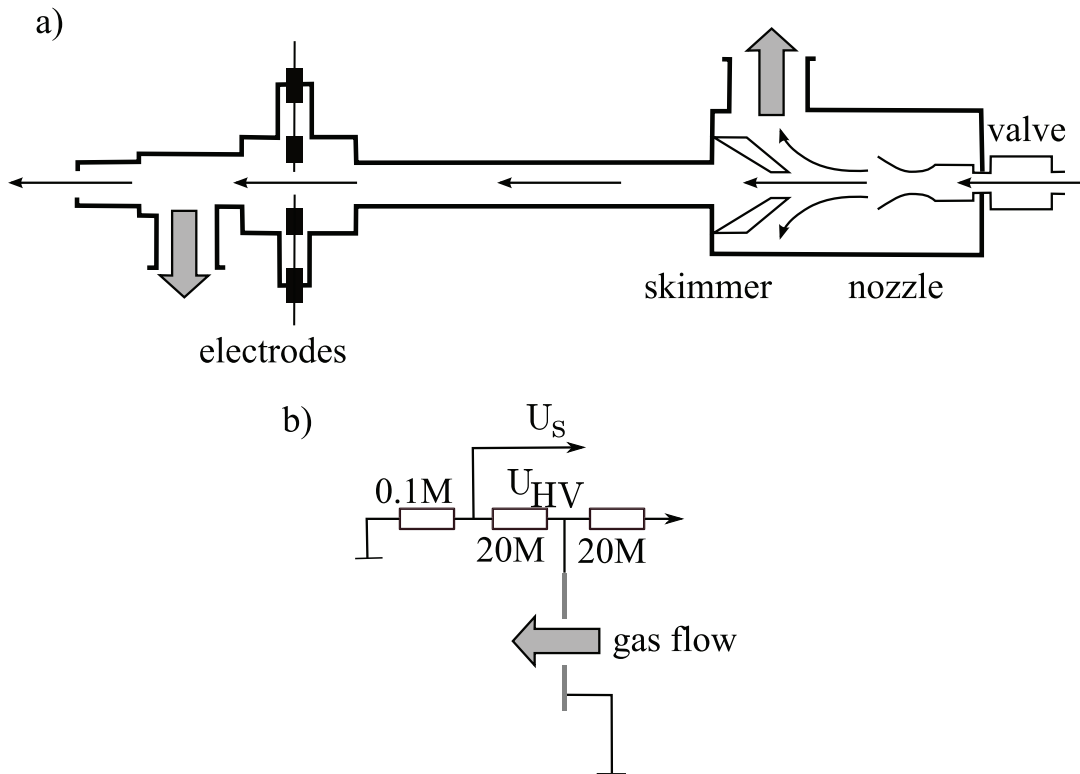


Figure 4.2: Schematics of the gas injection system: (a) the gas packet's path from the valve, through the nozzle and the skimmer, in between the electrodes to the vacuum vessel; (b) circuit diagram of the electrode pair measuring gas flow.

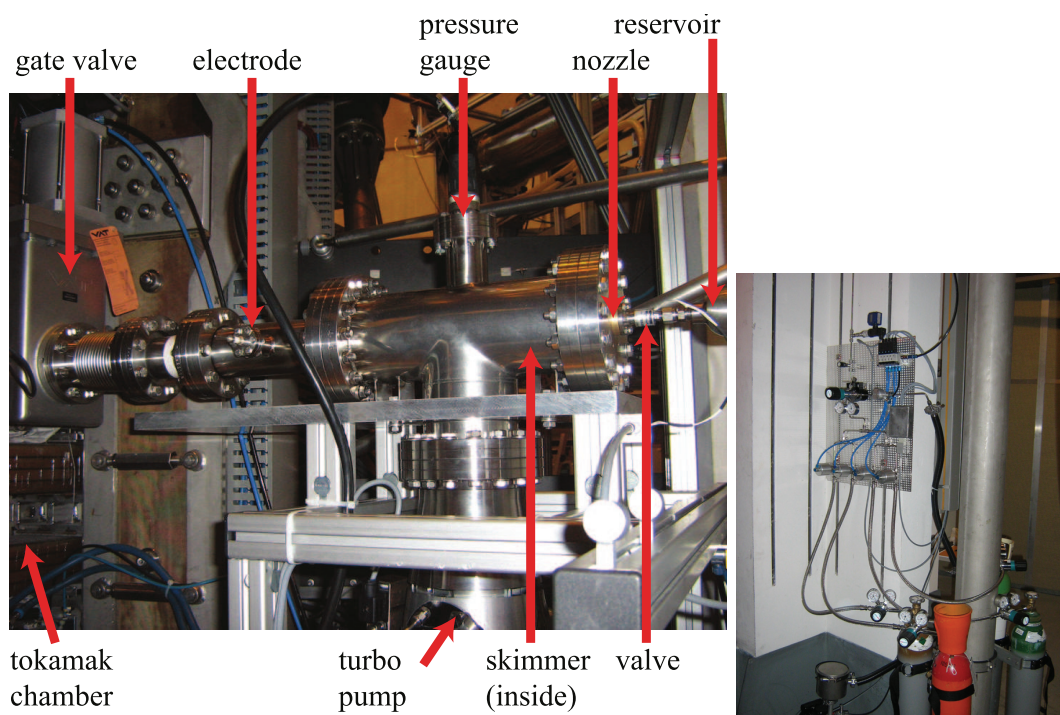


Figure 4.3: The multipurpose gas injection system on TCV (left). Gas bottles and the gas switcher on the -1 level (right).

input does not drop significantly during a gas pulse.

As the valve opens the gas enters into a nozzle (figure 4.2 (c)). The nozzle was manufactured in the mechanical workshop of the Wigner Research Centre for Physics in Budapest. The gas expands in the divergent part, passes through the throat, the narrowest part of the nozzle, then expands in the divergent part. If the gas reaches the local sound speed in the throat it will be further accelerated and will become supersonic. Parabolic (bell-shaped) convergent-divergent nozzles are efficient [Arrington et al., 1996] for attaining supersonic speeds. Connecting the valve's exit to the nozzle creates an unwanted buffer volume that decreases the nozzle's performance. During the design this volume was minimized.

After about 20 cm flight, the gas pulse encounters a skimmer, where its edge part is intercepted and removed by a turbo pump. The remaining gas, which now has a form of a collimated beam, continues towards the vacuum chamber. When the system is not used, the injector is isolated from the vacuum chamber by a gate valve. This protects the vacuum in the main chamber and allows maintenance on the injection system without breaking the TCV vacuum.

The gas pulse covers a distance of approximately 1 m from the valve across the nozzle, skimmer and the gate valve to the tokamak vacuum vessel.

4.3 Calibration

A series of calibration experiments were performed in-situ, that is with the system installed on the tokamak, but without plasma to characterize the injector. The number of injected particles and the arrival time were measured as a function of the filling pressure of the reservoir, the pulse length and the gas type. These calibration experiments are now detailed.

4.3.1 Number of injected particles

The number of injected particles were measured in the following way: the reservoir's volume (150 cm^3) was filled up to some pressure, then the gas was released in the empty torus by opening the valve. The difference in filling pressure before and after the injection was used to measure the number of injected particles. The accuracy of the reservoir's pressure gauge is around 0.05 bar, therefore the valve was opened repetitively 20-50 times, to reach

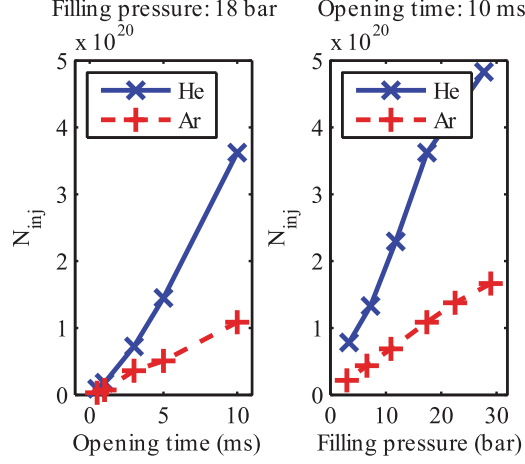


Figure 4.4: Number of injected particles for He and Ar as a function of (a) opening time at constant (18 bar) reservoir pressure, and (b) reservoir pressure at constant (10 ms) opening time. The measurements were performed with the large aperture valve.

measurable pressure drop. The pressure increase in the vacuum chamber – with no plasma – was also monitored. The number of injected particles calculated from the pressure drop in the reservoir and from the pressure increase in the vacuum vessel showed better than 5% agreement.

The result of these measurements, the number of injected particles are shown in figure 4.4 as a function of (a) the opening time and (b) the filling pressure. For both series of measurements, the large aperture valve was used. The number of injected particles is seen to depend linearly both on the opening time and the filling pressure with a slope that is larger for helium. The higher sound speed of the lighter helium, results in a larger number of injected particles at constant pressure and opening time. The reason for this is the following: as the valve opens, the gas in the reservoir expands to essentially vacuum. In this condition the outflow velocity is limited, or choked to sound speed. This means that a longer injection, at constant pressure, delivers more of the lighter gas, as observed in figure 4.4 (a). Increasing the plenum pressure compresses the gas in the reservoir and, at constant opening time, the larger density the greater the number of injected particles. Indeed, we see in 4.4 (b) that the number of particles depend linearly on the filling pressure. The JET and MAST DMVs [Finken et al., 2008, Thornton et al., 2012] systems shows similar dependences.

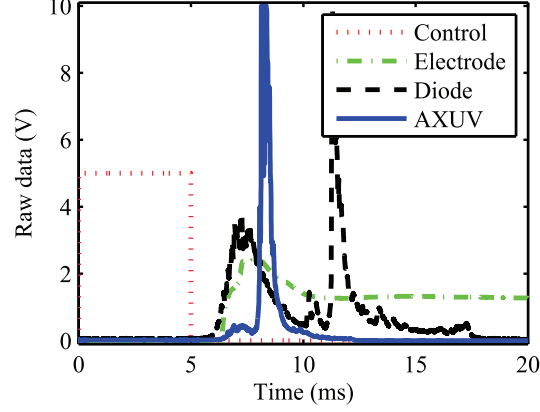


Figure 4.5: Typical signal shapes of the monitoring diagnostics of 5 ms long Ar injection: valve open-closed control signal (dotted) ; inverted, scaled and shifted voltage between the electrodes (dash-dotted) Dashed black line: visible observer diode (dashed), 1st AXUV channel (continuous).

4.3.2 Arrival time

The arrival time of the gas pulse was measured by means of a pair of electrodes, depicted in figure 4.2 (a) and also marked in figure 4.3. They are placed at 0.5 m distance from the nozzle's exit. We underline that the measurements were taken outside TCV plasma operations, without the presence of discharge in the torus.

The electrodes' circuit diagram is shown in figure 4.2 (b). When there is no gas flow between the electrodes, no current flows. The power supply voltage U_{HV} is dropped on the voltage divider and the output voltage U_s is measured:

$$U_s = \frac{0.1 \text{ M}\Omega}{20 \text{ M}\Omega + 20 \text{ M}\Omega} U_{HV}. \quad (4.1)$$

When the density in the inter-electrode gap is sufficient the gas breaks down, the atoms or molecules are ionized; a current flows and $U_s = 0$ is measured. The drop of U_s is used to indicate the arrival of the gas flow. It was found that $U_{HV} = 2 \text{ kV}$ is high enough to produce an arc in case gas is flowing across the electrode gap, but does not lead to arcing under vacuum conditions when the pressure is of the order of 10^{-8} mbar .

Typical measured signals of 5 ms long pulses with Ar are depicted in figure 4.5. We note that these signals were not measured simultaneously. The electrode signals were measured

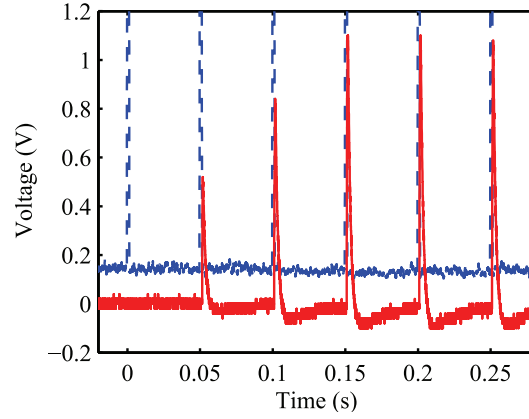


Figure 4.6: D_2 injection by the low aperture valve with 20 Hz repetition frequency, 1 ms opening time and 42 bar filling pressure. First injection is at 0 s: electrode voltage (continuous) and the valve's control signal (dashed).

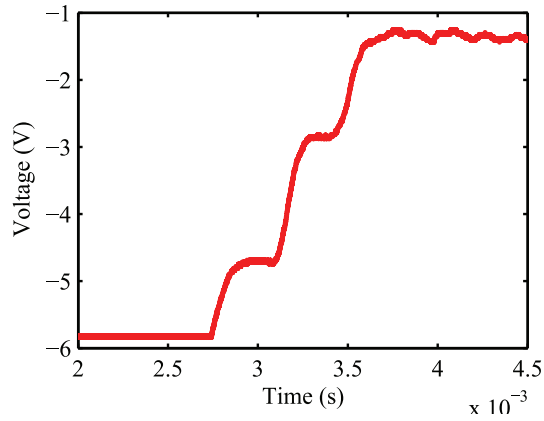


Figure 4.7: Increase of the electrode signal during D_2 injection made by the large aperture valve.

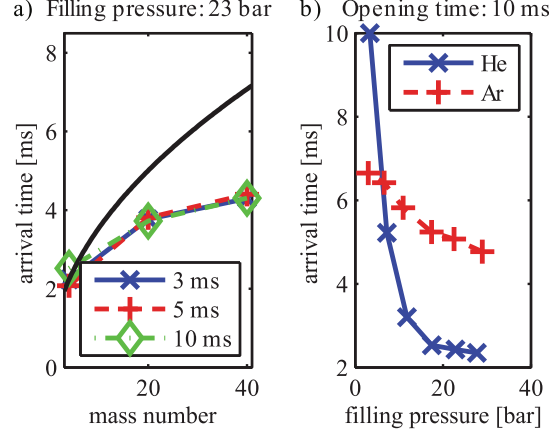


Figure 4.8: Arrival time as a function of (a) mass number for different opening times, and (b) as a function of the filling pressure for He and Ar. The injections were made by the large aperture valve.

without plasma, while the diode and the AXUV signals were recorded during gas injection provoked disruptions.

Only single pulses longer than 2 ms can be detected with the electrode system. For pulses shorter than 2 ms, a series of pulses were instead generated up to repetition frequencies of 100 Hz. This is the maximum repetition frequency where the gas can be pumped out efficiently. Only after the second or third pulse in the series the signal is detected. Figure 4.6 illustrates this behavior: the voltage between the electrodes is shown for repetitive, 1 ms pulses using the medium aperture valve. It can be clearly seen that only from the third pulse the signals are uniform. There are at least two possible explanations for this behavior:

1. the breakdown of the gas in the inter-electrode gap needs a certain threshold/residual gas density and for short pulses this threshold is only reached after several pulses,
2. for short pulses the flow in the nozzle is different from that for long pulses; again, some residual gas in the nozzle is necessary to obtain the same flow.

As a consequence of this threshold behavior we assume that the velocity measured for single pulses is probably underestimated, because some portion of the gas jet's rising edge is used up to create the necessary minimum pressure between the electrodes and/or in the

nozzle. The gas velocity measured in the repetitive experiments is found to be larger (for otherwise same conditions) than for single pulses.

Despite this small amount of residual gas, the signal of the electrodes dropped down in a few ms following the rise in case of the low and medium aperture valve (see figure 4.6). This indicates that the amount of the residual gas is not sufficiently high significantly perturb the tokamak plasma experiments on a longer timescale.

An interesting feature, and also an important limitation in the use of electrodes, is a strong dependence on the injected gas. The increase of the signal level was not so rapid and plateaus in the electrode current were observed when D₂ gas was injected. These can be seen in figure 4.7. The presence of the plateaus makes the arrival time difficult to define. The proposed explanation for this is as follows: when a molecular gas is used, the ionization, dissociation of the molecules and then the ionization of their parts happens on a slower timescale than pure ionization of single atoms. The plateaus correspond to the different energy levels of these ionization states.

Figure 4.8 shows (a) the arrival time as a function of mass number for different opening duration, and (b) as a function of the reservoir pressure. The arrival time is independent of the opening times and scales as \sqrt{A} where A is the mass number. This latter can be explained by the square root dependence of the sound speed on the mass number for a given temperature. The injections were made with the large aperture valve. According to these measurements the system has similar properties in the 15 bar - 25 bar filling pressure range and the arrival time is independent of the opening duration. The subsonic or supersonic behavior of a nozzle depends on the filling pressure of its reservoir. Thus, the properties of the gas beam going across the nozzle can change suddenly when the reservoir pressure is decreased, which may explain the measured arrival time-characteristics.

As the filling pressure is high enough for the nozzle to operate as a supersonic valve the arrival times are in reasonable agreement with those measured at the JET DMV [Finken et al., 2008]. The electrode - valve distance is only 2/3 of the vessel wall - valve distance which means higher delay times between the valve opening and the arrival at the vacuum vessel but they still remain comparable to the JET DMV capabilities and much lower than the time necessary for a tokamak control system to activate a DMV [Kruezi et al., 2009].

shot #	gas	disruption	density rise
35005	D	0.603 s	1.5 fr
35003	He	0.605 s	4 fr
35002	Ne	0.607 s	1.5 fr
35004	Ar	0.608 s	1.0 fr

Table 4.2: First disruption mitigation experiments. Injection: 5 ms pulse at $t = 0.6$ s.

4.4 Commissioning experiments

4.4.1 Disruptions

The very first observations related to commissioning experiments are summarized in table 4.2. Deuterium, helium, neon, argon all provoked disruptions in less than 1 ms. The delay between the valve opening and the disruption is consistent with the calibration experiments (see figure 4.8). In figure 4.9 we show an example disruption in more detail, where signals from various diagnostics are collected. The argon injection occurs at $t = 1.8$ s and the valve was opened for 10 ms (plenum pressure was 24.1 bar). The first sign of the injection can be seen, at $t = 1.806$ s, on an observation diode's signal equipped with Ar filter. 1 ms later, one of the outermost chords (channel #26) of an AXUV prototype camera [Degeling et al., 2004] also starts to increase. The plasma current continues for more than 11 ms after the injection. This is the time it takes the gas to travel through the injection system (transit time), to cool down the plasma edge and the core (thermal quench). The plasma current is quenched in about 2 ms.

The complex dynamics of the disruption can be also seen on the images of a fast framing camera system (FastCam). Thumbnails of the recorded 1024×1024 (full frame) images at 3000 fps are also shown in figure 4.9. The plasma edge in front of the injector appears as a bright spot. Also, long, toroidally elongated filaments are observed until the plasma collapses. From $t = 1.811$ s, the injector port's interior is illuminated.

4.4.2 Non-perturbative injections

Chapter 5 will present the impurity injection experiments performed with this system in detail. Here we only note that the main plasma properties such as density, current, etc. remain unchanged during the injection. Figure 4.10 shows several diagnostic signals from a demonstrative argon injection experiment with the gas injection system. The soft

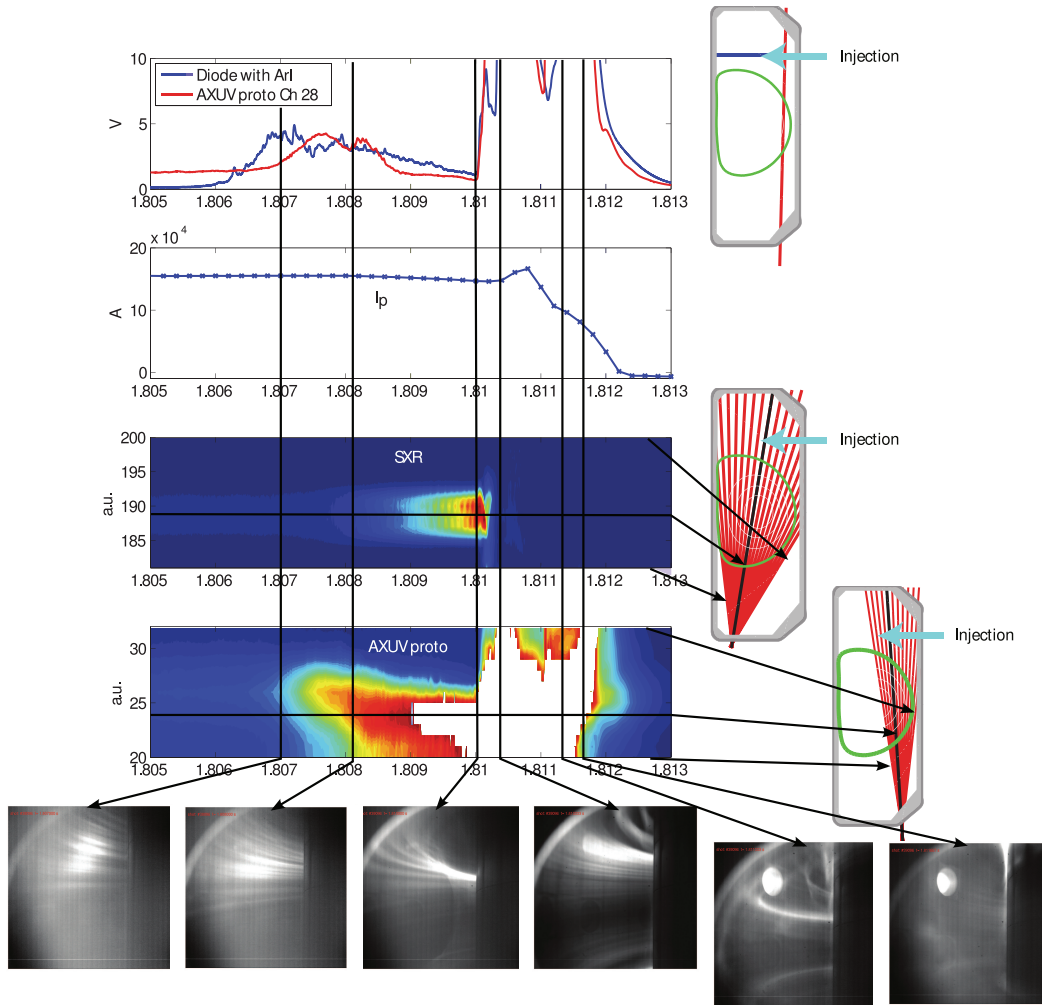


Figure 4.9: Disruption example (#39096). Ar injection at $t = 1.8$ s, 10 ms. Courtesy of Tál [2009]

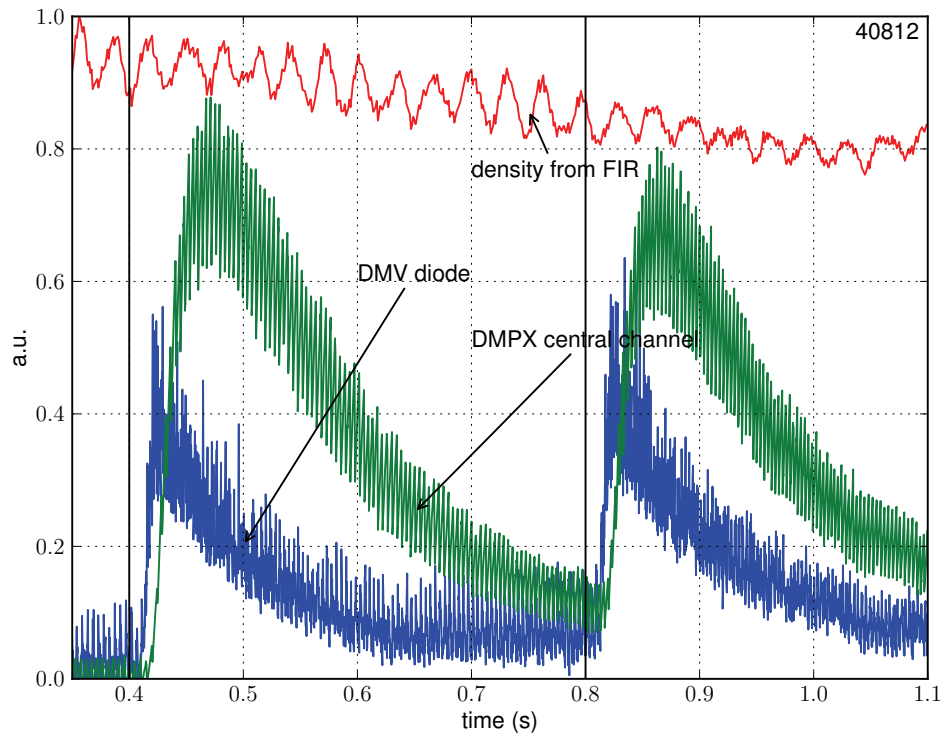


Figure 4.10: Ar injection as seen by different diagnostics: soft x-ray intensity on the DMPX central chord (green), a photodiode equipped with a 420 nm filter (blue) and the density from the interferometer (red). Injections are at $t = 0.4$ s and 0.8 s with a length of 1 ms. (TCV #40812)

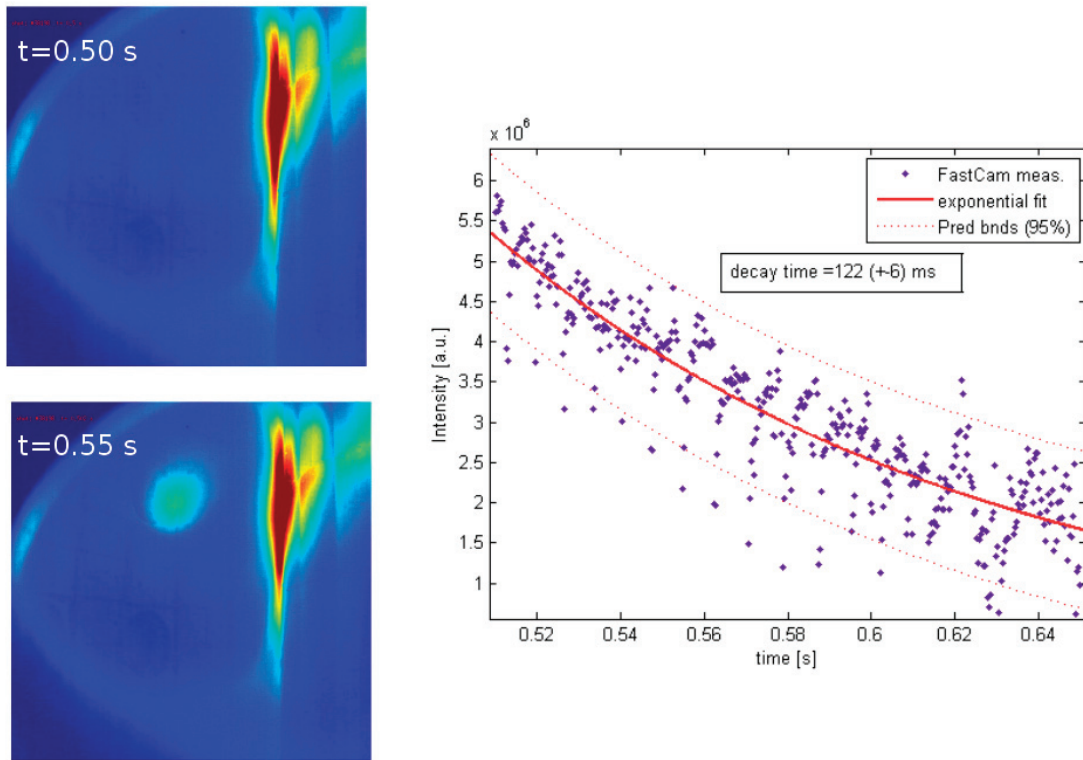


Figure 4.11: False color image of the injection. Deuterium injection as seen by the FastCam diagnostic (TCV #38198). The injected gas appears in the images as a bright 'patch' on the plasma surface. Courtesy of Bencze [2009]

x-ray traces are very similar to those presented by Guirlet et al. [2009].

Using the FastCam diagnostic visual confirmation of the injection can also be obtained. Figure 4.11 shows that the radiation in the visible range is highly localized and form a "patch" on the curved plasma surface (the camera view and the recording parameters are identical to those images of figure 4.9. The gas beam has a radial extension as wide as the port itself which suggests significant radial dispersion. It is also noticeable that the light intensity decays rather slowly compared to the opening time. The light spots maintains its shape and decreases exponentially with a time constant of about a 120 ms.

The interpretation of these experiments necessitates detailed modelling of the impurity penetration and its radiation pattern. The details of the modelling will be the subject of Chapter 6.

4.5 Summary

In this Chapter a new diagnostic tool, a multipurpose gas injection system on the TCV tokamak was presented. The fast gas injection valve, designed and built in the Wigner Research Centre for Physics, Budapest, was characterized in a series of calibration and commissioning experiments. The results are in reasonable agreement compared with similar systems on other machines [Guirlet et al., 2009, Finken et al., 2008]. When the system is operated with a large orifice valve, it provoked disruption with all the gases used (deuterium, helium, neon, argon). In a demonstrative experiment the plasma current was quenched in about 12ms after the valve opening. When a valve with a smaller orifice is used, the gas injection does not perturb the main plasma parameters such as density, temperature, but the SXR diagnostics provide sufficient amount of light to detect the injected argon and neon. The valve of the injector can be replaced in between experimental sessions, the injected gas can be changed in between plasma discharges providing a flexible tool for experiments with gas injections.

The relevant tokamak plasma physics phenomena presented in Chapter 2 and the general behavior of the gas injection system together provide us the necessary information to describe the impurity transport experiments performed on TCV.

Chapter 5

Impurity transport experiments in TCV

Injection of non-intrinsic impurities in plasmas provides a whole realm of transport experiments. In contrast to observations of intrinsic impurities these experiments have several advantages: the impurity species, the quantity and the time instance of injection can all be controlled externally which allows a better separation between the background signal and that produced by the injection of the impurity species in question. The most common impurity injection techniques are the laser blow-off [Friichtenicht, 1974] technique, seeded pellet injection [Behringer and Büchl, 1989] and gas injection, each having merits and difficulties [Guirlet et al., 2009]. In this thesis gas injection is employed, being the only one available presently on TCV.

In this chapter we present the impurity transport experiments performed with the injection system described in chapter 4. The goal of the experiments was to measure the SXR emission of the injected impurities under various plasma conditions and provide input for modelling (the topic of Chapter 6). In the simplest situation of impurity transport, impurities are present in low concentration with respect to the bulk species: they are solely transported by the background turbulence, but they do not influence it. We verify whether this condition holds experimentally by examining the effect of the injection on the background profiles. If the background profiles are not modified significantly, the impurity transport experiment is called *perturbative*. The experiments were aimed at studying the impurity behavior with respect to the main plasma parameters influencing confinement properties such as plasma current, shape and auxiliary heating.

The experiments presented in this chapter do not show the complete picture of impurity transport in TCV. However, the results obtained in this section permitted the simulation tools, presented in chapter 6, to be developed and tested, and trigger ideas for further, more detailed experiments.

Firstly, in section 5.1 we introduce typical argon and neon injection experiments. Then, in section 5.2, presenting experiments at lower electron density we study under what circumstances the plasma background parameters can be considered constant. Section 5.3 shows how a compromise between efficient injection and good diagnostic coverage can be achieved. In sections 5.4-5.6 we explore the effects of plasma current, heating power and plasma shape, respectively on the behavior of the injected argon and neon atoms. These parameters are known to affect the underlying turbulence, hence the transport. Finally, section 5.7 describe experiments to achieve stationary impurity concentration in the plasma; we saw in Chapter 3 that in stationary conditions profile gradients can be directly related to transport coefficients.

5.1 Argon and neon injections in L-mode, ohmic plasmas

In the first set of experiments, we compare argon and neon injections in typical TCV L-mode plasmas. The comparison was made on a shot-to-shot basis, in the same experimental session, with gas changes between pulses. Figure 5.1 shows time traces of various quantities of typical argon and neon injections experiments. The background parameters such as density, plasma current, temperature etc. are kept constant. Two injections were programmed at 0.5 and 1.0s and the fast valve stayed open for 10 ms. In figure 5.2 we show the electron density and temperature profiles for #43768 before and just after the first neon injection, near the time when the SXR radiation in the core peaks (the highest impurity concentration). It can be seen that the profiles are not affected by the injection. It was checked that this was also the case for argon injection.

The injections are clearly seen on the SXR traces (5.1 (c)). The rise and decay parts of the signals were fitted with functions of the form of $1 - \exp(-t/\tau_r)$ and $\exp(t/\tau_d)$, respectively, to obtain the characteristic rise and decay times τ_r and τ_d .

For argon, the central SXR signal starts to increase 20 ms after the injection with

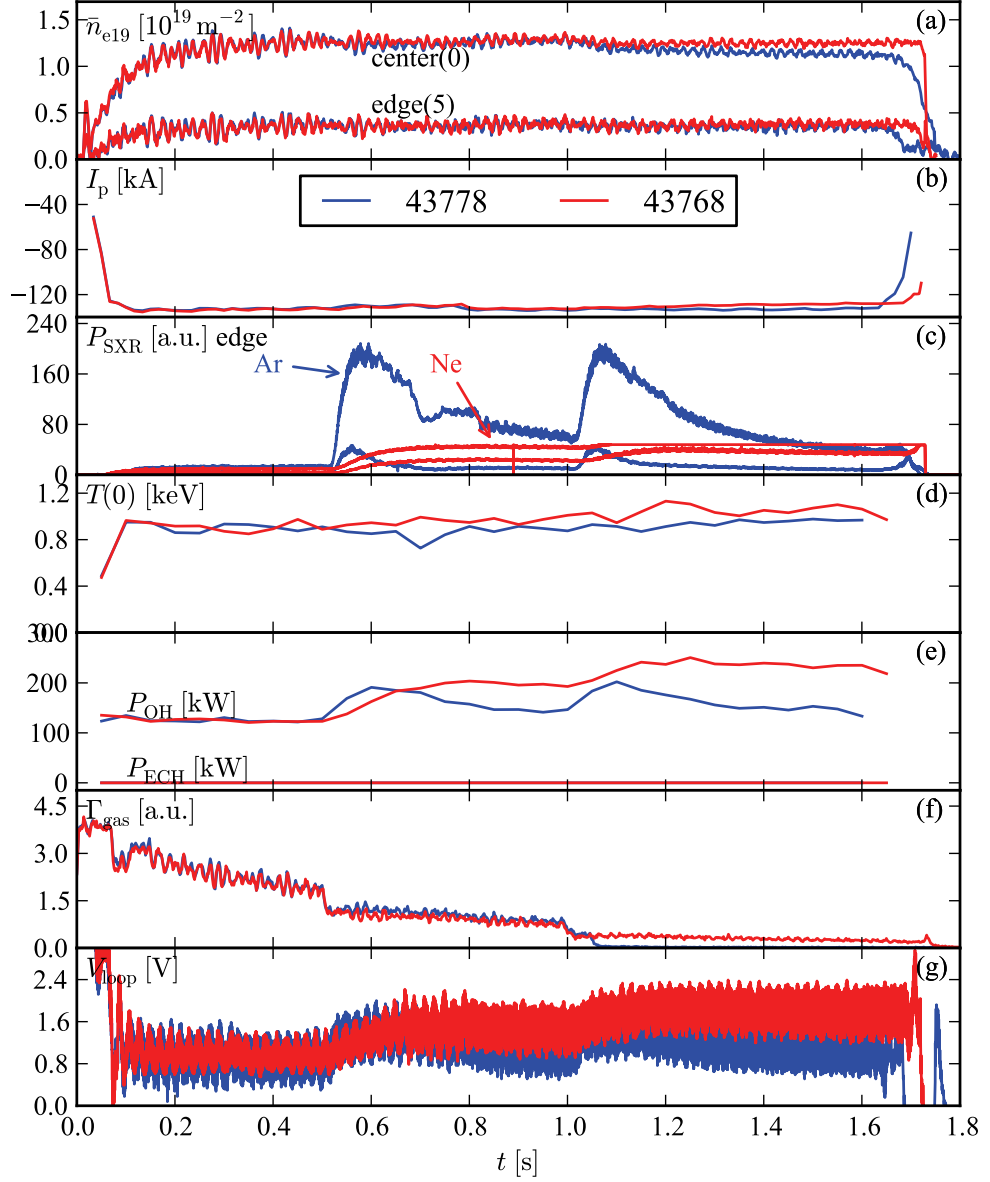


Figure 5.1: Time evolution of (a) the central and peripheral chords of the FIR interferometer, (b) the plasma current (c) the central and peripheral chord of DMPX, (d) the central electron temperature, (e) OH and ECH power and (f) the deuterium gas flux for 10 ms long argon (#42307, blue) and neon (#42314, red) injections at 0.5 and 1.0 s.

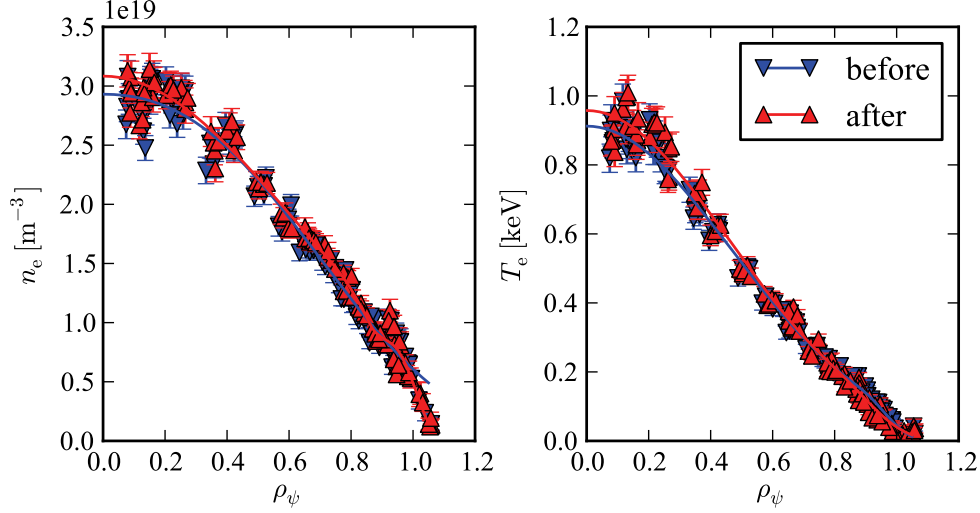


Figure 5.2: Electron density and temperature profiles before ($t = 0.25 - 0.50$ s) and after ($t = 0.5 - 0.75$ s) neon injection for #43768, ohmic plasma.

$\tau_r \approx 20$ ms. The characteristic decay time, τ_d , is around 200 ms, that is an order of magnitude slower than its rise. We see in figure 5.1 (c) that the SXR emissivity after the first injection did not decay completely at 1.0 s when the next gas pulse arrives. The time evolution of the SXR traces after neon injection is different. The central SXR emissivity increases with $\tau_r = 40$ ms and reaches its maximum about 0.3 s after the injection. The decay phase is slower than that of argon with a characteristic time of seconds.

Neon and argon, are noble gases and chemically inert. After they are lost from the plasma and neutralized near the wall, they may re-enter the plasma acting as a continued impurity source. This recycling process makes the analysis of the impurity density decay phase of the SXR traces difficult: recycling from the wall makes the apparent decay slower. In the next chapter we will explore this effect in detail.

The injections are also seen on the deuterium gas feed traces (figure 5.1 (f)). The ionization of the injected impurities creates an excess of electrons in the plasma. In the core, argon reaches the Ar^{16+} charge state (see figure 2.14 of chapter 2), that is every injected argon atom donates 16 electrons. The control system, programmed to keep the electron density constant, decreases the deuterium influx immediately following the injections. These can be seen on the gas flux trace at 0.5 and 1.0 s.

The loop voltage (figure 5.1 (c)) evolution is correlated with the SXR evolution. The plasma resistivity, and thus the measured loop voltage, depends on the plasma composition [Hutchinson, 2005]. This provides us an in-situ estimation of the number of injected particles, complementing the calibration experiments presented in the previous chapter (section 4.3). Assuming

$$V_{\text{loop}} \propto Z_{\text{eff}}, \quad (5.1)$$

where Z_{eff} is the *effective charge* of the plasma

$$Z_{\text{eff}} \equiv \frac{\sum_Z Z^2 n_Z}{n_e}, \quad (5.2)$$

where the summation is performed for all ion species, the change in plasma composition can be calculated. For the sake of simplicity, the calculation below is presented for argon. We assume that the plasma is composed of fully ionized deuterium, carbon and, when injected, all the argon atoms are present as He-like Ar^{16+} . The effective charge is then from equation 5.2

$$Z_{\text{eff}} = \frac{n_D + 6^2 n_C + 16^2 n_{\text{Ar}}}{n_e}. \quad (5.3)$$

From the quasi-neutrality condition

$$n_e = \sum_Z Z n_Z, \quad (5.4)$$

which in this case reads

$$n_e = n_D + 6n_C + 16n_{\text{Ar}}, \quad (5.5)$$

the deuterium density can be expressed and substituted into equation 5.3 giving

$$Z_{\text{eff}} = 1 + (6^2 - 6) \frac{n_C}{n_e} + (16^2 - 16) \frac{n_{\text{Ar}}}{n_e}. \quad (5.6)$$

During a typical 10 ms long argon injection we observe approximately 40% increase in the loop voltage. Using $n_C/n_e = 0.05$ this results in $n_{\text{Ar}}/n_e \approx 0.2\%$. The injected impurities attain a concentration in the plasma that is one order of magnitude lower than the carbon concentration, whilst providing approximately only 3 times more electrons per ion.

For neon injection, it can be seen that the loop voltage increases almost by a factor of two. In order to have a better measure of the change in Z_{eff} , we calculate the bootstrap

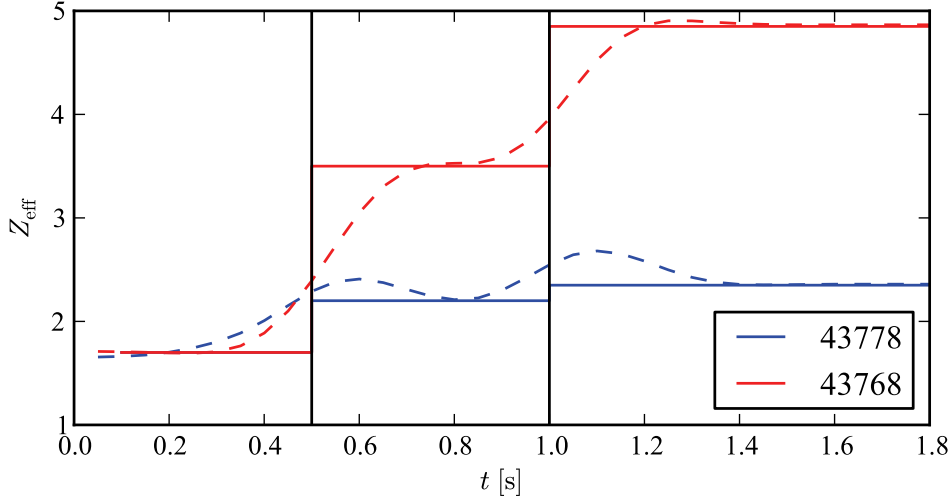


Figure 5.3: Z_{eff} as a function of time for argon (#43778) and neon (#43768) injections with OH alone. The vertical lines mark the injections at $t = 0.5, 1.0$ s.

current density and the neoclassical conductivity from the n_e and T_e profile measurements, using the neoclassical formulae by Sauter et al. [1999]. Assuming stationary state we would have $I_p = I_{\text{ohmic}} + I_{\text{bootstrap}}$ in an ohmic plasma. This is used to determine Z_{eff} , since the main dependence comes from the neoclassical resistivity. The result is shown in figure 5.3. For argon (#43788) it can be seen that the overall increase of Z_{eff} is 0.65, from 1.7 to 2.35. This gives $n_{\text{Ar}}/n_e \approx 0.27\%$ from the last term of equation 5.6, assuming constant n_C . On the other hand, Z_{eff} increases much more in the case of neon (#43768), by 3.15 from 1.7 to 4.85. This yields, using equation 5.6 with $(10^2 - 10)$, $n_{\text{Ne}}/n_e \approx 3.5\%$ and explains the SXR signals showing a build-up after the neon injections. This can be due to a larger source, stronger recycling or accumulation of neon in the core. However, the kinetic profiles are not much affected as seen by the value of T_{e0} (figure 5.1 (d)), which remains constant in both argon and neon cases. These experiments were repeated at lower electron density with 5 ms injections instead of 10 ms and smaller increase of Z_{eff} is observed: 0.2 and 1.2 for argon and neon, respectively. This leads to about three times less impurity concentration, but again with about ten times more neon concentration. This could be due in part to different recycling, as will be discussed below, but should be investigated with more detailed experiments.

5.2 Electron density scan

We repeated the argon and neon experiments into ohmic (OH) plasmas, presented above, requesting 50% lower electron density, leading effectively to about 35% lower n_e . Figure 5.4 shows the same signals as figure 5.1 for these experiments. The time evolution of the signals is very similar to those experiments in section 5.1, except in figure 5.4 (a), where after two puffs 30% increase of the electron density is observed. This may seem to contradict to the assumption that injection does not modify the background plasma significantly. We showed that the assumption on the low impurity concentration still holds, since from $I_p = I_{\text{ohmic}} + I_{\text{bootstrap}}$ and equation 5.6 we obtain $n_{\text{Ar}}/n_e \approx 0.1\%$ and $n_{\text{Ne}}/n_e \approx 1.3\%$. The observed density increase is related to a faulty density control caused by mirror vibrations in the FIR.

The line integrated density signals show oscillations that are highly reproducible between the two experiments that were performed on the same day. This can be seen in the traces of figure 5.1 (a): the oscillations of the blue and red curves superimpose. These oscillations were present in plasmas of other experiments too, without impurity injections. The peak to peak variation of the line integrated density on the central FIR chord due to the oscillations can be as large as $3 \times 10^{18} \text{ m}^{-2}$.

It was discovered [Andr  be, 2011] that the mirrors in the FIR optical system were loose due to the deformation of their support structure. During current ramp-up, coils and support structures experience significant forces. These deformations then caused the mirrors to vibrate. Since the interferometer signal is used for the feedback control of the main gas feed, the oscillating feedback signal caused a spurious gas feed command which can be seen in figure 5.1 (f). The FIR optical path was examined and the screws holding the mirrors tightened. In the standard shot of 4 July 2011 (#43588) significantly smaller oscillations were reported.

The impurity injections are followed by an increase of electron density because the deuterium flux is not reduced sufficiently. At this low density the proportional gain on the density feedback is reduced to ensure stable density feedback control despite the strong oscillations due to the FIR mirror vibrations. The lower gain results in a less sensitive feedback control that is not able to compensate the excess of impurity donated electrons by cutting the deuterium flux.

After the second argon injection in #42661 (from $t = 1 \text{ s}$) the density, although higher

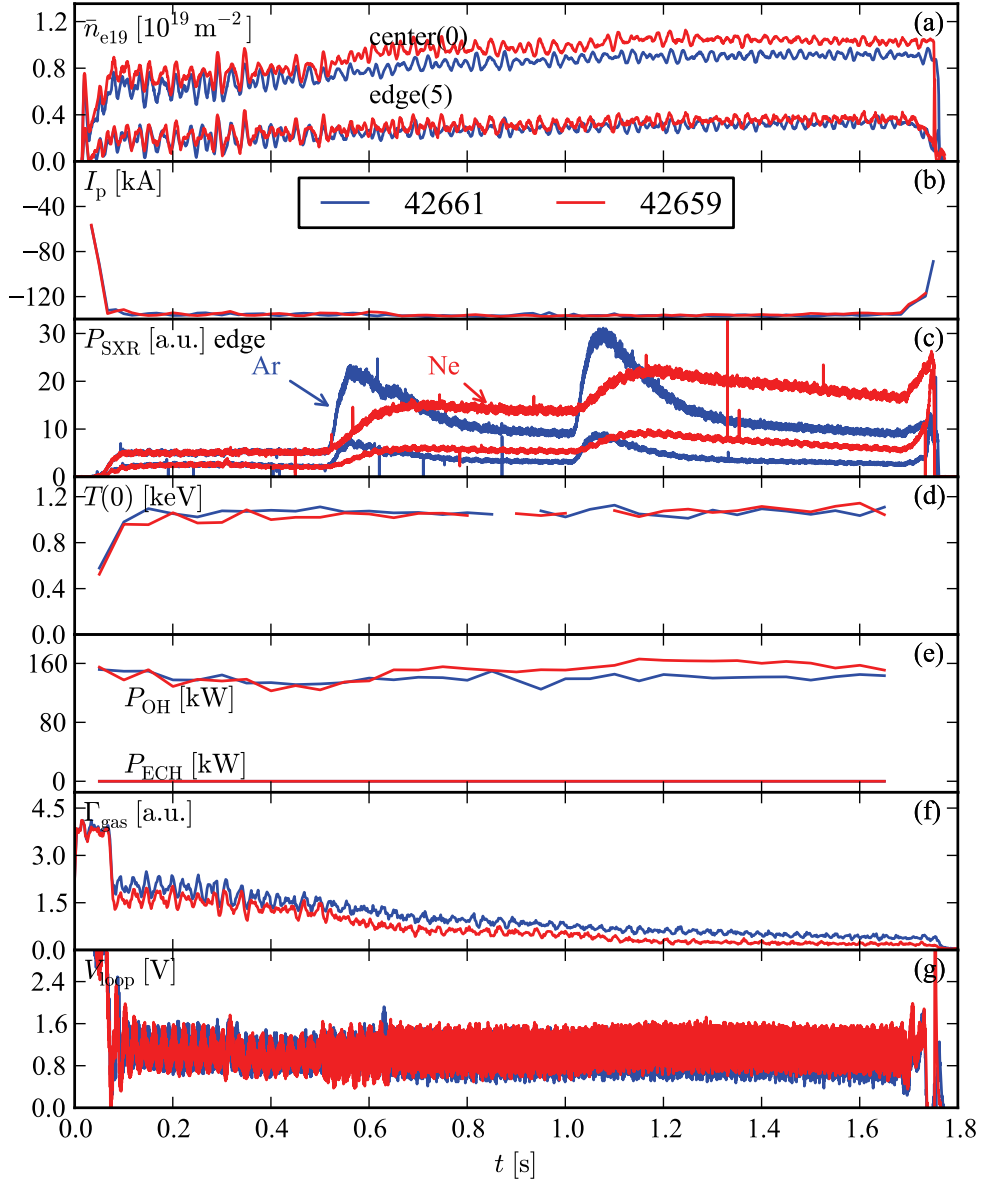


Figure 5.4: Same traces as in figure 5.1 but with 50% lower density request for both experiments. 5 ms argon (#42661) and neon (#42659) injections at $t = [0.5, 1.0]$ s

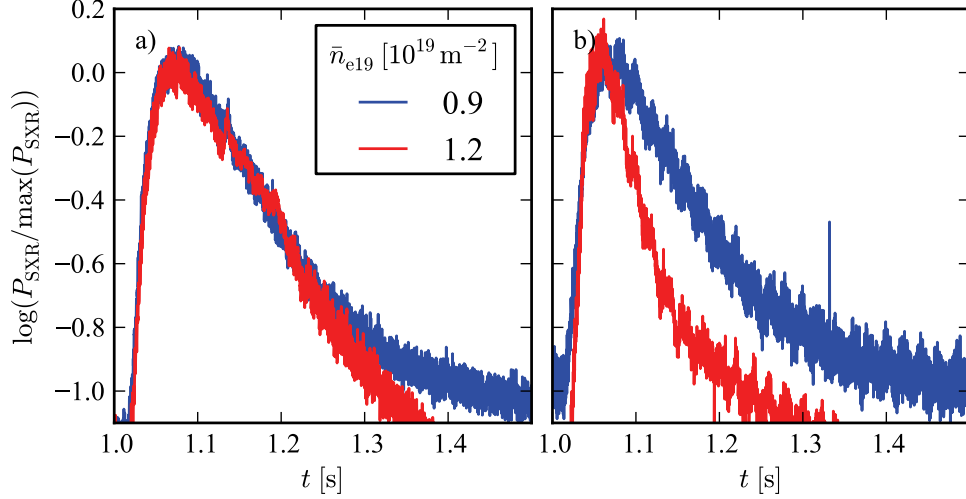


Figure 5.5: Density scan comparison with argon: the SXR signals of the second pulse in the plasma density scan experiments (figure 5.1 and 5.4) normalized to the signal’s maximal value for (a) the central and (b) peripheral chords.

than requested, is stable. In figure 5.5 we compare this phase to the high density experiment #43778. Figure 5.5 (a) and (b) show the SXR emissivity evolution of the central and of a peripheral chord, respectively. The signals are normalized to their maximal value and shown on a logarithmic plot to better observe any differences in rise and decay time scales. We see in figure 5.5 (a) that the rising parts of the SXR emissivity evolution on the central chord for the two experiments superimpose, with $\tau_r \approx 25$ ms, showing no observable difference between the low and high density cases.

On the peripheral chord, in figure 5.5 (b) the lower density experiment shows a slightly slower increase with $\tau_r \approx 15$ ms. Additionally, the lower density case shows longer decay with $\tau_d = 200$ ms, in contrast to $\tau_d = 100$ ms for the high density case. This difference can be explained by a variation in the deuterium gas feed in #43778. It can be seen in figure 5.1 (f) that at $t = 1.05$ s the gas valve fully closes, resulting in slowly decreasing electron density in the remainder of the pulse. The combined effect of decreasing electron and argon density yields a faster SXR decay compared to the low density case where the electron density actually increases. The sensitivity of the decay time scale on the gas feed suggests that the difference in rise time may also be due to variations in the effective

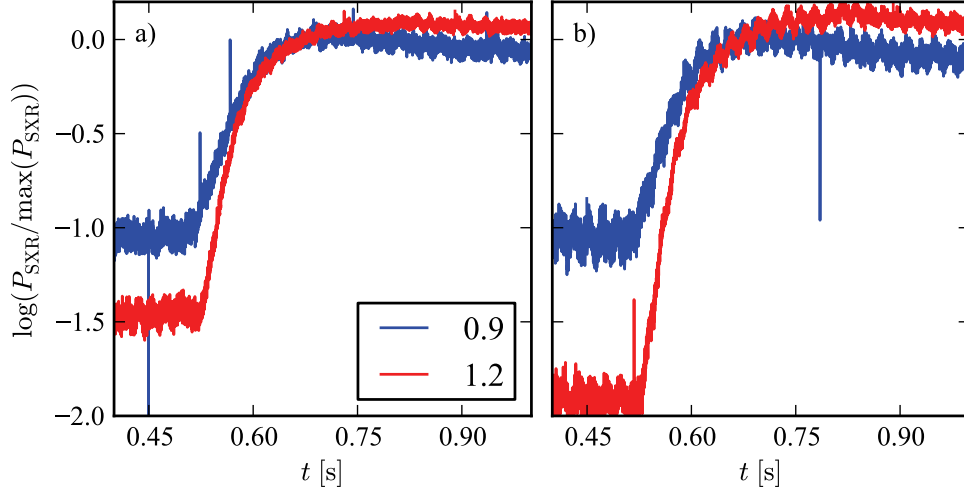


Figure 5.6: Density scan comparison for neon: the SXR signals of the second pulse in the plasma density scan experiments (figure 5.1 and 5.4) normalized to the signal's maximal value for (a) the central and (b) peripheral chords.

deuterium influx and not actual difference in argon transport.

We also compare the neon behavior for the two pulses with different densities. Despite the density increase described above, the SXR signals after the first pulse at $t = 0.5$ s are compared, because of saturation on the central SXR chord for the pulse #43768 at $t = 1.07$ s. The SXR rise times are $\tau_r = 80, 45$ ms for #42659 and #43768, respectively, that is the rise is faster for the higher density case. More importantly, the rise time is much slower for neon than for argon, albeit neon remains in the plasma, or better recycled as mentioned above. The large difference between argon and neon should be further investigated.

5.3 Plasma position relative to the injector

The impurity injector is positioned on an upper lateral port in sector 4 ($Z = 0.46$ cm), therefore plasmas in the upper half of the vacuum chamber are preferred for the injection experiments. As it was mentioned in section 2.1.1, however, some diagnostics, in particular the CXRS system (section 2.1.2), are positioned for plasmas at $Z = 0$. In the following

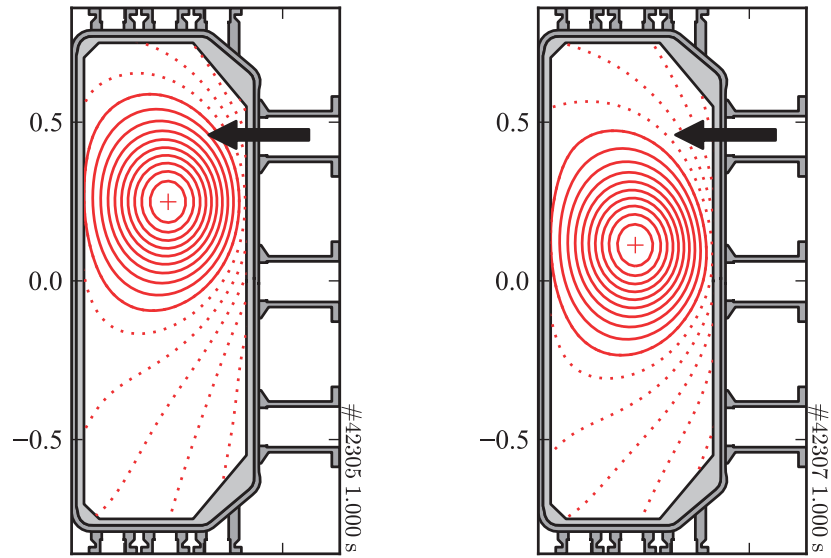


Figure 5.7: Comparison of plasma shapes with different vertical positions of the magnetic axis: $Z = 23$ cm (#42305) and $Z = 10$ cm (#42307). The arrow shows the position of impurity injection system on the top lateral port (see Chapter 4). Time traces of various diagnostics for the corresponding experiments are shown in figure 5.8.

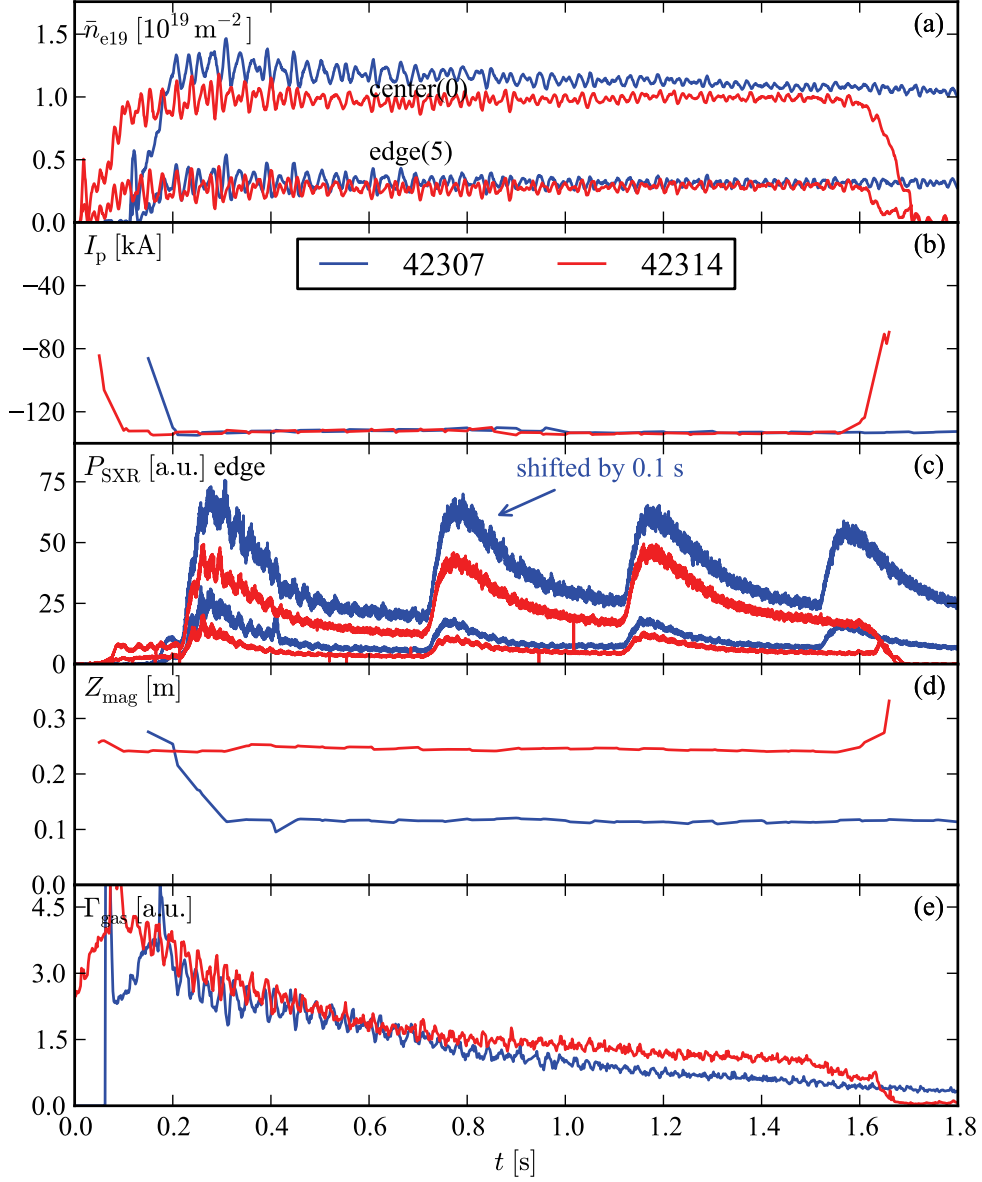


Figure 5.8: Z-axis comparison: time evolution of (a) the central and peripheral chords of the FIR interferometer, (b) the plasma current (c) the central and peripheral chord of DMPX, (d) the vertical position of the magnetic axis and (e) the deuterium gas flux. The time base for traces of #42307 is shifted by 0.1 s because of the different programming of the injections. 5 ms long Ar injections at $t = 0.2, 0.7, 0.9, 1.5$ s.

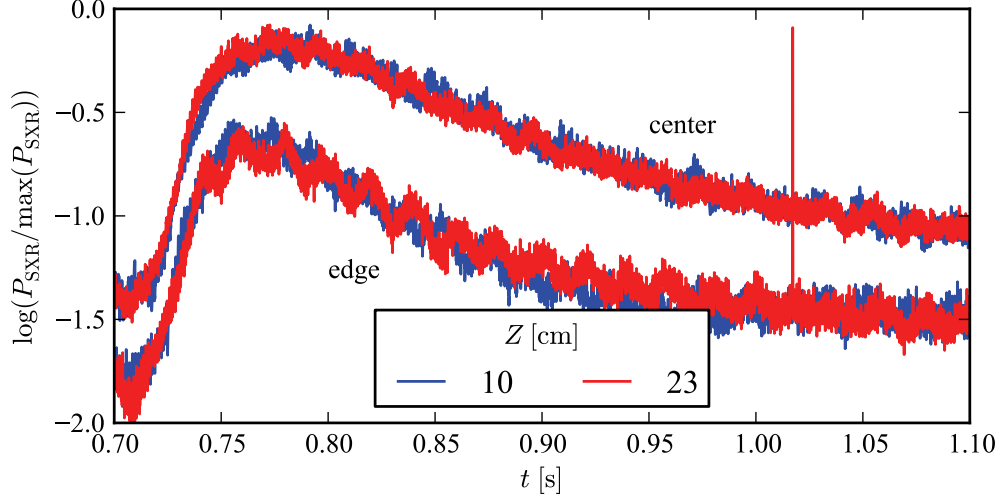


Figure 5.9: The SXR signals of the second pulse in the plasma Z -axis scan experiments (figure 5.8 (c)) normalized to the signal's maximal value for (a) the central and peripheral chords.

set of experiments we study the influence of the plasma's vertical position on the injection results.

Figure 5.7 shows the plasma shapes and location with respect to the injector. In these experiments, limited configurations with a moderate elongation ($\kappa_{\text{edge}} = 1.4$) and triangularity ($\delta_{\text{edge}} = 0.3$) were programmed. The magnetic axis was varied in the range of $Z = 23, 10, 0$ cm on a shot to shot basis, with $Z = 0$ being the vacuum vessel's horizontal midplane. It was found that at $Z = 0$ the injected gas at this elongation misses the confined region and the SXR signals show hardly any trace of the injection. We believe, that for this case the gas is pumped quickly and recycling from the wall is not sufficient to affect the SXR emission. Increasing the elongation could result in gas penetrating the core, however elongated plasmas are vertically less stable. We discuss the effect of the shape, later, in section 5.6.

Figure 5.8 compares the time traces of density, plasma current, SXR radiation and Z position for the two experiments with the magnetic axis at $Z = 23$ cm and $Z = 10$ cm. In the pulse #42307, the injections were programmed at $t = [0.1, 0.6, 1.0, 1.4]$. In #42314 all the injections were shifted 0.1 s later. For the sake of easier comparison, the time traces of

#42307 were shifted by +0.1 s.

The SXR time evolution for the two plasma positions are similar. The electron density is about 20% higher for $Z = 10$ cm, resulting in higher emissivity signals, as seen in figure 5.8 (c). For a better comparison of the SXR signals, in figure 5.9, we show the details of the second pulse, normalized to the signal's maximum values. It can be seen that signals of both the central and edge chords overlap for the two cases. The characteristic time of the exponential increase between $t = 0.72 - 0.77$ (linearly increasing phase in the semi logarithmic plot) is about $\tau_r = 30$ ms, whereas the decay time constant $\tau_d = 250$ ms.

This similarity suggests that, apart from the slight changes in background parameters, in particular, the electron density, there is no fundamental difference between $Z = 23$ cm and $Z = 10$ cm cases. The scenarios developed at $Z = 23$ cm were proven to be more reliable, therefore most of the experiments reported here were performed at this position. Some experiments, when the CXRS system was available, were repeated at $Z = 10$ cm to obtain ion temperature profiles for the modeling. Figure 5.9 also shows that the path of the injected gas 'jet' is not significant. It does not act as an edge localized source, independent on the poloidal angle of the injection point. This is good news for modeling, allowing for one dimensional simulations, only accounting for radial dependence. Additionally, it confirms that the main cause of the central SXR emissivity increase is due to the edge source of particles being transported inward by advection and diffusion. Faster rise and decay times can therefore be associated with larger transport and worse confinement properties.

5.4 Current scan

The plasma current was changed in the range of $I_p = [130, 230, 300]$ kA in pulses #42314, #42310, #42313, respectively. 5 ms long Ar pulses were injected at $t = [0.2, 0.7, 1.1]$ s except in #42313, where the injections were programmed 0.1 s earlier.

First we comment on the effect of plasma current on the electron density and temperature profiles which are shown in figure 5.10. A detailed comparative study of electron and carbon profiles in TCV L-mode plasmas can be found in Fable [2009], Martin et al. [2010], Sauter et al. [2010]. Increasing the current results in better confinement. Indeed, temperature profiles shown in figure 5.10 (b) become steeper in the radial range of $\rho_\psi = 0.5 - 1.0$ as I_p is increased. The electron density profiles are rather stiff that is the peakedness of the profile, especially outside of the $\rho_\psi \approx 0.5$ surface does not change significantly with

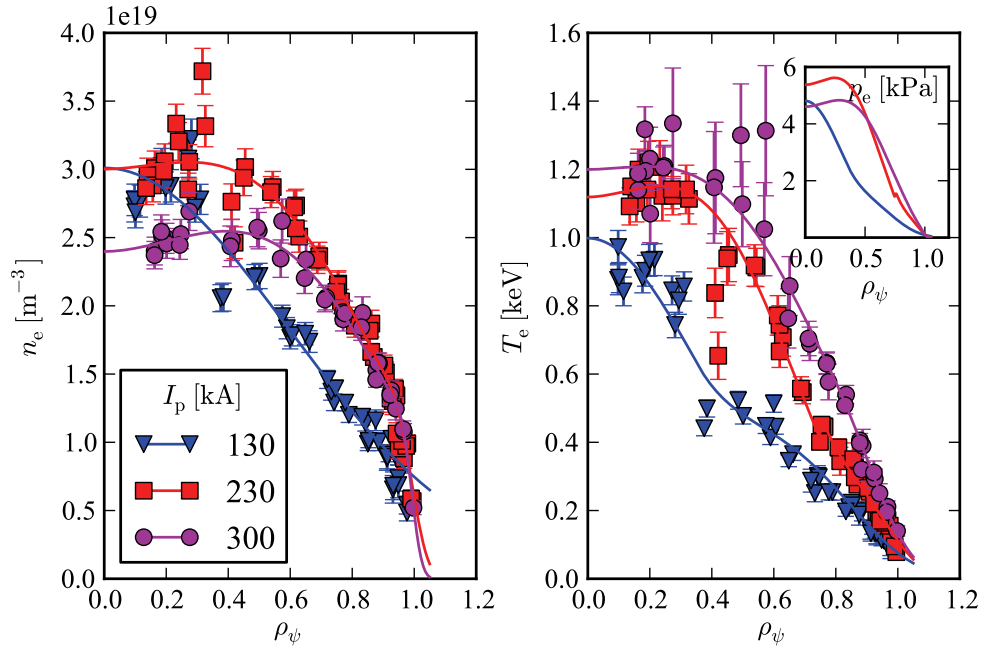


Figure 5.10: Electron density and temperature profiles for different values of plasma current (#42313, #42314, #42310, 0.6-0.7 s). Time traces are shown in figure 5.11.

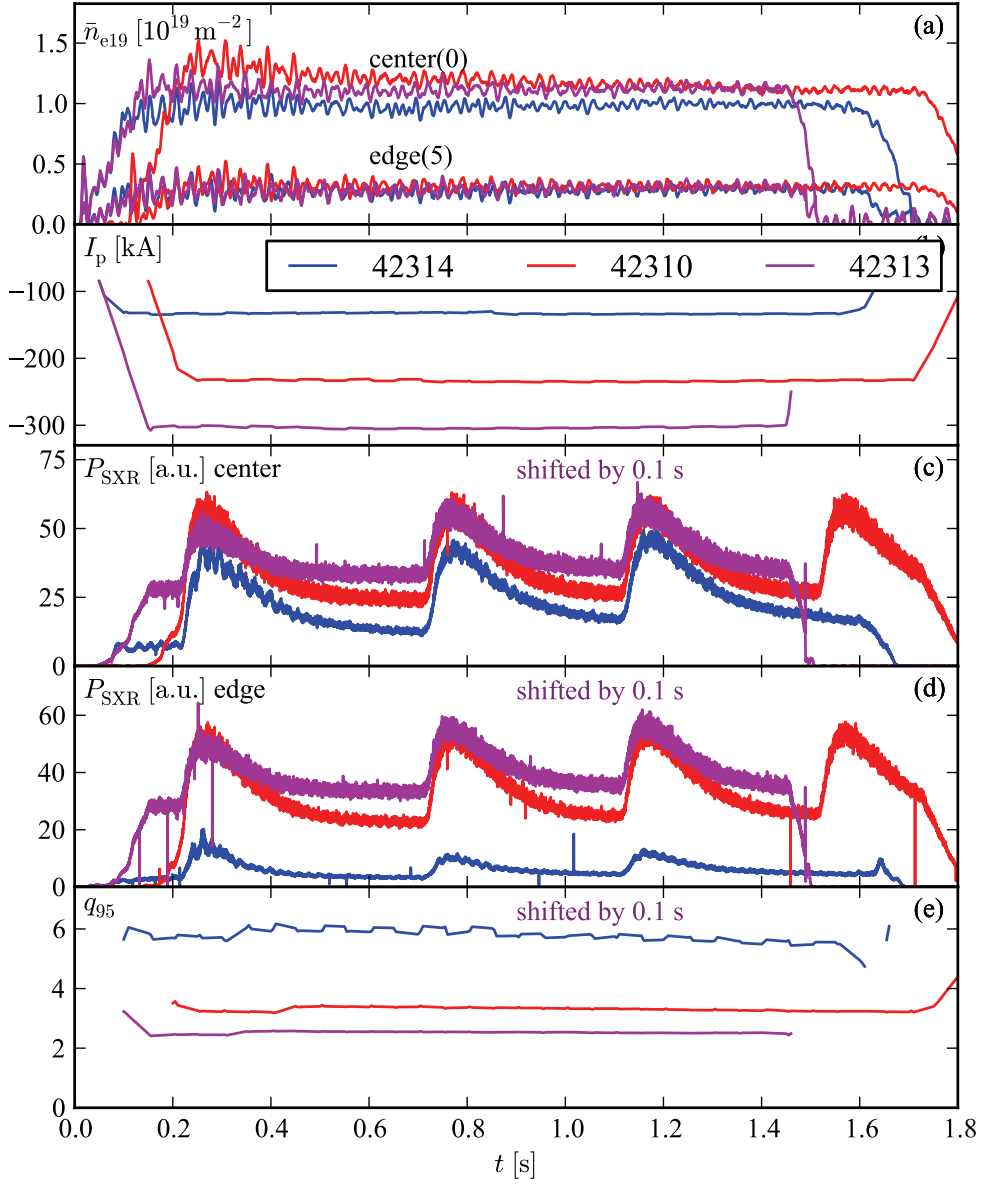


Figure 5.11: I_p scan: time evolution of (a) the central and peripheral chords of the FIR interferometer, (b) the plasma current (c) the central and (d) peripheral chord of DMPX and (e) the q_{95} value for three experiments with different plasma current. The time base shown of #42313 is shifted by 0.1 s because of the different programming of the injections. 5 ms long Ar injections at $t = 0.2, 0.7, 1.1, (1.5)$ s.

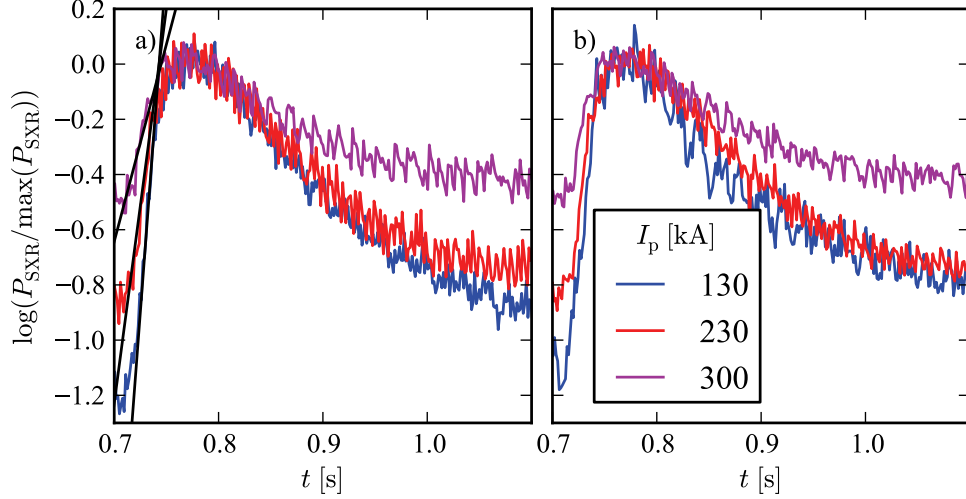


Figure 5.12: The SXR signals in the current scan experiments (figure 5.11 (c), (d)) normalized to the signal's maximal value for (a) the central and (b) peripheral chord.

I_p . On the other hand, as the current is increased the $q = 1$ surface and the sawtooth inversion radius increases, flattening the density and temperature profiles. We can see, for example in figure 5.10 (a) that for the $I_p = 300$ kA case the density profile is significantly flattened up to $\rho_\psi \approx 0.7$.

The time evolution of line integrated density, plasma current and SXR emissivity can be seen in figure 5.11. We compare the details of SXR evolution for the second pulse in figure 5.12, where the signals were normalized to their respective maximum values. It can be seen that the signal increase is slower with increasing current: the exponential fit, as shown in section 5.3, to the rising phase of the signals gives $\tau_r = 20, 35, 70$ ms for $I_p = [130, 230, 300]$ kA, respectively. The decay is also slower with increasing plasma current, which corresponds to better confinement (smaller diffusion coefficient) with increasing plasma current. It should be noted that usually more recycling is observed with increasing I_p , which could also lead to slower decay. Nevertheless, the simulations presented in section 6.3 confirm, that impurity transport does decrease with I_p , as expected.

5.5 ECH power

The temperature profile is known to strongly affect the electron transport (see Chapter 3), hence it is expected it may influence impurity transport. We used the X2 ECH system (section 2.1.1) to provide additional electron heating. In figure 5.13 the experiments shown previously in figure 5.1 were repeated with 240 kW of additional ECH power. The power is deposited in the center and absorption is close to 100%. The significant difference on the SXR signals between Ar and Ne remains. The emitted SXR power is higher and the emissivity profiles are broader with ECH than with OH alone due to the higher electron temperature.

In figure 5.15 we compare the details of the normalized SXR signal evolution following argon injection for OH alone (see in section 5.1) and with ECH. In figure 5.15 (a), it can be seen that the rise of the central chord is slightly faster with ECH: τ_r is about 15 ms compared to 25 ms. The normalized signals of the peripheral chords in figure 5.15 (b) superimpose, both having $\tau_r \approx 25$ ms. This confirms that ECH enhances transport near its deposition location, in this case at the center, resulting in faster increase of the central argon concentration, hence SXR emissivity, as observed recently on AUG-U [Sertoli et al., 2011].

Figure 5.16 shows the same quantities as figure 5.15, but for neon injections. The rise on both the central and peripheral chord is slower with ECH than OH alone with $\tau_r \approx 85$ ms and $\tau_r \approx 45$ ms, respectively. Neon shows again a much slower increase than argon and a very different behavior. The neon experiment should be repeated at $Z = 0$ cm, when the injection does not directly intercept the plasma in order to check the indirect neon injection.

5.6 Shape scan

Exploring the effect of the plasma shape on heat and particle confinement has always been at the focal point of research on TCV. In this section, we present impurity injection experiments in plasmas with various shapes, changing, in particular, the elongation and triangularity. Figure 5.17 overviews the plasma shapes used in these experiments: the plasmas are positioned on the triangularity-elongation, both measured on the last-closed flux surface, plane $(\delta - \kappa)$, that is plasmas with the same triangularity (elongation) appear

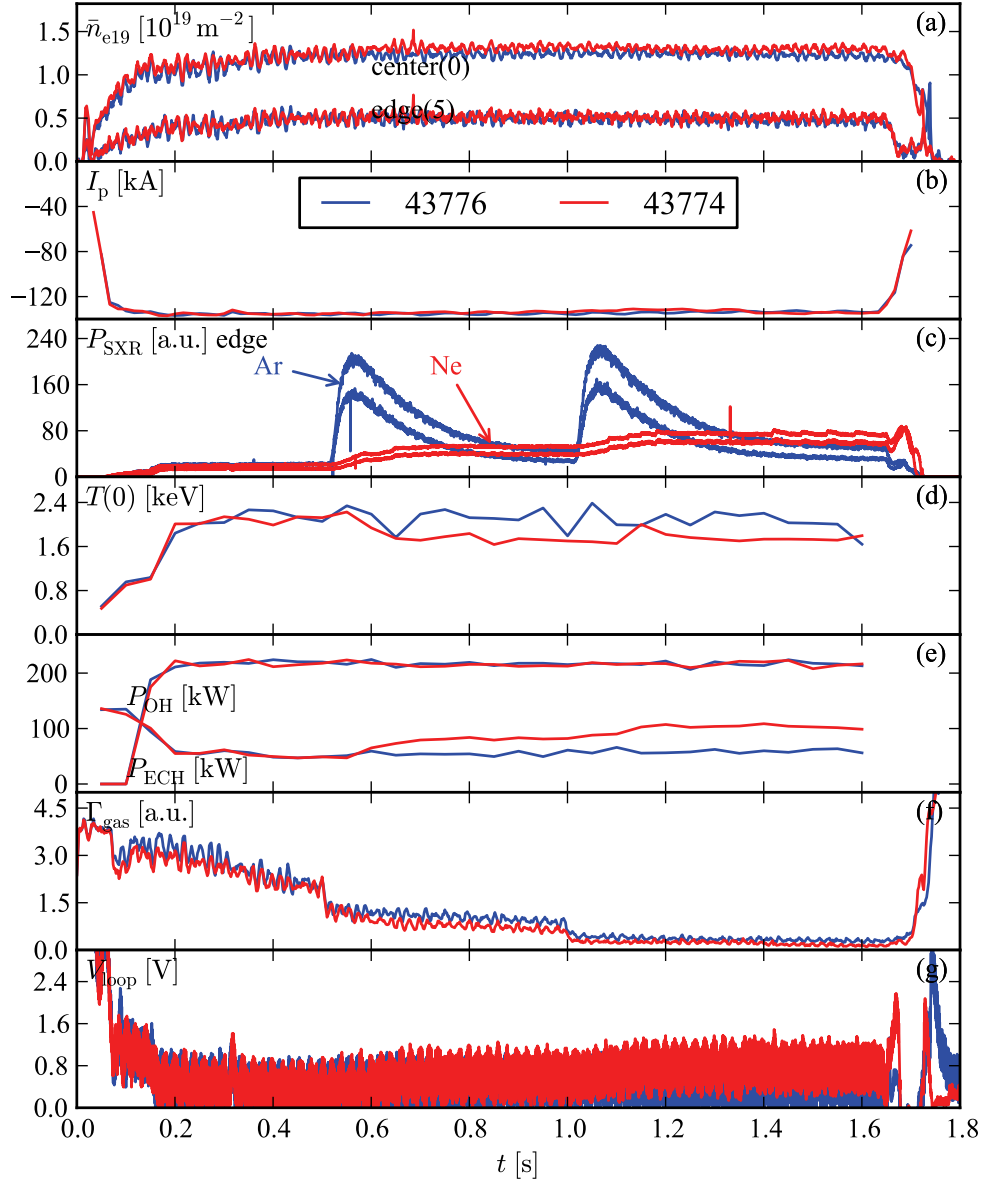


Figure 5.13: Argon and neon injection with ECH: same quantities as figure 5.1 with 240 kW additional ECH power. 10 ms long argon and neon injections at $t = 0.5, 1.0$ s.

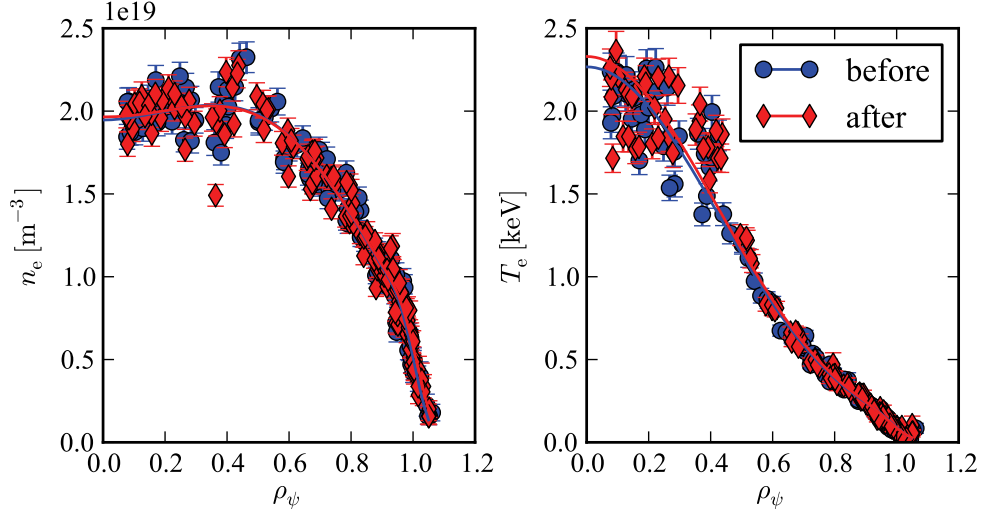


Figure 5.14: Electron density and temperature profiles before ($t = 0.25 - 0.50$ s) and after ($t = 0.5 - 0.75$ s) neon injection for #43776 with additional ECH.

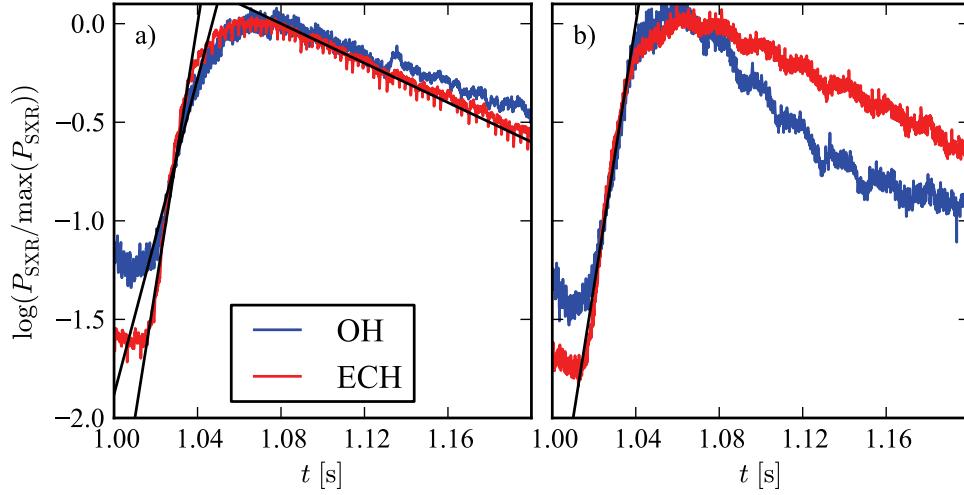


Figure 5.15: Comparison of the normalized SXR signals of argon injection in #43778 OH only (figure 5.1 (c)); and #43776 with central ECH figure 5.13 (c)) for (a) the central and (b) peripheral chord.

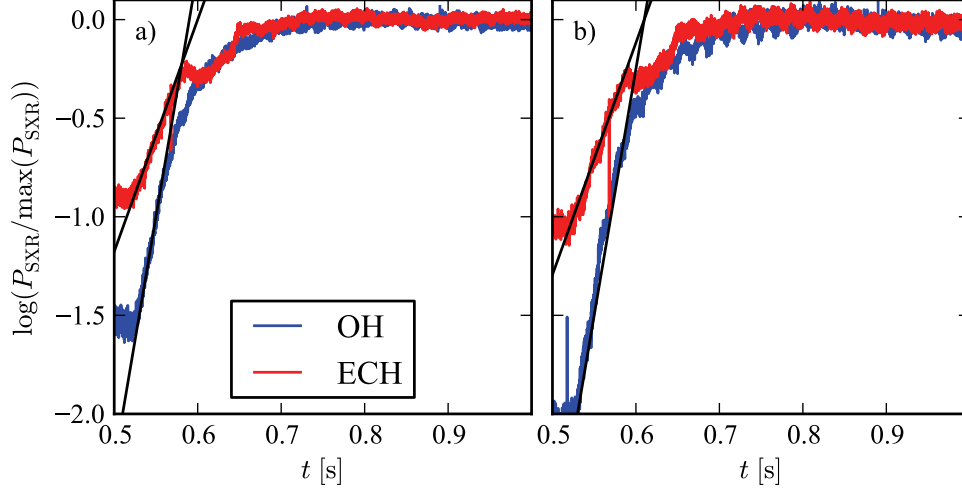


Figure 5.16: Same as 5.15 for neon injections in #42768 OH only and #43774 with ECH.

at the same horizontal (vertical) position.

5.6.1 Elongation scan

In TCV, it is possible to create extremely elongated plasmas up to $\kappa = 2.8$ (#19373), making the plasma almost fill the entire vacuum vessel. Highly elongated plasmas are vertically more unstable and may become impossible to control. Although extremely elongated plasmas may not have a direct relevance for a fusion power reactor, it remains important to understand the effect of elongation on transport, in particular on that of impurities.

When the elongation is increased, the plasma surface is increased, so higher current is required to sustain the same current density profile. We already saw in section 5.4 that the plasma current directly affects the sawtooth activity and the background electron density and temperature profiles. In order to rule out the current dependence in the elongation scan, we performed the elongation scan experiments at constant q_{95} value by increasing the plasma current in proportion to the elongation. There is no diagnostic on TCV capable of directly measuring the current density profile, however experience shows that, for these configurations (ohmic L-mode plasmas), q_{95} is a valid parameter to characterize the shape of the current profile.

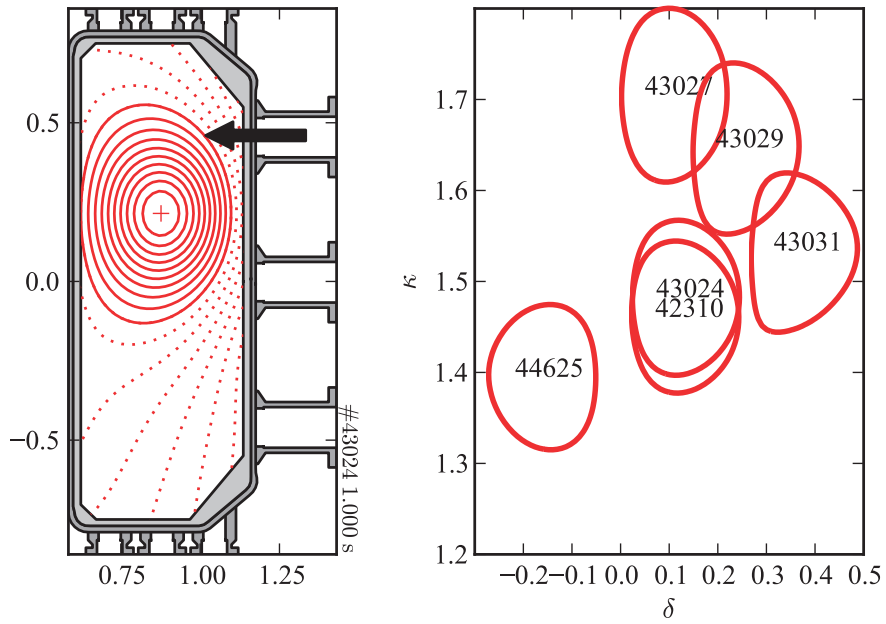


Figure 5.17: A typical shape (#43024 1.0 s) showing the plasma position relative to the injector (black arrow) and plasma shapes used in the experiments placed on the triangularity-elongation ($\delta - \kappa$) plane.

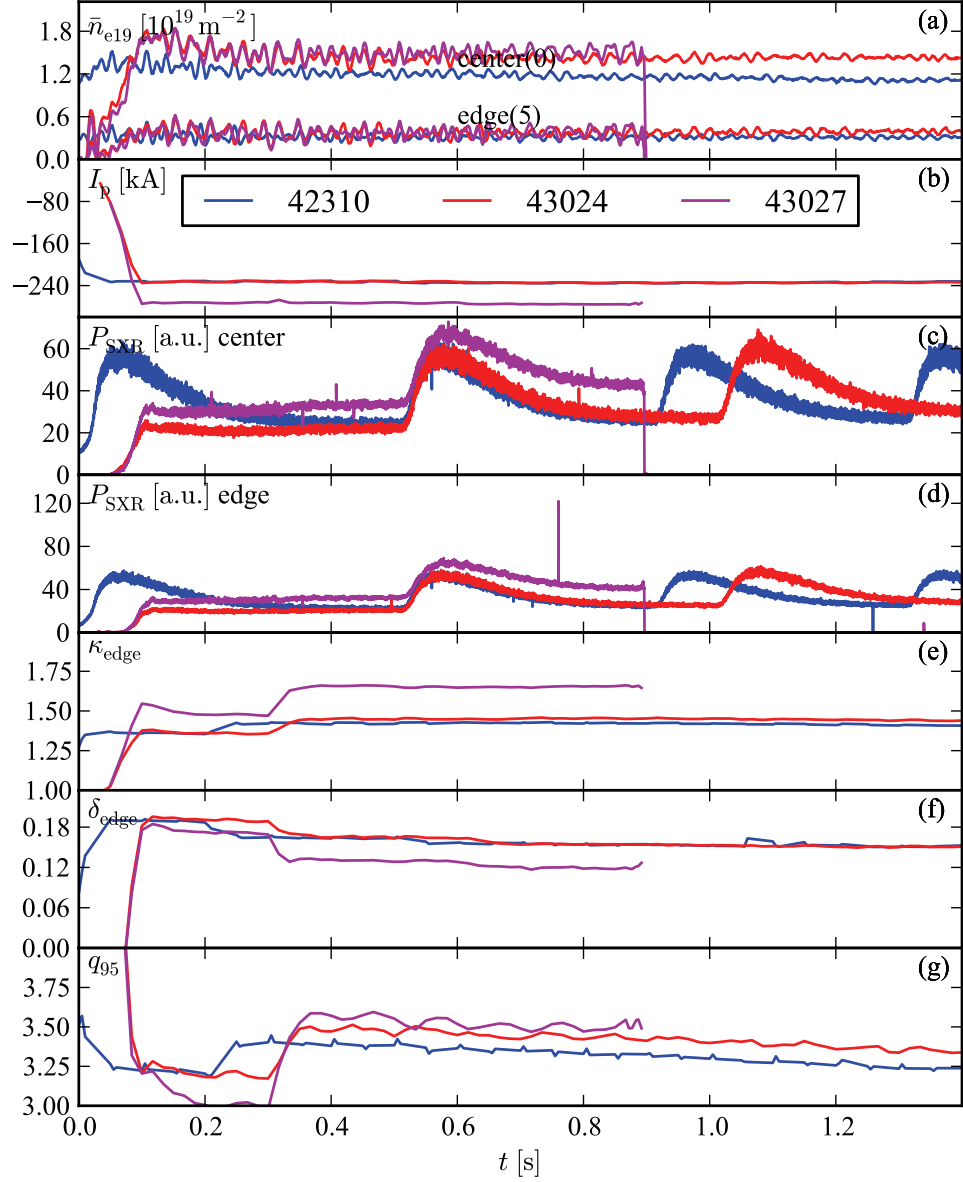


Figure 5.18: Elongation scan: time evolution of (a) the central and peripheral chords of the FIR interferometer, (b) the plasma current, (c) the central and (d) peripheral chord of DMPX, (e) the elongation, (f) the triangularity and (g) the q_{95} value for three argon injection experiments with different *elongation*. The time base for traces of #42310 is shifted by 0.1 s because of the different programming of the injections. 5 ms Ar injection at $t = 0.5$ s.

The elongation was varied $\kappa = [1.45, 1.5, 1.65]$ in the series of #42310, #43024, #43027. The plasma shapes of these experiments are shown in figure 5.17 and figure 5.18 shows the time traces of the density, the plasma current, the SXR emissivity, the elongation and the triangularity for three argon injection experiments. We note that the κ feedback system activated at $t = 0.3$ s, results in a sudden change in elongation, figure 5.18 (e). For #42310, this occurs at 0.2 s in the figure because the time traces are shown temporally displaced to account for the different programming of the injected gas pulse.

The rise time of the SXR signals following the injections are similar and the decay time of the higher κ case is slightly slower as expected from a better confinement. It was realized only after the experiment that the effective κ range was not sufficiently large to see a clear difference in the transport behavior. In addition, it is not easy to directly derive the transport related effect of the elongation on the SXR signals: due to geometric effects, the SXR signals will increase proportionally to the elongation. Indeed, we recall from section 2.1.3 (see figure 2.5) that the DMPX detectors are located on the bottom of the vacuum vessel so the line integrated chord intensities are proportional to $2\kappa a$, κ and a being the elongation and the minor radius of the plasma, respectively. This effect can be seen, in the SXR traces of figure 5.18 (c) and (d) by comparing the amplitude of the background signals at $t = 0.45$ s, for example.

For $\kappa \approx 1.45 - 1.5$ (#42310, #43024), the SXR signals following the injection at $t = 0.5$ s return close to the background level, that is to the signal amplitude before the injection. At $t = 0.9$ s the signal is 10% higher than the background. For $\kappa = 1.65$ (#43027) this difference is around 20% relative to the background.

With the XTOMO (see section 2.1.3) system the injection can be observed from different directions. Figure 5.19 shows the flux surfaces for the elongation scan experiments with lines of sight of central chords (solid) and those tangent to the $\rho_\psi = 0.5$ surface (dashed and the surface highlighted in red) for different cameras. Figure 5.20 shows the chord brightnesses as a function of time for the aforementioned chords. The signals' normalization is the same as in the previous sections. The semi-logarithmic plot shows that rise and decay times remain similar to those measured in section 5.1, with a small decrease of the decay time for higher elongation. Figure 5.20 also shows that similar SXR time evolution is observed independently of the line of sight, and if a chord looks above or below the midplane. This confirms that the transport can be interpreted on flux surfaces and do not depend on the poloidal angle, leading to dominant one dimensional effects.

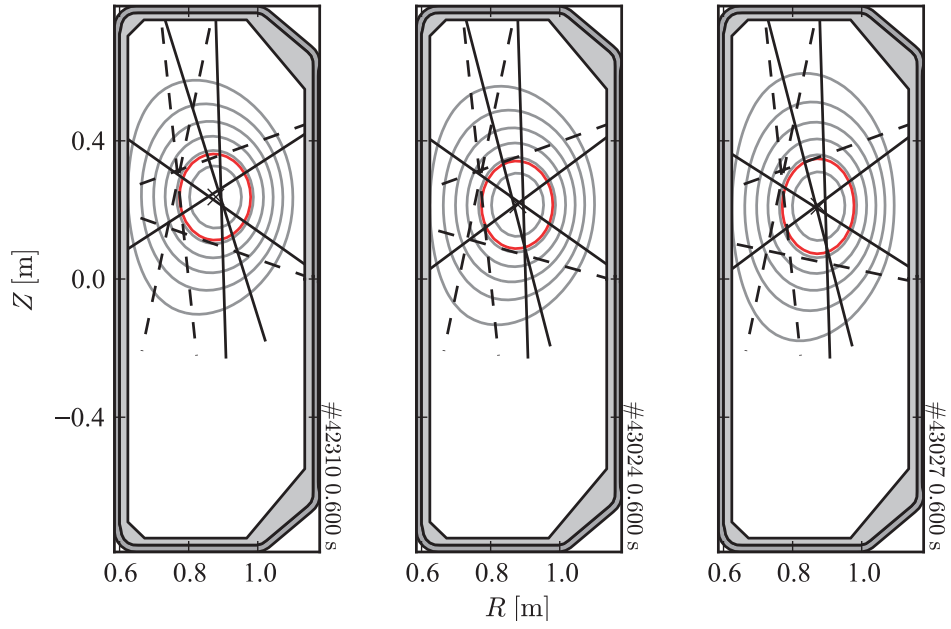


Figure 5.19: Central (solid) and peripheral (dashed) lines of sight of XTOMO's different cameras for the elongation scan experiments shown in Figure 5.18. The highlighted flux surface corresponds to $\rho_\psi = 0.5$.

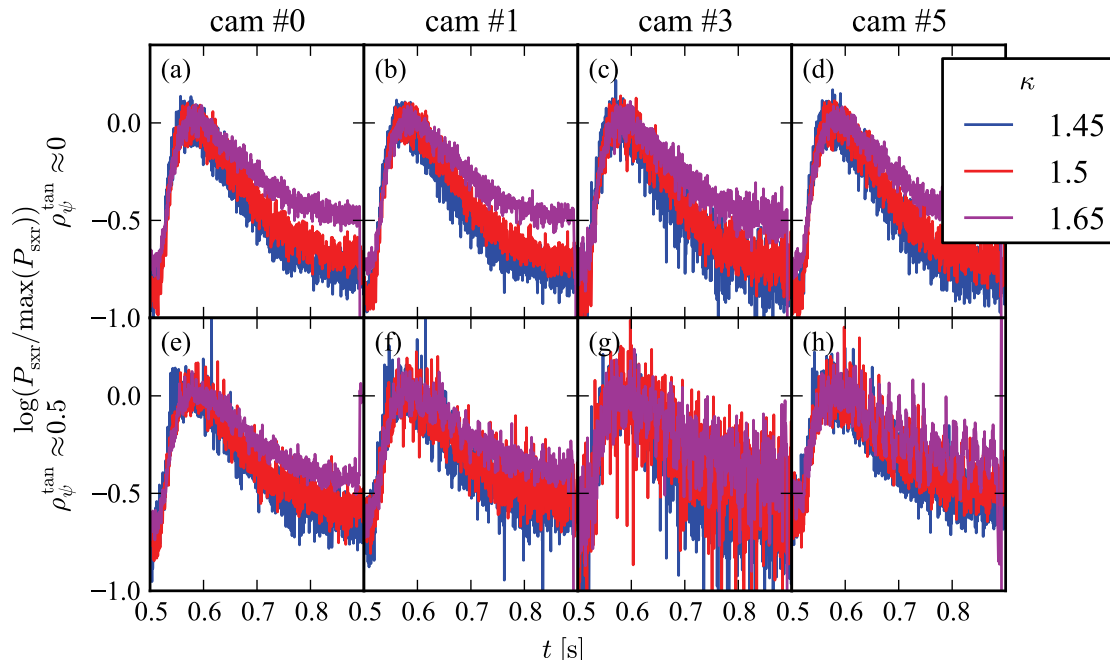


Figure 5.20: Time evolution of XTOMO chord brightnesses of different cameras in the elongation scan experiments for (a)-(d) central chords and (e)-(h) for chords with a tangency radius $\rho_{\psi}^{\text{tan}} \approx 0.5$. The geometry of the chords and the plasma shapes are shown in Figure 5.19.

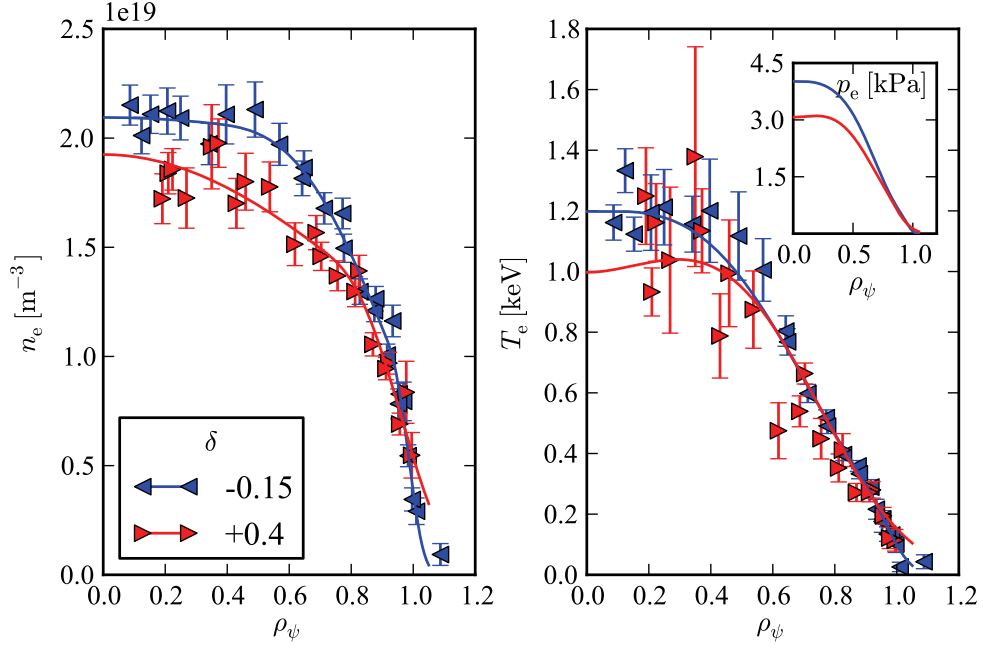


Figure 5.21: Electron density and temperature profiles for positive (#43031) and negative (#44227) triangularity experiments. Time traces are shown in figure 5.22.

5.6.2 Triangularity scan

In TCV, triangularity can also be programmed for extreme (positive and negative) values: $\delta \in -0.77 - 0.86$ (#11928, #8890). In this section we present a set of impurity injection experiments for a range of triangularity values $\delta = [-0.3, 0.3, 0.4]$ in the series of #44625, #42310, #43031. The plasma shapes used in these experiments are shown in figure 5.17. It is expected that confinement increases with decreasing triangularity [Camenen et al., 2007]. Therefore we first compare the electron density and temperature profiles for different values of the triangularity. These are shown in figure 5.21 for the smallest and largest triangularity cases. The negative triangularity case shows a slightly steeper electron density profile for $\rho_\psi < 0.8$, while, in this region, the electron temperature profiles are similar.

Figure 5.22 shows the same traces as figure 5.18 (except the q_{95} value). We note that the elongation increases slightly with increasing triangularity. As for the elongation scan, we show the emissivity evolution of different cameras of the XTOMO system, normalized

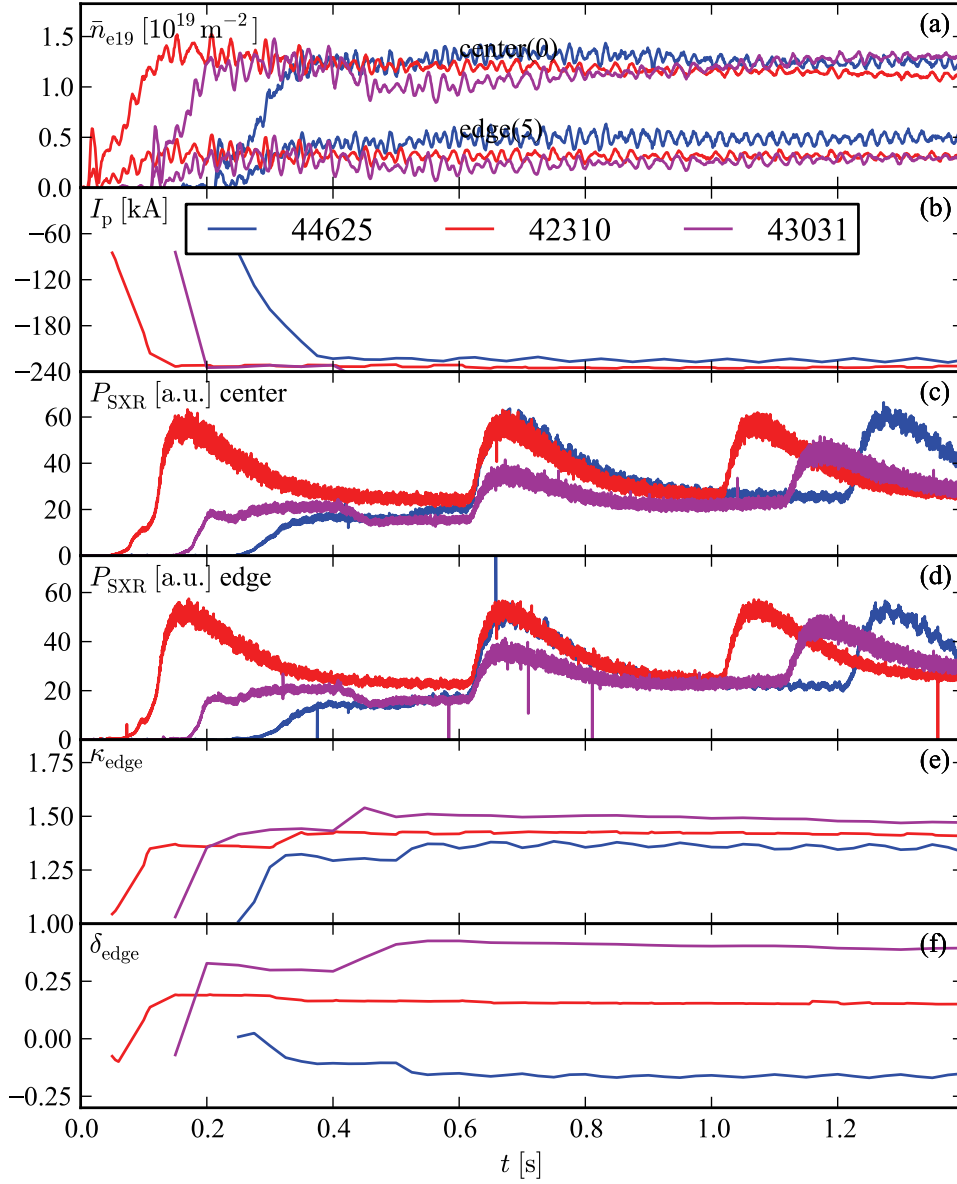


Figure 5.22: Triangularity scan: time evolution of (a) the central and peripheral chords of the FIR interferometer, (b) the plasma current, (c) the central and (d) peripheral chord of DMPX, (e) the elongation and (c) the triangularity for three argon injection experiments with different triangularity. The time bases for traces of #44625, #43031 are shifted by 0.2 and 0.1 s, respectively, because of the different programming of the injections. 10 ms Ar injection at $t = 0.7$ s.

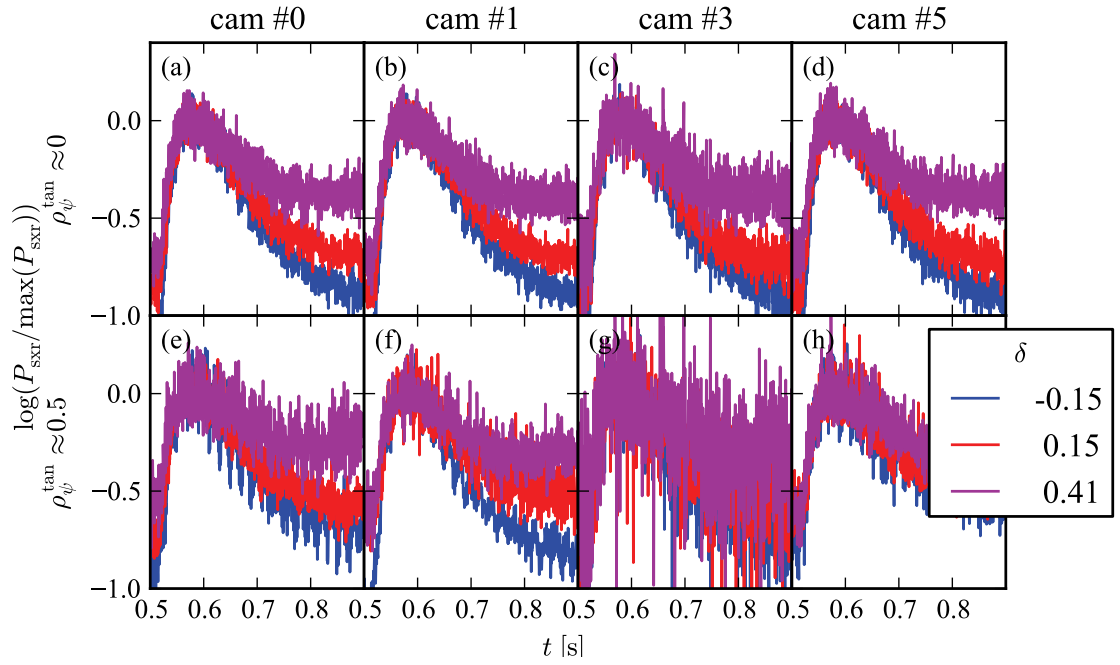


Figure 5.23: Triangularity scan: normalized SXR emissivities for various XTOMO chords. For the notations see figure 5.20.

with their respective maximum value in figure 5.23. The signals of different cameras for all the cases yield similar results. $\tau_r \approx 40$ ms for all the shapes, whilst the decay time increases with increasing triangularity ($\tau_d \approx 400$ ms for $\delta = 0.4$ vs. $\tau_d \approx 300$ ms for $\delta = -0.15$). Note that the elongation also increases during this scan and its effect on τ_r goes in the same direction. New experiments with δ scan should be performed with slightly decreasing κ in order to check the exact effect.

5.6.3 Limited vs. diverted configuration

All the experiments presented so far were limited plasma configuration. Despite the fact that limited and diverted plasmas are equally common on TCV, we preferred to perform our experiments in limited configurations, as the presence of divertor brings additional complexity through parameters that are not easily determined in TCV experiments (particle and heat flux on the divertor, recycling, radiation, etc.). It is not expected, however, that the presence of a divertor modifies the core behavior in general, however the boundary conditions may be significantly different.

Figure 5.24 compares the time evolution of various signals for limited and diverted configurations. We did not succeed in matching well the densities for these two experiments: during the current flat-top the difference in density between the two configurations is $7 \times 10^{18} \text{ m}^{-2}$ at $t \approx 0.5$ s, although the discrepancy decreases at later times. The difficulties of shape control are important in these experiments: for the diverted case the elongation and triangularity increase 10% and 50%, respectively, relative to the limited case. In the limited case the SXR signals reach their maximum in approximately 60 ms which is followed by a decay with a time constant of about 100 ms. For the diverted case the fast rising edge is similar but it is followed 0.15 s long constant or even slightly increasing period, then a decay with a time constant of about 0.4 s.

5.7 Multi-puff stationary experiments

In contrast to the experiments described above, a train of shorter pulses was programmed after an initial longer puff as shown in table 5.1. The aim was to obtain a stationary SXR radiation, hence impurity concentration, in order to better diagnose the stationary profiles. Figure 5.25 shows time traces of the electron density, the soft x-ray emission, the

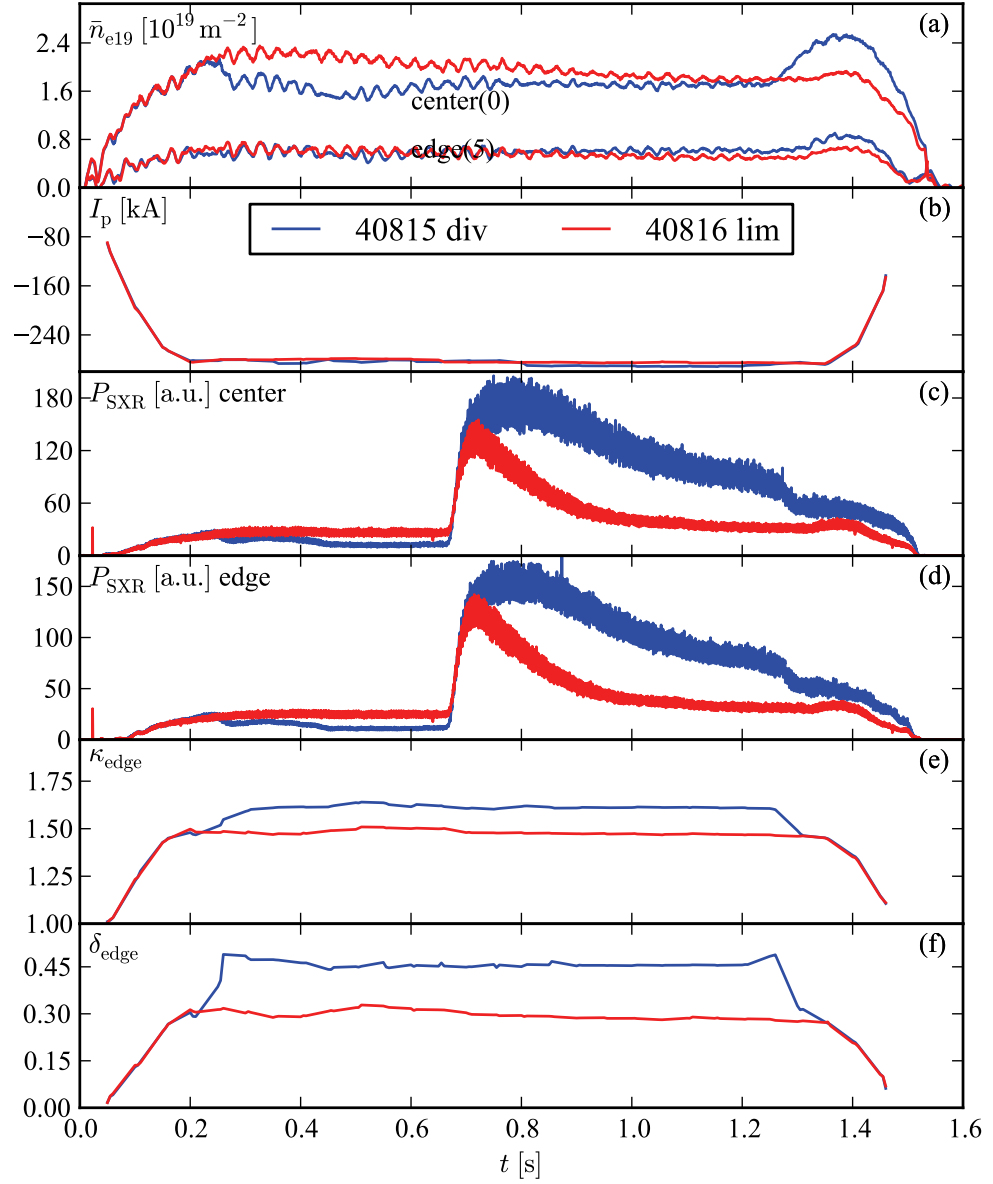


Figure 5.24: Limited and diverted comparison: the same as figure 5.18 for experiments with limited (#40815) and diverted (#40816) plasmas. 10 ms Ar injection at $t = 0.7$ s.

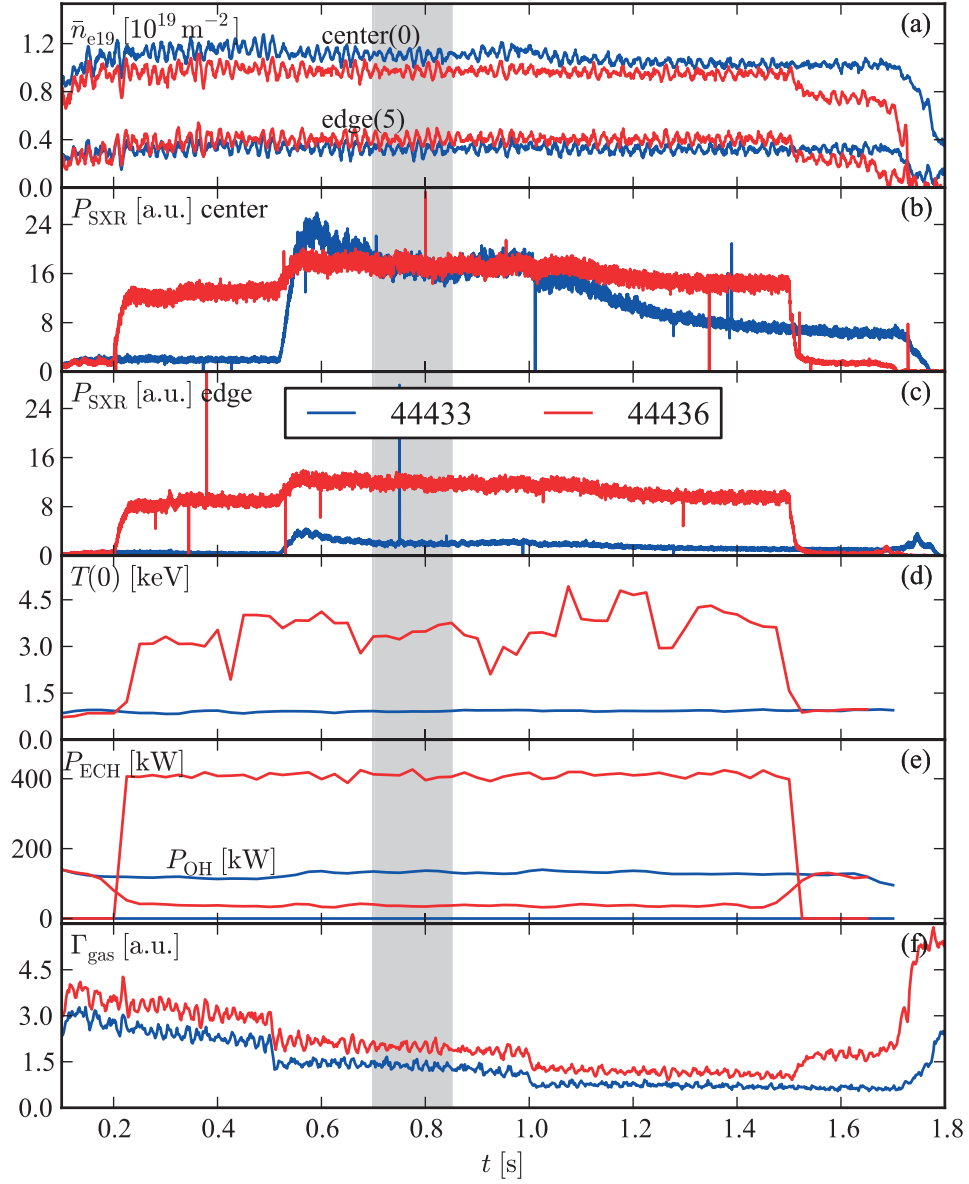


Figure 5.25: Multi-puff experiments: time evolution of (a) the central and peripheral chords of the FIR interferometer, (b) the central and (c) a peripheral chord of DMPX, (d) the central electron temperature, (e) the ohmic and ECH power and (f) the deuterium gas flux for two experiments with multiple argon puffs. The shaded region $t = 0.7 - 0.85$ s shows where the stationary analysis is placed. The programmed pulses are shown in table 5.1.

shot	(position [s], duration [ms])					
#44433	(0.5, 10)	(0.6, 5)	(0.7, 5)	(0.8, 5)	(0.9, 5)	(1.0, 5)
#44436	(0.5, 3)	(0.6, 1)	(0.7, 1)	(0.8, 1)	(0.9, 1)	(1.0, 1)

Table 5.1: Programmed pulses and their durations for the multi-puff experiments.

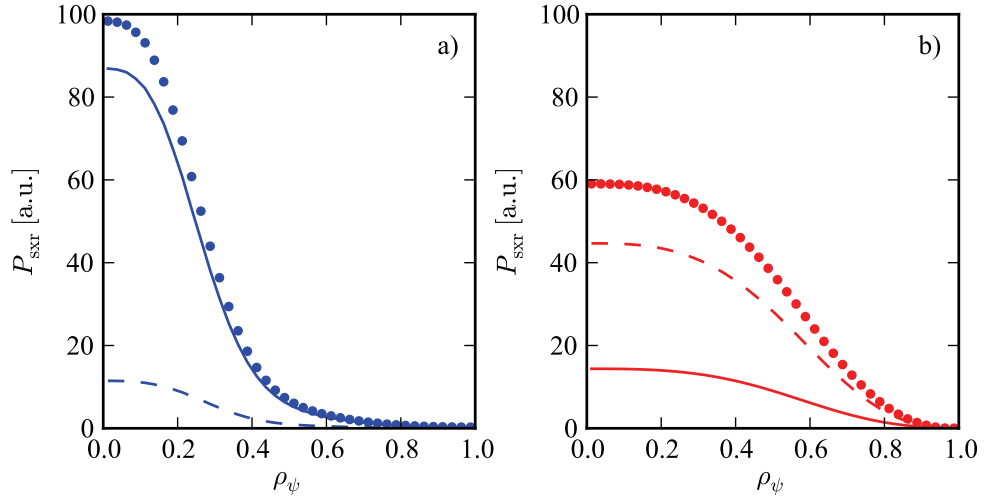


Figure 5.26: Experimental SXR emission profiles for (a) #44433 OH only and (b) #44436 with additional ECH: the background before injection (dashed), the active signal with argon (dotted), and the net radiation (solid)

τ_r	range	argon	neon
heating power	[OH, ECH]	[20, 15] ms	[40, 85] ms
electron density	$\bar{n}_e = [0.9, 1.2] \times 10^{19} \text{ m}^{-2}$	as OH	-
plasma position	$Z = [10, 23] \text{ cm}$	as OH	-
plasma current	$I_p = [130, 230, 300] \text{ kA}$	[20, 35, 70] ms	-
elongation	$\kappa = [1.45, 1.65]$	as OH	-
triangularity	$\delta = [-0.3, 0.3, 0.4]$	as OH	-

Table 5.2: Approximate rise times on the central DMPX chord for the argon and neon injection experiments.

central electron temperature, ohmic and ECH power and the deuterium gas flux for two experiments with OH only and with additional 400 kW of ECH. It can be seen that the consecutive puffs result in a stationary phase around $t = 0.7 - 0.85 \text{ s}$ where all the plasma parameters, including the soft x-ray emission profile are relatively constants. The inferred value of Z_{eff} (from $I_p = I_{\text{ohmic}} + I_{\text{bootstrap}}$) is also constant, around 2 for #44433 and 2.8 for #44436 at $t = 0.7 \text{ s}$. In case of a stationary impurity concentration the time dependent modelling can be (partially) avoided as we shall see in the next chapter.

5.8 Summary

In this chapter, time evolution of SXR and other measurements following short gas injections of argon and neon have been presented. The effects of varying background plasma parameters on the impurity response have been tested. Since both argon and neon are strongly recycling impurities, that is not directly captured by the carbon wall, the rising part of the SXR emissivity is a more reliable transport indicator and was measured in more detail. Table 5.2 summarizes the rise times for the various scans. It was shown that neon behaves very differently from argon in all cases studied. It stays considerably longer in the plasma (much more than the expected difference in transport properties) than argon and a clear build-up of the SXR emission is observed following successive puffs. This is observed in both OH and ECH cases and should motivate further experiments as transport coefficients are not expected to depend on the impurity charge [Giroud et al., 2007, Guirlet et al., 2009].

Argon displays a clear decay rate, including both the effects of a finite confinement time and recycling. The decay rate about 10 times slower than the rise time, which, incidentally,

shows that the impurity gas arrival rate is fast. It was shown that both the rise and decay time do not depend on the position of the injection incidence at the plasma surface as long as it directly reaches the plasma. No argon influx is measured when the plasma is centered at $Z = 0$ cm such that the injection 'misses' the plasma. However, due to the significant difference with neon, our results suggest that information would be gained by repeating these experiments with neon too. The similar SXR time evolution observed from different viewing SXR chords shows that the time evolution following argon injection is symmetric with respect to the poloidal angle. Therefore, one dimensional transport approximations are justified in the simulations.

It was also demonstrated that 5 – 10 ms, 'small' puffs with the multi-purpose gas injection system do not modify significantly the background plasma parameters (except Z_{eff}) and can be taken as perturbative. From the change of Z_{eff} , using the measured total ohmic and bootstrap current, $n_{\text{Ar}}/n_e \approx 0.1 - 0.3\%$ and $n_{\text{Ne}}/n_e = 1 - 3\%$ were inferred confirming the perturbative nature, at least for argon experiments.

By varying the background plasma parameters we have seen that electron density has little effect on the measured SXR time evolution following the impurity gas injection. On the other hand the plasma current scan show faster rise and decay rate at smaller plasma current, consistent with increased transport. This is also observed with increased elongation, although the range spanned was not sufficient for a definite statement. Since the plasma elongation varied during the triangularity scan and had, contrary to electron density, a similar effect (increasing κ and increasing δ), the shape experiments were inconclusive. The δ experiments could be too sensitive to boundary conditions and should be performed with greater care and including a constant κ or slightly decreasing κ in order to decouple these effects. We have also tried to test the effects of boundary conditions by comparing limited and diverted plasmas. Such a study also requires a detailed shape study (including the modifications of top and bottom triangularity independently) since a diverted shape is never exactly similar to a limited plasma configuration.

Finally, we compared ohmic and EC heated plasmas. The central SXR chords show faster rise and decay in the ECH case, as expected from a degraded confinement. Turbulence increases with increased heat flux, but this is not really the case for edge chords. This confirms recent AUG results [Sertoli et al., 2011], where transport coefficients near the ECH deposition were seen to be increased. In our case central deposition was performed. This suggests that further experiments using a range of off-axis ECH deposition at different

radial values should also be performed in TCV, using the analysis techniques developed in this chapter to complement our results.

Chapter 6

Transport studies with impurity injection

This chapter presents a new simulation method developed during this thesis to analyse results of TCV impurity transport experiments. It is then used to study some of the experiments described in Chapter 5, in particular to infer transport coefficients from the measured SXR emissivity profile time evolution. The problem of computing the impurity density evolution for given transport coefficients will be referred to as the *direct problem*. Conversely, the calculation of the transport coefficients based on the impurity density evolution will be called *inverse problem*. The identification of impurity transport coefficients from experiments with SXR observations requires the subsequent solution of the direct and inverse problems.

Section 6.1 deals with the direct problem and presents the radial transport model implemented in STRAHL to compute the impurity density and SXR emissivity profile evolution. It is studied how the various injection and background plasma parameters influence the impurity density profile evolution and the observed radiation. The context of the present work with respect to recent results is also discussed here. Then, Section 6.1.7 presents the method to find the transport coefficients, which combines STRAHL simulations with two inversion techniques, namely the matricial approach (MA, [Escande and Sattin, 2012]) and the gradient-flux (GF, [Sertoli et al., 2011]) method. After the method is tested on simulated signals, in section 6.2 it is used to compare argon transport coefficients with OH only and ECH; and, in section 6.3, with different plasma current.

Section 6.4 focuses on the analysis of the multi-puff experiments of section 5.7 and re-

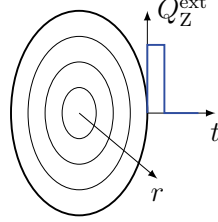


Figure 6.1: Transport experiment with impurity injection: neutral atoms are injected at the edge of the plasma.

lates the SXR profile peakedness to impurity density profile peaking. Finally, in section 6.6 summary and concluding remarks are given.

6.1 Modeling impurity injection

6.1.1 Diffusive-advective model of radial transport

Figure 6.1 outlines a transport experiment with gas puff. The working gas resides in a reservoir and an injection system injects the gas into the plasma, providing the time dependent source term $Q_Z^{\text{ext}}(t)$, the number of neutral particles entering in the computational domain. The injected gas is usually stored at room temperature, therefore the ionized part of the gas is negligible. We only consider the *radial* transport of the impurities. The model should not only provide the time evolution of the impurity density, but for the comparison with experiments, we also wish to compute the expected soft x-ray radiation of the injected impurity. This necessitates to write the transport equations for *all* charge states of the considered impurity. We assume that the density of the k -th charge state obeys a diffusive-advective (DA) equation:

$$\frac{\partial n_Z^k}{\partial t} = \nabla \cdot (-D \nabla n_Z^k + V n_Z^k) + Q_k. \quad (6.1)$$

As it was shown in the 2.2.1, this provides a reduced description of the full transport equation. The two transport coefficients are the diffusion coefficient D and the advection velocity V . Here, D and V are assumed to be the same for all charge states, independent of time, but they may change as a function of radius. Q_k collects the source and sink

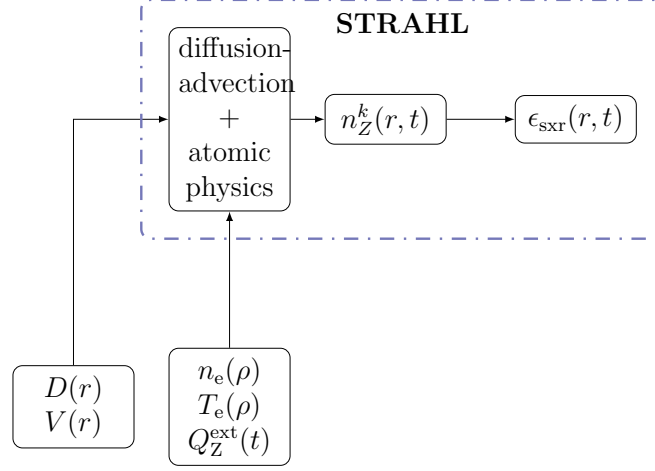


Figure 6.2: Diffusive-advective radial transport of impurities as implemented in STRAHL: for given transport coefficients D , V and plasma parameters the impurity density and SXR emissivity profile evolution are computed.

terms of the charge state due to ionization and recombination processes, as given by the right hand side of the system 2.25-2.27 of section 2.3.2. The injected neutrals appear in the source term for the neutral charge state ($k = 0$), which we write explicitly

$$Q_Z^0 = n_e \left(-n_Z^0 S_0 + n_Z^1 \alpha_0 \right) + Q_Z^{\text{ext}}, \quad (6.2)$$

where the term $Q_Z^{\text{ext}} = Q_Z^{\text{ext}}(t)$ is the external gas pulse from the injection system.

The solution of this direct problem is represented by a flowchart in figure 6.2. We use the numerical code STRAHL (see 2.4.5) to solve the 6.1 system of equations for given D , V , Q_Z^{ext} and plasma parameters n_e , T_e to obtain $n_Z^k(r, t)$ the impurity density evolution for all charge states.

From $n_Z^k(r, t)$, the SXR emissivity of the impurity is computed [Sertoli et al., 2011]

$$\epsilon_{\text{sxr}}(r, t) = n_e(r) n_Z(r, t) \sum_j y_j(r, t) k_j^{\text{sxr}}(r), \quad (6.3)$$

where $n_Z = \sum_{k=0}^Z n_Z^k$, $y_j = n_Z^k / n_Z$ and the photon emissivity rate coefficients k_j^{sxr} , taken from the ADAS database [Summers, 2004], consider all the radiative transitions of the ionization stage in the sensitivity range of the diagnostic.

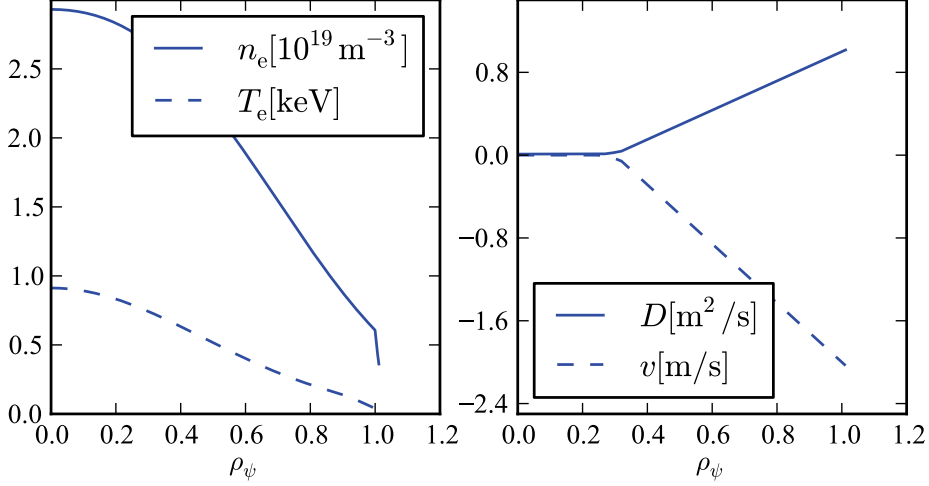


Figure 6.3: Input parameters for the reference case: (a) electron density and temperature (taken from #43768), (b) diffusivity and advection velocity profiles. $D(\rho_\psi \leq 0.3) = 0.01 \text{ m}^2/\text{s}$, $V(\rho_\psi \leq 0.3) = 0$ and $D(\rho_\psi = 1) = 1 \text{ m}^2/\text{s}$, $V(\rho_\psi = 1) = -2 \text{ m/s}$.

6.1.2 Reference parameters

A reference set of parameters is chosen to demonstrate the salient features of the transport simulations. Figure 6.3 shows the input profiles for this case. The electron density and temperature profiles are taken from an OH only phase of #43768. The background profiles and the time evolution of the main plasma parameters were already shown in figure 5.1 and 5.2), respectively. The neutral source has a rectangular waveform simulating a valve that opens for 5 ms.

The most important part of the transport simulation is the choice of the transport coefficients. These are the quantities which ultimately must be inferred from the experimental data. As reference we choose simple profiles with which the simulation gives qualitatively similar soft x-ray evolution to the experiments. We set the D and V profiles to be flat up to $\rho_\psi = 0.3$ with $D(\rho_\psi \leq 0.3) = 0.01 \text{ m}^2/\text{s}$ and $V(\rho_\psi \leq 0.3) = 0$, then they both are linearly increasing in absolute value such that $D(\rho_\psi = 1) = 1 \text{ m}^2/\text{s}$ and $V(\rho_\psi = 1) = -2 \text{ m/s}$. The negative V , inward advection, provides that the stationary impurity density profile is peaked, as it is observed in many experiments.

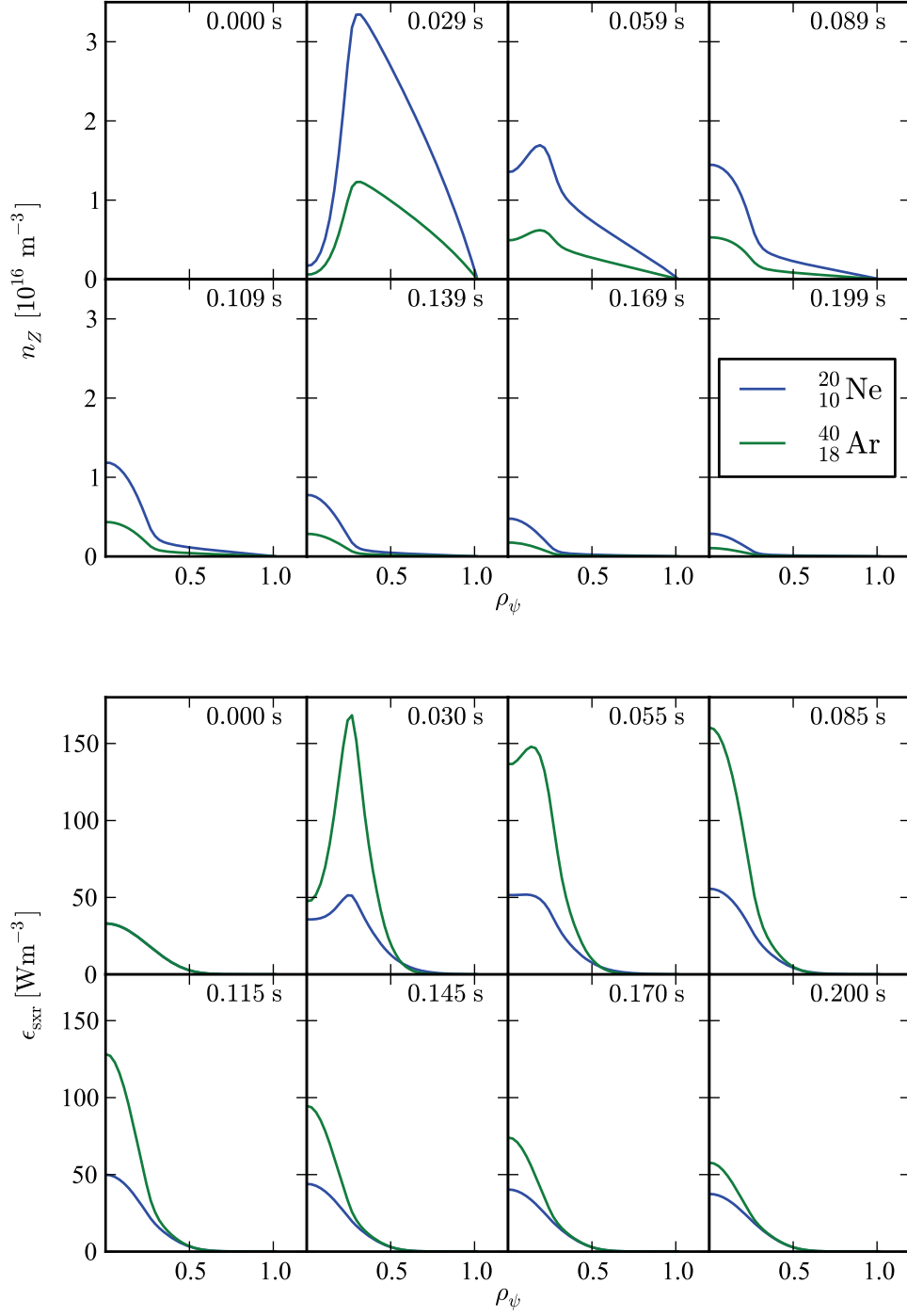


Figure 6.4: Simulated impurity density and SXR emissivity evolution for the reference case (see figure 6.3).

The reference parameter set was used to simulate neon and argon injections. Figure 6.4 shows the total impurity density n_Z and radiated power density in the soft x-ray range ϵ_{SXR} as a function of ρ_ψ at different times. In the calculation of the SXR emission the sensitivity the DMPX filter-detector combination was taken into account [Dux, 2011a]. The simulations were performed for both argon and neon with the same D and V profiles and the same source. The simulation results display twice the number of particles for neon because of the difference in ion mass and first ionisation energy.

At $t = 0$ the impurity density is zero. We may separate the impurity density evolution into two phases: the influx and the outflux phases. The influx phase lasts until the impurity density in the center ($\rho_\psi = 0$) reaches its maximum value. We see that reduced transport creates a barrier like structure in the center with rather elevated density gradients at $\rho_\psi = 0.3$. In the outflux phase the impurity density is decreasing self-similarly along the whole radial range.

At $t = 0$ the non-zero SXR emission comes from bremsstrahlung of the main ion species (deuterium). Obviously the background is the same for Ne and Ar simulations. The SXR radiation only differs significantly from the background at radii $\rho_\psi < 0.4$. This stems from the fact that the electron temperature is too low for $\rho_\psi \geq 0.4$ for the SXR emission to be measured. This shows again the limitation of the SXR diagnostics: we only obtain information from the areas where the electron temperature is high.

6.1.3 Pulse shape

The external impurity source is an input parameter of the modelling. The source is localized at the edge, however it will determine the time evolution of the density and, ultimately, the radiation from the core. Measuring the pulse shape *before* the gas enters into the plasma is a difficult task (see section 4.3). Moreover, no spectroscopic data were available to measure the population of low charge states which would give information about the impurity source.

In principle, there is no preferred pulse shape so long as its exact profile is known. An on-off, rectangular pulse corresponds to the ideal situation when the gas valve opens and closes abruptly. Figure 6.5 shows the shape and the parametrization of an ideal and a train of non-ideal pulses. Following the calibration experiments (see section 4.3) for 5-10 ms long pulses used in the impurity transport experiments $\tilde{\tau}_r \ll w$ holds well, therefore,

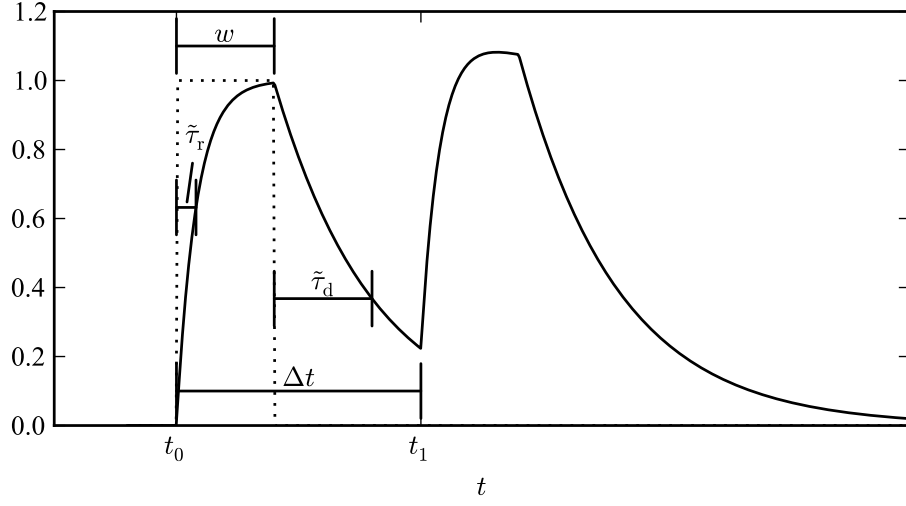
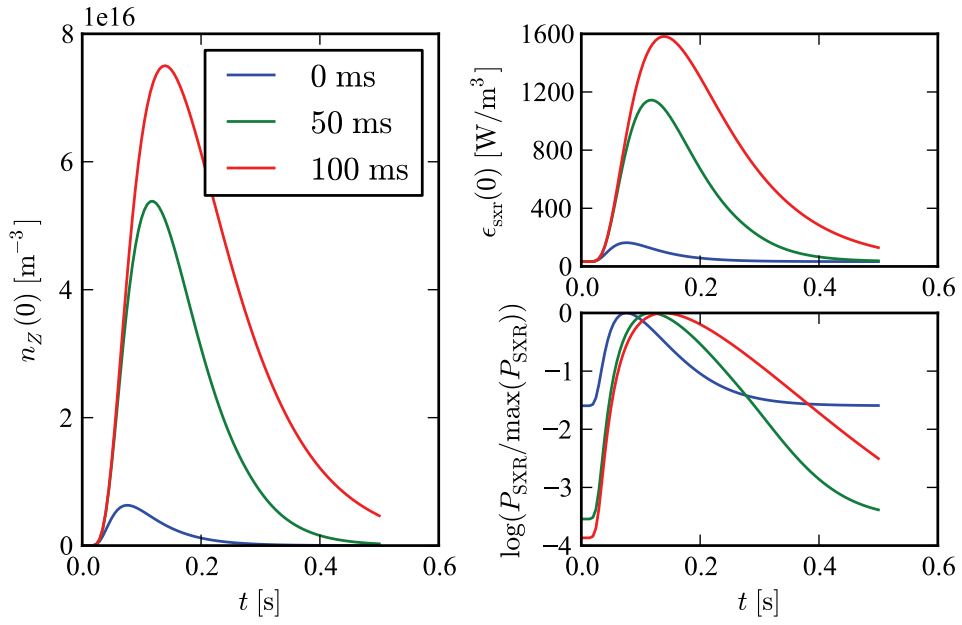


Figure 6.5: Neutral source with ideal (dotted) and realistic (solid) pulse shapes.

Figure 6.6: STRAHL simulation of 5 ms long argon injections with different τ_d source decay times. The other parameters were fixed according to the reference case.

in the following we will assume $\tilde{\tau}_r = 0$. In the experiments with many injections, the individual pulses were programmed far apart ($\Delta t \gg w$ and $\Delta t \gg \tilde{\tau}_d$) so that the pulses do not pile-up. Note that for neon the observed pile-up may be due to a larger than expected effective $\tilde{\tau}_d$.

Visible camera observation of the injector port (see figure 4.11) suggests that the gas packet delivered in the plasma possesses a non-negligible tail. In order to see the effect of the source decay time $\tilde{\tau}_d$ on the impurity density and SXR emission evolution, a set of simulations was performed for $\tilde{\tau}_d = 0, 50, 100$ ms. All other parameters were identical to the reference case (6.1.2).

Figure 6.6 shows the results of simulated argon injections. The longer the decay time, the larger the number of injected particles, which results in higher impurity concentration in the plasma during the experiment. The rate at which the density increases is slightly larger for non-ideal pulses, but very similar for the 50 ms and 100 ms cases. The main effect is that more particles are injected during the rise part and the maximal concentration is attained later and the larger number of particles takes more time to be transported out from the plasma. It can also be seen that the decay rate increases with increasing $\tilde{\tau}_d$.

6.1.4 Recycling

Impurity behavior outside the last closed flux surface is not well described by a one-dimensional model. To account for various impurity-wall interaction in the modelling, a recycling model is required to complement the radial diffusive-advective model. STRAHL has the options to use a rather complex edge model with recycling, sputtering etc. [Dux, 2011b]. Here, only the recycling parameter R , that defines the ratio of the lost particles that are reinserted (recycled) as neutrals in the close-field region, is used. The recycled neutrals appear as an additional source with strength of $R\Gamma_\perp$ source of neutrals at the edge, where Γ_\perp is the flux through the last flux surface. $R = 0$ means no recycling occurs, whereas $R = 1$ corresponds to complete recycling, so that once injected, impurity particles eventually appear as a constant edge source in equilibrium with the plasma particle exhaust.

Demonstrating the effect of the recycling, simulations with $R = [0, 0.5, 1.0]$ were performed. The evolution of the central impurity density and the radiated soft x-ray power is shown in Figure 6.7. The difference in the maximal impurity density in the core between the no recycling and the complete recycling case can be one order of magnitude. In addi-

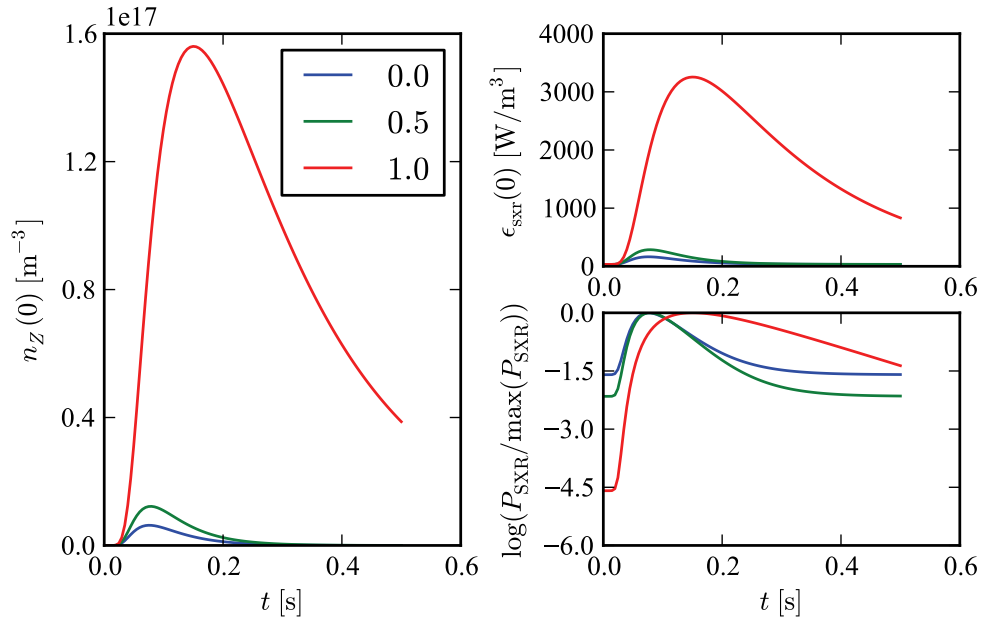


Figure 6.7: STRAHL simulation of 5 ms long argon injections with different values of the recycling coefficient R . The other parameters were fixed according to the reference case.

impurity	injection	main diag.	reference
Si, Al	LBO	SXR	TCV [Scavino, 2002]
Ni, Ar, Ne	LBO, gas puff	SXR, CXRS	JET [Puiatti et al., 2006] [Giroud et al., 2007]
Al, Cr, Ni, Ge, N	LBO, SMBI, gas puff	SXR, VUV	Tore Supra [Parisot et al., 2008] [Guirlet et al., 2009] [Guirlet et al., 2010]
Ar	gas puff	SXR	ASDEX-U [Sertoli et al., 2011]
Ca	LBO	HiReX	Alcator C-Mod [Howard et al., 2012]

Table 6.1: Recent studies with impurity transport experiments.

tion, it can be seen a clean change in the decay phase for the low and high recycling rates: at $R = 1$ a 'pile-up' behavior is observed and a very slow exponential decay is found.

6.1.5 Electron density and temperature profiles

We now investigate, in figure 6.8, how the background electron density and temperature profiles influence the radiation emitted by the impurity. We simulate argon injection with typical L-, H- and eITB plasma parameters. The profiles presented in figure 2.6 of section 2.1.4 are used. It is interesting to see that the background profiles do influence the resulting density and SXR profiles. The transport coefficients D and V determine the evolution of n_Z , but ϵ_{SXR} depends strongly on T_e and n_e leading to a very broad profile in the H-mode case, whilst the eITB case compensates low density with a high and broad T_e profile.

6.1.6 Relation to recent simulation studies

In the simulations discussed so far given $D(r)$ and $V(r)$ were used in the radial transport equations to obtain the 'predicted' $n_Z^k(r, t)$, $n_Z(r, t)$ and $\epsilon_{\text{SXR}}(r, t)$ as shown in figure 6.2. In order to find D and V compatible with the experiments, these coefficients need to be modified until the solution $n_Z(r, t)$ and/or $\epsilon_{\text{SXR}}(r, t)$ matches the measurements. This is done with a χ^2 minimization procedure with some weights on the radial points used for

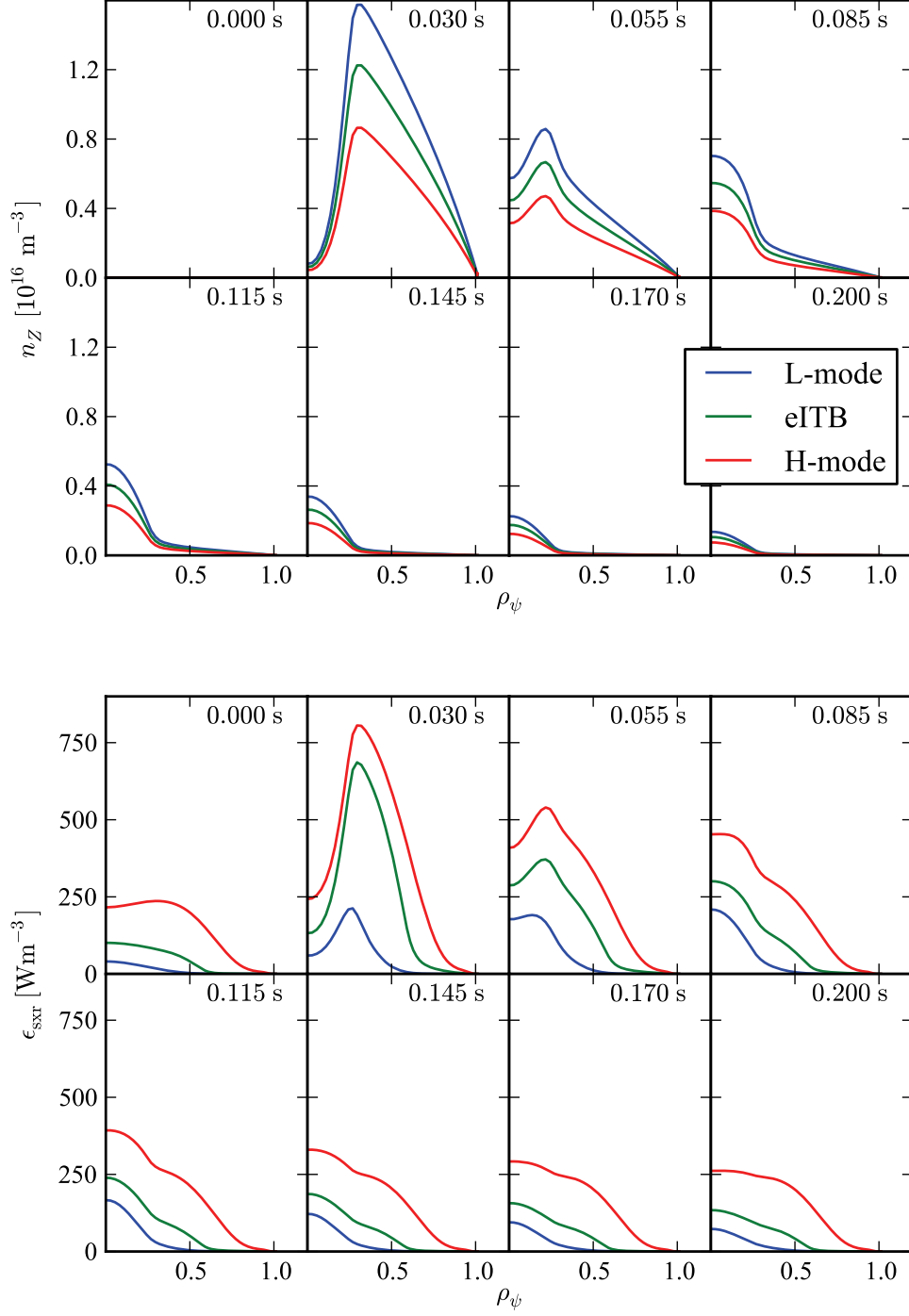


Figure 6.8: Same quantities as in figure 6.4 for simulated Ar injection into L-, H- mode and eITB plasmas. The corresponding electron density and temperature profiles are shown in figure 2.6).

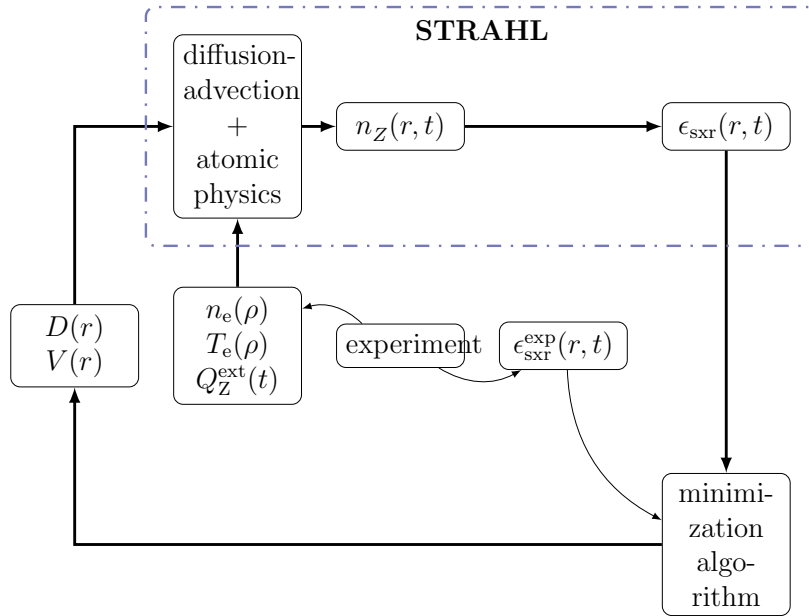


Figure 6.9: Direct minimization method: the transport coefficients are determined by subsequent solution of the direct problem in a minimization loop.

the comparison. This is illustrated in figure 6.9. This direct minimization procedure is the 'classical' method applied by almost all impurity transport studies to infer transport coefficients as shown in table 6.1 for the most recent papers.

The early experiments in TCV [Scavino, 2002] have shown a decrease in confinement with increasing elongation and current and, in particular, a large effect of sawteeth on the simulation results, probably explaining why positive (outward) advection was always found. Conversely, recent studies tend to find that impurity transport properties follow those of the main species and report weak Z -dependence. This latter was shown in JET [Giroud et al., 2007], Tore Supra [Guirlet et al., 2009] and the former on C-Mod [Howard et al., 2012] with non-linear gyrokinetic simulations and on AUG-U [Angioni et al., 2011] with quasi-linear gyrokinetic simulations.

Direct minimization methods have some drawbacks:

- the solution is searched in a reduced space of profiles. D and V are represented as polynomials and the minimization is performed over their coefficients,
- constraints to provide physical transport profiles, such as positive D or $V = 0$ on the magnetic axis, may be difficult to translate in constraints on the polynomial coefficients,
- the cost function is defined over a high dimensional space and finding the *global* minimum is not guaranteed. Usually it is possible to find an acceptable *local* minimum, however this may depend strongly on the initial conditions,
- direct problem is solved at every minimization step, making the method computationally expensive.

Recently, an inverse method was proposed by [Sertoli et al., 2011] to study the effect of ECH on impurity transport in AUG-U experiments. Local increase of transport near the ECH deposition location was found. The inverse method solves for $V(r)$, $D(r)$ given n_Z , as discussed later, and the overall method is shown in figure 6.10. The method is not limited to a subset of profiles as often the case in the direct minimization method. On the other hand, some iterations may still required when n_Z is not measured directly and n_Z is obtained from the comparison of simulated and measured SXR emissivities (figure 6.10). The gradient-flux method was used by Sertoli et al. [2011] to invert the linear relation between V , D and n_Z , ∇n_Z . The application of this method is difficult near the center

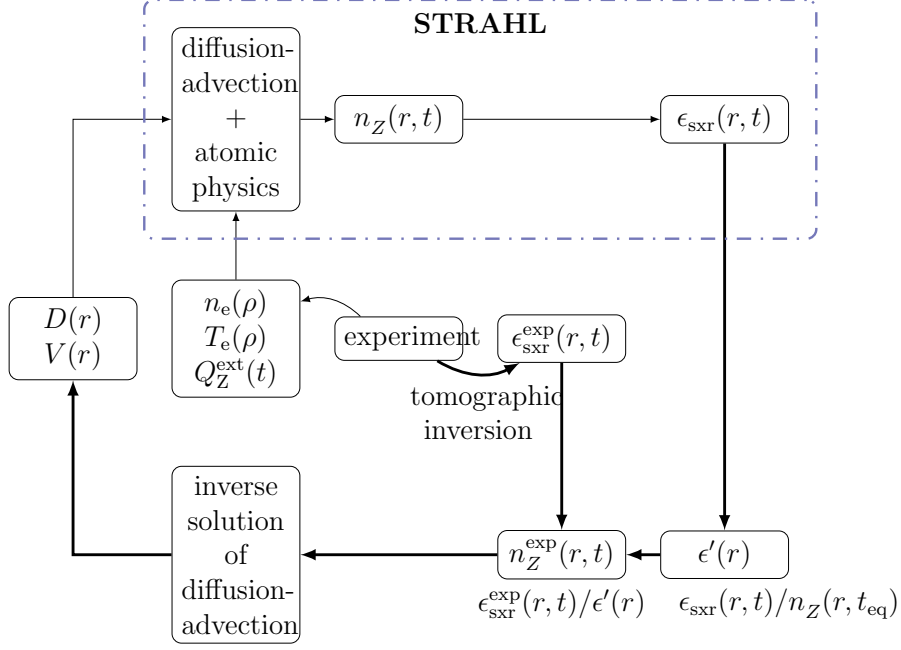


Figure 6.10: Application of the inverse method to determine D and V from SXR measurements.

where the profiles are flat or even hollow. Therefore we have also implemented a new approach, the matricial approach [Escande and Sattin, 2012, Sattin et al., 2012] inverting the problem in Fourier-space. This is discussed in more detail in the next section and in Appendix A.

6.1.7 Transport coefficients from the inverse solution

The flowchart of figure 6.10 presents the logic of determination of D , V from the experimental SXR evolution $\epsilon_{\text{SXR}}^{\text{exp}}(r, t)$. Based on an initial guess of D , V with the electron density and temperature profiles from the experiment, as well as the source term Q_Z^{ext} , the solution of the direct problem provides $n_Z(r, t)$ and $\epsilon_{\text{SXR}}^{\text{exp}}(r, t)$, as described in section 6.1.

From the simulation, the impurity density and emissivity evolution are available, thus the normalized emissivity function

$$\epsilon'(r) = \epsilon_{\text{SXR}}(r, t)/n_Z(r, t_{\text{eq}}) \quad (6.4)$$

may then be calculated. ϵ' does not depend strongly on the transport coefficients D and V [Sertoli et al., 2011]. t_{eq} is chosen to be the time when the impurity concentration at the center is maximal.

The numerically computed ϵ' and the experimentally measured $\epsilon_{\text{SXR}}^{\text{exp}}(r, t)$ are used to obtain the *experimental impurity density* evolution

$$n_Z^{\text{exp}}(r, t) = \frac{\epsilon_{\text{SXR}}^{\text{exp}}(r, t)}{\epsilon'(r)} \quad (6.5)$$

The last step is to solve equation 6.1 as an *inverse* problem, that is to obtain D and V from $n_Z^{\text{exp}}(r, t)$. To achieve this, two procedures are utilized in this thesis: the mathematical details of the gradient-flux (GF) method [Sertoli et al., 2011] and the matricial approach (MA) [Escande and Sattin, 2012, Sattin et al., 2012] are summarized in appendix A. The resulting D and V , that usually differ from the initial guess, can be used to recompute ϵ' , n_Z^{exp} and update D , V . Experience shows that the procedure converges after few iterations, that is D and V do not change with additional iterations. The main advantage is that the form of D and V are not constrained a priori and, as we will see, for example V can change sign across the minor radius.

6.1.8 Inverse method on synthetic signals

Before we apply these inverse methods on experimental data, we demonstrate the reconstruction of D and V from simulated signals. The procedure is shown in figure 6.11: on the route (a) the simulated impurity density is fed to the inverse method; whereas on (b), n_Z^{exp} is computed similarly to equation 6.5, and then the inverse method is applied.

We apply the MA (with $f = 2$ Hz) and GF inverse methods on the simulation results of the reference case (see section 6.1.2). If the methods work correctly the reconstructed profiles are equal to those of the reference case. In figure 6.12 solid lines show the initial transport coefficient profiles with which the simulation was started, while symbols show the reconstructed profiles, that is the inverse solutions.

The profiles in figure 6.12 (a) were obtained using the MA on the total impurity density profile evolution. We can see that initial and the reconstructed transport coefficients match perfectly. In figure 6.12 (b) the same method was used but with n_Z^{SXR} obtained from ϵ_{SXR} . The reconstructed profiles match in the region, up to $\rho_\psi \approx 0.3$, where the SXR emission is

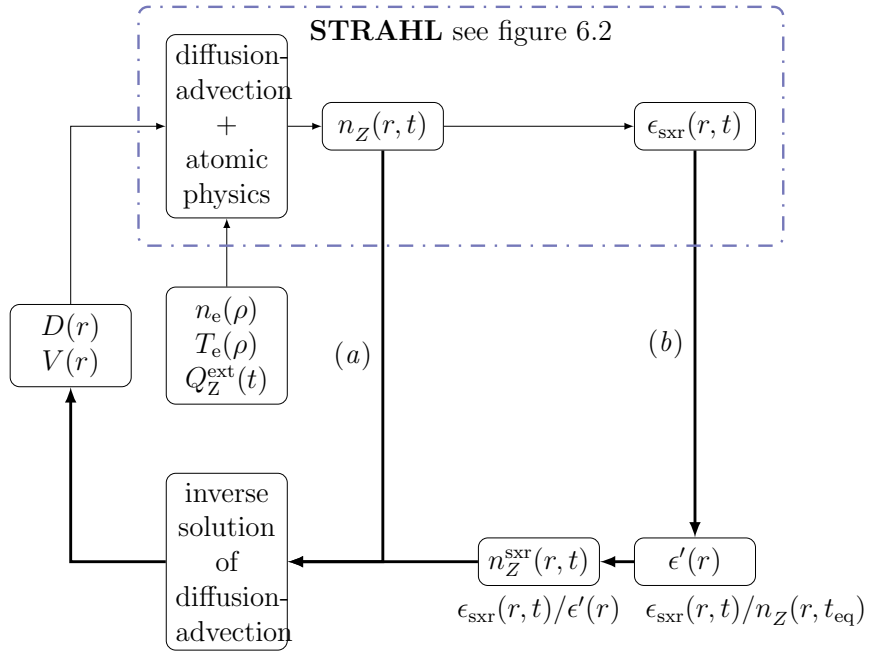


Figure 6.11: Application of the inverse method on synthesized signals: (a) from the simulated impurity density evolution and (b) from the simulated SXR evolution.

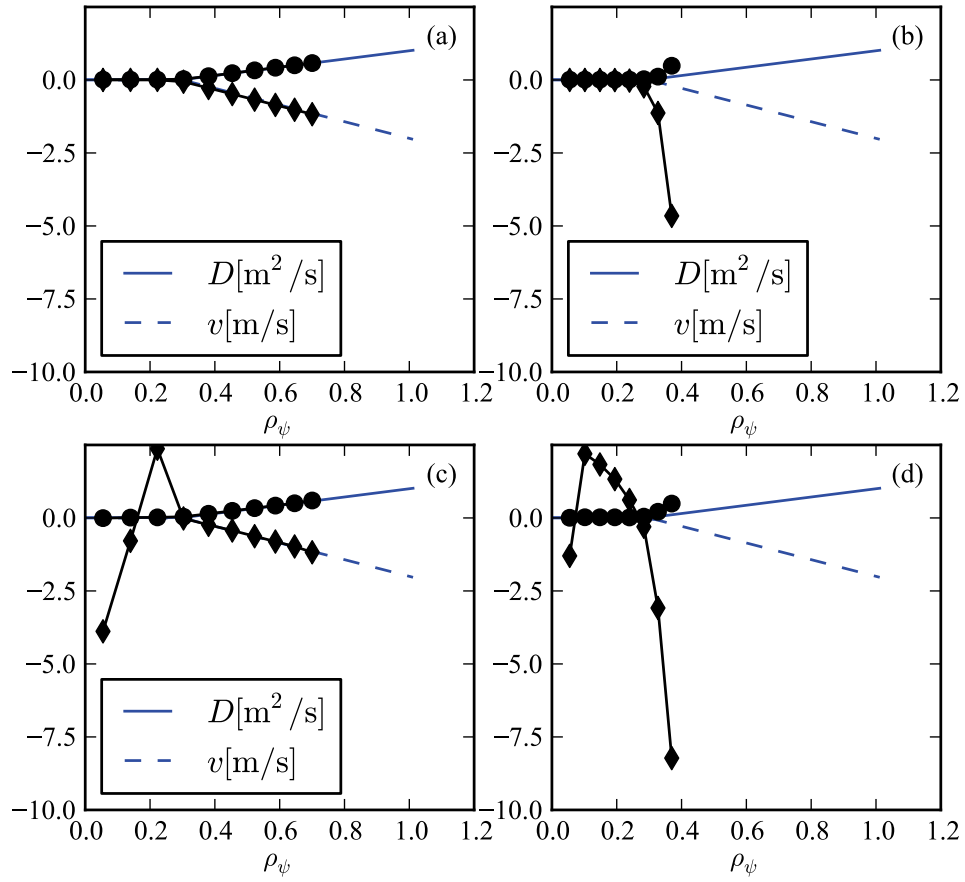


Figure 6.12: Reconstruction of the transport coefficients D and V for the reference case from (a), (c) the simulated impurity density evolution; (b), (d) the simulated SXR evolution using MA ((a), (b)) and GF ((c), (d)) methods

localized (see 6.4). No profile reconstruction can be done outside the sensitivity range of the detector.

In figure 6.12 (c) the GF method- n_Z combination is shown: the reconstructed profiles align well with their expected values, but the reconstructed V exhibits spurious oscillations near the center. The GF method extracts the transport coefficients from the linear relationship A.14. At the center, where the impurity density gradient and flux terms are small the linear fit is very poorly conditioned, and the fitted parameters have large errors.

Finally, figure 6.12 (d) plots the result of the GF method using n_Z^{SXR} , where both the error in the linear fit and the limitation by the SXR detector's sensitive region hamper the reconstruction. For this reason we privileged the MA method and in the following the MA method will be used as in the profile reconstruction.

6.2 Effect of ECH

In figure 6.10 the method of determining the transport coefficients from SXR signals was presented. In this section we apply this method to analyse the argon injection into OH only pulse #43778 (see figure 5.1) and pulse #43776 (see figure 5.13), with additional 240 kW ECH.

The electron temperature, density and the geometry (volume as a function of ρ_ψ) are taken from the experiment. We start the optimization loop (see figure 6.10) by setting D and V according to the reference case. ϵ' and n_Z^{SXR} are computed according to equations 6.4 and 6.5, respectively. Outside the sensitive region of the SXR diagnostic, for $\rho_\psi > 0.5 - 0.6$ (depending on the electron temperature), n_Z^{SXR} is set to decay linearly to zero at $\rho_\psi = 1$.

n_Z^{SXR} is then Fourier transformed (only in time) and the MA method is applied using four harmonics with the largest amplitudes. The method, therefore, yields four pairs of D and V . The mean value of the transport coefficients obtained are shown in figure 6.13, together with the $-v/D$ ratio indicating the impurity density peakedness in a stationary state. The colored bands in figure 6.13 (a) and (b) correspond to the standard deviation of the obtained D and V , respectively. Outside $\rho_\psi \approx 0.4$ SXR emissivity after the injection does not differ sufficiently from that of background to provide meaningful transport coefficients.

To compare the experimental SXR emissivity evolution with that simulated using the obtained transport coefficients, the values for D and V for $\rho > 0.4$ are required. This problem arises for every SXR based transport analysis (see table 6.1). Here, the method

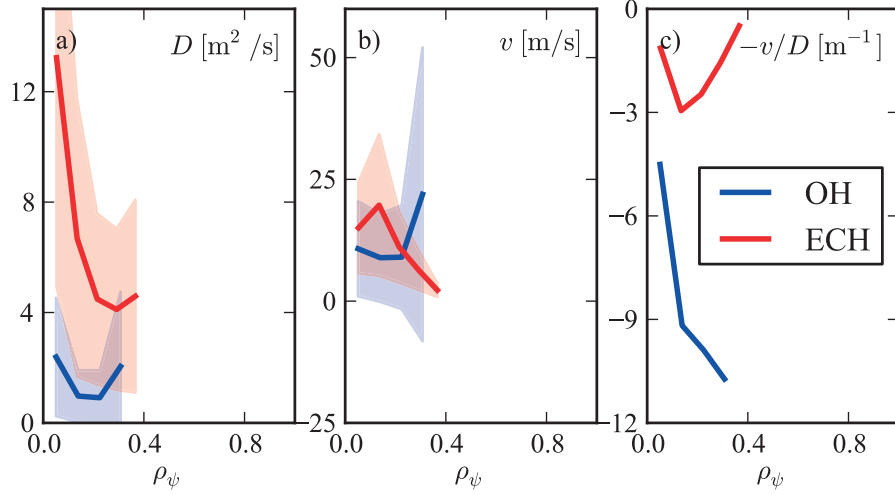


Figure 6.13: Argon (a) diffusion coefficient, (b) advection velocity and (c) density peaking factor profiles for #43778 OH alone and #43776 with additional 240 kW ECH.

used by Sertoli et al. [2011] is applied: outside the reconstruction region V is smoothly brought to zero and D to a constant value. The idea is to provide some ‘average’ transport that introduces the delay between the valve opening and the SXR signals’ rise.

The simulated impurity density and SXR profile evolution (solid) with the obtained transport coefficients are shown in figure 6.14 together with the experimental impurity density and SXR emissivity (dashed) for the OH alone and ECH cases. We compare the simulated and the experimental SXR evolution such that

$$t^{\text{sim}} = t^{\text{exp}} - t_0^{\text{exp}}, \quad (6.6)$$

where t^{sim} is the time in the simulation, t^{exp} is the experimental time, t_0^{exp} is the moment when the valve-open command is issued. In the remainder of this chapter $t \equiv t^{\text{sim}}$ unless otherwise stated.

In the simulation the SXR emission of the main ion (deuterium in all experiments) is taken into account. ϵ_{SXR} is rescaled with a constant factor to match the simulation at $\rho_\psi = 0$ and $t = 0$. We see in figure 6.14 that the simulated and the rescaled experimental background match well along the whole radius at $t = 0$.

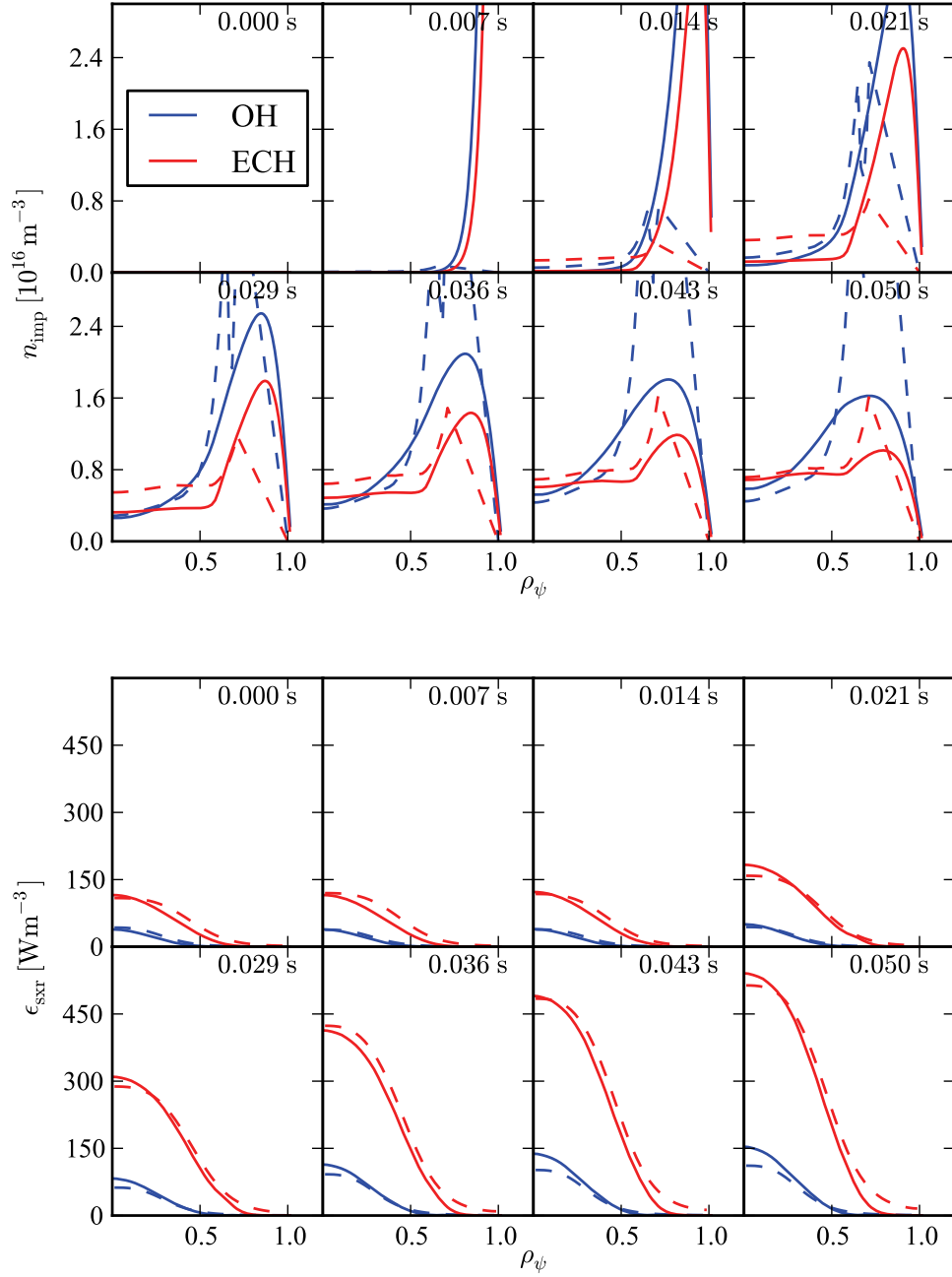


Figure 6.14: Time evolution of simulated (solid) and experimental (dashed) impurity density and SXR emission profiles for #43778 OH alone and #43777 with additional 240 kW ECH. The profiles match in the decay phase as well.

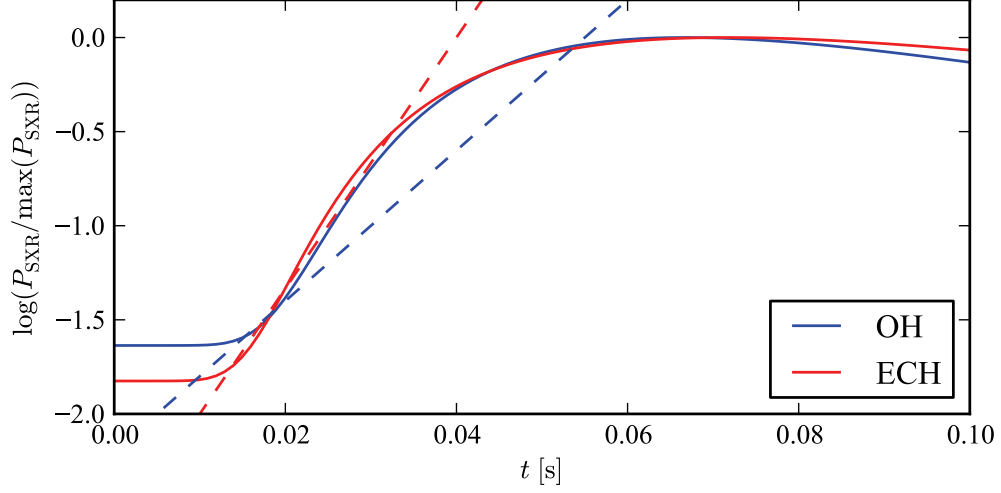


Figure 6.15: Synthesized DMPX central chord time evolution (solid) for #43778 OH alone and #43777 with additional 240 kW of ECH. The dashed lines are with the same slope as in figure 5.15.

In Scavino [2002] no systematic study of ECH is performed, however, some preliminary experiments suggested the reduction of aluminium confinement time when ECH was added. Sertoli et al. [2011] reports an enhancement of the diffusion coefficients and the rise of a positive convection around the ECH deposition radius. This is also observed in TCV experiments as mentioned in section 5.5. The larger diffusion coefficient obtained with ECH is consistent with a faster rise, also measured experimentally (figure 5.15). However the slower rise of the ohmic case is not fully recovered, albeit the simulations follow $\epsilon_{\text{SXR}}^{\text{exp}}(r, t)$ quite well, as shown in figure 6.14.

On the other hand positive V is obtained which yields hollow n_z profiles as seen in figure 6.14, as was also the case in Scavino [2002]. This can be accounted for the sawteeth activity, but may be more related to insensitivity to ϵ_{SXR} . This will be further discussed at the end of this chapter.

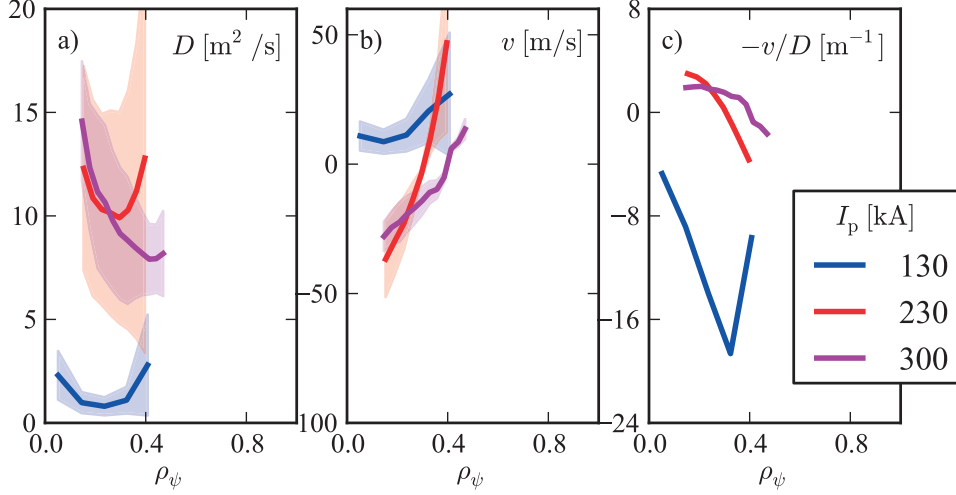


Figure 6.16: Argon (a) diffusion coefficient, (b) advection velocity profiles and (c) density peaking factor for the pulses #42314, #42310, #42313 with $I_p = [130, 230, 300]$ kA, respectively.

6.3 Current scan

Similarly to the OH and ECH comparison above, we now analyse the current scan experiments presented in section 5.4. Figure 6.16 shows the obtained transport coefficients, and figure 6.17 the evolution of n_Z and ϵ_{SXR} (solid) compared with n_Z^{SXR} and $\epsilon_{\text{SXR}}^{\text{exp}}$ (dashed) density and SXR emissivity profiles.

Figure 6.16 shows larger D value for higher current which could be interpreted as worse confinement. However, looking more closely, it can be seen that it is related in a large part to the fact that the measured $\epsilon_{\text{SXR}}^{\text{exp}}$ is much broader for higher current. This is recovered in the simulation with a large D , to have flat central profile and V becoming negative to reduce the hollow n_Z characteristic figure 6.17. The larger flat part with increasing I_p is related to the large sawtooth inversion radius and the significant profile flattening effect of the sawteeth. Therefore, this larger effective D is consistent with the average effect of sawteeth providing strong radial diffusion. Looking in more detail at the resulting rise phase, we compare in figure 6.18 the simulations with the fitted rise time values on the experimental results (figure 5.12). It can be seen that the experimental τ_d values match

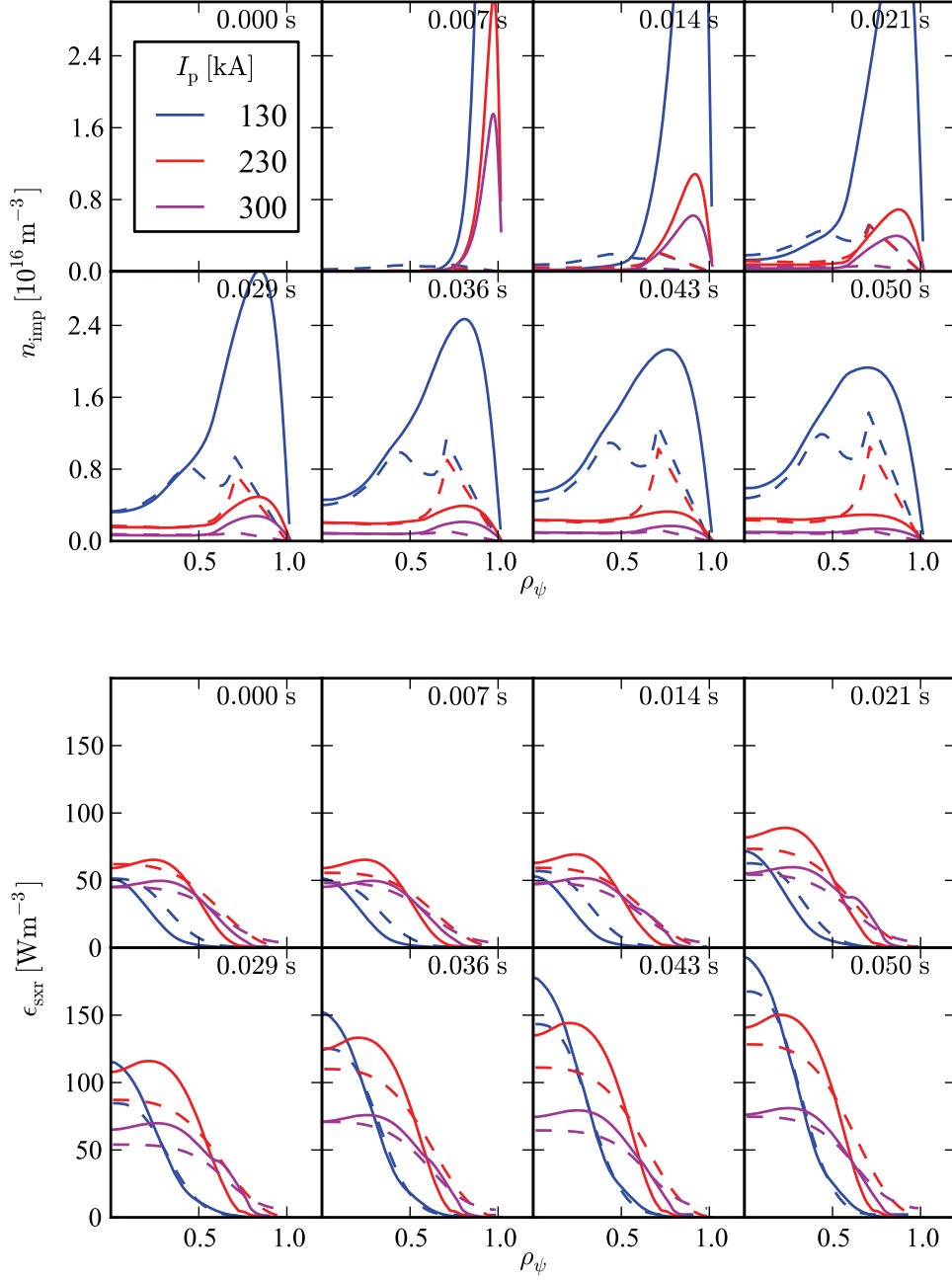


Figure 6.17: Time evolution of simulated (solid) and experimental (dashed) impurity density and SXR emission profiles for #42314, #42310, #42313 with $I_p = [130, 230, 300]$ kA, respectively.

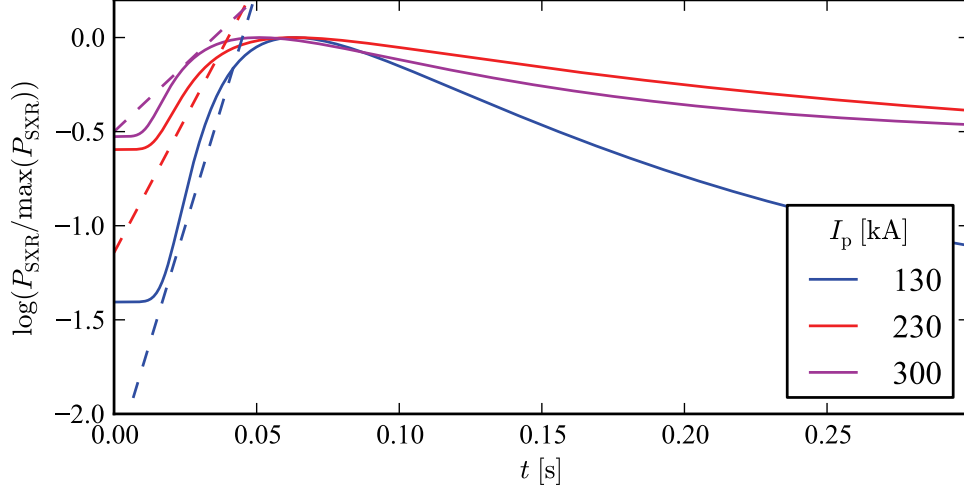


Figure 6.18: Synthesized DMPX central chord time evolution (solid) for #42314, #42310, #42313 with $I_p = [130, 230, 300]$ kA, respectively. #43778 OH alone and #4377 with additional 240 kW of ECH. The dashed lines are with the same slope as in figure 5.12

well with the simulations with a slower rise time at higher current. A faster decay at low current is also obtained in the simulations. Although usually the D coefficient mainly determine the rise and decay rate, here the combination with V changing sign is such as to reproduce the overall slower evolution (better confinement) at higher current.

6.4 Analysis of the multi-puff experiments

6.4.1 SXR decay time as confinement time

The simplest way to characterize particle transport is to introduce a τ confinement, or residence time, that is a characteristic time during which particles, or in our case, a certain impurity species is lost from the plasma. Here we are interested in how the SXR signal decay rate relates to the particle confinement time. In this section we construct a one-dimensional model that treats ionization and loss of impurities, following derivation by Carolan et al. [1990]. We replace the transport related components in equation 6.1 with a simple $-y_k/\tau$ term, defining the particle confinement time, and neglect recombination only

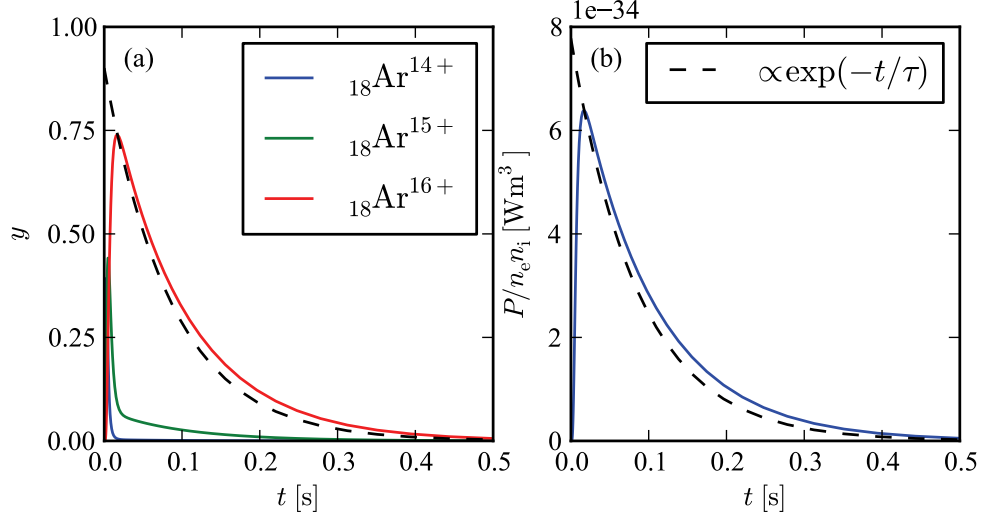


Figure 6.19: Time evolution of (a) the relative abundance of different states, and (b) the radiation function of argon for a particle confinement time of 0.1 s

retaining the ionization terms. The state balance for the k -th charge state is now written

$$\frac{dy_k}{dt} = n_e (y_{k-1} S_{k-1} - y_k S_k) - \frac{y_k}{\tau}. \quad (6.7)$$

The system of equation generated by equation 6.7 is solved numerically with the initial condition

$$y_k(t=0) = \begin{cases} 1 & \text{if } k = 0 \\ 0 & \text{otherwise} \end{cases} \quad (6.8)$$

Simulation of the evolution of argon ionization stages are shown in figure 6.19 (a) for $n_e = 1 \times 10^{19} \text{ m}^{-3}$ and $T_e = 1 \text{ keV}$ with $\tau = 0.1 \text{ s}$. We see that lower ionization stages are rapidly ionized until the He-like Ar^{16+} state is reached.

We also see that, at this temperature, in the decay phase the Li-like Ar^{15+} charge state is relatively unpopulated, therefore the relative abundance of the He-like Ar^{16+} obeys

$$\frac{dy_{16}}{dt} = -n_e y_{16} S_{16} - \frac{y_{16}}{\tau} \quad (6.9)$$

with the solution

$$\frac{dy_{16}}{dt} \propto \exp \left[- \left(S_{16}n_e + \frac{1}{\tau} \right) t \right] = \exp \left[- \frac{t}{\tau_m} \right], \quad (6.10)$$

where τ_m is the measured decay rate. With the parameters above $S_{16}n_e = 1.511 \text{ s}^{-1}$ yielding $\tau_m = 0.087 \text{ s}$.

6.4.2 Impurity density peaking from SXR emission peakedness

The stationary solution ($\partial n_Z / \partial t = 0$) of equation 6.1 yields the relation

$$- \frac{1}{n_Z} \frac{\partial n_Z}{\partial r} = - \frac{V}{D}. \quad (6.11)$$

We can see that the peakedness fixes only the V/D ratio, however this information can be used to compare with the transport coefficients obtained from the time dependent analysis.

The next step, and again the more difficult part of the problem is, to relate the peakedness of the *soft x-ray emission profile* to the transport coefficients. In section 2.3.2 the time dependent collisional-radiative model was introduced. This model is also used in STRAHL to compute the abundance of the ionisation stages of the respective impurity atom. Let us assume that individual impurity particles spend τ time in the plasma, then the average population of the k -th ionization stage is given by averaging over τ time period [Carolan and Piotrowicz, 1983]:

$$\bar{y}_k = \frac{1}{n_e \tau} \int_0^{n_e \tau} y_k(n_e t) d(n_e t). \quad (6.12)$$

In the plasma there will be an ensemble of impurities which have entered the plasma at different times. In this simple particle confinement picture, individual impurities spend identical periods of time in the plasma, therefore a temporal averaging is equivalent to an ensemble averaging. In this case, the integration period can be interpreted as the impurity confinement time [Carolan and Piotrowicz, 1983]. \bar{y}_k is the fractional abundance of the k -th ionization corresponding to τ confinement time. With the density of the ionization stages the ensemble averaged radiated power can be computed (see section 2.3.3).

Motivated by the graphs of Carolan and Piotrowicz [1983], figure 6.20 compares the time dependent and ensemble averaged radiation functions to that in coronal equilibrium for carbon, neon and argon. At temperatures lower than that where the first radiation peak occurs ($T_e \approx 10 \text{ eV}$ for carbon) there is little fall-off in radiated power when $\tau \ll \tau_{ss}$.

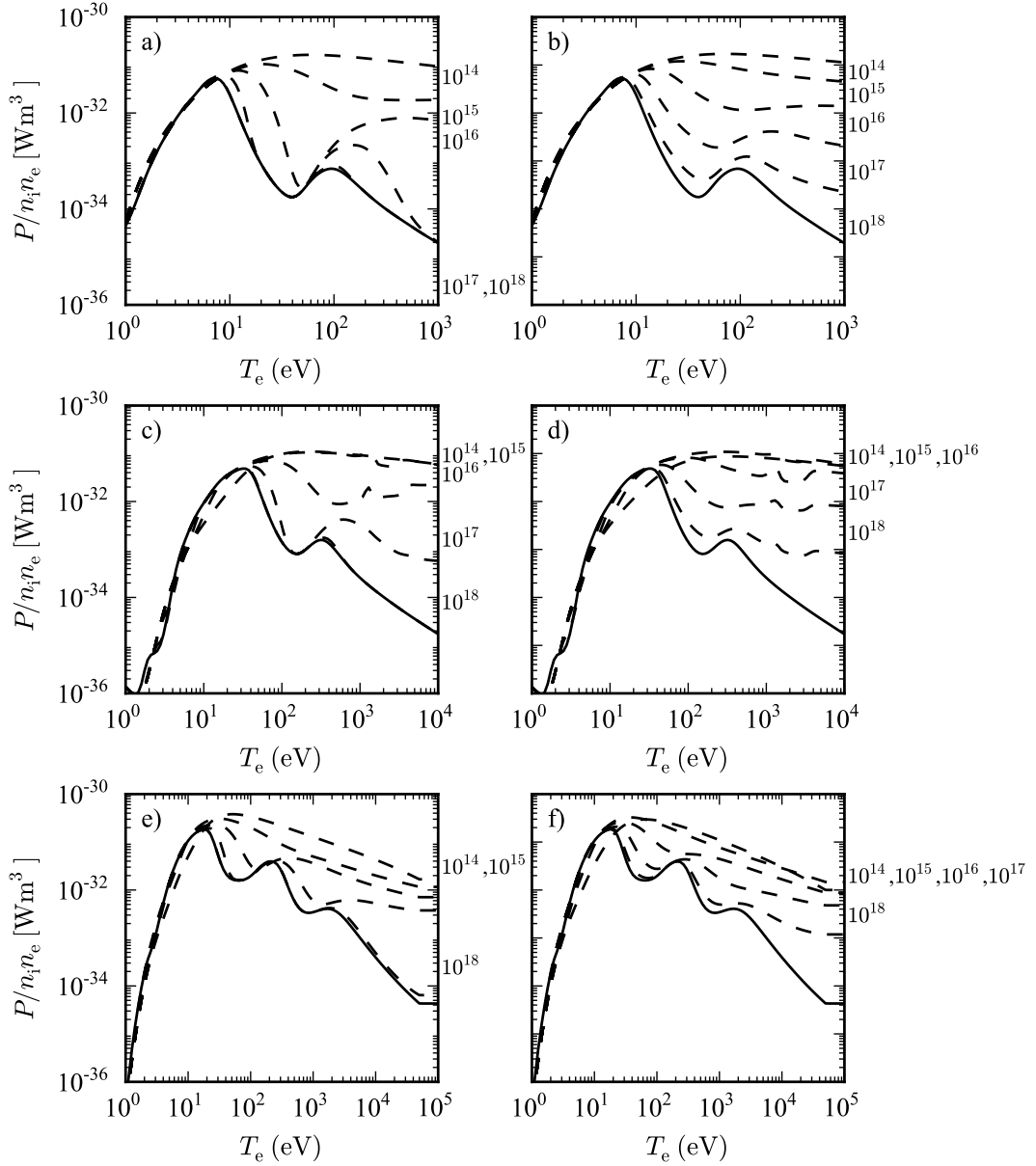


Figure 6.20: Time dependent ((a), (c), (e)) and ensemble ((b), (d), (f)) averaged radiation function as a function of the temperature for carbon ((a), (b)) neon ((c), (d)) and argon ((e), (f)). The dashed curves show different $n_e \tau$ values, the solid lines correspond to coronal equilibrium.

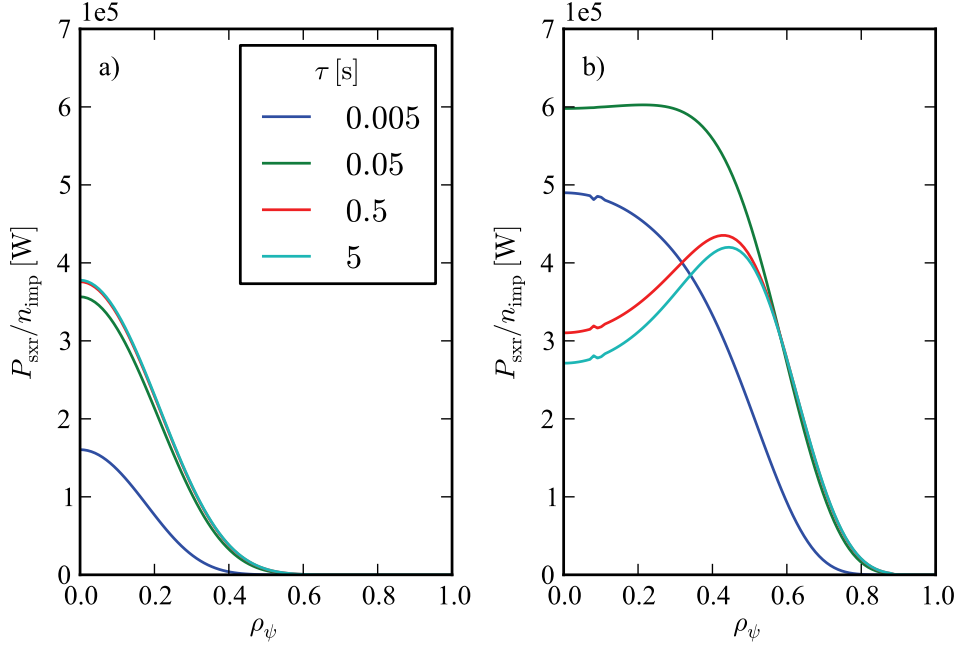


Figure 6.21: Simulated specific radiated power of argon in the SXR range with different argon confinement times for (a) #44433 OH and (b) 44436 with additional ECH.

At larger temperatures and far from coronal equilibrium (small confinement time) the difference in radiated power can be many orders of magnitudes larger than that with coronal equilibrium. Thus local or transient radiation losses can greatly exceed those at coronal equilibrium [Carolan and Piotrowicz, 1983].

6.4.3 Comparison of OH and ECH

In this section we present the detailed analysis of the multi-puff experiments described in section 5.7. We analyse #44433 with OH only and #44436 with 400 kW additional ECH (see Figure 5.25) in detail. Figure 5.26 plots the soft x-ray emissivity profiles for the background without argon, during the stationary phase with argon and the difference of these, the net emissivity.

As it was outlined in section 6.4 the population of the ionisation stages and the SXR radiated power was computed for $\tau = [0.005, 0.05, 0.5, 5]$ s. Figure 6.21 shows the results

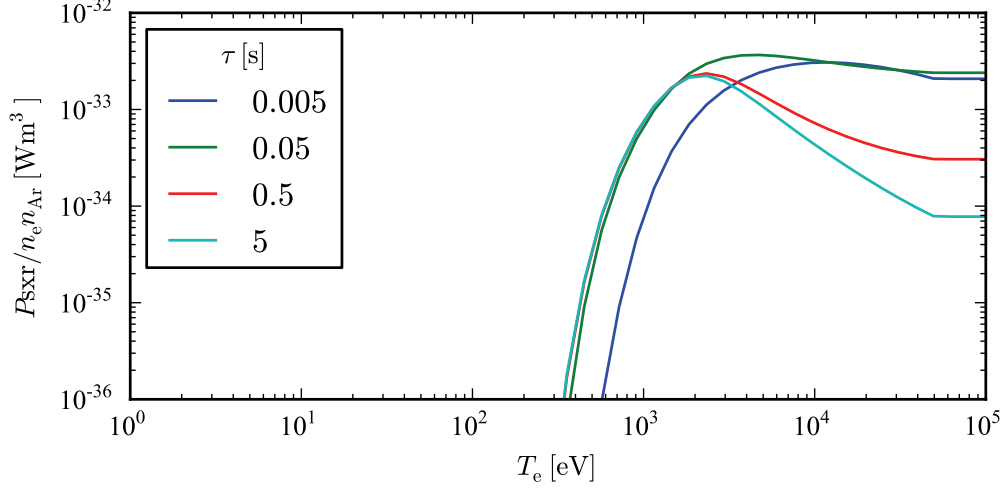


Figure 6.22: Filtered ($E_{\text{photon}} > 1 \text{ keV}$) specific radiated power of argon as a function of temperature for different confinement times.

of this calculation, the radiated power per impurity atom P/n_{imp} for the OH and ECH cases. In the OH case the P/n_{imp} curves are peaked and all but that of the smallest τ overlap. This means that from $\tau = 0.05 \text{ s}$ onwards the population of the ionisation stages is close to coronal equilibrium. The key parameter is the electron temperature T_e : indeed, in figure 2.14 we can see that steady-state time τ_{ss} for argon shows a local minimum at $T_e \approx 1 \text{ keV}$

On the other hand, for the ECH case, the $\tau = 0.005 \text{ s}$ curve is rather peaked, whilst $\tau = 0.05$ is flat, then hollow. This behavior can be understood from figure 6.22 which shows the radiation function of argon for the considered values of τ as a function of temperature, when only photons with $E_{\text{photon}} > 1 \text{ keV}$ are considered (similar to figure 2.16 in section 2.3.3). The temperature profile spans values up to 3 keV at the center. At small τ the radiation increases with T_e , however at larger τ it peaks at about 1 keV (figure 2.16). The profile will peak around the radius where $T_e = 1 \text{ keV}$, as seen in figure 6.23(b). The experimental impurity density is obtained by dividing the soft x-ray emissivity by the modelled specific emissivity:

$$n_Z^{\text{exp}} = P_{\text{sxr}}^{\text{exp}} / \left(\frac{P_{\text{sxr}}}{n_{\text{imp}}} \right). \quad (6.13)$$

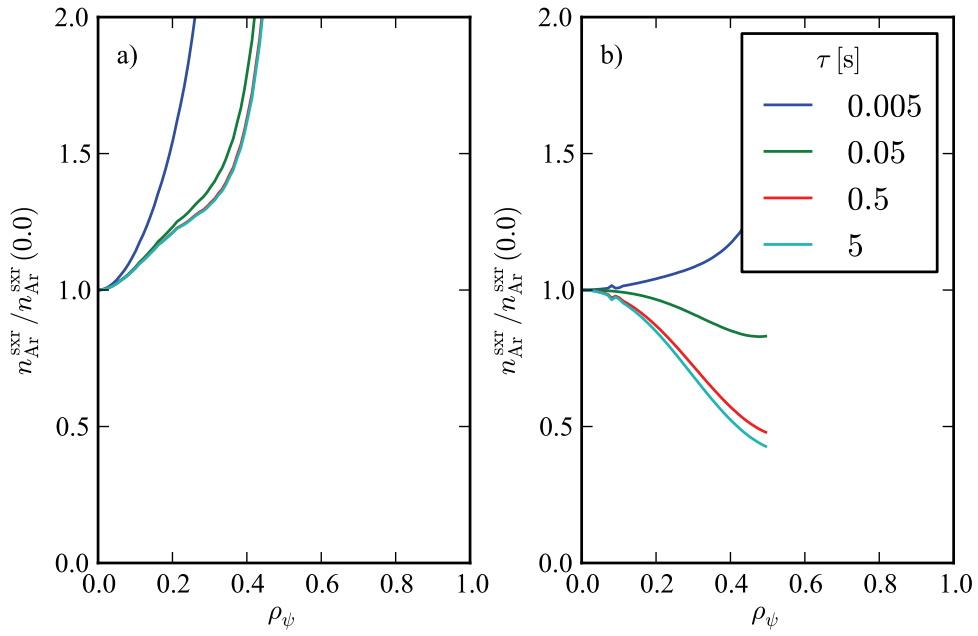


Figure 6.23: Relative argon density profiles $n_{\text{Ar}}/n_{\text{Ar}}(0)$ from the experimental SXR emissivity (figure 5.26) and the modelled specific power (figure 6.21) for different argon confinement times.

$P_{\text{SXR}}^{\text{exp}}$ is a result of a tomographic inversion and given in arbitrary units, therefore only the relative values n_Z^{exp} are meaningful. n_Z^{exp} normalized to its central value is shown in figure 6.23 for the OH and ECH cases. For the OH case in figure 6.23 (a) n_Z^{exp} is hollow for all τ up to $\rho_\psi \approx 0.3$. The sudden increase between $\rho_\psi = 0.3 - 0.5$ means that the modelled emissivity decays much faster than that measured. The DMPX detectors are also sensitive to photons lower than 1 keV, which means that modelled emissivity from the lower temperature regions has been underestimated.

The ECH case shows, on the other hand, a flat or peaked profile. As discussed above this comes in a large part from the hollow modelled radiated power per impurity atom (figure 6.21). Since peaked or hollow n_Z profiles are interpreted in terms of local transport properties the sensitivity of the results need to be checked. This will be discussed in the next chapter.

6.5 On the central profile of $n_Z(\mathbf{r})$

As shown in the previous section, the resulting $n_Z(r, t)$ profiles tend to be very hollow outside $\rho \approx 0.4$, where the SXR diagnostic is not sensitive leading to positive values of V . Here, a scan of D and V are performed on the results obtained for the low and high current cases of the current scan.

Starting from the $I_p = 130$ kA, case, figures 6.16 and 6.17 the resulting V profiles are multiplied by a factor of $[1, 0.5, -0.5, 1.]$, keeping D constant. In figure 6.24 the resulting n_Z profiles are shown displaying significant variation in the center. However, the effects on the normalized $\epsilon_{\text{SXR}}(r, t)$, figure 6.25, are very small. A positive V allow a slightly broader profile to be obtained. Since the experimental profile (dashed) is broader than that simulated (solid) a positive V is obtained from the inverse method.

Using the most negative V from the previous scan and scaling D by a factor of 1, 2 and 5, it is seen again a large change in n_Z and a limited effect on ϵ_{SXR} (figures 6.26 and 6.27). This shows the limitation that n_Z^{exp} not directly measured and the strong dependence of ϵ_{SXR} on $T_e(r)$.

If we look, on the other hand the time evolution of the central SXR chord (figures 6.28 and 6.29), it is seen, that mainly the value of D changes the rise and decay time. This is similar for the high current scan (figures 6.30 and 6.31) except in this case the V term also influences the decay rate. For completeness, we also show in figures 6.32-6.35 $n_Z(r, z)$ and

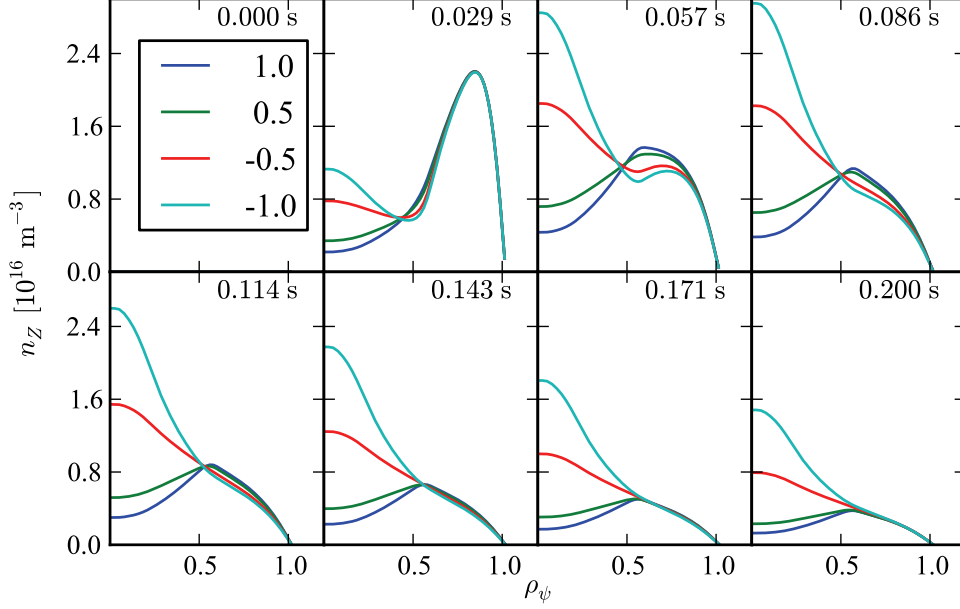


Figure 6.24: Scaling V starting from the transport coefficients obtained for #42314 with $I_p = 130$ kA (see figure 6.16), the total impurity density profile evolution for different scaling factors.

$\epsilon_{\text{sxr}}(r, t)$ for the V and D scaling starting from the $I_p = 300$ kA profiles (figure 6.16).

6.6 Summary

A new method based on the direct solution of impurity transport system of equations using the STRAHL code and the inverse solution using the matricial approach (MA) for the equations of the total impurity density was presented. This is similar to the recent work of Sertoli et al. [2011] on AUG-U, except they used the gradient flux method to solve the inverse problem to find the value of D and V . D and V can be assumed constants in time and for all the charge states if the experiment is perturbative, which was shown to be the case in the previous chapter. We have shown that our method is correctly implemented by testing it on a simulated reference case. We have also seen that the MA method is more reliable near the center where the gradients are small as compared to the GF method. The

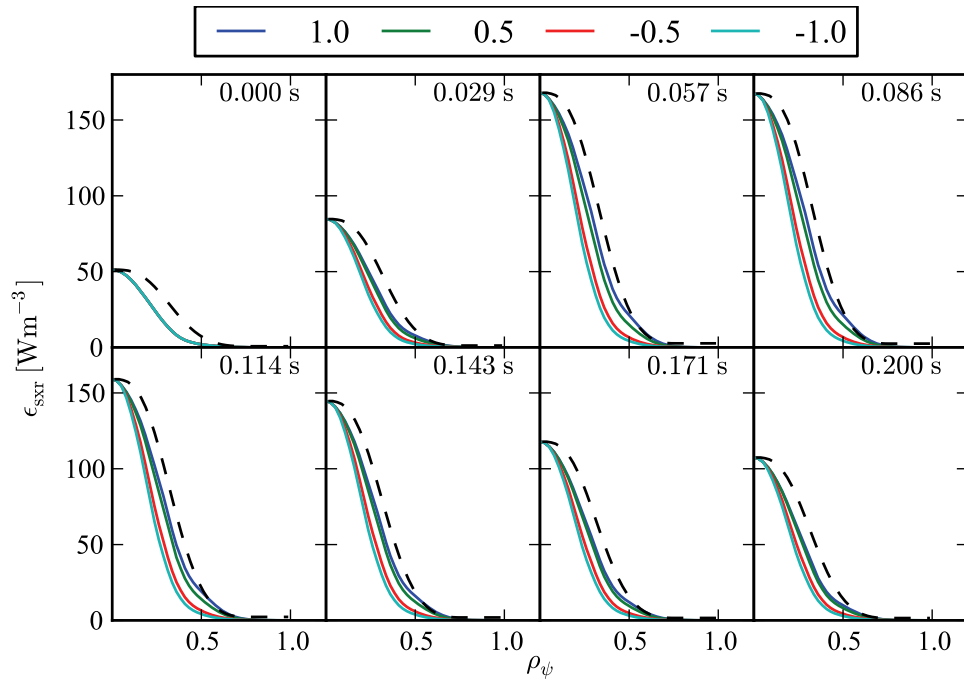


Figure 6.25: Scaling V starting from the transport coefficients obtained for #42314 with $I_p = 130$ kA (see figure 6.16), the simulated SXR emissivity normalized to the maximal value of the experimental emissivity (dashed) for different scaling factors.

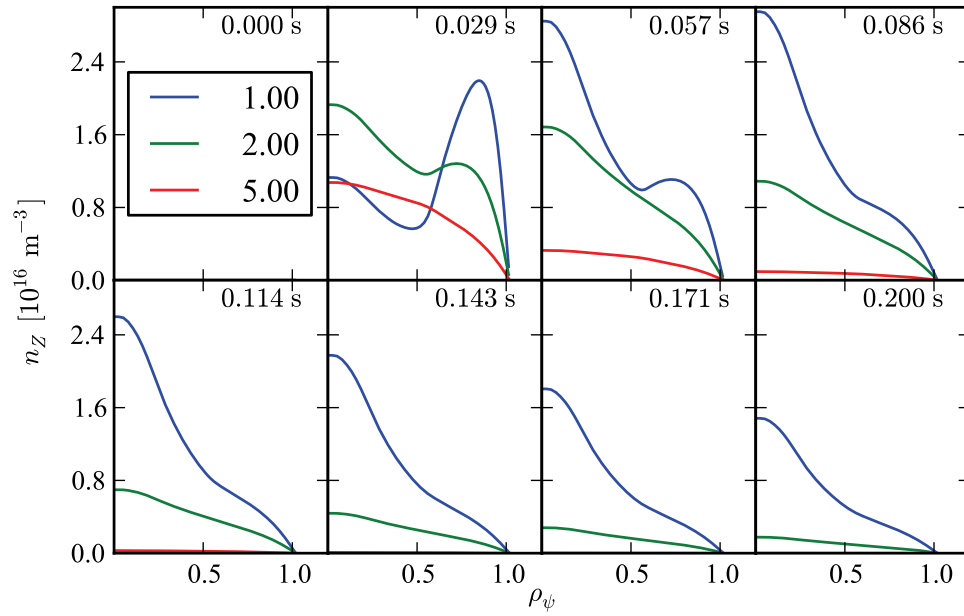


Figure 6.26: Scaling D starting from the transport coefficients obtained for #42314 with $I_p = 130 \text{ kA}$ (see figure 6.16), the total impurity density profile evolution for different scaling factors.

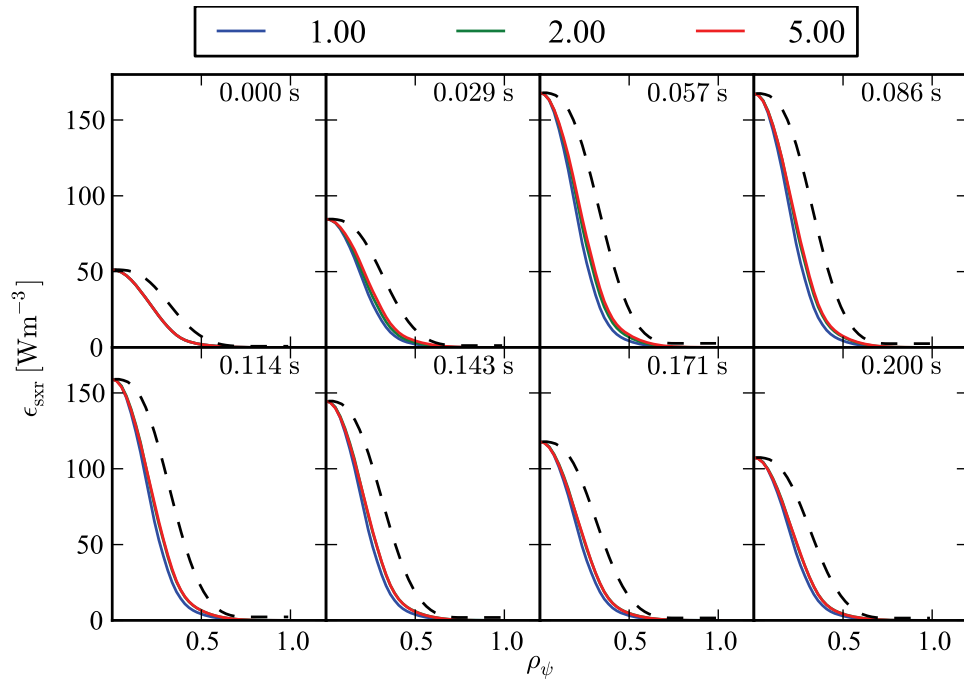


Figure 6.27: Scaling D starting from the transport coefficients obtained for #42314 with $I_p = 130$ kA (see figure 6.16), the simulated SXR emissivity normalized to the maximal value of the experimental emissivity (dashed) for different scaling factors.

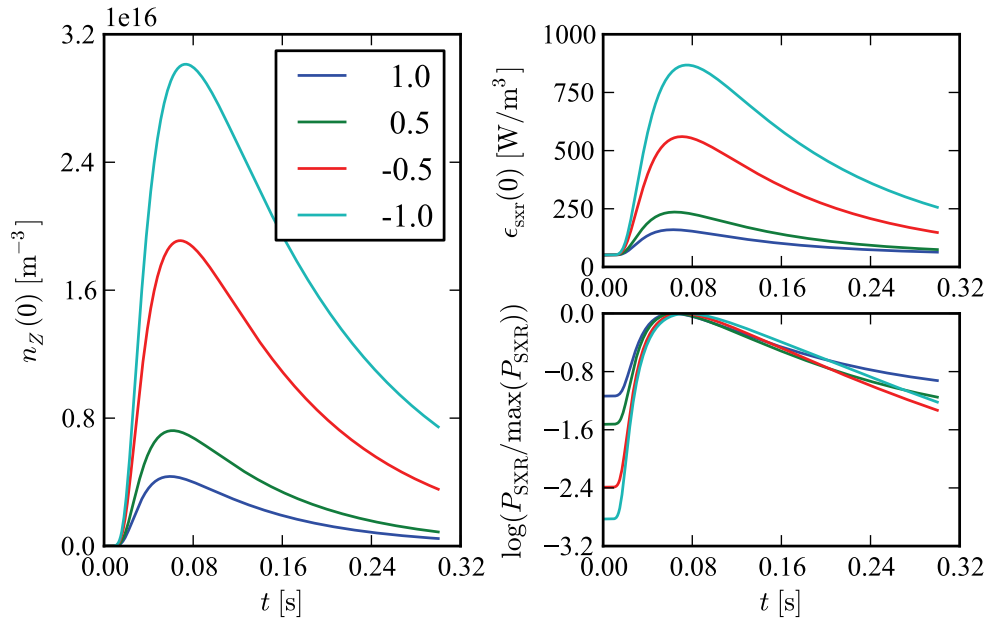


Figure 6.28: Scaling V starting from the transport coefficients obtained for #42314 with $I_p = 130$ kA (see figure 6.16), the central impurity density and SXR emissivity evolution for different scaling factors.

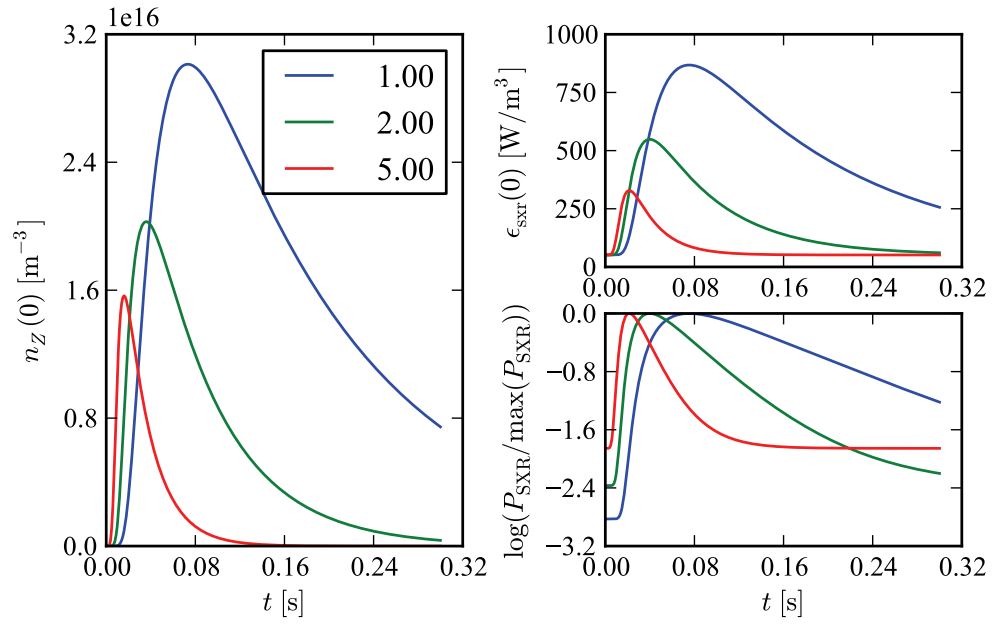


Figure 6.29: Scaling D starting from the transport coefficients obtained for #42314 with $I_p = 130$ kA (see figure 6.16), the central impurity density and SXR emissivity evolution for different scaling factors.

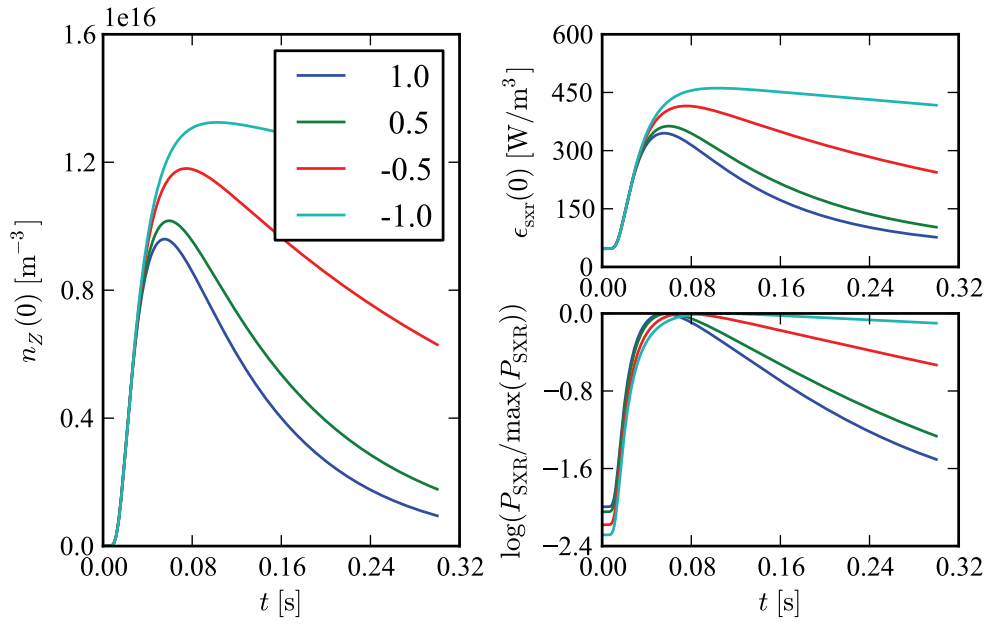


Figure 6.30: Scaling V starting from the transport coefficients obtained for #42313 with $I_p = 300$ kA (see figure 6.16), the central impurity density and SXR emissivity evolution for different scaling factors.

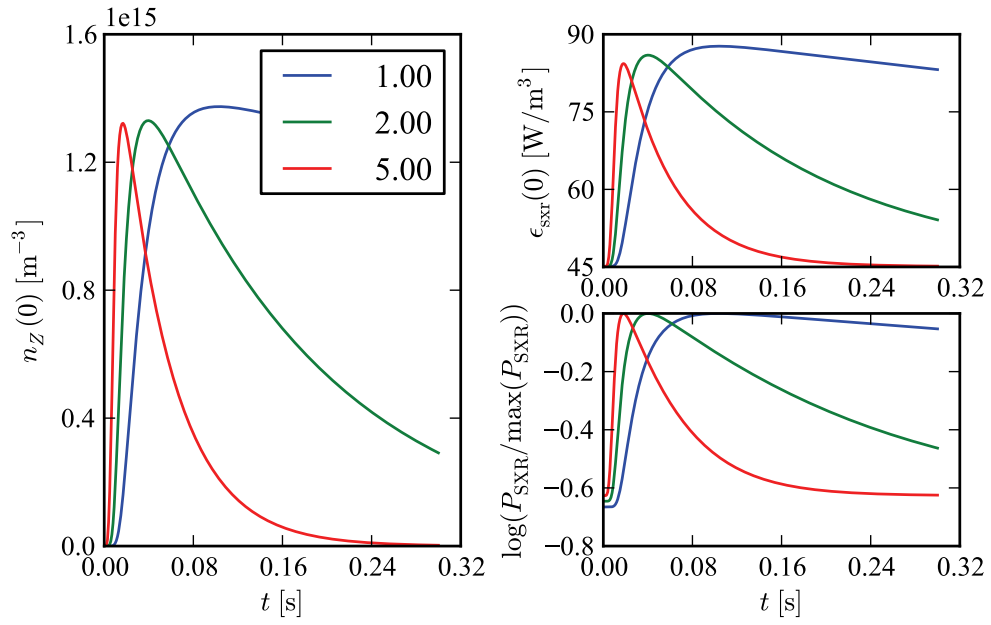


Figure 6.31: Scaling D starting from the transport coefficients obtained for #42313 with $I_p = 300$ kA (see figure 6.16), the central impurity density and SXR emissivity evolution for different scaling factors.

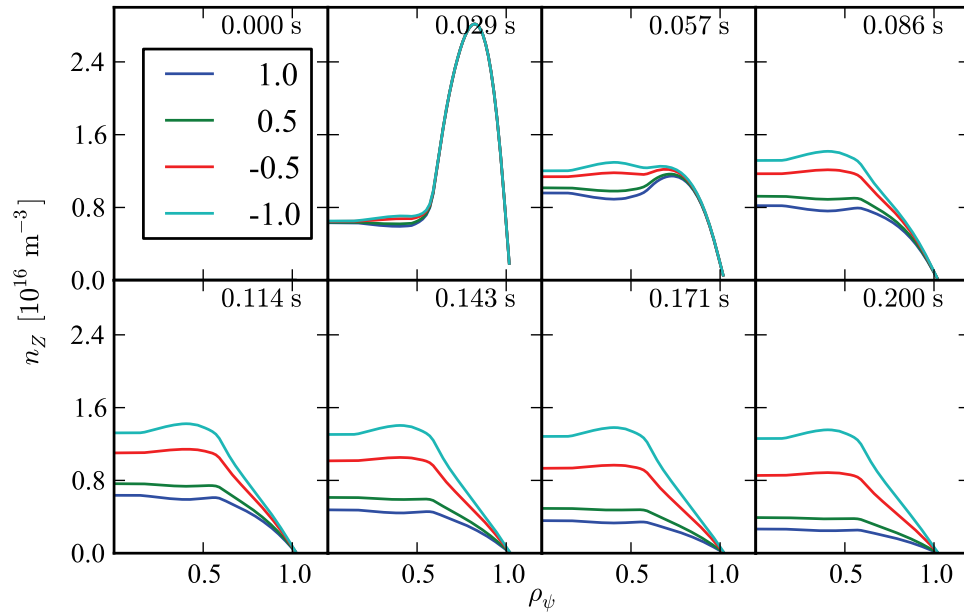


Figure 6.32: Scaling V starting from the transport coefficients obtained for #42313 with $I_p = 300 \text{ kA}$ (see figure 6.16), the total impurity density profile evolution for different scaling factors.

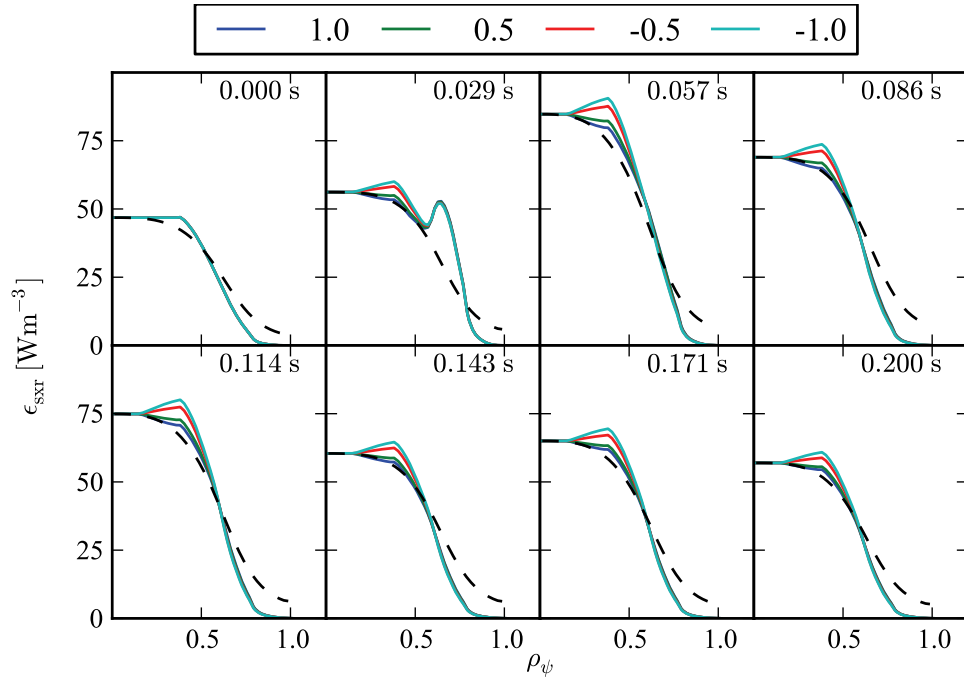


Figure 6.33: Scaling V starting from the transport coefficients obtained for #42313 with $I_p = 300 \text{ kA}$ (see figure 6.16), the simulated SXR emissivity normalized to the maximal value of the experimental emissivity (dashed) for different scaling factors.

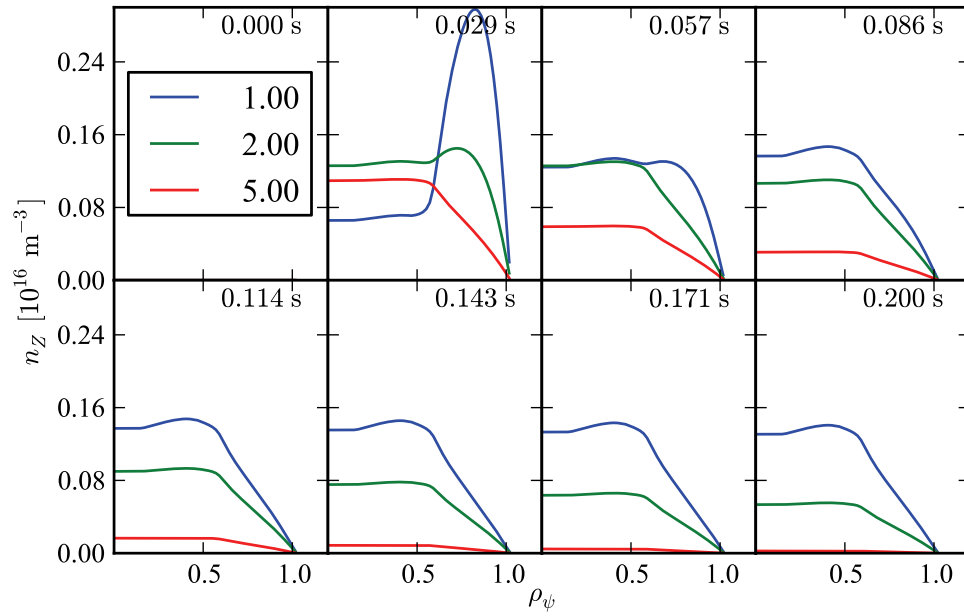


Figure 6.34: Scaling D starting from the transport coefficients obtained for #42313 with $I_p = 300 \text{ kA}$ (see figure 6.16), the total impurity density profile evolution for different scaling factors.

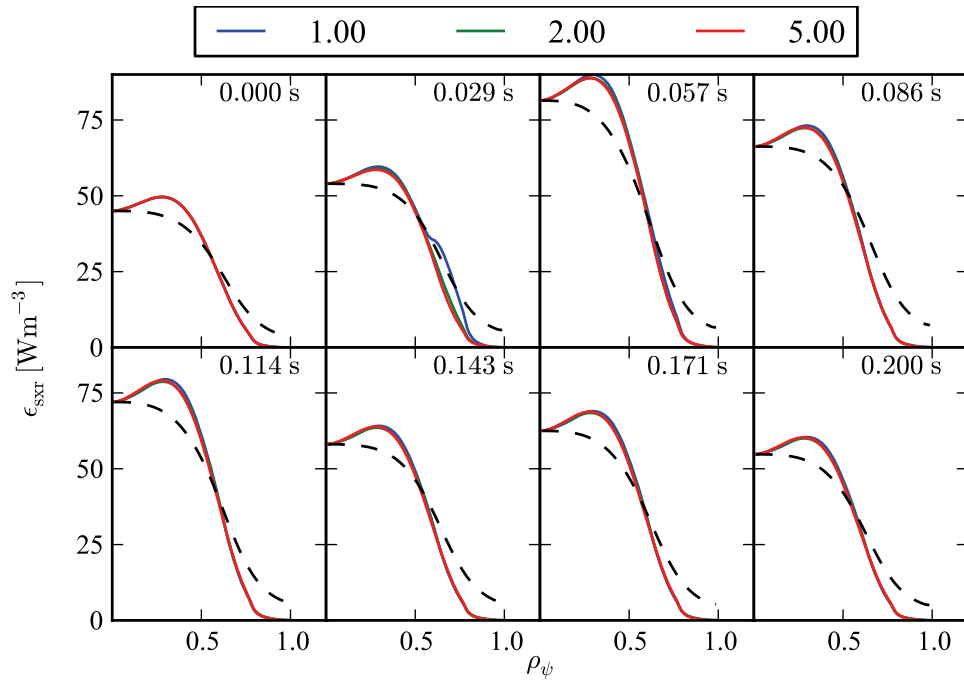


Figure 6.35: Scaling D starting from the transport coefficients obtained for #42313 with $I_p = 300$ kA (see figure 6.16), the simulated SXR emissivity normalized to the maximal value of the experimental emissivity (dashed) for different scaling factors.

standard method using a minimization procedure and the direct solution is often limited by the choice of the form of D and V .

The OH, ECH as well as the current scan experiments were simulated and D and V profiles were found reproducing the time evolution of the SXR measurements. The advection velocity V was found to be positive and negative. Analysing the stationary experiments (obtained with multiple puffs) and the sensitivity of ϵ_{SXR} on varying D and V in the current scan, it was showed that the sign of V is not well constrained. This is due to the difficulty to model accurately the ϵ_{SXR} peaking, since it is strongly influenced by the temperature profile, in particular and the location of the inversion radius. The restriction of ϵ_{SXR} to small radii (typically $\rho_\psi < 0.4$ limits greatly the determination of the sign of V , even in stationary cases.

It was demonstrated that the time evolution of the combined rise and decay of the central chord is a good indication of confinement properties. We have shown that that recycling and the effective pulse shape needs to be taken into account.

Chapter 7

Summary and conclusions

This thesis has been devoted to electron and impurity transport studies on the TCV tokamak. The electron particle transport analysis was based on previous work related to L-mode plasmas and electron internal transport barriers [Fable et al., 2008, Fable, 2009, Fable et al., 2010] and extended to H-mode plasmas. Gyrokinetic quasi-linear simulations, using the GS2 code [Kotschenreuther et al., 1995], have been used to successfully predict density profile peakedness in TCV H-mode plasmas.

The analysis of electron particle transport in H-mode (Chapter 3) was motivated by the observation that the density peaking factor increased with increasing collisionality [Maslov et al., 2006], contrary to most other reported experiments [Weisen et al., 2006, Angioni et al., 2011] and also been observed in T-10 [Razumova et al., 2009]. A database of H-mode discharges with well-diagnosed density and temperature profiles was constructed in order to better understand the relative importance of the various plasma parameters. We found that not only did the collisionality vary, but also T_e/T_i , R/L_{Te} , R/L_{Ti} and the Ware pinch. Gyrokinetic simulations using the method defined by Fable et al. [2010] and the results of linear GS2 runs have been performed. The conditions for stationary states with zero particle flux near $\rho_\psi = 0.6$ have been determined for a range of parameters. The main result is that the model can, indeed, predict an increase of R/L_n with increasing collisionality. The simulations show, in addition, that this is not due to the collisionality in itself, that has a weak effect on the turbulence in these cases, but to the change of T_e/T_i , L_{Ti}/L_{Te} and the Ware pinch. These parameters changed, in particular, because high collisionality high density cases are ohmic H- modes, whilst low collisionality cases are EC heated H-modes on TCV. This complex dependence of R/L_n on the background plasma parameters was

demonstrated to be related, as in L- mode plasmas, to the competition between TEM and ITG modes. R/L_n is, thus, much better determined when the average mode frequency $\langle\omega_r\rangle$ is considered [Fable et al., 2010]. R/L_n is maximum near $\langle\omega_r\rangle \approx 0$ and decreases towards TEM dominated ($\langle\omega_r\rangle < 0$) or ITG dominated ($\langle\omega_r\rangle > 0$) plasmas. The TCV cases have been shown to evolve from TEM dominated towards $\langle\omega_r\rangle$ slightly positive, leading to an increase of R/L_n in spite of an increased collisionality. Taking our results, combined with AUG results [Angioni et al., 2011] and TCV L-modes [Fable et al., 2010], shows that a general dependence of R/L_n on $\langle\omega_r\rangle$ can be determined. This should allow the development of simpler predictive models for particle transport. Nevertheless, our studies should, in the future, be pursued with nonlinear gyrokinetic simulations, in particular to examine cases closer to marginal stability.

The impurity transport studies were motivated by earlier TCV results showing unexpected positive V/D values and decreasing transport properties with increasing elongation and current [Scavino, 2002]. More recent results on other tokamaks did not show such effects and found little dependence of the transport coefficients on the impurity charge Z . The laser blow-off diagnostic was no longer available on TCV, so another diagnostic tool was developed. This was achieved by modifying the massive gas injector first intended for disruption studies. After development, sufficient control of the gas injected was obtained and permitted the injection of small, localized (in time) gas puffs. The development and commissioning of this diagnostic is presented in Chapter 4.

Impurity transport has been studied recently in several tokamaks, in particular AUG [Sertoli et al., 2011, Angioni et al., 2011], C-Mod [Howard et al., 2012] JET [Giroud et al., 2007, Puiatti et al., 2006] and Tore Supra [Guirlet et al., 2009, 2010]. As mentioned above, our studies were also motivated by earlier TCV results [Scavino, 2002]. A large part of this thesis work was dedicated in developing and commissioning a new system, a multi-purpose gas injection system based on the massive gas injector, such that it could be used for impurity transport experiments (Chapter 5). This was required as the laser blow-off diagnostic has, in the meanwhile, been removed and dismantled. We have also developed a chain of analysis tools (Chapter 6) to solve the system of transport equations for the impurities, for comparison with the SXR measurements (including the link to ADAS atomic database) and to obtain an estimate of the effective D and V radial profiles. These transport coefficients can be assumed constant if the gas injected does not perturb significantly the background plasma parameters. The multi-purpose gas injector has been

shown to fulfil this task, since the kinetic profiles (n_e and T_e) do not change during the presence of the injected impurities. Several experiments were performed (Chapter 5). We have first shown, by changing the plasma vertical position, that for argon the time evolution of the central SXR chord does not depend on the location of the gas injection, as long as it directly impinges the plasma boundary. In addition, the time evolution is essentially independent of the poloidal angle, and can be modeled with one dimensional radial simulation. The resulting decay time ($\approx 100 - 200$ ms) is about ten times slower than the rise time (≈ 15 ms). Neon, on the other hand, behaves very differently, showing almost no decay and cumulating with successive injection puffs. New experiments have been proposed related in particular to the role of recycling, in order to better understand these differences that remain extremely difficult to comprehend since both are noble gases.

The density level did not show a significant effect on impurity transport. On the other hand, a clear slower rise and decay is observed with higher plasma current. Although expected from other machines it was not clearly observed in earlier TCV experiments [Scavino, 2002]. We have, however, shown that the effect of sawteeth and that of the SXR sensitivity is restricted to the central region can hinder the modeling (Chapter 6).

The studies related to the effects of plasma shape (elongation, triangularity and diverted/ limited) did not show a significant effect. Due to this limited dependence, analysis showed that they are all inter-related, including the effects of boundary conditions and recycling. It was concluded that new experiments, dedicated to study these coupled shape effects should be designed if these effects are to be separated.

The new analysis tools for impurity transport on TCV were developed, benchmarked and preliminary results shown in Chapter 6. The recycling coefficient and the exact input pulse shape were shown to require better determination if small effects on transport are to be studied. In addition, the analysis would greatly benefit from a new diagnostic capable of measuring directly the impurity density, even at just two radial positions. This is due to the "natural" peaking of the SXR radiation and the strong dependence on the peaked temperature profile. This suggests new experimental studies using off-axis ECH could be used to provide a broad and high T_e profile.

The new analyses, using the inverse solution, does allow very different $V(r)$, $D(r)$ profiles to be obtained, including possible $V(r)$ sign changes (related to hollow profiles) which is harder to obtain usually with a minimization method. However the problem of the sign of V remains. It has been shown to be related to the sensitivity of the SXR

measurements to $T_e > 500$ eV and to $\rho_\psi \leq 0.4$.

The experimental and simulation results of impurity transport show that in this domain it is extremely difficult to obtain a clear observation. Therefore this thesis attempts to highlight these difficulties and demonstrate their avoidance , where possible, in the hope of facilitating further studies in the domain.

Appendix A

Direct and inverse solution of diffusive-advective systems

Equation 2.6 is in a form

$$\partial_t n = -\nabla \cdot \Gamma(n) + S, \quad \Gamma = -D\nabla n + Vn \quad (\text{A.1})$$

This system is called *diffusive-advective*, because the flux Γ is expressed as a diffusive and advective term, characterized by the transport coefficients D and V . Equation A.1 expresses the conservation of n ; indeed, by integrating over a bound volume Ω and using the divergence theorem one obtains:

$$\frac{d}{dt} \int_{\Omega} n \, dV = - \int_{\partial\Omega} \Gamma \, dA + \int_{\Omega} S \, dV. \quad (\text{A.2})$$

This balance equation has a very natural meaning [Raviart, 1996]: the time variation of $\int_{\Omega} n \, dV$ is equal to the sum of losses through the boundary $\partial\Omega$ and the sources/sinks in the domain. In this appendix the direct and inverse solution of systems of the form of A.1 is presented.

A.1 Direct solution with finite elements

The direct solution of the system A.1 means obtaining $n(r, t)$ for given D and V and $S(r, t)$. The literature on the analytical and numerical solution of such system is vast [Raviart,

1996]. For simple model studies we implement the numerical solution with finite elements. The detailed numerical analysis of the impurity injection experiments is done with the STRAHL code which also provides a direct solution of a diffusive-advective system.

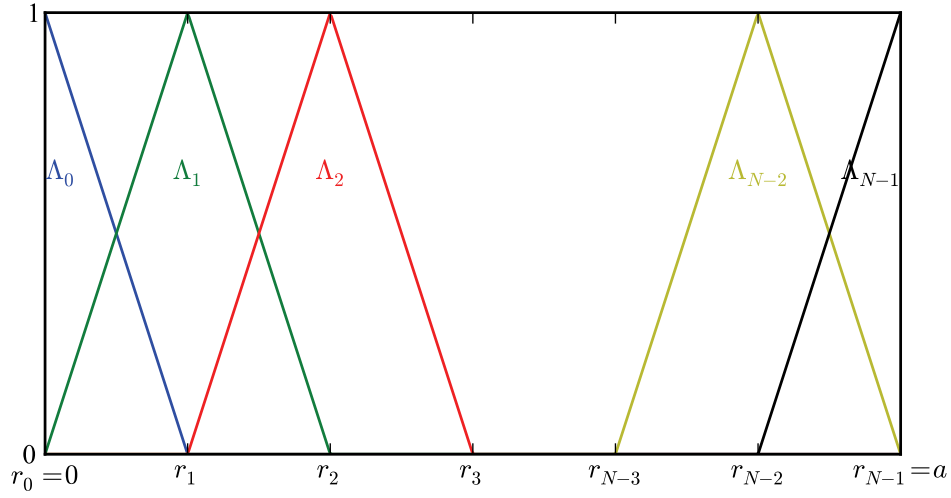


Figure A.1: Linear basis functions used in the solution with the finite elements method.

The first step of the derivation is to arrive to the weak form of A.1 by multiplying it by a test function η and integrating over a bound domain. The terms containing a full divergence are transformed to surface integrals over the boundary of the domain using Green's identity:

$$\int_{\Omega} (\psi \nabla \cdot \Gamma + \Gamma \cdot \nabla \psi) dV = \int_{\partial\Omega} \psi (\Gamma \cdot n) dS \quad (\text{A.3})$$

The left hand side is:

$$\frac{\partial}{\partial t} \int_{\Omega} \eta n dV. \quad (\text{A.4})$$

The first term of the right hand side becomes

$$\begin{aligned} \int_{\Omega} \eta \cdot \nabla \cdot (-D \nabla n + V n) dV &= \int_{\partial\Omega} \eta (-D \nabla n + V n) \underline{n} dS \\ &\quad - \int_{\Omega} \nabla \eta \cdot (-D \nabla n + V n) dV, \end{aligned} \quad (\text{A.5})$$

while the second term on the right hand side simply

$$\int_{\Omega} \eta S \, dV. \quad (\text{A.6})$$

We express the differential operators in cylindrical coordinates:

$$\nabla \cdot \rightarrow r^{-1} \partial_r \circ r \quad (\text{A.7})$$

$$\nabla \rightarrow \partial_r. \quad (\text{A.8})$$

Expanding η and n on the basis $\{\Lambda_i\}$:

$$\eta = \sum_j \eta_j \Lambda_j \quad n = \sum_j n_j \Lambda_j,$$

we obtain the final result

$$\begin{aligned} \sum_j \left(\left[\Lambda_i r \left(-D \frac{d\Lambda_j}{dr} + V \Lambda_j \right) \right]_0^R + \int_0^R \frac{d\Lambda_i}{dr} r \left(D \frac{d\Lambda_j}{dr} - V \Lambda_j \right) dr \right) n_j = \\ = \int_0^R S \Lambda_i r \, dr. \end{aligned} \quad (\text{A.9})$$

This in a form of a linear system

$$\sum_j A_{ij} n_j = b_i \quad (\text{A.10})$$

which can be solved by standard techniques. Using the first order basis functions depicted in Figure A.1 the A matrix is tridiagonal.

Figure A.2 shows the amplitude and the phase of the solution for $\omega = [0, 2, 20]$ with the parameters $D = 0.5$, $V = -0.5r$ and $S = \exp[(r - 0.8)^2 / 0.2^2]$. As expected from the negative (inward) advection velocity, the stationary solution ($\omega = 0$) is peaked. As the frequency increases, the peakedness of the amplitude decreases and the perturbation at the edge is less and less influential in the core. In other words the diffusive-advective system at the center (near $r = 0$) behaves as a low-pass filter, and sufficiently low frequencies are required to 'probe' the center with harmonic perturbations at the edge.

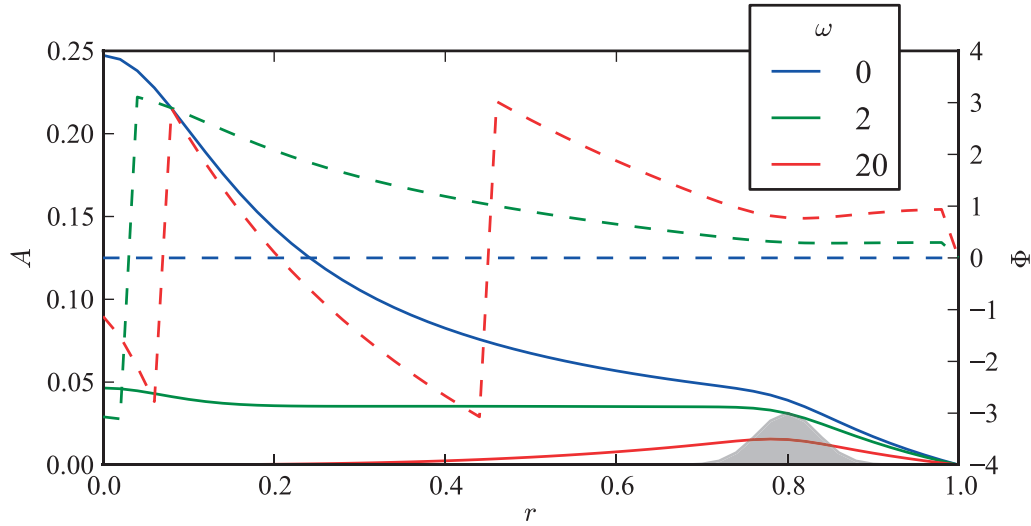


Figure A.2: Amplitude (solid) and phase (dashed) of the solution for different frequencies ω . The shaded are represents the localisation of the source.

A.2 Inverse solution

The inverse solution of the system A.1 means obtaining D and V for given $n(r, t)$ and $S(r, t)$. That is if one measures the system's spatio-temporal response to a given perturbation, the underlying characteristics of the system can be deduced. We saw in Chapter 6 that interpretation of transport experiments requires one to go in this direction. The solution of inverse problems is an even more formidable task than that of the direct problem. In this appendix we review two methods that were proposed recently to support such transport experiments.

A.2.1 Matricial approach

The *matricial approach* method was proposed by Escande and Sattin [2012]. For the sake of completeness we outline the derivation presented there. We note that Sattin et al. [2012] extends this paper with more discussion and examples of experimental data analysis. It is interesting to note that this method was already proposed, in a different context, by Fable [2009], however it was not exploited as completely as by Escande and Sattin [2012].

Equation A.1 is Fourier-transformed and written in cylindrical geometry using r as

radial coordinate

$$-i\omega n_\omega = r^{-1} \partial_r [r (D \partial_r n - V n)] + S_\omega, \quad (\text{A.11})$$

where n_ω is the system's response to a harmonic perturbation with amplitude S_ω and angular frequency ω . After integrating this equation with respect to r and using the boundary condition $\Gamma(r=0) = 0$ we arrive to:

$$M \cdot Y = \Gamma \quad (\text{A.12})$$

$$Y = \begin{pmatrix} D \\ V \end{pmatrix},$$

$$M = \begin{bmatrix} -A' \cos \varphi + A \varphi' \sin \varphi & A \cos \varphi \\ -A' \sin \varphi - A \varphi' \cos \varphi & A \sin \varphi \end{bmatrix},$$

$$\Gamma = \begin{bmatrix} r^{-1} \int_0^r dz z (S_r(z) - \omega A(z) \sin \varphi(z)) \\ r^{-1} \int_0^r dz z (S_i(z) + \omega A(z) \cos \varphi(z)) \end{bmatrix} \quad (\text{A.13})$$

where $A' \equiv \frac{dA}{dr}$ and $n = A(r) \exp(i\varphi(r))$.

From the experimental data the linear system A.12 can be assembled and solved by standard techniques. We see that inverse solution requires to know $n(r, t)$ and most importantly its derivatives $\frac{\partial n}{\partial r}$, $\frac{\partial n}{\partial t}$. Therefore the experimental data must be smoothed accordingly.

Figure A.3 compares the initial and reconstructed transport coefficients obtained by solving the inverse problem followed by the direct solution of Equation A.1. The example is shown in dimensionless cylindrical coordinates where $r \equiv r_{\text{vol}}$ with $D = 0.5$, $V = -0.5r$, $S = \exp[(r - 0.8)^2 / 0.2^2]$ and $\omega = 1$. The direct solution is obtained using the finite elements method described above. We can see that the agreement is very good except in the region where the source is localized and the problem is singular [Sattin et al., 2012].

A.2.2 Gradient-flux method

The linear relationship between the gradient and flux is evident in the diffusive-advective equation. This relation was used recently in the context of impurity transport in Sertoli et al. [2011]. From the expression of Γ in A.1:

$$\frac{\Gamma}{n} = -D \left(\frac{\nabla n}{n} \right) + V \quad (\text{A.14})$$

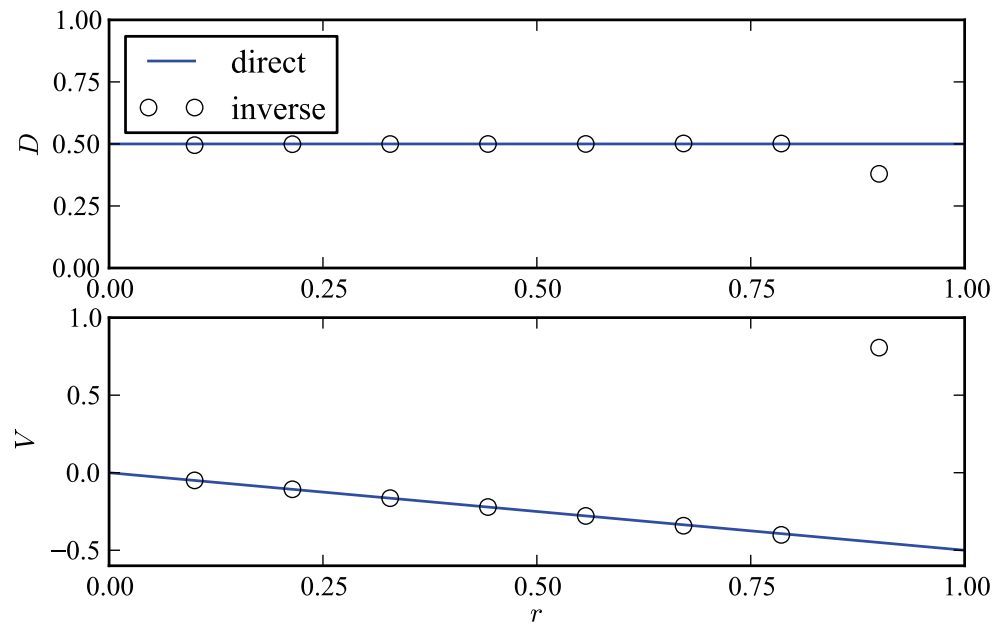


Figure A.3: Inverse solution of the diffusive advective system A.1 in cylindrical coordinates utilizing the matricial approach (MA) method.

follows. This relation states that at each radial point Γ/n is linear in $\nabla n/n$.

$$\Gamma(r_{\text{vol}}, t) = -\frac{1}{r_{\text{vol}}} \int_0^{r_{\text{vol}}} \frac{\partial n(r'_{\text{vol}}, t)}{\partial t} r'_{\text{vol}} \, dr'_{\text{vol}} \quad (\text{A.15})$$

where $r_{\text{vol}} = \sqrt{V/(2\pi^2 R_{\text{mag}})}$ with V being the volume enclosed by the flux surface.

For each radial point D and V can be determined performing a linear fit. It is interesting to note that r_{vol} is a very convenient coordinate to describe radial transport, since the transport equation remains similar for arbitrarily shaped plasmas.

Bibliography

- S. Alberti, G. Arnoux, L. Porte, J.P. Hogge, B. Marletaz, P. Marmillod, Y. Martin, S. Nowak, and the TCV team. Third-harmonic, top-launch, ECRH experiments on TCV tokamak. *Nuclear Fusion*, 45(11):1224, 2005. doi:10.1088/0029-5515/45/11/002.
- Y. Andr  be. CRPP scientific meeting: R  duction des vibrations sur le diagnostic "Interf  rom  tre FIR", Jul 2011. URL <http://crpplocal.epfl.ch/wiki/index.php/Seminars/DetailsM?ID=1117>.
- C. Angioni and O. Sauter. Neoclassical transport coefficients for general axisymmetric equilibria in the banana regime. *Physics of Plasmas*, 7(4):1224, 2000. doi:10.1063/1.873933.
- C. Angioni, A.G. Peeters, X. Garbet, A. Manini, F. Ryter, and the ASDEX Upgrade team. Density response to central electron heating: theoretical investigations and experimental observations in ASDEX Upgrade. *Nuclear Fusion*, 44(8):827, 2004. doi:10.1088/0029-5515/44/8/003.
- C. Angioni, A.G. Peeters, F. Jenko, and T. Dannert. Collisionality dependence of density peaking in quasilinear gyrokinetic calculations. *Physics of Plasmas*, 12(11):112310, 2005a. doi:10.1063/1.2135283.
- C. Angioni, A.G. Peeters, F. Ryter, F. Jenko, G.D. Conway, T. Dannert, H.U. Fahrbach, M. Reich, W. Suttrop, the ASDEX Upgrade team, et al. Relationship between density peaking, particle thermodiffusion, ohmic confinement, and microinstabilities in ASDEX Upgrade L-mode plasmas. *Physics of Plasmas*, 12(4):040701, 2005b. doi:10.1063/1.1867492.
- C. Angioni, R. Dux, E. Fable, and A.G. Peeters. Non-adiabatic passing electron response and outward impurity convection in gyrokinetic calculations of impurity transport in

- asdex upgrade plasmas. *Plasma Physics and Controlled Fusion*, 49(12):2027, 2007a. doi:10.1088/0741-3335/49/12/006.
- C. Angioni, H. Weisen, O. Kardaun, M. Maslov, A. Zabolotsky, C. Fuchs, L. Garzotti, C. Giroud, B. Kurzan, P. Mantica, et al. Scaling of density peaking in H-mode plasmas based on a combined database of AUG and JET observations. *Nuclear Fusion*, 47(9):1326, 2007b. doi:10.1088/0029-5515/47/9/033.
- C. Angioni, E. Fable, M. Greenwald, M. Maslov, A.G. Peeters, H. Takenaga, and H. Weisen. Particle transport in tokamak plasmas, theory and experiment. *Plasma Physics and Controlled Fusion*, 51(12):124017, 2009. doi:10.1088/0741-3335/51/12/124017.
- C. Angioni, R.M. McDermott, E. Fable, R. Fischer, T. Pütterich, F. Ryter, G. Tardini, and the ASDEX Upgrade team. Gyrokinetic modelling of electron and boron density profiles of H-mode plasmas in ASDEX Upgrade. *Nuclear Fusion*, 51(2):023006, 2011. doi:10.1088/0029-5515/51/2/023006.
- M. Anton, H Weisen, M J Dutch, W von der Linden, F. Buhlmann, R. Chavan, B. Marletaz, P. Marmillod, and P Paris. X-ray tomography on the TCV tokamak. *Plasma Physics and Controlled Fusion*, 38(11):1849, 1996. doi:10.1088/0741-3335/38/11/001.
- L. A. Arrington, B. D. Reed, and A. Riviera Jr. A performance comparison of two small rocket nozzles. Technical report, Glenn Research Center, 1996. URL <http://hdl.handle.net/2060/19960050633>.
- R. Balescu. *Transport processes in plasmas*. North-Holland Amsterdam, 1988.
- R. Balescu. Is Onsager symmetry relevant in the transport equations for magnetically confined plasmas? *Physics of Fluids B: Plasma Physics*, 3(3):564–579, 1991. doi:10.1063/1.859855. URL <http://link.aip.org/link/?PFB/3/564/1>.
- R. Balescu. *Aspects of anomalous transport in plasmas*. Inst of Physics Pub Inc, 2005.
- M. A. Beer. *Gyrofluid Models of Turbulent Transport in Tokamaks*. PhD thesis, Princeton University, 1994. URL <http://w3.pppl.gov/~hammett/collaborators/mbeer/afs/thesis.html>.

- K. H. Behringer. Spectroscopic studies of plasma-wall interaction and impurity behaviour in tokamaks. *Journal of Nuclear Materials*, 145:145–153, 1987. doi:10.1016/0022-3115(87)90319-9.
- K.H. Behringer and K. Büchl. Impurity transport studies in asdex by means of neon-seeded pellets. *Nuclear Fusion*, 29(3):415, 1989. doi:0.1088/0029-5515/29/3/005.
- A. Bencze. Private communication, December 2009.
- A. Bortolon. *Plasma rotation and momentum transport studies in the TCV tokamak based on charge exchange spectroscopy measurements*. PhD thesis, EPFL, Lausanne, 2009. URL <http://library.epfl.ch/theses/?nr=4569>.
- A. Bottino, O. Sauter, Y. Camenen, and E. Fable. Linear stability analysis of microinstabilities in electron internal transport barrier non-inductive discharges. *Plasma Physics and Controlled Fusion*, 48(2):215, 2006. doi:10.1088/0741-3335/48/2/004.
- C. Bourdelle, X. Garbet, F. Imbeaux, A. Casati, N. Dubuit, R. Guirlet, and T. Parisot. A new gyrokinetic quasilinear transport model applied to particle transport in tokamak plasmas. *Physics of Plasmas*, 14(11):112501, 2007. doi:10.1063/1.2800869.
- S. A. Bozhnikov, M Lehnert, K.H. Finken, M W Jakubowski, R C Wolf, R Jaspers, M Kantor, O V Marchuk, E Uzgel, G Van Wassenhove, O Zimmermann, D Reiter, and the TEXTOR team. Generation and suppression of runaway electrons in disruption mitigation experiments in textor. *Plasma Physics and Controlled Fusion*, 50(10):105007, 2008. doi:10.1088/0741-3335/50/10/105007.
- A. J. Brizard and T. S. Hahm. Foundations of nonlinear gyrokinetic theory. *Rev. Mod. Phys.*, 79:421–468, Apr 2007. doi:10.1103/RevModPhys.79.421.
- S. Brunner. *Global approach to the spectral problem of microinstabilities in tokamak plasmas using a gyrokinetic model*. PhD thesis, EPFL, Lausanne, 1997. URL <http://library.epfl.ch/theses/?nr=1701>.
- Y. Camenen. *Étude du transport d'énergie thermique dans les plasmas du Tokamak à Configuration Variable au moyen de chauffage électronique cyclotronique*. PhD thesis, EPFL, Lausanne, 2006.

- Y. Camenen, A. Pochelon, R. Behn, A. Bottino, A. Bortolon, S. Coda, A. Karpushov, O. Sauter, G. Zhuang, et al. Impact of plasma triangularity and collisionality on electron heat transport in tcv l-mode plasmas. *Nuclear fusion*, 47(7):510, 2007. doi:10.1088/0029-5515/47/7/002.
- P. G. Carolan and V. A. Piotrowicz. The behaviour of impurities out of coronal equilibrium. *Plasma Physics and Controlled Fusion*, 25:1065, 1983. doi:10.1088/0032-1028/25/10/001.
- P.G. Carolan, A. Patel, M.C. Sexton, and M.J. Walsh. First measurements of the particle confinement in a reversed field pinch by the laser ablation method. *Nuclear Fusion*, 30(12):2616, 1990. doi:10.1088/0029-5515/30/12/015.
- A. Casati, C. Bourdelle, X. Garbet, F. Imbeaux, J. Candy, F. Clairet, G. Dif-Pradalier, G. Falchetto, T. Gerbaud, V. Grandgirard, et al. Validating a quasi-linear transport model versus nonlinear simulations. *Nuclear Fusion*, 49(8):085012, 2009. doi:10.1088/0029-5515/49/8/085012.
- S. Coda. Progress and scientific results in the TCV tokamak. *Nuclear Fusion*, 51(9):094017, 2011. doi:10.1088/0029-5515/51/9/094017.
- S. Coda and The TCV Team. Overview of Recent and Current Research on the TCV Tokamak. In *24th IAEA Fusion Energy Conference*, pages OV/4–4, 2012. URL <http://www.fec2012.com/>, <https://crpplocal.epfl.ch/pinboard/papers/128614303.pdf>.
- S. Coda, S. Alberti, P. Blanchard, T.P. Goodman, M.A. Henderson, P. Nikkola, Y. Peysson, and O. Sauter. Electron cyclotron current drive and suprathermal electron dynamics in the tcv tokamak. *Nuclear Fusion*, 43(11):1361, 2003. doi:10.1088/0029-5515/43/11/008.
- S. Coda, E. Asp, E. Fable, T.P. Goodman, O. Sauter, V. S. Udintsev, R. Behn, M. A. Henderson, A. Marinoni, G. P. Turri, et al. The physics of electron internal transport barriers in the TCV tokamak. *Nuclear Fusion*, 47(7):714, 2007. doi:10.1088/0029-5515/47/7/023.
- PC De Vries, MF Johnson, B. Alper, P. Buratti, TC Hender, HR Koslowski, and V. Riccardo. Survey of disruption causes at jet. *Nuclear Fusion*, 51:053018, 2011. doi:10.1088/0029-5515/51/5/053018.

- AW Degeling, H. Weisen, A. Zabolotsky, B.P. Duval, RA Pitts, M. Wischmeier, P. Lavanchy, P. Marmillod, and G. Pochon. Axuv bolometer and lyman- α camera systems on the tev tokamak. *Review of scientific instruments*, 75(10):4139–4141, 2004. doi:10.1063/1.1787131.
- P. H. Diamond, S-I Itoh, and K Itoh. *Physical Kinetics of Turbulent Plasmas*, volume 1 of *Modern Plasma Physics*. Cambridge University Press, 2010.
- R. Dux. Private communication, August 2011a.
- R. Dux. *STRAHL User Manual*, January 2011b.
- R. Dux and A.G. Peeters. Neoclassical impurity transport in the core of an ignited tokamak plasma. *Nuclear Fusion*, 40(10):1721, 2000. doi:10.1088/0029-5515/40/10/304.
- D. R. Ernst, P. T. Bonoli, P. J. Catto, W. Dorland, C. L. Fiore, R. S. Granetz, M. Greenwald, A. E. Hubbard, M. Porkolab, M. H. Redi, et al. Role of trapped electron mode turbulence in internal transport barrier control in the Alcator C-Mod tokamak. *Physics of Plasmas*, 11(5):2637, 2004. doi:10.1063/1.1705653.
- D. R. Ernst, N. Basse, W. Dorland, C. L. Fiore, L. Lin, A. Long, M. Porkolab, K. Zeller, and K. Zhurovich. Identification of TEM turbulence through direct comparison of nonlinear gyrokinetic simulations with phase contrast imaging density fluctuation measurements. In *Proceedings of 21st IAEA Fusion Energy Conference, Chengdu, China*, number TH/1-3 in Book of Abstracts, 2006. URL http://www-pub.iaea.org/MTCD/Meetings/PDFplus/2006/cn149_BookOfAbstracts.pdf.
- D. R. Ernst, J. Lang, W. M. Nevins, M. Hoffman, Y. Chen, W. Dorland, and S. Parker. Role of zonal flows in trapped electron mode turbulence through nonlinear gyrokinetic particle and continuum simulation. *Physics of Plasmas*, 16(5):055906, 2009. doi:10.1063/1.3116282.
- D. F. Escande and F. Sattin. Calculation of transport coefficient profiles in modulation experiments as an inverse problem. *Physical Review Letters*, 108:125007, Mar 2012. doi:10.1103/PhysRevLett.108.125007.
- E. Fable. *Experimental and theoretical study of particle transport in the TCV tokamak*. PhD thesis, EPFL, Lausanne, 2009. URL dx.doi.org/10.5075/epfl-thesis-4334.

- E. Fable, C. Angioni, and O. Sauter. Gyrokinetic calculations of steady-state particle transport in electron internal transport barriers. *Plasma Physics and Controlled Fusion*, 50(11):115005, 2008. doi:10.1088/0741-3335/50/11/115005.
- E. Fable, C. Angioni, and O. Sauter. The role of ion and electron electrostatic turbulence in characterizing stationary particle transport in the core of tokamak plasmas. *Plasma Physics and Controlled Fusion*, 52:015007, 2010. doi:10.1088/0741-3335/52/1/015007.
- K.H. Finken, G. Mank, A. Krämer-Flecken, and R. Jaspers. Mitigation of disruptions by fast helium gas puffs. *Nuclear fusion*, 41:1651, 2001. doi:10.1088/0029-5515/41/11/315.
- K.H. Finken, M. Lehnen, and S. A. Bozhnikov. Gas flow analysis of a disruption mitigation valve (DMV). *Nuclear Fusion*, 48(11):115001, 2008. doi:10.1088/0029-5515/48/11/115001.
- J.P. Freidberg. *Plasma physics and fusion energy*. Cambridge University Press, 2007.
- E. A. Frieman and Liu Chen. Nonlinear gyrokinetic equations for low-frequency electromagnetic waves in general plasma equilibria. *Physics of Fluids*, 25(3):502–508, 1982. doi:10.1063/1.863762.
- J. F. Friichtenicht. Laser-generated pulsed atomic beams. *Review of Scientific Instruments*, 45(1):51–56, 1974. doi:10.1063/1.1686447.
- Ivo Furno. *Fast transient transport phenomena measured by soft x-ray emission in TCV tokamak plasmas*. PhD thesis, SB, Lausanne, 2001.
- X. Garbet, Y. Idomura, L. Villard, and T.H. Watanabe. Gyrokinetic simulations of turbulent transport. *Nuclear Fusion*, 50(4):043002, 2010. doi:10.1088/0029-5515/50/4/043002.
- C. Giroud, R. Barnsley, P. Buratti, I.H. Coffey, M. von Hellermann, C. Jupén, K.D. Lawson, A. Meigs, M. O’Mullane, A.D. Whiteford, K.-D. Zastrow, and JET EFDA Contributors. Method for experimental determination of z dependence of impurity transport on jet. *Nuclear Fusion*, 47(4):313, 2007. doi:10.1088/0029-5515/47/4/010.
- T.P. Goodman and the TCV team. Experience in integrated control of the multi-megawatt electron cyclotron heating system on the tcv tokamak: the first decade. *Nuclear Fusion*, 48(5):054011, 2008. doi:10.1088/0029-5515/48/5/054011.

- T. Görler, X. Lapillonne, S. Brunner, T. Dannert, F. Jenko, S. K. Aghdam, P. Marcus, B.F. McMillan, F. Merz, O. Sauter, et al. Flux-and gradient-driven global gyrokinetic simulation of tokamak turbulence. *Physics of Plasmas*, 18(5):056103, 2011. doi:10.1063/1.3567484.
- R. Guirlet, D. Villegas, T. Parisot, C. Bourdelle, X. Garbet, F. Imbeaux, D. Mazon, and D. Pacella. Anomalous transport of light and heavy impurities in Tore Supra ohmic, weakly sawtoothed plasmas. *Nuclear Fusion*, 49(5):055007, 2009. doi:10.1088/0029-5515/49/5/055007.
- R. Guirlet, A. Sirinelli, T. Parisot, R. Sabot, JF Artaud, C. Bourdelle, X. Garbet, P. Hennequin, GT Hoang, F. Imbeaux, et al. Particle transport in low core turbulence Tore-Supra plasmas. *Nuclear Fusion*, 50(9):095009, 2010. doi:10.1088/0029-5515/50/9/095009.
- K. Hallatschek and W. Dorland. Giant electron tails and passing electron pinch effects in tokamak-core turbulence. *Physical Review Letters*, 95(5):55002, 2005. doi:10.1103/PhysRevLett.95.055002.
- A. Hasegawa and K. Mima. Pseudo-three-dimensional turbulence in magnetized nonuniform plasma. *Physics of Fluids*, 21(1):87–92, 1978. doi:10.1063/1.862083.
- Akira Hasegawa and Masahiro Wakatani. Plasma edge turbulence. *Phys. Rev. Lett.*, 50: 682–686, Feb 1983. doi:10.1103/PhysRevLett.50.682.
- P. Helander, R. J. Akers, M. Valovič, Y. Peysson, and the MAST team. The effect of non-inductive current drive on tokamak transport. *Plasma Physics and Controlled Fusion*, 47(12B):B151, 2005. doi:10.1088/0741-3335/47/12B/S12.
- TC Hender, JC Wesley, J. Bialek, A. Bondeson, AH Boozer, RJ Buttery, A. Garofalo, T.P. Goodman, RS Granetz, Y. Gribov, et al. Mhd stability, operational limits and disruptions. *Nuclear fusion*, 47:S128, 2007. doi:10.1088/0029-5515/47/6/S03.
- F. L. Hinton and R. D. Hazeltine. Theory of plasma transport in toroidal confinement systems. *Reviews of Modern Physics*, 48(2):239–308, 1976. doi:10.1103/RevModPhys.48.239.

- SP Hirshman and DJ Sigmar. Neoclassical transport of impurities in tokamak plasmas. *Nuclear Fusion*, 21:1079, 1981. doi:10.1088/0029-5515/21/9/003.
- F. Hofmann and G. Tonetti. Tokamak equilibrium reconstruction using Faraday rotation measurements. *Nuclear Fusion*, 28(10):1871, 1988. doi:10.1088/0029-5515/28/10/014.
- F. Hofmann, J.B. Lister, W. Anton, S. Barry, R. Behn, S. Bernel, G. Besson, F. Buhlmann, R. Chavan, M. Corboz, et al. Creation and control of variably shaped plasmas in TCV. *Plasma Physics and Controlled Fusion*, 36:B277, 1994. doi:10.1088/0741-3335/36/12B/023.
- E.M. Hollmann, T.C. Jernigan, P.B. Parks, J.A. Boedo, T.E. Evans, M. Groth, D.A. Humphreys, A.N. James, M.J. Lanctot, D. Nishijima, D.L. Rudakov, H.A. Scott, E.J. Strait, M.A. Van Zeeland, J.C. Wesley, W.P. West, W. Wu, and J.H. Yu. Measurements of injected impurity assimilation during massive gas injection experiments in DIII-D. *Nuclear Fusion*, 48(11):115007, 2008. doi:10.1088/0029-5515/48/11/115007.
- W. Horton. Drift waves and transport. *Reviews of Modern Physics*, 71(3):735–778, 1999. doi:10.1103/RevModPhys.71.735.
- WA Houlberg, KC Shaing, SP Hirshman, and MC Zarnstorff. Bootstrap current and neoclassical transport in tokamaks of arbitrary collisionality and aspect ratio. *Physics of Plasmas*, 4:3230, 1997. doi:10.1063/1.872465.
- N.T. Howard, M. Greenwald, D.R. Mikkelsen, M.L. Reinke, A.E. White, D. R. Ernst, Y. Podpaly, and J. Candy. Quantitative comparison of experimental impurity transport with nonlinear gyrokinetic simulation in an Alcator C-Mod L-mode plasma. *Nuclear Fusion*, 52(6):063002, 2012. doi:10.1088/0029-5515/52/6/063002. URL <http://stacks.iop.org/0029-5515/52/i=6/a=063002>.
- I.H. Hutchinson. *Principles of Plasma Diagnostics*. Cambridge University Press, 2005. ISBN 9780521675741. URL <http://books.google.ch/books?id=pUUZKLR00RIC>.
- B. B. Kadomtsev. On disruptive instability in tokamaks. *Soviet Journal of Plasma Physics*, 1:710–715, October 1975.

- A. N. Karpushov, B. P. Duval, C. Schlatter, V. I. Afanasyev, and F.V. Chernyshev. Neutral particle analyzer diagnostics on the TCV tokamak. *Review of Scientific Instruments*, 77: 033504, 2006. doi:10.1063/1.2185151.
- M. Keilhacker, A. Gibson, C. Gormezano, P.J. Lomas, P.R. Thomas, M.L. Watkins, P. Andrew, B. Balet, D. Borba, C.D. Challis, I. Coffey, G.A. Cottrell, H.P.L. De Esch, N. Deliyanakis, A. Fasoli, C.W. Gowers, H.Y. Guo, G.T.A. Huysmans, T.T.C. Jones, W. Kerner, R.W.T. König, M.J. Loughlin, A. Maas, F.B. Marcus, M.F.F. Nave, F.G. Rimini, G.J. Sadler, S.E. Sharapov, G. Sips, P. Smeulders, F.X. Söldner, A. Taroni, B.J.D. Tubbing, M.G. von Hellermann, D.J. Ward, and JET Team. High fusion performance from deuterium-tritium plasmas in jet. *Nuclear Fusion*, 39(2):209, 1999. doi:10.1088/0029-5515/39/2/306.
- J. E. Kinsey and M. Choi. The TORAY electron cyclotron heating and current drive code. Technical report, General Atomics, La Jolla, CA 92186, April 2003. URL <http://w3.pppl.gov/NTCC/TORAY/toray.ps>. Version 1.60.
- Y. Kishimoto. Anomalous transport. *Journal of Plasma and Fusion Research*, 76(12):1280–1308, 2000. ISSN 09187928. URL <http://ci.nii.ac.jp/naid/110003825453/en/>.
- M. Kotschenreuther, G. Rewoldt, and W. M. Tang. Comparison of initial value and eigenvalue codes for kinetic toroidal plasma instabilities. *Computer Physics Communications*, 88(2-3):128–140, August 1995. doi:10.1016/0010-4655(95)00035-E.
- U. Kruezi, PD Morgan, M. Lehnen, S. A. Bozhnikov, S. Jachmich, MF Stamp, I. Coffey, S. Brezinsek, PC De Vries, G. Sergienko, et al. Massive gas injection experiments at jet-performance and characterisation of the disruption mitigation valve. In *Proc. 36th EPS Conf. on Plasma Physics Sofia, Bulgaria*, 2009. URL http://epsppd.epfl.ch/Sofia/pdf/P2_153.pdf.
- J. Lang, Y. Chen, and S.E. Parker. Gyrokinetic δf particle simulation of trapped electron mode driven turbulence. *Physics of Plasmas*, 14(14):082315, 2007. doi:10.1063/1.3567484.
- X. Lapillonne, S. Brunner, O. Sauter, L. Villard, E. Fable, T. Görler, F. Jenko, and F. Merz. Non-linear gyrokinetic simulations of microturbulence in TCV electron internal transport

- barriers. *Plasma Physics and Controlled Fusion*, 53(5):054011, 2011. doi:10.1088/0741-3335/53/5/054011.
- Xavier Lapillonne. *Local and Global Eulerian Gyrokinetic Simulations of Microturbulence in Realistic Geometry with Applications to the TCV Tokamak*. PhD thesis, SB, Lausanne, 2010.
- M. Lehnen, A. Alonso, G. Arnoux, S. A. Bozhnikov, S. Brezinsek, T. Eich, K.H. Finken, A. Huber, S. Jachmich, U. Kruezi, et al. First experiments on massive gas injection at jet-consequences for disruption mitigation in jet and iter. In *Proc. 36th EPS Conf. on Plasma Physics Sofia, Bulgaria*, 2009. URL http://epsppd.epfl.ch/Sofia/pdf2/02_001.pdf.
- H. Lütjens, A. Bondeson, and O. Sauter. The CHEASE code for toroidal MHD equilibria. *Computer Physics Communications*, 97(3):219–260, 1996. doi:10.1016/0010-4655(96)00046-X.
- Y. Martin, M. A. Henderson, S. Alberti, P. Amorim, Y. Andrébe, K. Appert, G. Arnoux, R. Behn, P. Blanchard, P. Bosshard, et al. Accessibility and properties of ELMy H-mode and ITB plasmas in TCV. *Plasma Physics and Controlled Fusion*, 45(12A):A351, 2003. doi:10.1088/0741-3335/45/12A/023.
- Y. Martin, E. Fable, C. Angioni, Y. Camenen, D. Wágner, B.P. Duval, L. Federspiel, A. Karpushov, V. Piff, O. Sauter, and H. Weisen. Impurity transport in tcv: Neoclassical and turbulent contributions. In *Proceedings of 23rd IAEA Fusion Energy Conference, Daejeon, Republic of Korea*, number EXC/P8–13, 2010. URL http://www-pub.iaea.org/mtcd/meetings/PDFplus/2010/cn180/cn180_papers/exc_p8-13.pdf.
- M. Maslov, H. Weisen, A. Zabolotsky, L. Porte, C. Angioni, M. Beurskens, and the TCV team. Density peaking in TCV and JET H-modes. In *Proceedings of the 2006 33rd EPS Conf. on Plasma Physics (Rome)*, volume 301, pages O–3.005, 2006. URL http://epsppd.epfl.ch/Roma/pdf/03_005.pdf.
- M. Maslov, C. Angioni, and H. Weisen. Density profile peaking in JET H-mode plasmas: experiments versus linear gyrokinetic predictions. *Nuclear Fusion*, 49(7):075037, 2009. doi:10.1088/0029-5515/49/7/075037.

- K. Matsuda. Ray tracing study of the electron cyclotron current drive in DIII-D using 60 GHz. *Plasma Science, IEEE Transactions on*, 17(1):6–11, feb 1989. doi:10.1109/27.21664.
- F. Merz and F. Jenko. Nonlinear interplay of TEM and ITG turbulence and its effect on transport. *Nuclear Fusion*, 50(5):054005, 2010. doi:10.1088/0029-5515/50/5/054005.
- J.M. Moret. A software package to manipulate space dependencies and geometry in magnetic confinement fusion. *Review of scientific instruments*, 76(7):073507–073507, 2005. doi:10.1063/1.1946608.
- L. Onsager and S. Machlup. Fluctuations and irreversible processes. *Phys. Rev.*, 91:1505–1512, Sep 1953. doi:10.1103/PhysRev.91.1505. URL <http://link.aps.org/doi/10.1103/PhysRev.91.1505>.
- T Parisot, R Guirlet, C Bourdelle, X Garbet, N Dubuit, F Imbeaux, and P R Thomas. Experimental impurity transport and theoretical interpretation in a tore supra lower-hybrid heated plasma. *Plasma Physics and Controlled Fusion*, 50(5):055010, 2008. doi:10.1088/0741-3335/50/5/055010.
- P.B. Parks and W. Wu. Limitations of extended gas delivery tubes used for fuelling mitigated plasma disruptions, and a unique injection concept for prompt gas delivery. *Nuclear Fusion*, 51(7):073014, 2011. doi:10.1088/0029-5515/51/7/073014.
- A.G. Peeters. Reduced charge state equations that describe pfirsch schlüter impurity transport in tokamak plasma. *Physics of Plasmas*, 7:268, 2000. doi:10.1063/1.873812.
- F. Piras, S. Coda, B. P. Duval, B. Labit, J. Marki, S.Y. Medvedev, J-M. Moret, A. Pitzschke, and O. Sauter. “Snowflake” H-mode in a tokamak plasma. *Physical Review Letters*, 105(15):155003, 2010. doi:10.1103/PhysRevLett.105.155003.
- Andreas Pitzschke. *Pedestal Characteristics and MHD Stability of H-Mode Plasmas in TCV*. PhD thesis, SB, Lausanne, 2011.
- L. Porte, S. Coda, S. Alberti, G. Arnoux, P. Blanchard, A. Bortolon, A. Fasoli, T.P. Goodman, Y. Klimanov, Y. Martin, et al. Plasma dynamics with second and third-harmonic ECRH and access to quasi-stationary ELM-free H-mode on TCV. *Nuclear Fusion*, 47(8):952, 2007. doi:10.1088/0029-5515/47/8/029.

- M. E. Puiatti, M. Valisa, C. Angioni, L. Garzotti, P. Mantica, M. Mattioli, L. Carraro, I. Coffey, and C. Sozzi. Analysis of metallic impurity density profiles in low collisionality joint european torus h-mode and l-mode plasmas. *Physics of Plasmas*, 13(4):042501, 2006. doi:10.1063/1.2187424.
- P.A. Raviart. *Numerical approximation of hyperbolic systems of conservation laws*, volume 118. Springer Verlag, 1996. ISBN 0387945296, 9780387945293.
- KA Razumova, VF Andreev, A.Y. Kislov, NA Kirneva, SE Lysenko, Y.D. Pavlov, TV Shafranov, AJH Donné, G.M.D. Hogewij, GW Spakman, et al. Tokamak plasma self-organization and the possibility to have the peaked density profile in iter. *Nuclear Fusion*, 49:065011, 2009. doi:10.1088/0029-5515/49/6/065011.
- M. Romanelli, G. T. Hoang, C. Bourdelle, C. Gormezano, E. Giovannozzi, M. Leigheb, M. Marinucci, D. Marocco, C. Mazzotta, L. Panaccione, et al. Parametric dependence of turbulent particle transport in high density electron heated FTU plasmas. *Plasma Physics and Controlled Fusion*, 49(6):935, 2007. doi:10.1088/0741-3335/49/6/016.
- F. Ryter, C. Angioni, M. Beurskens, S. Cirant, GT Hoang, G. M. D. Hogewij, F. Imbeaux, A. Jacchia, P. Mantica, W. Suttrop, et al. Experimental studies of electron transport. *Plasma Physics and Controlled Fusion*, 43:A323, 2001. doi:10.1088/0741-3335/43/12A/325.
- F Sattin, D F Escande, Y Camenen, A T Salmi, T Tala, and JET EFDA Contributors. Estimate of convection–diffusion coefficients from modulated perturbative experiments as an inverse problem. *Plasma Physics and Controlled Fusion*, 54(12):124025, 2012. doi:10.1088/0741-3335/54/12/124025.
- O. Sauter. CHEASE code repository, 2012. URL <https://crppsvn.epfl.ch/repos/CHEASE/chease/trunk/>.
- O. Sauter, C. Angioni, and Y. R. Lin-Liu. Neoclassical conductivity and bootstrap current formulas for general axisymmetric equilibria and arbitrary collisionality regime. *Physics of Plasmas*, 6(7):2834–2839, 1999. doi:10.1063/1.873240. URL <http://link.aip.org/link/?PHP/6/2834/1>.

- O. Sauter, B. P. Duval, L. Federspiel, F. Felici, T. P. Goodman, A. Karpushov, S. Puddu, J. Rossel, and the TCV team. Effects of ECH/ECCD on Tearing Modes in TCV and Link to Rotation Profile. In *23rd IAEA Fusion Energy Conference*, 2010. URL <http://www-pub.iaea.org/MTCD/Meetings/Announcements.asp?ConfID=38091>, <http://crpplocal.epfl.ch/pinboard/papers/107813702.pdf>.
- E. Scavino. *Transport of laser-ablated impurities in the TCV tokamak*. PhD thesis, Lausanne, 2002.
- C. Schlatter. *Turbulent ion heating in TCV tokamak plasmas*. PhD thesis, EPFL, Lausanne, 2009. URL dx.doi.org/10.5075/epfl-thesis-4479.
- M. Sertoli, C. Angioni, R. Dux, R. Neu, T. Pütterich, and V. Igoshina. Local effects of ECRH on argon transport in L-mode discharges at ASDEX Upgrade. *Plasma Physics and Controlled Fusion*, 53:035024, 2011. doi:10.1088/0741-3335/53/3/035024.
- David H Sharp. An overview of rayleigh-taylor instability. *Physica D: Nonlinear Phenomena*, 12(1):3–18, 1984.
- J. Stober, R. Dux, O. Gruber, L. Horton, P. Lang, R. Lorenzini, C. Maggi, F. Meo, R. Neu, J.M. Noterdaeme, et al. Dependence of particle transport on heating profiles in ASDEX Upgrade. *Nuclear Fusion*, 43(10):1265, 2003. doi:10.1088/0029-5515/43/10/030.
- H. Sugama and W. Horton. Entropy production and Onsager symmetry in neoclassical transport processes of toroidal plasmas. *Physics of Plasmas*, 3(1):304–322, 1996. doi:10.1063/1.871856.
- H. P. Summers. *ADAS - Atomic Data and Analysis Structure - User manual*. University of Strathclyde, 2nd edition, 2004. URL <http://www.adas.ac.uk/manual.php>. Version 2.7.
- B. Tál. Private communication, December 2009.
- The GS2 developer team. Gyrokinetic simulations - homepage for gs2, AstroGK, Trinity, 2012. URL <http://gyrokinetics.sourceforge.net>.
- A. J. Thornton, K. J. Gibson, J. R. Harrison, M. Lehnen, R. Martin, A. Kirk, and the MAST Team. Characterization of disruption mitigation via massive gas injection on

- mast. *Plasma Physics and Controlled Fusion*, 54(12):125007, 2012. doi:10.1088/0741-3335/54/12/125007.
- D. Wágner, E. Fable, A. Pitzschke, O. Sauter, H. Weisen, and the TCV team. Understanding the core density profile in tcv h-mode plasmas. *Plasma Physics and Controlled Fusion*, 54(8):085018, 2012. doi:10.1088/0741-3335/54/8/085018. URL <http://stacks.iop.org/0741-3335/54/i=8/a=085018>.
- Shaojie Wang. Transport formulation of the gyrokinetic turbulence. *Physics of Plasmas*, 19(6), June 2012. ISSN 1070-664X. doi:10.1063/1.4729660.
- D J Ward. The physics of DEMO. *Plasma Physics and Controlled Fusion*, 52(12):124033, 2010. doi:10.1088/0741-3335/52/12/124033.
- A. A. Ware. Pinch effect for trapped particles in a tokamak. *Physical Review Letters*, 25(1):15–17, Jul 1970. doi:10.1103/PhysRevLett.25.15.
- J. Weiland, A.B. Jarmén, and H. Nordman. Diffusive particle and heat pinch effects in toroidal plasmas. *Nuclear Fusion*, 29(10):1810, 1989. doi:10.1088/0029-5515/29/10/015.
- H. Weisen, D. Pasini, A. Weller, and A.W. Edwards. Measurement of light impurity densities and zeff in jet using x-ray tomography. *Review of Scientific Instruments*, 62(6):1531–1538, 1991. doi:10.1063/1.1142482.
- H. Weisen, A. Zabolotsky, M. Maslov, M. Beurskens, C. Giroud, and D. Mazon. Scaling of density peaking in JET H-modes and implications for ITER. *Plasma Physics and Controlled Fusion*, 48:A457, 2006. doi:10.1088/0741-3335/48/5A/S47.
- J. Wesson. *Tokamaks*, volume 149. OUP Oxford, 2011.
- J.A. Wesson, R.D. Gill, M. Hugon, FC Schüller, J.A. Snipes, D.J. Ward, D.V. Bartlett, D. J. Campbell, P.A. Duperrex, A.W. Edwards, et al. Disruptions in jet. *Nuclear Fusion*, 29:641, 1989. doi:10.1088/0029-5515/29/4/009.
- A. Zabolotsky, H. Weisen, and A. N. Karpushov. Influence of particle sources on electron density peaking in TCV and JET. *Nuclear Fusion*, 46(10):594, 2006. doi:10.1088/0029-5515/46/5/010.

Publications and Conference Contributions

Publications in referred journals as main author

- D Wágner *et. al.* Understanding the core density profile in TCV H-mode plasmas. *Plasma Physics and Controlled Fusion*, 54 (8) 085018, 2012. doi:10.1088/0741-3335/54/8/085018.

Contributions to publications in referred journals

- G Szepesi *et. al.* incl. **D Wágner** Analysis of lithium driven electron density peaking in FTU liquid lithium limiter experiments *Plasma Physics and Controlled Fusion*, accepted, 2013
- A Pochelon *et. al.* incl. **D Wágner** Recent TCV Results - Innovative Plasma Shaping to Improve Plasma Properties and Insight *Plasma Fusion Research* 7, 2502148, 2012

Conference proceedings

- D Wágner, O Sauter Impurity transport experiments in TCV L-mode plasmas. Joint Annual Meeting of SPS and ÖPG. 2011
- D Wágner *et. al.* Particle transport in TCV H-modes 37th EPS Conference on Plasma Physics. P1.1101, 2010 <http://ocs.ciemat.es/EPS2010PAP/pdf/P1.1101.pdf>

Contributions to conference proceedings

- A Pochelon, et.al. incl. **D Wágner** Recent TCV results - Innovative plasma shaping to improve plasma properties and insight. 21st International Toki Conference on Integration of Fusion Science and Technology for Steady State Operation. 2011
- F Piras et.al. incl. **D Wágner** Plasma start-up in the TCV tokamak 37th EPS Conference on Plasma Physics P 2.186. 2010 <http://ocs.ciemat.es/EPS2010PAP/pdf/P2.186.pdf>
- O Sauter et.al. incl. **D Wágner** Impurity transport in TCV: neoclassical and turbulent contributions 23th IAEA Fusion Energy Conference. 2010
- A Bencze et.al. incl. **D Wágner** Visible video diagnostic systems on TCV. International Conference on Plasma Diagnostics, Pont--Mousson, France 2010

Dávid Wágner

engineering physicist

Chemin de Pré-Fleuri 1
1006 Lausanne
Switzerland

+41 77 480 4346

wagdav@gmail.com

STRONG POINTS

- theory–experiment liaison
- wide range of computational skills
- early adopter of new technologies
- project coordination experience in an international team

EDUCATION

Ecole Polytechnique Fédéral de Lausanne

PhD (physics) — 2008-2013

Doctoral thesis work

- studied transport processes related to nuclear fusion oriented plasma physics in EPFL's largest experimental facility (TCV)
- developed computational models to help the theoretical understanding of the influence of the different experimentally controllable parameters.

Responsible of the visible video diagnostic systems

- coordinated a major upgrade of two video camera systems
- improved the image quality and plant control integration

Scientific program coordinator of the institute's PhD seminars

- acquired a broad overview of the lab's different research areas.
- the seminar series improved the professional interaction between the PhD students.

Budapest University of Technology and Economics

MSc (engineering physicist) — 2003-2008

Master thesis work

- numerical simulation of fuelling magnetically confined nuclear fusion plasmas
- analysed numerical methods to solve partial differential equations of conservation laws
- extended a hydrodynamic code to model the ablation of cryogenic pellets.

I participated in the edition of a English-Hungarian plasma physics specific technical dictionary.

SKILLS

- deep knowledge of computer languages (Python, C, C++)
- broad knowledge of information technologies (Linux based systems, networking, distributed version control, database systems)
- expert in numerical modelling
- experienced in organising, team coordination
- problem solving attitude

LANGUAGES

- Hungarian (mother tongue)
- English (fluent)
- French (proficient)
- German (beginner)

PERSONAL

Born 1 December 1984, unmarried

Hungarian citizenship with Swiss residency permit B

